Dijet Angular Decorrelation with the ATLAS Detector at the LHC

A Dissertation Presented

by

Julia Gray

to

The Graduate School

in Partial Fulfillment of the

Requirements

for the Degree of

Doctor of Philosophy

in

Physics

Stony Brook University

May 2012

Stony Brook University
The Graduate School

Julia Gray

We, the dissertation committee for the above candidate for the Doctor of Philosophy degree, hereby recommend acceptance of this dissertation.

Professor Michael Rijssenbeek - Dissertation Advisor
Department of Physics

Professor George Sterman - Chairperson of Defense
C. N. Yang Institute of Theoretical Physics

Professor Thomas Hemmick
Department of Physics

Dr. Michael Begel
Brookhaven National Laboratory

This dissertation is accepted by the Graduate School

Charles Taber
Interim Dean of the Graduate School

Abstract of the Dissertation

Dijet Angular Decorrelation with the ATLAS Detector at the LHC

by

Julia Gray

Doctor of Philosophy

in

Physics

Stony Brook University

2012

The Large Hadron Collider at CERN is a proton-proton collider where gluon-gluon interactions dominate. Many of the hadron collider's signatures for Stand Model processes and for physics beyond the Standard Model involve gluons in the initial state. It is important then that the gluon evolution be well understood. The angular decorrelation between the two highest momentum jets in an event can be used to study the dynamics of multi-jet events. The differential cross-section has been measured as a function of the opening angle in ϕ and the opening angle in y between the two highest momentum jets in an event, using $\int \mathcal{L} dt = 36\,\mathrm{pb}^{-1}$ of proton-proton collisions collected by the ATLAS detector in 2010. The resulting cross-section has been compared with predictions for several Monte Carlo generators and a NLO calculation. The sub-leading jet is required to have a transverse momentum greater than 80 GeV with the leading most jet bounded by transverse momentum regions where the lowest p_T>110 GeVand the highest p_T> 800 GeV. All jets are required to be within $|y| < 2.8$ to be considered.

To my husband, Ty Gray,
my guidepost on the path of life.

May we share countless more adventures
as we discover the universe in our daily lives.

Contents

List of Figures

List of Tables

Acknowledgements

I would like to thank my adviser, Michael Rijssenbeek, for his invaluable advice and perspective during my thesis. I would especially like to thank those individuals with whom I worked closely during the completion of my dissertation project: Stephanie Majewski, for her day to day guidance, tireless answering of questions, and dispensing of advice; Michael Begel, for listening through many dinners as my work progressed lending insight and direction; and the University College of London group, for future extensions to this work. I would also like to thank my thesis committee: Michael Begel, Thomas Hemmick, Michael Rijssenbeek, and George Sterman. Their comments and feedback were instrumental in improving my thesis.

Chapter 1

Introduction

The Large Hadron Collider (LHC) is an accelerator and a proton-proton collider at the Conseil Europenne pour la Recherche Nuclaire (CERN) situated outside of Geneva, Switzerland on the Franco-Swiss border. The accelerator has four main experiments situated around the main ring as well as several special purpose experiments. The four main experiments are the ALICE, ATLAS, CMS, and LHCb detectors. ALICE is designed to study heavy ion collisions and LHCb looks at b-quark physics. The ATLAS and CMS detectors are both general purpose experiments designed to have the best identification and measurement resolution for leptons (electrons, muons, and taus) and quark and gluon jets over the largest possible solid angle. While intended primarily for the study of proton-proton collisions, ATLAS and CMS also study heavy ion collisions periods. This thesis concerns itself with the full dataset of $\int \mathcal{L} dt = (36 \pm 4)\,\mathrm{pb}^{-1}$ taken during 2010 with the proton-proton collisions provided by the LHC collider operating at 3.5 TeV per beam.

1.1 CERN

CERN was founded in 1954 and has grown to include 20 member states as well as 44 observer and non-member states and scientific contacts with an additional 19 states. Approximately half of the world's particle physicists currently use the facilities at CERN to conduct their research. The LHC began operating in 2008, and by 2009 had produced the highest center-of-mass (CM) energy collisions in the world. The CM energies of the collisions at the LHC have continued to break records, setting a new record in 2010 with CM energy collisions of 7 TeV. The LHC has also provided the highest intensity beams at any high energy physics experiment with a luminosity of $3 \times 10^{33} \mathrm{cm}^{-2}\mathrm{s}^{-1}$ in 2011. The capacity for fundamental science in high energy physics will continue to increase in the coming years of the LHC.

1.2 The Large Hadron Collider

The design energy of the LHC [1] [2] [3] is a CM energy of 14 TeV. Reaching the design energy involves training of the superconducting accelerator magnets as well as experience in running the machine as the machine will reach energies in excess of seven times the previously highest energy machine in the world. In the 2010 run, the accelerator was able to reach CM collisions at 7 TeV setting a new record for the world's most energetic proton-proton collisions.

The LHC is 27 km in circumference. The protons are first produced in a Duoplasmatron and accelerated in the linear accelerator (LINAC) 2, and then accelerated in increasingly energetic synchrotrons before being injected into the LHC, passing through the proton synchrotron booster (PSB), proton synchrotron (PS), and super proton synchrotron (SPS) respectively, see Fig. 1.1 [3].

The Duoplasmatron takes the place of the older generation of Cockcroft-Waltons. The Duoplasmatron is an ion beam source. A hot cathode filament introduces electrons into a vacuum along with H_2 gas. The gas is ionized by interactions with the electrons and then accelerated by charged plates. The beam leaves the Duoplasmatron through a small aperture. The beam is then accelerated in the LINAC 2 and PSB before being passed to the PS, where the protons are accelerated to an energy of 25 GeV. At the time of the PS's turn-on in 1959, it was the world's highest energy particle accelerator.

The protons are then passed to the SPS which is 7 km in circumference for further acceleration. In 1983, the SPS was responsible for the discovery of the W and Z bosons earning the 1984 Nobel Prize for C. Rubbia and S. van der Meer. The SPS uses room temperature magnets to bend the protons while accelerating them to an energy of 450 GeV. The protons are then injected to the LHC for their final round of acceleration.

The LHC is 27 km in circumference and guides protons or heavy ions around its ring with superconducting magnets. The superconducting magnets must be cooled to a temperature of about 2 K. As of 2010, the proton beams had reached a CM energy of 7 TeV. The protons are accelerated to reach this final energy before collision at one of the four main experiments ATLAS, CMS, LHCb, and ALICE.

1.3 The Experiments

The LHC is designed to deliver the world's highest energy collisions to the four main experiments situated around the ring, see Fig. 1.2 [2]. While much is understood through the theory and experimental confirmation of the Standard Model, see Chap. 3, this cannot be the entire story. By collecting information at the LHC experiments ATLAS, CMS, LHCb, and ALICE, the gaps in our understanding can hopefully be filled.

1.3.1 ATLAS

ATLAS (A Toriodal LHC ApparatuS) [4] [5] is one of two general purpose detectors on the LHC. ATLAS is the detector used in this analysis. By volume, it is the largest high energy particle detector ever built. The detector consists of several different sub-detectors. The inner detector provides tracking and measures the momentum of charged particles bending in the magnetic field provided by the detector's solenoid magnet. The calorimeter provides energy measurement with both electromagnetic and hadronic calorimetry. The calorimeters are surrounded by a large toriodal air core magnet instrumented with muon tracking detectors. The muon spectrometer identifies and measures the momentum of muons.

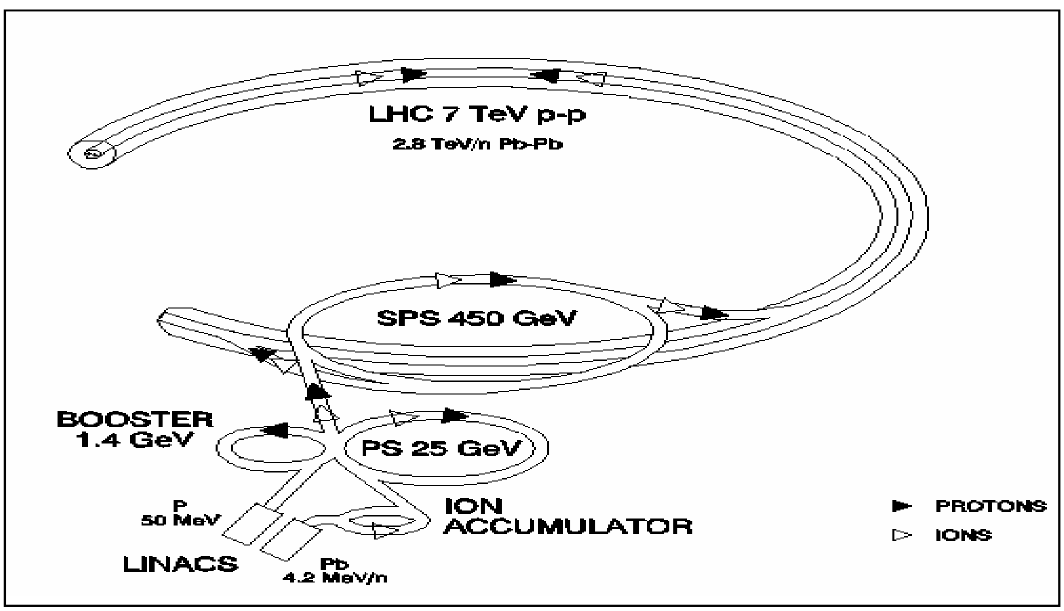

Figure 1.1: The CERN accelerator complex and the LHC (not to scale).

The detectors together provide full coverage in ϕ and extensive coverage in rapidity. The data collected by the detector is managed through a series of trigger decisions, deciding whether the event is of interest and should be written to storage. The large amount of coverage, capacity for handling data, and variety of detectors allows the ATLAS detector the flexibility needed to be involved in many different kinds of particle searches. In Chap. 2, the ATLAS detector will be described in detail.

1.3.2 CMS

CMS (Compact Muon Solenoid) [6] [7] is the other of the two general purpose detectors at the LHC. The operation of two general purpose detectors with different detector technologies allow for competition and cross checking of important results.

The CMS detector has several layers used for tracking and identification. The pixel and silicon tracker provide the tracking information. The preshower, electromagnetic calorimeter, and hadronic calorimeter are used for energy measurement and particle identification. The muon detectors are layered within the solenoid magnet. These detectors together allow for flexible particle searches with this general purpose detector.

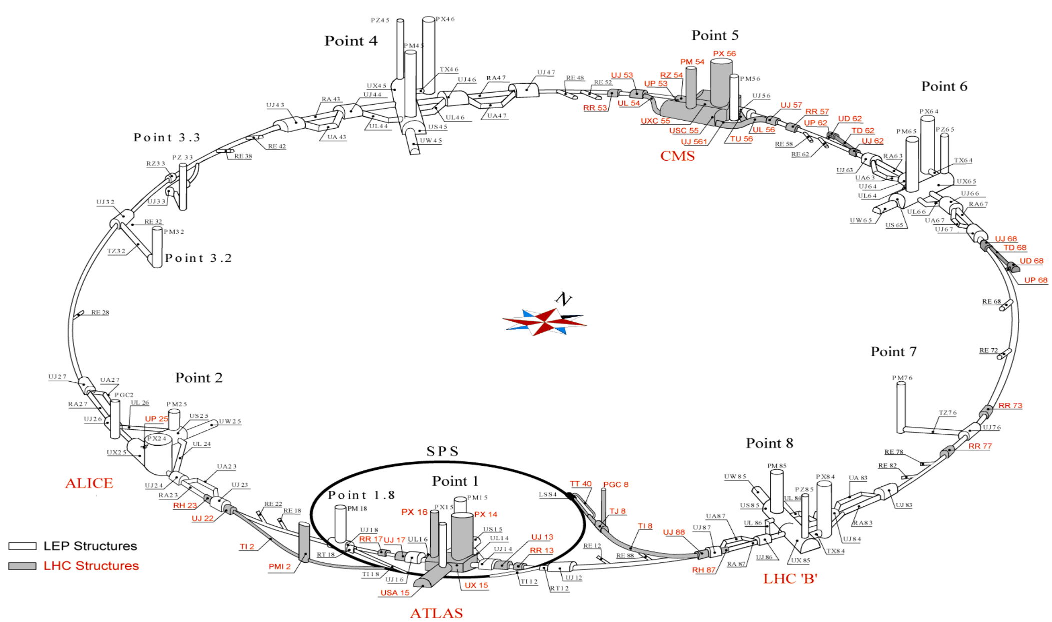

Figure 1.2: The four main experiments at CERN situated around the LHC.

The distinguishing characteristics of the CMS detector are its high-field solenoid, extensive silicon inner tracker, and a scintillating crystal electromagnetic calorimeter.

1.3.3 LHCb

LHCb (Large Hadron Collider beauty) [8] is specifically designed to detect beauty quarks (b-quarks). The experiment will try to measure the difference in production of and decay to antimatter and matter to explain the matter-antimatter asymmetry that is present in the current universe.

To take advantage of the large forward production of quarks at the LHC, the LHCb detector has a single forward spectrometer design. There are tracking detectors close to the interaction point followed by magnets. These tracking detectors are known as the Vertex Locator (VELO) and are used to measure the b hadron decay length. After the magnet, there are electromagetic calorimeter, hadronic calorimeter, and muon system for particle identification.

1.3.4 ALICE

ALICE (A Large Ion Collider Experiment) [9] [10] utilizes heavy ions accelerated by the LHC instead of protons for its experiment. ALICE was built to study the properties of heavy ion collisions, especially a state of matter resulting from collisions called the quark-gluon plasma. The detector consists of a central barrel close to the interaction point and a single forward muon detector. These sub-detectors are used in the tracking and identification of particles created in the heavy ion collisions.

The detectors closest to the interaction point are used in tracking. The tracking consists of a pixel detector, which is situated closest to the beam line, as well as a drift chamber and silicon strip detectors moving out from the beam. The Time Projection Chamber (TPC) is used for momentum and ionization measurement allowing for particle identification at "low" p_T and the Transition Radiation Detector (TRD) is used for electron identification.

The particle identification is aided by further timing resolution provided by the time of flight (TOF) detectors and with the High Momentum Particle Identification (HMPID) component. Electron identification is done using this information along with the information from the TRD. The muon spectrometers are used to identify and meausre muons.

Chapter 2

ATLAS

ATLAS [4] [5] [11] is one of four main experiments situated along the LHC. ATLAS was commissioned as a general purpose detector. In order to satisfy the needs of a broad base physics program, the detector must have complete coverage in ϕ and high rapidity coverage. It must have accurate tracking, precision electromagnetic and hadronic calorimetry, and muon identification. The detector must be able to handle the large collision rate at the design luminosity of 10^{34} cm^{-2} s^{-1}. The data rate is managed with several levels of fast trigger decisions.

The ATLAS detector and it's subcomponents are oriented around the beam line, see Fig. 2.1. The coordinate system used to describe the position of the particles in the detector with z, ϕ, and rapidity (y). The x-axis is oriented with the positive direction toward the center of the ring, and the y-axis is oriented with the positive direction toward the surface. The z-axis is defined as $z = \hat{x} \times \hat{y}$. The positive and negative z-axis correspond to the A-side and C-side, respectively, of the detector. The azimuthal coordinate (ϕ) is defined as the angle with the positive x-axis in the x, y plane. See Fig. 2.2 for illustration of coordinate system [12]. The rapidity (y) of a particle with momentum $\vec{p} = (p_x, p_y, p_z)$ and energy E is defined as:

$$y \equiv \frac{1}{2} \ln \left(\frac{E + p_z}{E - p_z} \right) = \frac{1}{2} \ln \left(\frac{1 + \beta \cos\theta}{1 - \beta \cos\theta} \right), \tag{2.1}$$

where θ is the polar angle of the particle with the z-axis and $\beta \equiv \frac{p}{E} = \frac{v}{c}$ the velocity of the particle in units of lightspeed c. In the limit of a particle of mass $m = 0$ ($\beta = 1$ and $|\vec{p}| = E$), rapidity becomes a simple function of polar angle equal to the definition of pseudorapidity (η):

$$\eta \equiv \frac{1}{2} \ln \left(\frac{1 + \cos\theta}{1 - \cos\theta} \right) = -\log \left(\tan \frac{\theta}{2} \right) \tag{2.2}$$

For the study of dijet azimuthal and rapidity decorrelation, an accurate jet detection and measurement is needed. The measurement of jets largely takes place in the ATLAS calorimeters, so I will discuss those in more detail in Sec. 2.2. The ATLAS detector is discussed more generally in the following sections.

2.1 Inner Detector

The inner detector is surrounded by a solenoid magnet which bends the charged particles for momentum measurement and aids in their identification. The inner detector of ATLAS consists of several subdetectors: pixel, semiconductor tracker, and transition radiation tracking (TRT) detectors. Each of the subdetectors consists of a set of barrel layers surrounding the beam pipe near the center and end-cap disks layers located in the forward direction from the interaction point to measure forward particle radiation, see Fig. 2.3.

The resolutions and coverage of each component are shown in Tab. 2.1.

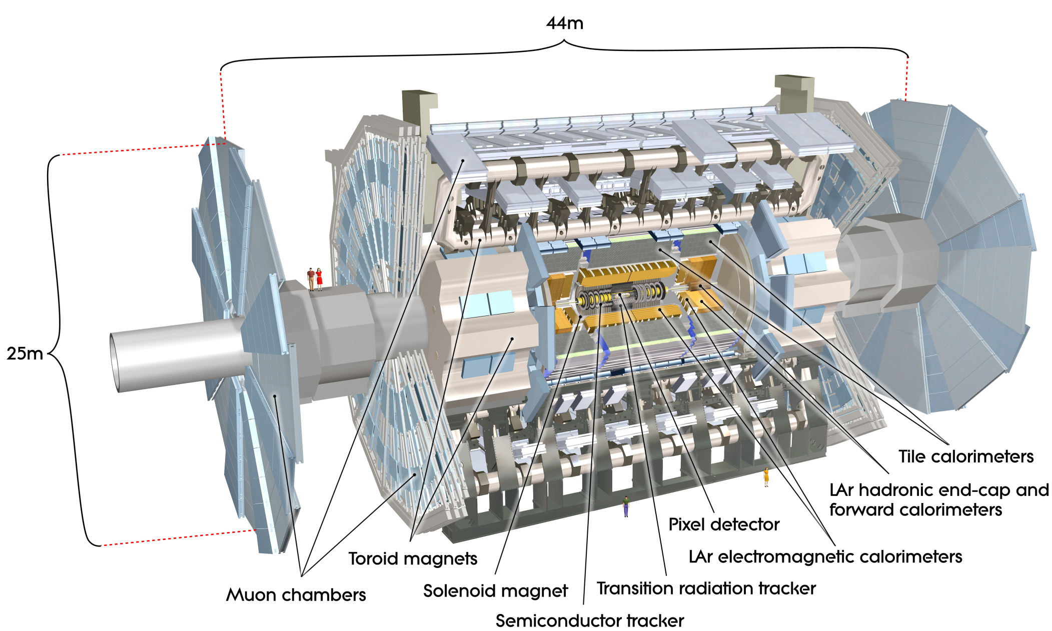

Figure 2.1: The ATLAS detector and its components. People are shown in figure to give scale.

Table 2.1: Inner detector components.

System	Position	Resolution σ (μm)	η Coverage
Pixels	Removable barrel layer (B-layer)	Rϕ: 12, z: 66	$\pm$2.5
	2 Barrel layers	Rϕ: 12, z: 66	$\pm$1.7
	5 end-cap disks per side	Rϕ: 12, R: 77	$\pm$1.7-2.5
SCT	4 barrel layers	Rϕ: 16, z: 580	$\pm$1.4
	9 end-cap wheels per side	Rϕ: 16, R: 580	$\pm$1.4-2.5
TRT	Axial barrel straws	170 (per straw)	$\pm$0.7
	Radial end-cap straws	170 (per straw)	$\pm$0.7-2.5

2.1.1 Pixel Detector

The pixel detector is designed to provide the most extensive coverage close to the interaction point because vertex information is important for many studies. However, being close to the interaction point requires the pixel detector to be radiation hard.

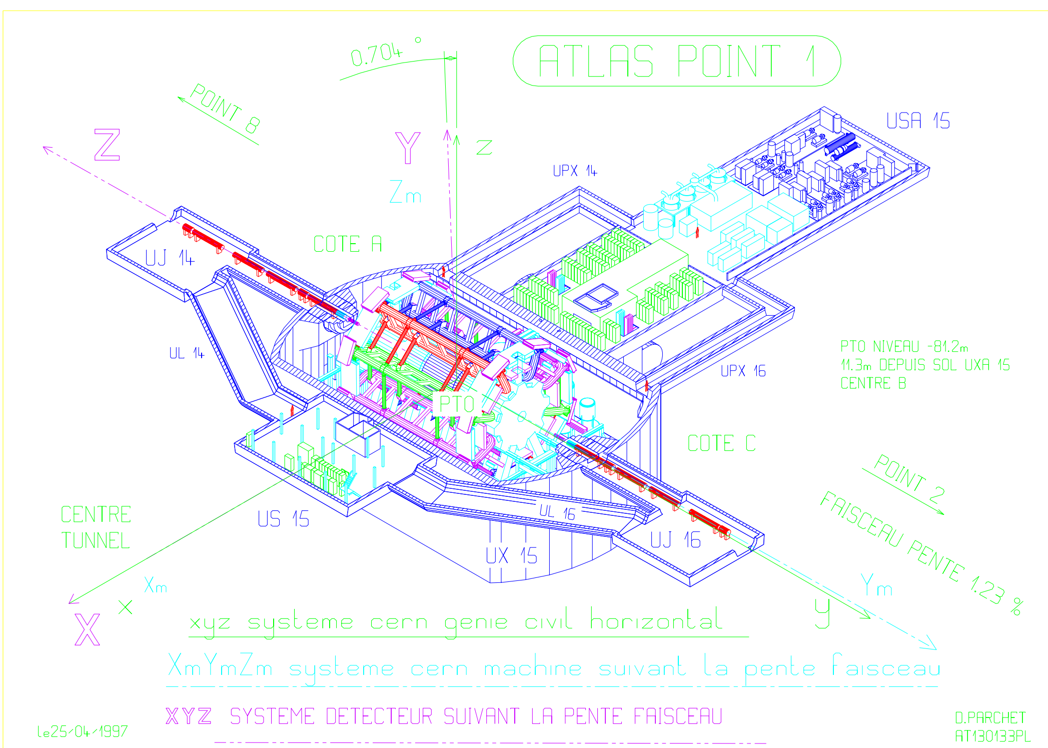

Figure 2.2: The coordinate system for the ATLAS detector.

The pixel detector provides full ϕ coverage and extends up to $\eta = 2.5$. The detector is a silicon pixel detector which provides two dimensional coverage, the next generation of silicon detectors. Each pixel readout chip is bump-bonded to the substrate of the detector. There are 61,440 pixel elements read out by 16 chips in each pixel module. There are 1,500 barrel modules and 700 disk modules.

Reading out two dimensions of particle track information requires sophisticated electronics. The charge signals are read out directly from the pixels by the bump bonded readout chip. That information is sent to a separate clock-and-control circuit and information is stored in a buffer while awaiting the Level 1 (L1) trigger decision which decides whether the information should be read out. The pixel modules are arranged in an overlapping pattern, see Fig. 2.4 [13].

2.1.2 Semiconductor Tracker

The semiconductor tracker (SCT) is a silicon strip detector. The strips have a high granularity. There are eight barrel layers of silicon strip detectors

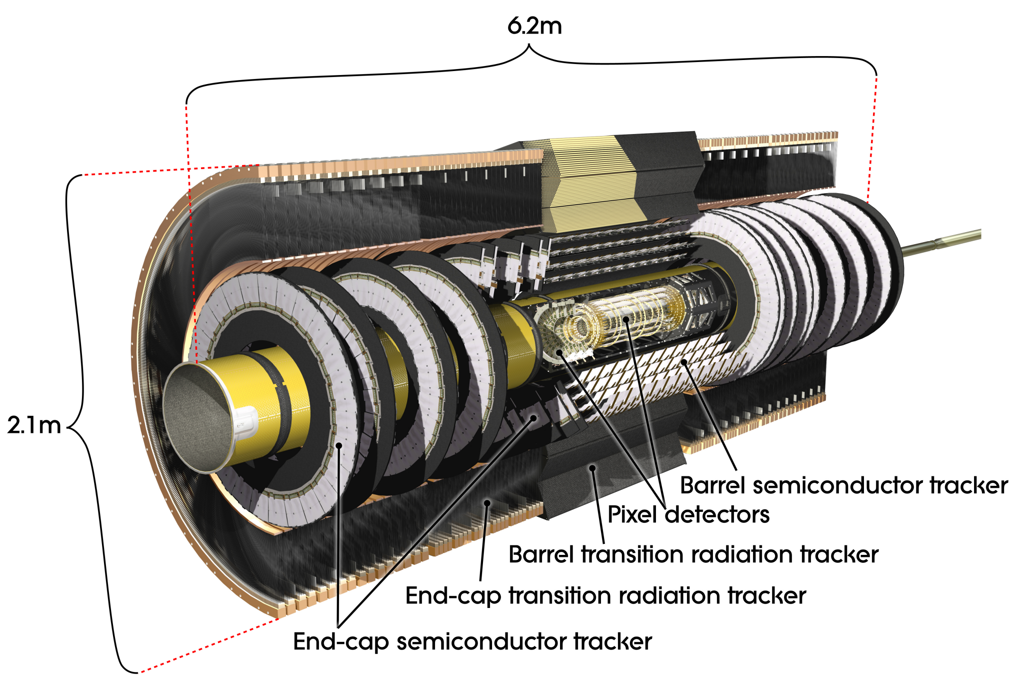

Figure 2.3: Three-dimensional view of the ATLAS Inner Detector.

that provide eight precision r, ϕ-coordinates for track reconstruction.

The SCT must withstand a high flux of radiation because of high lumi-

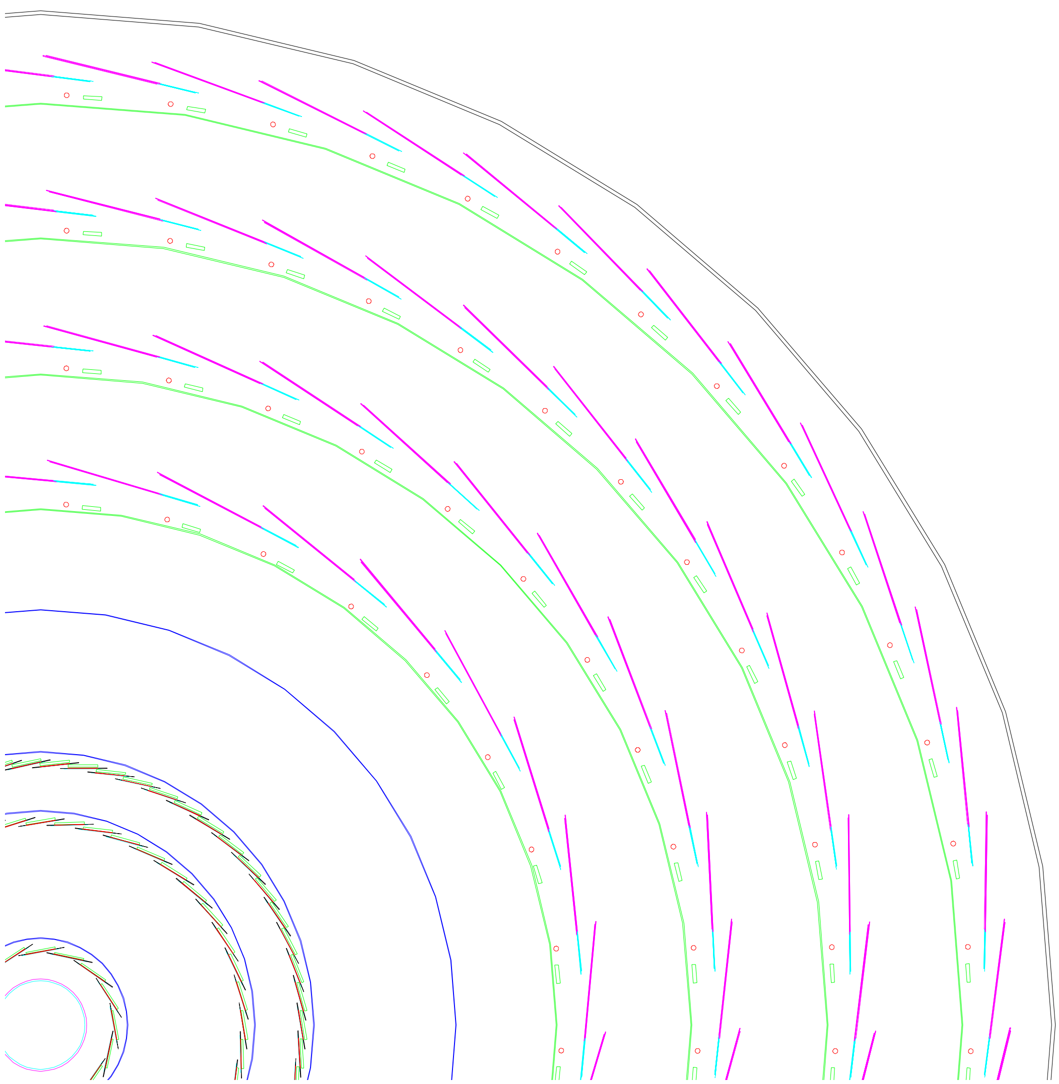

Figure 2.4: Transverse view of a quadrant of the ATLAS Inner Detector (precision layers only). From the center (lower left-hand corner) are: a) the beam pipe, b) three layers of the barrel pixel tracker: ladder support structure (green), silicon crystal (black) with the active regions (red) and support cylinders (dark blue), c) the overall cylindrical stiffener of the barrel pixel detector (dark blue), d) four layers of the SCT tracker: support (green), lumped power cables and cooling (red circles), active silicon (pink) and electronics boards (pale blue), and e) the SCTs insulating layer (black).

nosity. The SCT is surrounded by a cooling system and heat sinks to remove the heat produced by the electronics and reduce the leakage current from the irradiated detectors.

2.1.3 Transition Radiation Tracker

The transition radiation tracker (TRT) is based on a straw detector design, with small diameter straws containing isolated wires in volumes of gas. The gas mixture used is 70% Xe, 20% CO_2, and 10% CF_4. The detector performs tracking as well as detection of "charge blobs" for transition radiation emitted when high-gamma charged particles cross the wall-gas interfaces. The detector is radiation hard. Good coverage is obtained with a barrel module in the center and end-cap modules to measure in the forward regions.

The detector needs to maintain accuracy despite high occupancy and counting rates. While a high rate of particles will reduce the accuracy of drift time measurements due to the accumulation of ionic space charge in the straws, hits on many straws for each track will allow for an accuracy of 50 μm at the LHC design luminosity, averaged over all straws.

The Xe gas is there to efficiently convert the soft transition radiation X-rays from high-gamma electrons into ionization in the gas. The Xe gas is intended to give highly effective electron identification; however, some electron identification capability has been sacrificed to optimize the tracking reconstruction. The straw spacing has been optimized for tracking resolution while a longer path length through the radiator material with fewer straws would have enhanced electron identification. The TRT detector enables a greater electron vs. pion discrimination than from calorimetry alone.

2.2 Calorimetry

The ATLAS liquid argon calorimeter and tile calorimeter, see Fig. 2.5 [14] measure energy deposits of charged leptons, photons, and hadrons. The electromagnetic calorimetry is done with the liquid argon calorimeter. The hadronic calorimeter consists of hadronic liquid argon end-cap calorimeter and a Fe-scintillator tile barrel and extended barrels. The liquid argon forward detectors allow for further hadronic calorimetry before the muon spectrometer. The resolution and coverage for each component is listed in Tab. 2.2. See Figs. 2.6-2.7 for the radiation lengths and interaction lengths for the different sections of the ATLAS calorimeter [11].

2.2.1 Hadronic Calorimetry

Hadronic calorimetry [15] follows the model of sampling calorimeters, such as scintillating tiles which measure the ionization signals from particles produced in the showering in the absorber sections of the detector. This signal is proportional to the energy of the primary particle that starts the shower. Segmentation in ϕ and η allow for position measurements to be made.

The interactions in hadronic calorimeters produce secondary particles from the original interacting particles in the form of neutral particles π^0's, η's, and neutrons and charged particles $\pi^{\pm}$, p, $K^{\pm}$, and others. The π^0 decays immediately into two photons and the η also decays to photons as well as to $\pi^+\pi^-\pi^0$ 28% of the time. These photons lead to high-energy electromagnetic cascades. The charged secondaries deposit energy through ionization and excitation and interactions with nuclei. A fraction of the hadronic energy is not measured due to endothermic spallation losses, nuclear recoils, and late neutron capture. The fraction of unmeasured energy ranges from 20% - 35%, depending on the absorber and energy of the incident particle. The total hadronic energy must be corrected for this unmeasured fraction.

The hadronic calorimetry at ATLAS provides coverage through $|\eta| < 4.9$ using different technologies. The detector provides 11 interaction lengths (λ) at $\eta = 0$. The different detectors include the tile calorimeter and the liquid argon hadronic end-cap calorimeters and forward calorimeters.

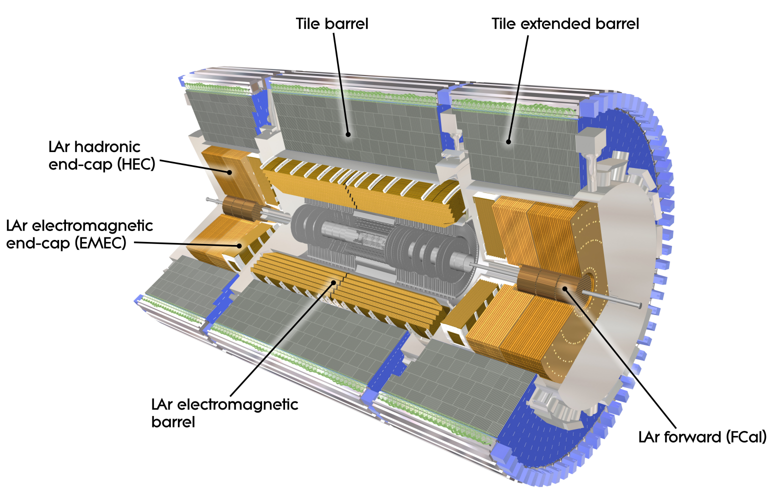

Figure 2.5: The LAr and Tile detectors for electromagnetic and hadronic calorimetry at ATLAS.

Table 2.2: Calorimeter components.

System	Sampling	$\Delta\eta \times \Delta\phi$	Coverage
Presampler	Barrel 1	0.025x0.1	$\|\eta\| = 1.52$
	End-cap 1	0.025x0.1	$1.5 < \|\eta\| < 1.8$
LAr	Barrel 1	0.003x0.1	$\|\eta\| = 1.475$
	Barrel 2	0.025x0.025	$\|\eta\| = 1.475$
	Barrel 3	0.05x0.025	$\|\eta\| = 1.475$
	End-cap 1	0.025x0.1	$1.375 < \|\eta\| < 1.5$
		0.003x0.1	$1.5 < \|\eta\| < 1.8$
		0.004x0.1	$1.8 < \|\eta\| < 2.0$
		0.006x0.1	$2.0 < \|\eta\| < 2.5$
		0.1x0.1	$2.5 < \|\eta\| < 3.2$
	End-cap 2	0.025x0.025	$1.375 < \|\eta\| < 2.5$
		0.1x0.1	$2.5 < \|\eta\| < 3.2$
	End-cap 3	0.05x0.025	$1.5 < \|\eta\| < 2.5$
Hadronic LAr	End-cap 1 and 2	0.1x0.1	$1.5 < \|\eta\| < 2.5$
	End-cap 3 and 4	0.2x0.2	$2.5 < \|\eta\| < 3.2$
Hadronic Tile	Barrel 1 and 2	0.1x0.1	$\|\eta\| = 1.0$
	Barrel 3	0.2x0.1	$\|\eta\| = 1.0$
	Extended Barrel 1 and 2	0.1x0.1	$0.8 < \|\eta\| < 1.7$
	Extended Barrel 3	0.2x0.1	$0.8 < \|\eta\| < 1.7$
Forward	Forward 1, 2, and 3	-0.2x0.2	$3.1 < \|\eta\| < 4.9$

2.2.2 Liquid Argon Detector

The liquid argon calorimeter is used for both electromagnetic and hadronic calorimetry. The portion of the liquid argon detector that is devoted to electromagnetic calorimetry consists of a barrel and two end-cap detectors. The hadronic end-cap (HEC) detectors and the forward calorimeter (FCAL) detectors are used for hadronic calorimetry. The barrel has a gap in coverage that translates in an η region from $1.4 < |\eta| < 1.7$ with worse resolution due to the gap between the barrel and the end-caps. The end-cap is divided into two sections, an outer wheel and an inner coaxial wheel, covering $1.375 < |\eta| < 2.5$ and $2.5 < |\eta| < 3.2$ respectively. See Fig. 2.8.

Electromagnetic Barrel

The barrel detector has an accordion geometry to reduce gaps in azimuthal coverage and provide complete azimuthal symmetry. The accordion detector consists of layers of lead absorber plates and active LAr, see Fig. 2.9 [14]. It has a radial coverage up to 3.2 in η. The barrel is divided into three sections of different granularity, see Tab. 2.2. The three sections together are >24 radiation lengths (X_0) deep. The presampler is positioned ahead of these three sections directly after the cryostat walls and the superconducting solenoid coil. The presampler allows corrections to be made in estimating this energy loss from the upstream material.

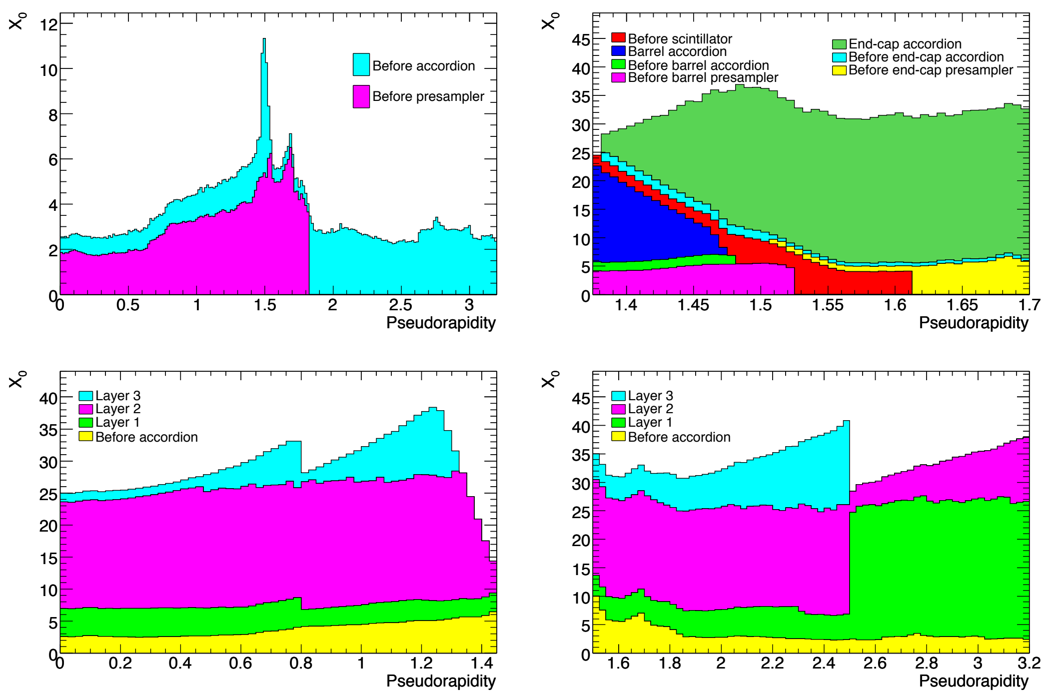

Figure 2.6: Cumulative amounts of material, in units of radiation length X_0 and as a function of $|\eta|$, in front of and in the electromagnetic calorimeters. The top left-hand plot shows separately the total amount of material in front of the presampler layer and in front of the accordion itself over the full η-coverage. The top right-hand plot shows the details of the crack region between the barrel and end-cap cryostats, both in terms of material in front of the active layers (including the crack scintillator) and of the total thickness of the active calorimeter. The two bottom figures show, in contrast, separately for the barrel (left) and end-cap (right), the thicknesses of each accordion layer as well as the amount of material in front of the accordion.

Hadronic End-cap

The hadronic end-cap (HEC) calorimeters consist of two wheels on either side of the detector. The wheels consist of layers of copper plates and LAr gaps. The copper plates are 25 mm thick and 50 mm thick for the wheels positioned closer to the interaction point and further downstream respectively. In between the copper plates lies the readout electrodes structured as an electrostatic transformer (EST) with an EST ratio of two.

The HEC wheels consist of 32 modules, and the HEC offers coverage out to $|\eta| = 3.2$. This ensures overlap with the forward calorimeters, which begin at $|\eta| = 3.1$. The overlap minimizes the drop in coverage with good resolution in the transition between detectors.

Forward Calorimeter

The forward calorimeter (FCAL) is located 4.7 m downstream from the interaction point on either side of the detector. It consists of three layers in depth, one with copper absorbers and two with tungsten absorbers. The

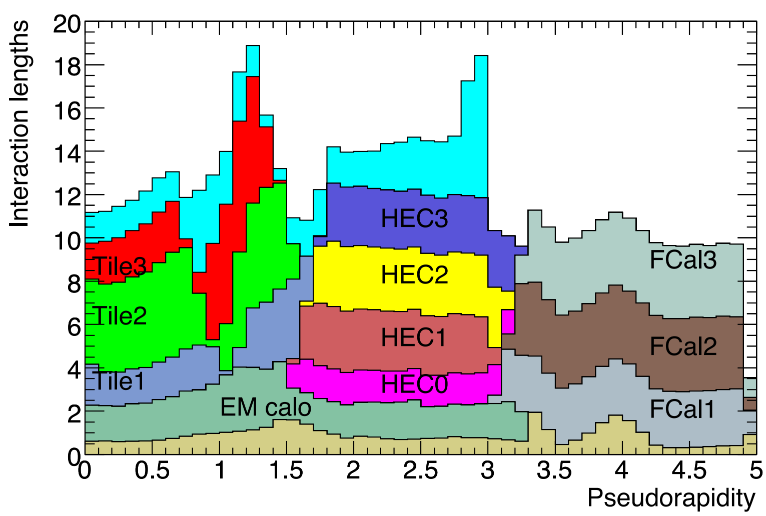

Figure 2.7: Cumulative amount of material, in units of interaction length, as a function of $|\eta|$, in front of the electromagnetic calorimeters, in the electromagnetic calorimeters themselves, in each hadronic layer, and the total amount at the end of the active calorimetry. Also shown for complete-ness is the total amount of material in front of the first active layer of the muon spectrometer (up to $|\eta| < 3.0$).

FCAL is close to the beam pipe where most of the energy flow goes and must filter everything but muons efficiently; therefore, the detector has a very dense design and allows for 9.5 interaction lengths with a high density design.

The FCAL is arranged in cylindrical layers. These layers are contained in the end-cap cryostat. The detector consists of a metal (Cu or W) matrix filled with concentric rods and tubes. The rods are at positive voltage and the tubes are at ground. LAr fills the gaps which may be as small as 250 μm in the first section.

2.2.3 Tile Detector

The tile calorimeter is primarily used for hadronic calorimetry. It consists of layered iron and scintillating tiles. The signals from the scintillating materials are read out with wavelength shifting fibers (WLS) and then the light is converted by photomultiplier tubes (PMT), two per readout section for redundancy. The tile calorimeter consists of a barrel and two extended barrel detectors. The tile detector is positioned behind the electromagnetic LAr calorimeter with respect to the interaction point.

The tile calorimeter has coverage up to 1.7 in eta with a granularity of

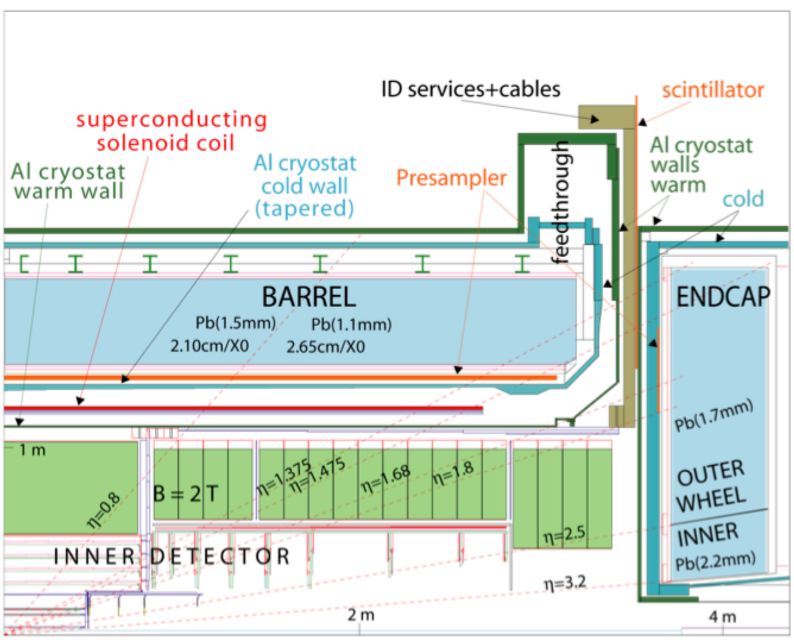

Figure 2.8: The LAr barrel and end-cap EM detector layout at different η regions.

$\eta \times \phi = 0.2 \times 0.1$. The fibers of the PMTs associated with each readout cell are grouped in pseudorapidity such that they form "pseudo-projective" towers pointing towards the nominal center of the detector. The scintillation from the tiles and collection on the WLS fibers are fast. The PMTs also operate quickly producing a pulse of FWHM of 50 ns ready to be read out by the electronics.

2.3 Muon Spectrometer

The muon spectrometer is immersed in ATLAS's second magnet system, which provides a large toroidal field to bend muons. The central barrel toroid is complemented for the eta range between $1.4 < |\eta| < 2.7$ by two end-cap toroidal magnets at both ends of the main toroid. While the muon spectrometer is the outermost detector component in ATLAS, it still sees a high flux of radiation due to penetrating particles created in the primary collision and also radiation from secondary interactions with LHC and ATLAS materials. See Fig. 2.10 for layout.

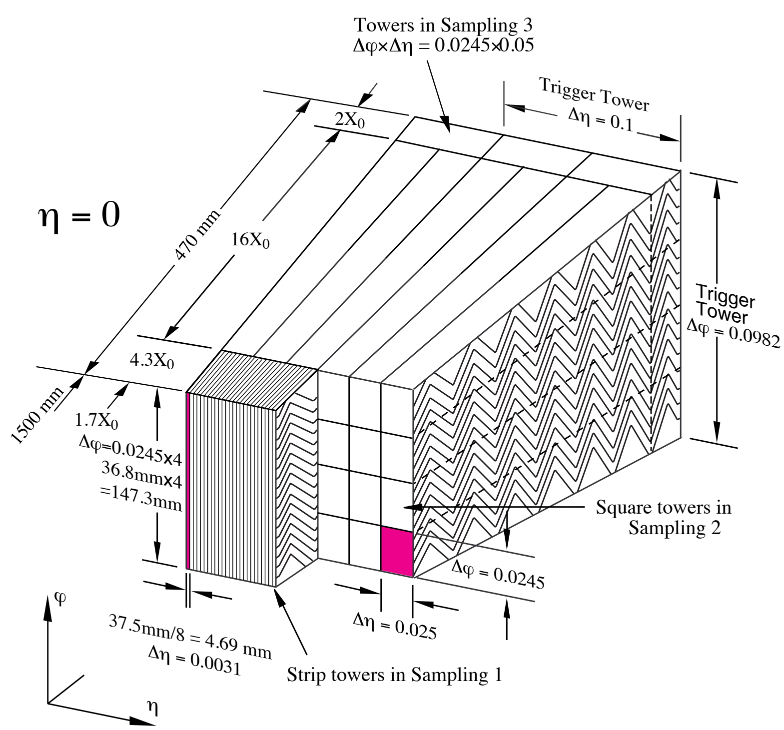

Figure 2.9: The LAr barrel and end-cap detector layout at different η regions.

The detector elements and triggers were designed with this in mind. The muon spectrometer consists of a barrel with monitored drift tube chambers, thin gap chambers, resistive plate chambers, and cathode strip chambers.

2.3.1 Monitored Drift Tube Chambers

The monitored drift tube chambers (MDT) are composed of 5500 m^2 of aluminum drift tubes. The tubes are filled with a gaseous mixture of 93% Ar and 7% CO_2 and kept at a pressure of 3 bar. To allow for pattern recognition using the single wire detectors, the inner and middle or outer stations use 2×4 monolayers and 2×3 monolayers respectively, see Fig. 2.11 [16].

The tubes are read out at a single end by a low-impedance current sensitive preamplifier with a threshold that is five times the expected noise level. This is then followed by a differential amplifier, a shaping amplifier, and finally a discriminator. The shaping amplifier output is also sent to an ADC to correct the drift-time measurement for time-slewing.

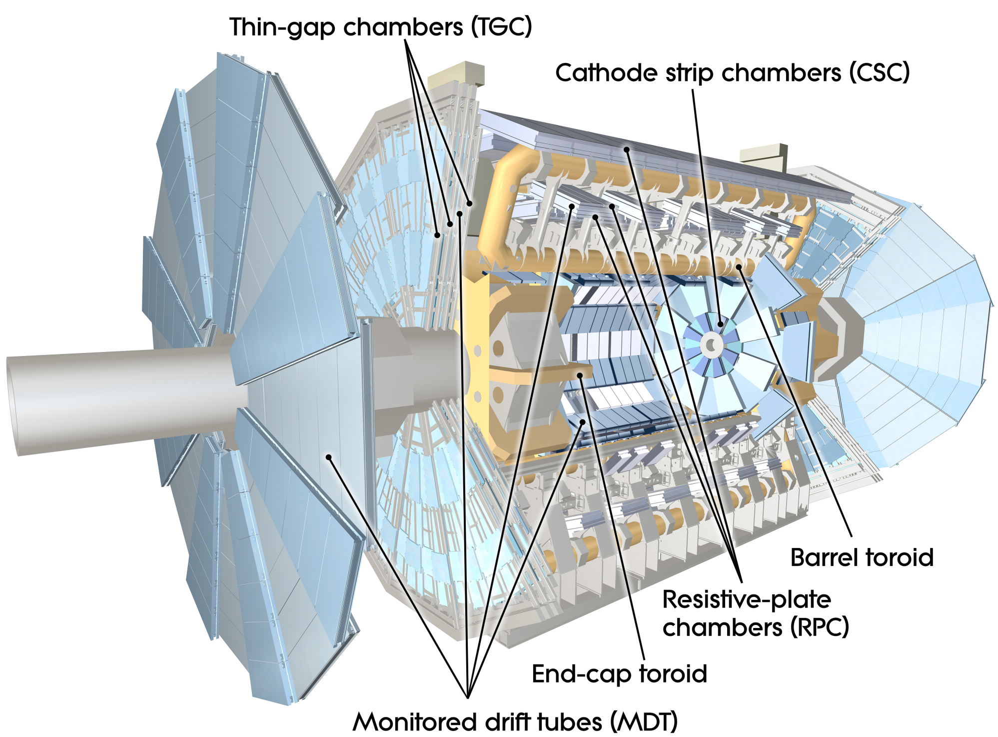

Figure 2.10: Three-dimensional view of the muon spectrometer instrumentation indicating the areas covered by the four different chamber technologies.

2.3.2 Thin Gap Chambers

The thin gap chambers (TGCs) located in the barrels are similar to multiwire proportional chambers except that the anode wire pitch is larger than the distance between the cathode and the anode. The TGCs are filled with a gaseous mixture that is composed of 55% CO_2 and 45% n-pentane (n-C_5H_{12}) which is highly flammable and requires extra safety precautions to be made. The gas mixture is highly quenching and along with the cell geometry allows for operation in saturated mode.

The TGCs anode wires are parallel to the MDT sense wires (to best measure the bend in the toroidal field). Cathode strips are arranged orthogonal to the wires to provide the second muon coordinate.

2.3.3 Resistive Plate Chambers

The resistive plate chamber (RPC) detector located in the wheels is formed with two high-resistivity plates separated by a gap filled with tetrafluoroethane ($C_2H_2F_4$) mixed with a small amount of SF_6 gas. The ionizing particles create a cascade in the uniform electric field of 4.5 kV/mm, which is quenched by the high resistance electrodes.

Each RPC consists of two resistive plates and four readout panels. A set of two orthogonal readout panels are devoted to reading out the η-direction and ϕ-direction. These panels are parallel to the MDT wires in eta and orthogonal

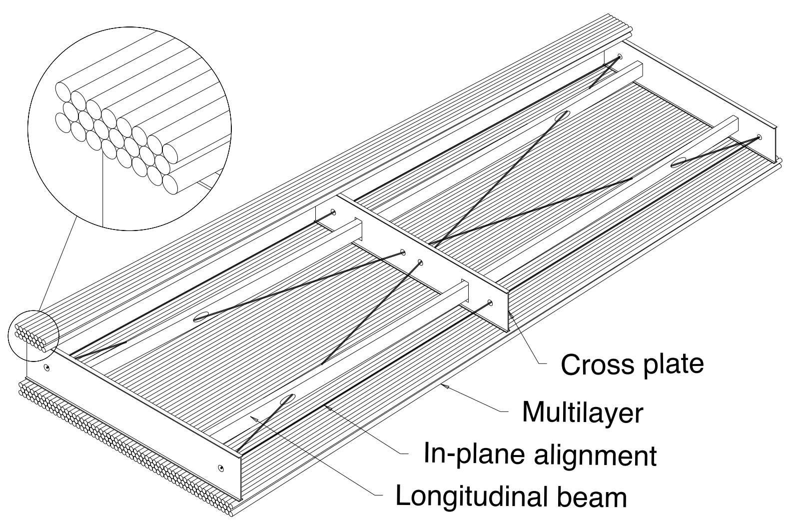

Figure 2.11: The schematic of MDT with multilayers of three monolayers.

in ϕ, and thus provide the necessary second coordinate measurement needed for offline pattern recognition for track reconstruction.

High transverse momentum muons are identified by the L1 trigger using the trigger chambers, RPCs in the barrel, and TGCs in the end-caps.

2.3.4 Cathode Strip Chambers

The cathode strip chambers (CSCs) are gaseous detectors with anode wires for charge collection and segmented cathode strips for signal readout. The gaseous mixture is 30% Ar, 50% CO_2, and 20% CF_4. Neutron background contamination is limited by the choice to exclude hydrogen from the gas mixture.

The cathode strips are orthogonal to the anode wires, and the segmentation and charge sharing over several adjacent cathode strips yields a precision position measurement of 80 μm . The front-end electronics use a preamplifier and pulse shaping amplifier before storing information about the charge collected from the cathodes. The peak of the cathode pulse is passed to the L1 muon trigger.

2.4 Magnet System

As indicated before, there are two large magnets in the ATLAS magnet system, a solenoid magnet and a toroid magnet. The solenoid magnet lies just outside the inner detector and provides a magnetic field for the precision tracking. The toroid magnet supplies a magnetic field for the muon spectrometer and consists of on large central toroid with two small end-cap magnets.

The solenoid magnet provides a consistent, central field of 2T with a peak field at 2.6 T near the superconductor. The toroid magnets provide a a peak field of 3.9 T and 4.1 T for the barrel toroid and the end-cap toroids respectively. The barrel and end-cap toroids overlap in the eta region $1.3 < |\eta| < 1.6$.

2.4.1 Solenoid Magnet

As the solenoid is placed between the inner detector and the calorimeter, the thickness of the solenoid must be minimized in order to minimize the amount of energy loss due to dead material before the energy measurement can be done in the calorimeter. Therefore, the solenoid and the LAr detector share a vacuum to reduce the redundancy in material from two vacuum walls. The solenoid coil superconductor uses an aluminum stabilizer, which is doped to increase mechanical strength. The solenoid is a superconducting NbTi magnet cooled indirectly by liquid He flowing through tubes welded onto the windings. The magnet is kept at a temperature of 4.5 K.

2.4.2 Toroid Magnet

The barrel and two end-cap toroids each consist of eight different coils. The magnets are superconducting with 20.5 kA aluminum-stabilized NbTi. Each barrel toroid coil is housed in its own cryostat, and the cryostats are linked together with structures providing the needed mechanical stability during operation. The windings of the end-cap toroid magnets are all housed in the same cryostat, one for each end-cap on either side of the detector. The magnets are all cooled by liquid He and are also kept at a temperature of 4.5 K.

2.5 Trigger System

There are three levels of online decisions for the trigger [17] and data-acquisition (DAQ) system at ATLAS. Each level builds on the preceding trigger decision and adds additional selection criteria. The initial rate of 40 MHz of bunch crossings is reduced to ideally 200 Hz and 400 Hz normally in operation before the events are written out and permanently stored. This is projected from the design luminosity rate of 10^{34} cm^{-2}s^{-1} with about 20 interactions/crossing. As the actual luminosity delivered to ATLAS has continued to increase towards the design luminosity, the trigger/DAQ system has been tuned to potential new physics processes such as Higgs and SUSY.

The three levels of triggering consist of the Level 1 (L1) Trigger, Level 2 (L2) Trigger, and the Event Filter (EF). After a positive EF decision, the event is written out by the DAQ system.

The L1 trigger is designed to filter and accept events with less than 5% deadtime up to 75 kHz (100 kHz in the future), and pass these events on to L2. The first task of the L1 trigger is to identify which bunch crossings are of interest and will be kept for further decision review. The design bunch-crossing interval is 25 ns, so the decision must be made very quickly. The time-of-flight to the muon spectrometer is on the order of the bunch crossing, and the pulse shape in the calorimeter is on the order of several bunch crossings leading to extra challenges for the L1 trigger decision. The L1 trigger latency, the time available to make a decision and send it to the front-end electronics, must then be 2.5 μs or less. The L1 trigger was designed to achieve a 2.0 μs latency. This number for trigger latency is calculated as follows: 40 MHz/100 kHz * 25 ns = 10 μs. This would mean a 100% deadtime. Statistical fluctuations then tell you you must be about a factor 4-5 smaller to get a deadtime less than 5%.

If the event is accepted by L1, the stored event data is read by readout drivers (RODs) and sent to readout buffers (ROBs). The ROBs hold all the detector information until a decision can be made by the L2 trigger and the information is either dumped or sent on to the EF. The L2 trigger is designed to reduce the event rate to the EF to 1 kHz or less. The L2 trigger has a latency of about 1-10 ms. QCD jet production is the dominant high-p_T process at the LHC proton-proton collider. Additional rejection can be done with the L2 trigger from regions of interest (ROIs) passed from the L1 trigger. The L2 trigger uses a simple cone algorithm to make additional selection requirements and reduces the rate to an acceptable level for the EF selection.

The EF is the last of the online event filters. It utilizes the calibration and alignment information along with the magnetic field map. This selection aims to reduce the event rate from L2 by an order of magnitude to deliver the final $\sim$100 Hz of selected physics events.

Chapter 3

Theory

3.1 The Standard Model

The Standard Model (SM) [18] [19], born in the late 1960's from Glashow-Weinberg-Salam model, has explained the phenomenology of high energy particle physics with high precision with only 18 free parameters. The SM starts with a "periodic table" of elements - twelve fermionic particles of matter and four bosonic forces and postulates the symmetries that govern the building blocks of most everyday matter the interactions between them.

The fundamental fermions are grouped in three generations, each generation of four fermions splits into a pair of (left-handed) leptons and a pair of (left-handed) quarks. The lepton pair consists of an electrically neutral neutrino and a charged electron-like lepton, while the quark pair consists of an up-type quark with charge $+2/3$ and a down-type quark with charge $-1/3$. While the leptons are color-neutral and thus only feel the electroweak interaction, the quarks come in three different color charges and thus also feel the strong interaction. The members of the lepton (and quark) doublet are distinguished by the z-component of the weak isopin quantum number, I_z: the up-type member has $I_z = +1/2$ and the down-type member has $I_z = -1/2$. The right-handed components of the leptons and quarks have weak isospin $I = 0$.

The interactions are mediated by spin-1 gauge bosons; the color-neutral $W^{\pm}$, Z, and the photon for the electroweak interaction, and eight colored electrically neutral gluons that mediate the strong interaction. As a Yang-Mills theory, the SM contains a very specific (gauge-) symmetry, necessary for it to be renormalizable and be Lorentz invariant. The SM postulates three underlying symmetries: U(1) of weak hypercharge $Y = 2(Q - I_z)$, where Q is the fermion's electric charge; the group SU(2) of weak isospin I, and the group SU(3) of color.

This simple postulate defines the SM almost entirely. The bosons mediate the forces of electromagnetic, weak, and strong interactions. The Standard Model predictions were found to be highly accurate with only a small set of parameters and each of the particles was eventually discovered at high energy experiments.

The SM has proved to be an elegant and powerful tool for explanation and prediction in high energy physics. However, there are things for which the SM does not provide predictive power which are needed for a complete theory of high energy particle physics. The SM does not predict why particle masses vary to the degree that is observed. Due to this mass hierarchy, the Higgs boson gets some quantum corrections from virtual particles which are larger than the mass of the Standard Model Higgs. Therefore the bare mass of the Higgs must be fine-tuned to cancel these quantum corrections.

The SM explains the electromagnetic and weak forces as components of the electroweak force, and the vector bosons $W^{\pm}$, Z, and the photon as linear combinations of the basic gauge fields of the U(1) and SU(2) groups. The unification of the electromagnetic and weak forces takes place at energies around 100 GeV, much higher than experienced in everyday life. It is natural to expect that the electroweak and the color forces will also unify, at even higher energies. Supersymmetry is one of the dominant theoretical approaches to accomplish that unification. Experimental evidence for Supersymmetry and weak isospin singlets (the right-handed quarks) so far is non-existent, although a suggestive hint is provided by the fact that supersymmetry makes the couplings of the U(1), SU(2), and SU(3) gauge groups converge at a single value at energies around 10^{16} GeV [20] [21]. Many theories that go beyond the SM (BSM) [22] [23], and in which the SM is embedded as a "low-energy" approximation, have been proposed to overcome the fundamental flaws of the SM. Most of these theories predict the existence of entirely new particles and gauge fields at energies of 10^{2-4} GeV and are therefore presumably testable at the LHC.

3.1.1 Quarks

Quarks are matter particles which carry fractional electrical charge and carry a color charge. There are three generations, SU(2) doublets of quarks with each generation composed of a quark which carries $+\frac{2}{3}$ charge (up, charm, top) and one that carries $-\frac{1}{3}$ charge (down, strange, bottom).

The first generation quarks and gluons make up, together with virtual quark-antiquark pairs, the protons and neutrons that are the components of atomic nuclei. In the simplest view, protons are composed of two up quarks and one down quark (+1 total charge) and neutrons are composed of two down quarks and one up quark (±0 total charge). Second and third generation quarks are produced in high energy interactions in nature and laboratories.

3.1.2 Strong Force

The strong force is responsible for binding of quarks into baryon ($qq'q''$)-states and meson ($q\bar{q}'$)-states, such as protons, neutrons, pions, and Kaons. The strong force is mediated by the spin-1 gluon which is itself colored and thus self-interacting. Because of this, the strength of the color force is proportional to the distance between color-charged particles at large distances. Therefore, the color force gets more attractive the further apart two colored quarks are from one another, thereby explaining the non-observation of free quarks.

3.1.3 Jets

Jets are not fundamental particles, but are very important for our description of quark and gluon interactions in our detector [24]. Jets are the manifestation of quarks and gluons as they are ejected from the collision and create a trail of hadrons in their wake, converting their initial momentum and energy into a cascade of hadrons. Hence the jet's four vector is a good representation of its parent (gluon or quark) four vector.

Unfortunately, the precise definition of a jet depends on the reconstruction algorithm used to select the hadrons that form part of the jet. Hence, it is important to use a jet reconstruction that approximates best the original parton that created it. The reconstruction algorithm used for this analysis is described in Sec. 4.2.

3.2 Quantum Chromodynamics

Quantum Chromodynamics (QCD) [25] [26] is the theory that governs the color interactions of quarks and gluons. Quarks were first posited to explain the SU(3) symmetry observed in the properties and interactions of baryons and mesons of hadronic matter. Baryons were assumed to consists of three quarks, and mesons were assumed to consist of a quark-antiquark pair. As low-mass baryons have half-integer spin, the constituent quarks must also have half-integer spin. While explaining the experimental observations, this leaves the quarks in the spin-$\frac{3}{2}$ baryons with $S = 0$, e.g. the uuu state Δ^{++}, in a symmetric state with respect to its wave function. However, as quarks are

Table 3.1: The properties of the three generations of quarks.

Quark	Symbol	Charge	Baryon Number	Isospin	Mass (GeV)
Up	u	$+\frac{2}{3}$	$\frac{1}{3}$	$+\frac{1}{2}$	0.0017-0.0031
Down	d	$-\frac{1}{3}$	$\frac{1}{3}$	$-\frac{1}{2}$	0.0041-0.0057
Charm	c	$+\frac{2}{3}$	$\frac{1}{3}$	0	$1.26^{+0.05}_{-0.11}$
Strange	s	$-\frac{1}{3}$	$\frac{1}{3}$	0	$0.1^{+0.03}_{-0.02}$
Top	t	$+\frac{2}{3}$	$\frac{1}{3}$	0	$172.9 \pm 0.6 \pm 0.9$
Bottom	b	$-\frac{1}{3}$	$\frac{1}{3}$	0	$4.19^{+0.18}_{-0.06}$

fermions and must obey Fermi-Dirac statistics, they cannot all have the same quantum numbers and the wave function must be antisymmetric. This led to the positing of a new quantum number: the so-called color charge of the quarks, whimsically designated as red, blue, and green. As there is no naked color observed in nature, there needs to be an added constraint on the color degree of freedom to avoid a proliferation of states. The constraint is that hadrons can only exist as color singlet states in nature; this means that the quarks in baryons and mesons can only carry color charges such that the combined color charge of the quarks remains neutral (hence the choice of red, blue, and green which combined give neutral white).

QCD dictates that baryons and mesons be composed of quarks which are bound by the color force. Antimatter carries the opposite and therefore neutralizing color charge of anti-red, anti-blue, and anti-green. The properties of the six known quarks are described in the table, Tab. 3.1. The color of the components of mesons and baryons combine to form a color neutral state. The theory of SU(3) color interactions was experimentally motivated and has subsequently been overwhelmingly supported by additional experimental data, such as the neutral pion lifetime [27].

3.2.1 Lagrangian

The strong force and the effect it exerts on quarks and gluons which have color charge can be written in an explicit relation in the QCD Lagrangian. The QCD Lagrangian [28] can be separated in three parts:

$$\mathcal{L}_{QCD} = \mathcal{L}_{classical} + \mathcal{L}_{gauge-fixing} + \mathcal{L}_{ghost} \tag{3.1}$$

where each part can be described in the following equations:

$$\mathcal{L}_{classical} = -\frac{1}{4}F^{A}_{\alpha\beta}F^{\alpha\beta}_{A} + \sum_{flavors} \overline{q}_a(i\gamma_\mu D^\mu - m)_{ab}q_b \tag{3.2}$$

$$\mathcal{L}_{gauge-fixing} = -\frac{1}{2\lambda}\left(\eta^\alpha \mathcal{A}^A_\alpha\right)^2 \tag{3.3}$$

$$\mathcal{L}_{ghost} = \partial_\alpha \eta^{A\dagger}(D^\alpha_{AB}\eta^B) \tag{3.4}$$

This Lagrangian describes the behavior of spin-$\frac{1}{2}$ quarks q_a of mass m and massless spin-1 gluons.

The field strength tensor, $F^A_{\alpha\beta}$, is related to the gluon field $\mathcal{A}^A_\alpha$ by the relation in Eq. 3.5, where g is the coupling constant for interactions of colored quanta, and A, B, C run over the eight color degrees of freedom.

$$F^A_{\alpha\beta} = \left[\partial_\alpha \mathcal{A}^A_\beta - gf^{ABC}\mathcal{A}^B_\alpha \mathcal{A}^C_\beta\right] \tag{3.5}$$

In the summation in Eq. 3.2, f^{ABC} is the structure constant, defined further in Eq. 3.8, and the symbol γ_μ stands for Dirac matrices which statisfy the anticommutation relations along with the metric given as $g^{\alpha\beta} = diag(1, -1, -1, -1)$ such that:

$$\{\gamma^\mu, \gamma^\nu\} = 2g^{\mu\nu} \tag{3.6}$$

The symbol D^μ is the covariant derivative. When acting upon the triplet and octet color fields, the following relations hold:

$$(D_\alpha)_{ab} = \partial_\alpha \delta_{ab} + ig(t^C \mathcal{A}^C_\alpha)_{ab}, \qquad (D_\alpha)_{ab} = \partial_\alpha \delta_{ab} + ig(T^C \mathcal{A}^C_\alpha)_{ab} \tag{3.7}$$

where t and T are the generators of the SU(3) group and δ is the Kronecker delta. The generators are the fundamental representation, t, and the adjoint representation T of color SU(3), such that:

$$[t^A, t^B] = if^{ABC}t^C, \quad [T^A, T^B] = if^{ABC}T^C, \quad (T^A)_{BC} = -if^{ABC} \tag{3.8}$$

These fundamental operators must consist of traceless, Hermitian, linearly independent matrices by definition, we use the Gell-Mann matrices for the

SU(3) group such that $t^A = \frac{\lambda^A}{2}$ are the generator matrices. As the fundamental operators are the generators of SU(3) and are represented by $n \times n$ matrices with $n = 3$; they operate in the color space of the three fundamental colors red, blue, green. There are $n^2 - 1$ independent matrices; hence there are 8 gluons in $SU_C(3)$.

Each quark must carry a color charge, and an antiquark an anticolor charge. Gluon interactions generally transform from one color charge to another and therefore the gluon carries a superposition color-anticolor charges.

Each of the colored quarks are acted on by the SU(3) group of 3×3 unitary operator matrices. Therefore one can represent each quark as a column vector carrying a color as in the Eq. 3.9. In the same way, antiquarks can be represented as row vectors.

$$\begin{pmatrix} 1 \\ 0 \\ 0 \end{pmatrix}, \text{red} \qquad \begin{pmatrix} 0 \\ 1 \\ 0 \end{pmatrix}, \text{blue} \qquad \begin{pmatrix} 0 \\ 0 \\ 1 \end{pmatrix}, \text{green} \tag{3.9}$$

There are eight linearly independent Gell-Mann matrices representing the eight gluons. The term in Eq. 3.5 with the coupling constant is non-Abelian and gives rise to the asymptotic freedom in QCD such that the field strength is stronger over larger distance while quarks become free at short distances.

The second term in our Lagrangian, in Eq. 3.3, allows for fixing of the gauge. Fixing the gauge allows the propagator of the gluon field to be properly defined. The gauge parameter is λ, and the gauge-fixing is covariant. As QCD is a non-Abelian theory, the ghost term, defined in Eq. 3.4, is needed to balance the gauge-fixing term and cancel non-physical degrees of freedom which would propagate with covariant gauge fields [29]. The η term is a complex scalar field.

3.2.2 The Strong Coupling Constant

The dimensionless coupling constant α_s determines the strength of the color interaction between colored partons, and depends on the energy scale Q of the interaction. The reasons for the energy dependence are very much similar to the Q-dependence of the electromagnetic coupling "constant" α_{EM}.

For an energy scale Q we define a dimensionless physical observable R such that R is dependent on this single energy scale. Taking R as a perturbation series in the coupling constant $\alpha_s = g_3^2/4\pi$, one finds that there are divergences that require the introduction of another mass scale, μ^2, for renormalization. Our R then becomes dependent on the ratio Q^2/μ^2 and is not constant.

Because the choice of μ is arbitrary, we must assume that R is independent of the choice of μ. It follows then that

$$\mu^2 \frac{d}{d\mu^2} R(Q^2/\mu^2, \alpha_s) \equiv \left[\mu^2 \frac{\partial}{\partial \mu^2} + \mu^2 \frac{\partial \alpha_s}{\partial \mu^2} \frac{\partial}{\partial \alpha s} \right] R = 0, \tag{3.10}$$

neglecting masses. For simplification we define the following

$$t = \ln \left(\frac{Q^2}{\mu^2} \right), \qquad \beta(\alpha_s) = \mu^2 \frac{\partial \alpha_s}{\partial \mu^2} \tag{3.11}$$

such that we can rewrite Eq 3.10 in the form

$$\left[-\frac{\partial}{\partial t} + \beta(\alpha_s) \frac{\partial}{\partial \alpha_s} \right] R(e^t, \alpha_s) = 0 \tag{3.12}$$

If we allow α_s to run with the energy scale, $\alpha_s(\mu^2)$, we can solve our partial differential equation with the implicit definition of $\alpha_s \equiv \alpha_s(\mu^2)$ as follows

$$t = \int_{\alpha_s}^{\alpha_s(Q^2)} \frac{dx}{\beta(x)} \tag{3.13}$$

If we differentiate the equations in Eq. 3.13 we find the relations

$$\frac{\partial \alpha_s(Q^2)}{\partial t} = \beta\left(\alpha_s(Q^2)\right), \qquad \frac{\partial \alpha_s(Q^2)}{\partial \alpha_s} = \frac{\beta\left(\alpha_s(Q^2)\right)}{\beta(\alpha_s)} \tag{3.14}$$

We see that a solution to Eq. 3.12 is given by $R(1, \alpha_s(Q^2))$. That means that all the scale dependence of R comes from $\alpha_s(Q^2)$. As QCD is an asymptotically free theory, $\alpha_s(Q^2)$ becomes smaller as Q increases. This implies that for a sufficiently large Q, we can always find a solution to our Eq. 3.14 and therefore can predict the variation of R with Q. For a sufficiently large Q, we find this solution using perturbation theory.

3.3 pQCD and PDF

The Large Hadron Collider at CERN is a proton-proton collider where gluon-gluon interactions dominate. Many of the hadron collider's signatures for Standard Model processes and for physics beyond the Standard Model involve gluons in the initial state. It is important then that the gluon distribution be well understood. The angular decorrelation between the two highest momentum jets in an event can be used to study the dynamics of multi-jet events and the DGLAP to BFKL transition for parton distribution functions (PDF) evolution. DGLAP sums up powers of $\ln(Q^2)$ and BFKL sums up powers of $\ln(1/x)$ where x is the momentum fraction carried by the parton. These parton evolutions will be discussed further in Sec. 3.3.1 and Sec. 3.3.2. PDF are essential for calculating the cross sections for the observed physical processes.

To understand how partons evolve with perturbative QCD (pQCD), we must understand how the partons are distributed in the initial state. The main contributions to uncertainties in the PDF parameterizations come from theoretical uncertainties; global fits to experimental data from deep inelastic scattering, Drell-Yan, and other data; and from DGLAP evolution to higher-order Q^2 [30]. The methods used to estimate the uncertainties from PDF in this analysis are varying the chosen mass scale, μ, and taking an envelope of results from different initial PDF.

The cross section for QCD processes studied here are calculated using the factorization formula, describing the probability of finding parton a (b) in beam hadron h_1 (h_2) respectively

$$\begin{aligned} \sigma(p_1, p_2; Q) &= \sum_{a,b} \int dx_1 dx_2 f_{a/h_1}(x_1, Q^2) f_{b/h_1}(x_1, Q^2) \\ &\times \hat{\sigma}(x_1 p_1, x_2 p_2; Q; \alpha_s(Q)) + O((\Lambda_{QCD}/Q^2)^p) \end{aligned} \quad (3.15)$$

where a, b are the parton flavors $(g, u, \bar{u}, d, \bar{d})$ and $f_{(a,b)/h_1}$ are the parton distribution functions. We can see from this equation that our cross section σ also depends on the scattering energy scale Q^2 and parton momentum fraction x. The parton cross section $\hat{\sigma}$ is discussed further in Eq. 3.16. The $O((\Lambda_{QCD}/Q^2)^p)$ stands for non-perturbative contributions (such as hadronization effects, multiparton interactions, contributions of soft underlying event). We can see in Fig. 3.1 the resultant Q^2 and x values for producing a parton with mass M at rapidity y for a fixed center-of-mass energy ($\sqrt{s}$) such as one would see at the LHC.

The formula from Eq. 3.15 is simple and is infrared safe, meaning the cross section is independent of soft radiation. The cross section values are plotted for different hard processes as a function of $\sqrt{s}$. The expected values at the LHC are denoted in the figure, see Fig. 3.2.

For the case of 2→2 production, the dijet differential cross section at LO is

$$\frac{E_3 E_4 d^6\hat{\sigma}}{d^3p_3 d^3p_4} = \frac{1}{2\hat{s}} \frac{1}{16\pi^2} \overline{\sum} |\mathcal{M}|^2 \delta^4(p_1 + p_2 - p_3 - p_4) \quad (3.16)$$

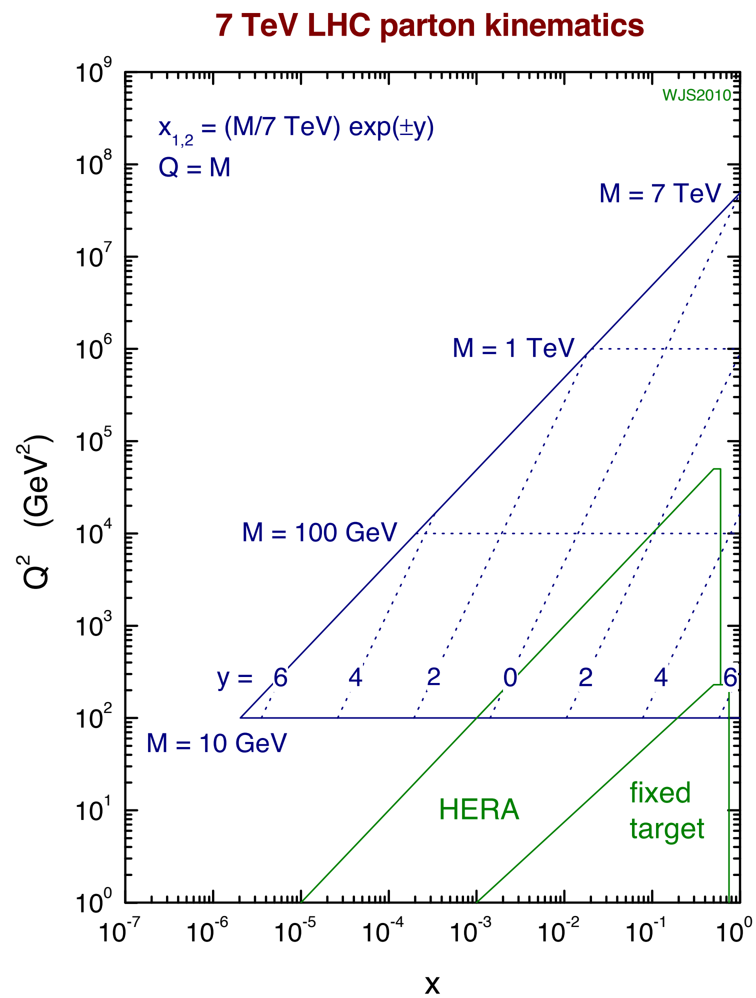

Figure 3.1: The parton momentum fraction x as a function of scattering energy scale Q^2 for the LHC at $\sqrt{s}$=7. The resultant Q^2 and x values for producing a parton with mass M at rapidity y for a fixed $\sqrt{s}$ with scattering partons of momentum fraction $x_{1,2}$.

where $\overline{\sum}$ represents the average over inital and sum over final state spins and colors respectively, (p_1 and p_2) and (p_3 and p_4) are the incoming and outgoing particles in the 2→2 interaction, and $\mathcal{M}$ is the scattering matrix element and a function of the Mandelstam variables $\hat{s} = (p_1 + p_2)^2$, $\hat{t} = (p_1 - p_3)^2$, and $\hat{u} = (p_2 - p_3)^2$.

For the Feynman diagrams at LO, see Fig. 3.3. As the LHC produces mainly gluon-gluon interactions, the 2→2 interaction with gluon-gluon scat-

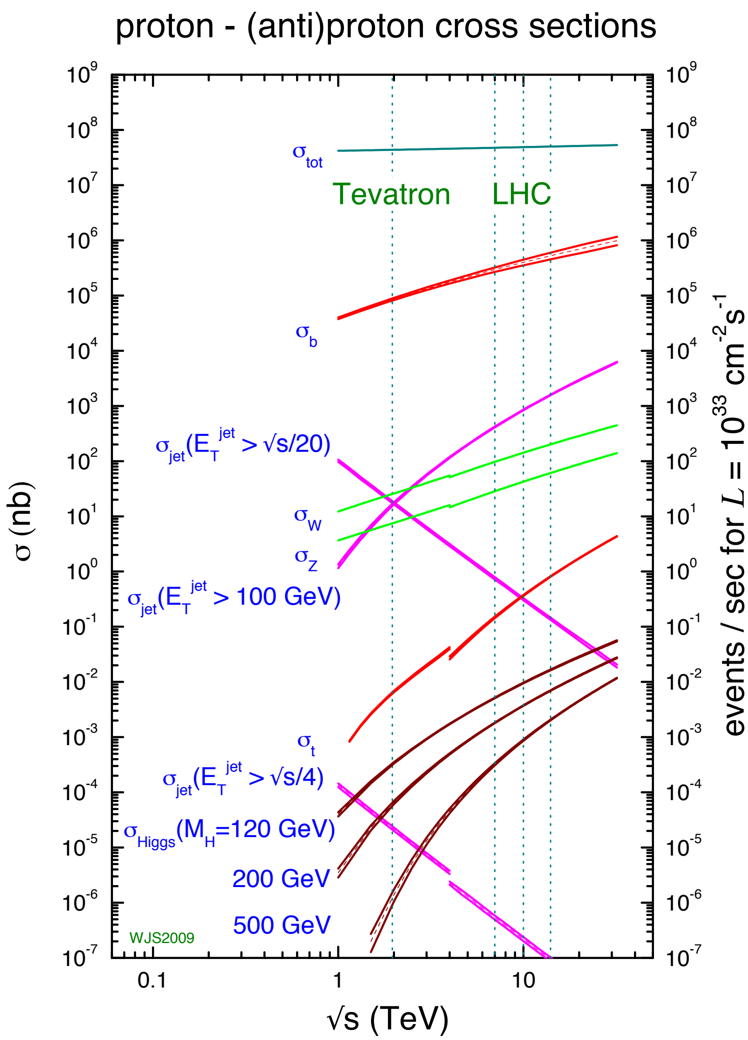

Figure 3.2: Cross section contributions of different parton processes for the inclusive jet cross section at the Tevatron and LHC $\sqrt{s}$ scales.

tering $gg \to gg$

$$\overline{\sum}|\mathcal{M}|^2/g^4 = \frac{9}{2}\left(3 - \frac{\hat{t}\hat{u}}{\hat{s}^2} - \frac{\hat{s}\hat{u}}{\hat{t}^2} - \frac{\hat{s}\hat{t}}{\hat{u}^2}\right), \tag{3.17}$$

is of most interest. For incoming partons (i, j) and outgoing partons (k, l), using Eq. 3.16 the two-jet inclusive cross section becomes

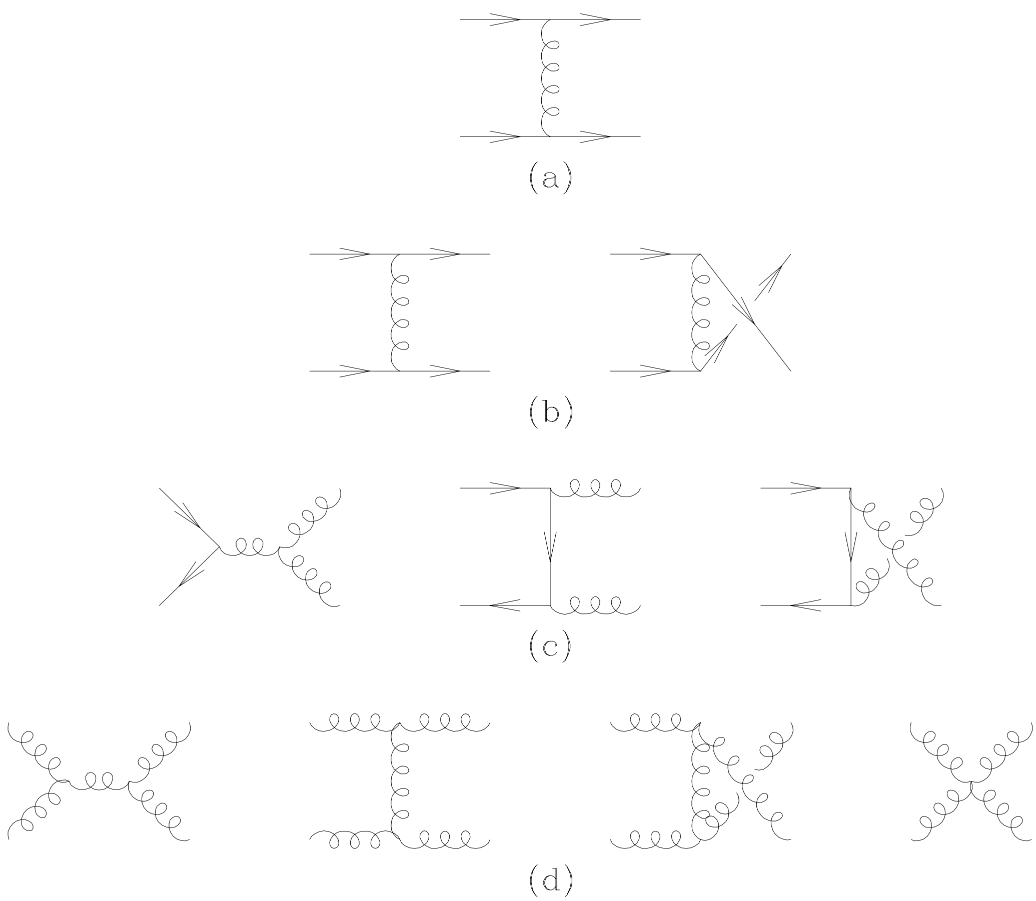

Figure 3.3: The LO diagrams for scattering of a. qq' b. qq c. $q\bar{q}$ d. gg

$$
\begin{aligned}
\frac{d^3\sigma}{dy_3 dy_4 dp_T^2} &= \frac{1}{16\pi s^2} \sum_{i,j,k,l=q,\bar{q},g} \frac{f_i(x_1,\mu^2)}{x_1}\frac{f_i(x_2,\mu^2)}{x_2} \\
&\times \overline{\sum} |\mathcal{M}|^2 \delta^4(p_1+p_2-p_3-p_4)
\end{aligned}
\quad (3.18)
$$

3.3.1 DGLAP Evolution

Dokshitzer-Gribov-Lipatov-Altarelli (DGLAP) evolution follows a strong ordering in transverse momentum $k_{Tn}^2 \gg k_{Tn-1}^2 \gg ... \gg k_{T1}^2$ and a soft ordering in momentum fraction $x_n < x_{n-1} < ... < x_1$ for the parton cascade.

The parton evolution is typically well described by DGLAP evolution [31]

[32] [33] except in the low-x, low-Q^2 regime and also the very high x regime where it breaks down.

The DGLAP equation for a quark PDF $q(\xi, t)$, where ξ is the momentum fraction carried by a pointlike quark constituent, is defined by taking the partial derivative of the structure function of the renormalized "bare" quark distribution:

$$t\frac{\partial}{\partial t}q(x,t) = \frac{\alpha_s(t)}{2\pi}\int_x^1 \frac{d\xi}{\xi}P\left(\frac{x}{\xi}\right)q(\xi,t) \tag{3.19}$$

where $t = \mu^2$ and μ is the factorization scale, and $P(\xi)$ is the splitting function defined as $P(\xi) = C_F\frac{1+\xi^2}{1-\xi}$ with a form specific to the qqg vertex of QCD. Here C_F along with C_A are the $SU(N_c)$ color factors where $C_A = N_c = 3$ and $C_F = \frac{4}{3}$. This equation describes the running of our strong coupling constant α_s with factorization scale t.

Eq. 3.19 is a simplification that does not take into account the higher order expansion and the renormalization group equation along with the description of the $(2n_f + 1)$ space of quarks, anti-quarks, and gluons. The full form of the equation is

$$\begin{aligned} t\frac{\partial}{\partial t}\begin{pmatrix} q_i(x,t) \\ g(x,t) \end{pmatrix} &= \frac{\alpha_s(t)}{2\pi}\sum_{q_j,\bar{q}_j}\int_x^1 \frac{d\xi}{\xi} \\ &\times \begin{pmatrix} P_{q_iq_j}\left(\frac{x}{\xi},\alpha_s(t)\right) & P_{q_ig}\left(\frac{x}{\xi},\alpha_s(t)\right) \\ P_{gq_j}\left(\frac{x}{\xi},\alpha_a(t)\right) & P_{gg}\left(\frac{x}{\xi},\alpha_a(t)\right) \end{pmatrix}\begin{pmatrix} q_i(\xi,t) \\ g(\xi,t) \end{pmatrix} \end{aligned} \tag{3.20}$$

Since the LHC is primarily a gluon-gluon collider, we will only concern ourselves with the gg matrix element in the following derivations.

The splitting function P is defined as a power series expansion

$$P_{gg}(z,\alpha_s) = P_{gg}^{(0)}(z) + \frac{\alpha_s}{2\pi}P_{gg}^{(1)}(z) + \cdots \tag{3.21}$$

where $z = |k^2|/(2\nu)$, k^μ is the four-momentum and $|k^2|$ is the virtuality, and $\nu = p \cdot q$ where p is the target momentum and q is the momentum transfer.

The splitting function in leading order has the following expression assuming a parton with momentum fraction x that is a very small fraction of the longitudinal momentum of the parent particle and a transverse momentum squared much less then μ^2 and where $x < 1$.

$$\begin{aligned} P_{gg}^{(0)}(x) &= 2C_A\left[\frac{x}{(1-x)_+} + \frac{1+x}{x} + x(1-x)\right] \\ &+ \delta(1-x)\frac{(11C_A - 4n_fT_R)}{6} \end{aligned} \tag{3.22}$$

so that for any sufficiently smooth function the integral with the "plus" distribution is defined as

$$\int_0^1 dx \frac{f(x)}{(1-x)_+} = \int_0^1 dx \frac{f(x)-f(1)}{(1-x)} \tag{3.23}$$

For the NLO we define $p_{gg}(x) = \frac{1}{1-x} + \frac{1}{x} - 2 + x(1-x)$ such that the splitting function for gg at NLO is defined as

$$\begin{aligned} P_{gg}^{(1)}(x) = \; & C_F T_f \Big\{ -16 + 8x + \tfrac{20}{3}x^2 + \tfrac{4}{3x} \\ & -(6+10x)\ln x - (2+2x)\ln^2 x \Big\} \\ & + C_A T_f \Big\{ 2 - 2x + \tfrac{26}{9}\left(x^2 - \tfrac{1}{x}\right) - \tfrac{4}{3}(1+x)\ln x - \tfrac{20}{9} p_{gg}(x) \Big\} \\ & + C_A^2 \Big\{ \tfrac{27}{2}(1-x) + \tfrac{67}{9}\left(x^2 - \tfrac{1}{x}\right) \\ & - \left(\tfrac{25}{3} - \tfrac{11}{3}x + \tfrac{44}{3}x^2\right)\ln x + 4(1+x)\ln^2 x + 2p_{gg}(-x)S_2(x) \\ & + \left[\tfrac{67}{9} - 4\ln x \ln(1-x) + \ln^2 x - \tfrac{\pi^2}{3}\right] p_{gg}(x) \Big\} \end{aligned} \tag{3.24}$$

where $S_2(x)$ is defined as the function

$$S_2(x) = \int_{\frac{x}{1+x}}^{\frac{1}{1+x}} \frac{dz}{z} \ln\left(\frac{1-z}{z}\right) \tag{3.25}$$

$$= -2Li_2(-x) + \frac{1}{2}\ln^2 x - 2\ln x \ln(1+x) - \frac{\pi^2}{6} \tag{3.26}$$

and where $Li_2(-x)$ is the dilogarithmic function, $Li_2(x) = -\int_0^x dy \frac{\ln(1-y)}{y}$.

This definition for $P^{(1)}$ can be extended to all values of x by fixing the endpoint of contributions for the value $x = 1$. Taking into account conservation of momentum fraction, we find

$$\delta P_{gg}^{(1)} = \left[C_A^2 \left\{ \frac{8}{3} + 3\zeta(3) \right\} - C_F T f - \frac{4}{3} C_A T_f \right] \delta(1-x) \tag{3.27}$$

where ζ is the Riemann zeta function. In the small x limit, we find that

$$S_2 = \frac{1}{2}\ln^2 x - \frac{\pi^2}{6} + O(x) \tag{3.28}$$

$$P_{gg} \rightarrow \frac{2C_A}{x} + \frac{\alpha_s}{2\pi}\frac{12C_F T_f - 46 C_A T_f}{9x} \tag{3.29}$$

In the large-x limit the splitting function becomes

$$P_{gg} \quad \to \quad \frac{2C_A}{(1-x)_+}\left(1+\frac{\alpha_s}{2\pi}\kappa\right) \tag{3.30}$$

where $\kappa = C_A\left(\frac{67}{18}-\frac{\pi^2}{6}\right) - T_f\frac{10}{9}$. The fraction $\frac{1}{1-x}$ is taken in the one-sided limit from the right side of the limit.

An alternate description to the evolution equations is in terms of the moments of the parton distributions. The moments (Mellin transforms) are defined as

$$f(j,t) = \int_0^1 dx x^{j-1} f(x,t), \qquad f = q_i, g \tag{3.31}$$

in terms of moments, the DGLAP equation, see Eq. 3.20, becomes

$$\begin{aligned} t\frac{\partial}{\partial t}\begin{pmatrix} \Sigma(j,t) \\ G(j,t) \end{pmatrix} &= \frac{\alpha_s(t)}{2\pi} \\ &\times \begin{pmatrix} \gamma_{qq}(j,\alpha_s(t)) & 2n_f\gamma_{qg}(j,\alpha_s(t)) \\ \gamma_{gq}(j,\alpha_s(t)) & \gamma_{gg}(j,\alpha_a(t)) \end{pmatrix}\begin{pmatrix} \Sigma(j,t) \\ G(j,t) \end{pmatrix} \end{aligned} \tag{3.32}$$

where $\Sigma(j,t)$ and $G(j,t)$ are the moments of the singlet quark and gluon respectively, the moment number is j, $n_f = 4$, and $\alpha_s/2\pi = 1/30$. We also define the anomalous dimension, γ_{gg}, as the following

$$\gamma_{gg}(j,\alpha_s) = \int_0^1 dx d^{j-1} P_{qq}(x,\alpha_s) \tag{3.33}$$

The LO anomalous dimension for the gluon-gluon scattering is

$$\gamma_{gg}^{(0)}(j) = 2C_A\left[-\frac{1}{12}+\frac{1}{j(j-1)}+\frac{1}{(j+1)(j+2)}-\sum_{k=2}^{j}\frac{1}{k}\right]-\frac{2}{3}n_f T_R \tag{3.34}$$

The moment number j dependence of the LO and NLO anomalous dimension of Eq. 3.32 are analogous to the splitting functions and are formed from the basic integrals

$$\int_0^1 dx x^{j-1}\frac{1}{x} = \frac{1}{j-1} \tag{3.35}$$

$$\int_0^1 dx x^{j-1}\frac{1}{(1-x)_+} = -\int_0^1 dx\frac{x^{j-1}-1}{x-1} \sim -\ln j, \quad j\to\infty \tag{3.36}$$

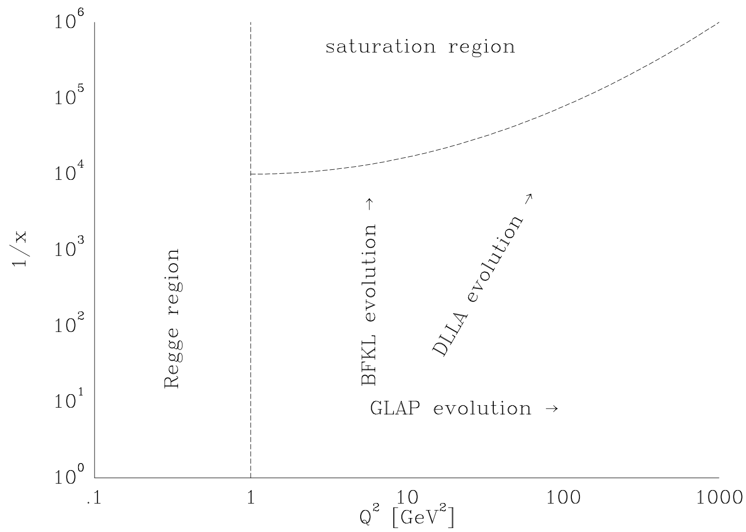

Figure 3.4: DGLAP and BFKL evolution in 1/x and Q^2 space.

We see here that the anomalous dimension grows with $\ln j$ as j gets large. We also see that as $j \to 1$, the theory of fixed-order perturbation begins to break down as we have a pole at $j = 1$. We will see this effect as we go to small-x, see Sec. 3.3.2.

The cross section at NLO must take into account Feynman diagrams in addition to the 2→2 diagrams, see Eq. 3.15, for scattering processes and internal loops with 2→3, 2→4, ..., 2→n diagrams. The generalized cross function becomes

$$\sigma^n = \sum_{i,j,k_1,\ldots,k_n=q,\bar{q},g} = \int_0^1 dx_1 dx_2 f_i(x_1,\mu^2) f_j(x_2,\mu^2) \hat{\sigma}^{i,j\to k_1,\ldots,k_n} \tag{3.37}$$

We take the case of 2→3 to demonstrate how NLO modifies the LO $\hat{\sigma}$, see Eq. 3.16, for the process $g(p_1) + g(p_2) \to g(p_3) + g(p_4) + g(p_5)$. The matrix element for this process [34] is

$$\overline{\sum}|\mathcal{M}|^2 = \frac{g^6 N^3}{240(N^2-1)} \left[\sum_P \{12\}^4\right] \left[\sum_P \{12\}\{23\}\{34\}\{45\}\{51\}\right] \times \left(\prod_{i<j}\{ij\}\right)^{-1} \tag{3.38}$$

where the dot product of two four-momenta has the notation $\{ij\} \equiv p_i \cdot p_j$. The sum is taken over P of the three cyclical permutations of the momentum of the final-state gluons.

Assuming the three-particle massless phase space, we can then write the differential cross section as

$$\frac{d^4\hat{\sigma}}{dx_3 dx_4 d\cos\theta_1 d\psi} = \frac{1}{1024\pi^4}\overline{\sum}|\mathcal{M}|^2 \tag{3.39}$$

3.3.2 BFKL Evolution

The Balitsky-Fadin-Kuraev-Lipatov (BFKL) equation was developed [35] [36] to give an appropriate description of scattering at low-x and low-Q^2. At the LHC, jets will be produced at high forward rapidities and moderate transverse momenta with higher statistics than previous experiments [37]. This becomes a logical place to look for transition from DGLAP evolution to BFKL evolution [38] [39]. Large logrithms in the low-x region can be resummed using the method of BFKL and their well known equation so that meaningful physics predictions can be made in this regime. The BFKL resummation method is also valid for the production of jet pairs at large rapidity separation, Δy.

The cross section for BFKL processes increases with rapidity like $\hat{\sigma}_{gg} \approx e^{\lambda|\Delta y|}$ for dijet production. Thus, jets with a large separation in rapidity allow for more statistics for studying BFKL. This is not a LO effect [40] [41]. However, the increase in the gluon-gluon cross section with Δy is to be folded with the gluon PDF which decrease rapidly with Δy, resulting in an overall decrease of the total jet cross section.

To counteract the decrease with Δy from the PDF contributions, an observable is selected where there are differences between BFKL and fixed-order QCD. The opening angle in ϕ between the two highest p_T jets ($\Delta\phi$) is predicted to have larger deviations from $\Delta\phi = \pi$ in BFKL than otherwise predicted due to the emission of gluons between the two jets. In LO QCD, the $\Delta\phi$ between the two leading jets is (almost) completely correlated as there is no hard or soft radiation and they should be produced back to back independent of the separation in rapidity. In naive BFKL, there is no price for emitting a gluon at LO as additional jets are ignored and combined with virtual gluons contributions [38]. Therefore, one can expect additional radiation in the event such that $\Delta\phi$ becomes decorrelated. As the separation in rapidity between the two leading jets increases, BFKL predicts more additional radiation. Thus the decorrelation becomes stronger at larger Δy.

One can also look for the Δy increase in the cross section by looking at the ratio at two different center-of-mass energies for corresponding parton momentum fractions such that the PDF contributions cancel.

The momentum fraction carried by the partons from $2 \to 2$ kinematics is

$$x_1 = \frac{2p_{T1,2}}{\sqrt{s}} e^{+y_{ave}} \cosh(\Delta y/2), \qquad x_2 = \frac{2p_{T1,2}}{\sqrt{s}} e^{-y_{ave}} \cosh(\Delta y/2) \tag{3.40}$$

where $y_{ave} = (y_1 + y_2)/2$. We define the scattering scale to be

$$Q = \sqrt{p_{T,1} p_{T,2}} \tag{3.41}$$

From Eq. 3.40 we find, taking the assumption that our particles are produced within a rapidity range of $|y_{1,2}| \leq 2.8$ with a jet separation of $R = 0.6$, a minimum $p_T = 80$ GeV, and a leading jet range of $p_T^{max} = 110 - 160$ GeV, that we can probe a minimum of $x = 0.086$.

To find the cross section for dijet events as a function of $\Delta\phi$, we use the BFKL relation [39]

$$\begin{aligned} \frac{d\sigma_{gg}}{dp_{T,1}^2 dp_{T,2}^2 d\Delta\phi} &= \frac{\alpha_s^2 C_A^2 \pi}{2p_{T,1}^3 p_{T,2}^3} \frac{1}{2\pi} \sum_{n=-\infty}^{+\infty} e^{in\Delta\phi} \\ &\times \frac{1}{2\pi} Re \int_{-\infty}^{+\infty} dz \exp\left(2t\chi_n(z) + iz\ln(p_{T,1}^2/p_{T,2}^2)\right) \end{aligned} \tag{3.42}$$

let $t = \alpha_s C_A \Delta y/\pi$ and $\chi_n(z) = Re\left[\psi(1) - \psi\left(\frac{1}{2}(1+|n|) + iz\right)\right]$. In this case, ψ is the Digamma function, i.e. the derivative of the logarithmic Gamma function. For this derivation, we define

$$\Delta\phi = |\phi_1 - \phi_2| - \pi \tag{3.43}$$

so that $\Delta\phi = 0$ when the jets are completely correlated, i.e. produced back-to-back.

Integrating over the transverse momenta,

$$\left.\frac{d\sigma_{gg}}{d\Delta\phi}\right|_{p_{T,1}^2, p_{T,2}^2 > P_T^2} = \frac{\alpha_s^2 C_A^2 \pi}{2P_T^2} \frac{1}{2\pi} \sum_{n=-\infty}^{+\infty} e^{in\Delta\phi} C_n(t) \tag{3.44}$$

where P_T is some minimum p_T and $C_n(t) = \frac{1}{2\pi}\int_{-\infty}^{+\infty} \frac{dz}{z^2+\frac{1}{4}} \exp\left(2t\chi_n(z)\right)$. This gives us the integrand

$$C_n(t) = \frac{1}{2\pi}\int_{-\infty}^{+\infty} \frac{dz}{z^2+\frac{1}{4}} \exp\left(2tRe\left[\psi(1) - \psi\left(\frac{1}{2}(1+|n|)+iz\right)\right]\right) \tag{3.45}$$

Using the following Digamma function relations [42]

$$\begin{aligned} \psi(1) &= -\gamma \\ \psi(z+n) &= \psi(z) + \sum_{k=0}^{n-1}(z+k)^{-1}, n \in \mathbb{N} \\ \Im\psi(iy) &= \frac{1}{2}\left(\pi\coth(\pi y) + \frac{1}{y}\right) \end{aligned} \tag{3.46}$$

where γ is the Euler-Mascheroni constant, along with the additional identities

$$\gamma = \sum_{m=2}^{\infty}(-1)^m \frac{\zeta(m)}{m} \tag{3.47}$$

$$\zeta(2n) = (-1)^{n+1}\frac{B_{2n}(2\pi)^{2n}}{2(2n)!} \tag{3.48}$$

$$\coth(x) = x^{-1} + \sum_{n=0}^{\infty}\frac{2^{2n}B_{2n}x^{2n-1}}{2n!} \tag{3.49}$$

$$\int_0^{\infty}\frac{x^2}{e^x-1}dx = 2\zeta(3) \simeq 2.40, \tag{3.50}$$

where ζ is the Riemann zeta function and B_{2n} is a Bernoulli number, we can solve for the cross section such that:

$$\sigma_{gg} = \frac{\alpha_s^2 C_A^2 \pi}{2P_T^2} C_\circ(t), \tag{3.51}$$

where $C_\circ(t)$ is defined as

$$C_{\circ}(t)\begin{cases} = 1 & \text{for} \quad t = 0 \\ \sim \left[\frac{1}{2}\pi 7\zeta(3)t\right]^{-1/2} e^{4ln2t} & \text{for} \quad t \to \infty \end{cases} \tag{3.52}$$

When $\Delta\phi$ is defined as $\Delta\phi = |\phi_1 - \phi_2|$ we see that $C_{\circ}(t) = 1$ when $\Delta\phi = \pi$. In the analysis, $\Delta\phi$ will be defined as $\Delta\phi = |\phi_1 - \phi_2|$.

From Eq. 3.51 we see that the cross section is proportional to $\sigma_{gg} \sim e^{\lambda\Delta y}$, where $\lambda = 4\alpha_s C_A \ln 2/\pi$. Thus our cross section will increase as Δy increases.

However our parton function also depends on Δy. We find that the effects of the rapid increase in cross section from Δy disappears in the kinematic limit

$$\Delta y = 2\cosh^{-1}\left(\sqrt{s}/2P_T\right) \tag{3.53}$$

so that it is difficult to see the increase in the cross section due to the increasing separation in rapidity.

This analysis increases the rapidity range under study to look at the larger phase space afforded by the LHC kinematics. A comparison to NLO calculation done by NLOJet++ is made in this analysis. Comparison to the Monte Carlo models PYTHIA, HERWIG, and ALPGEN are also made.

Chapter 4

Physics Observables

4.1 Introduction

The LHC is a high center-of-mass energy proton-proton (pp) collider providing a high rate of multijet events. This signature allows for investigations of Quantum Chromodynamics (QCD).

Dijet production at leading order (LO) results in two jets being produced in an event. These jets are fully correlated in in azimuth: they will be produced back to back with an azimuthal difference $\Delta\phi = \pi$. The opening angles in ϕ and rapidity between the two highest p_T jets in an event change with the addition of soft radition or additional production of jets. Small deviations from π will generally be observed when soft radiation is produced in the event either in the initial state or in the final state. Larger deviations from π are indicative of hard radiation, forming additional jets in the event. For three-jet production the azimuthal angle between the two leading jets becomes $\Delta\phi \geq 2/3\pi$. For more than one additional jet, the region below $2/3\pi$ will become populated. See Fig. 4.1.

Thus, distributions of $\Delta\phi$ test higher-order perturbative QCD (pQCD) calculations without requiring the reconstruction of additional jets and offer a way to examine the transition between soft and hard QCD processes with a single observable. The proper description of QCD radiation is important for a wide range of precision measurements as well as for searches for new physical phenomena. The opening angle in rapidity up to $|y| < 5.6$ allows for an exploration of larger region of Q^2 and possible observation of the transition from DGLAP evolution to BFKL evolution.

The following analysis looks at the normalized differential cross sections $(1/\sigma_{\text{dijet}})(d\sigma_{\text{dijet}}/d\Delta\phi)$ and $(1/\sigma_{\text{dijet}})(d\sigma_{\text{dijet}}/d\Delta y)$ for the 2010 data set with the total integrated luminosity $\int \mathcal{L} dt = (36 \pm 4)\,\text{pb}^{-1}$. The $\Delta\phi$ and Δy distributions are studied separately and also the two dimensional distributions

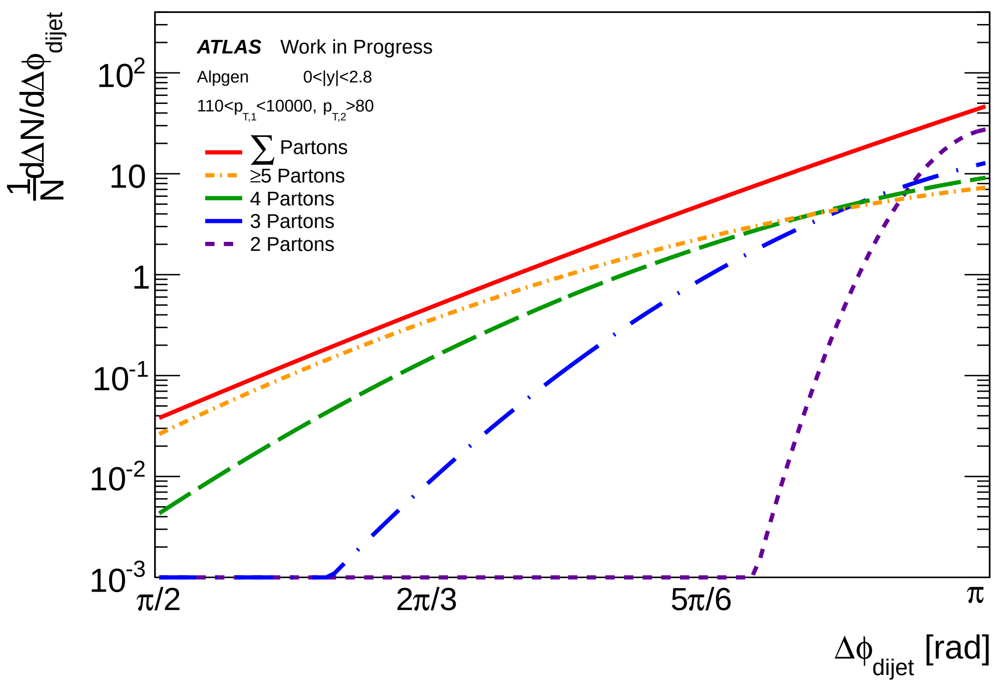
ATLAS Work in Progress
Alpgen 0<|y|<2.8
110<p_{T,1}<10000, p_{T,2}>80
∑ Partons
≥5 Partons
4 Partons
3 Partons
2 Partons
1/N dΔN/dΔφ_dijet
10^2
10
1
10^-1
10^-2
10^-3
π/2
2π/3
5π/6
π
Δφ_dijet [rad]

(a)

Figure 4.1

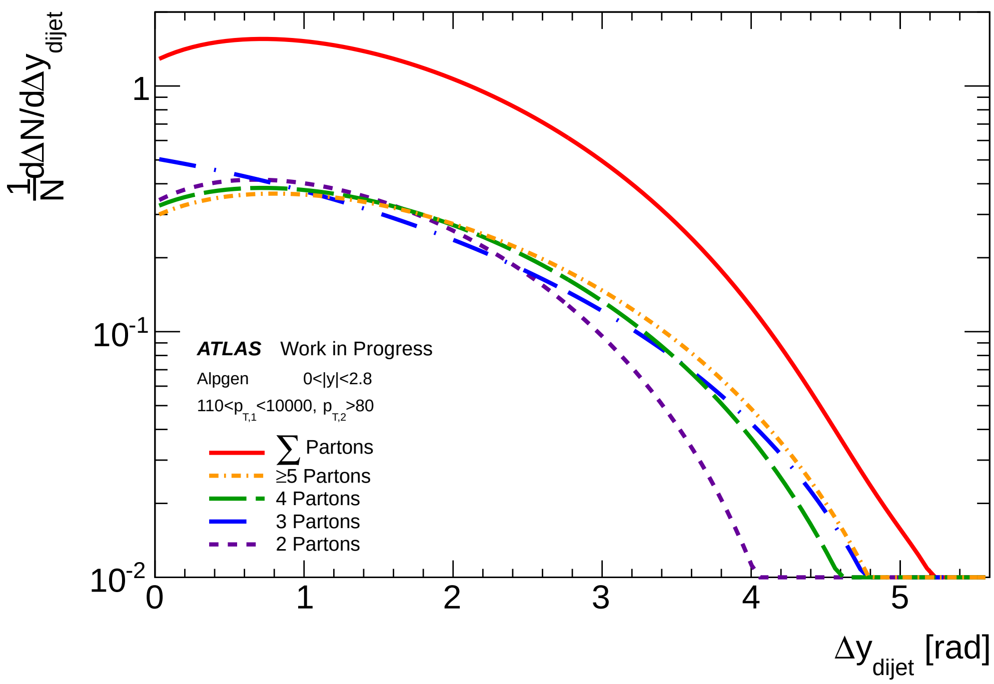

(b)

Figure 4.1: The $\Delta\phi$ and Δy distribution for varying amounts of additional soft and hard radiation contributions. Individual contributions from $2 \rightarrow 2$ (purple dashed line), 3 (blue dot-long dashed line), 4 (green long dashed line), and ≥ 5 (orange dot-dashed line) production with ALPGEN for N number of events are shown. The total contribution (Σ Partons) is represented by the solid red line. The subleading jet p_T requirement is 80 GeV, and the leading jet p_T must be >110 GeV.

in both variables. This analysis is an extension of the previous ATLAS measurement of the $\Delta\phi$ as a function of the normalized differential cross section which was limited to central jets within $|y| < 0.8$ [43]. Unfolding in the Δy observable is added to this analysis as well. The ATLAS Δy analysis looking at radiation between the two leading jets was extended to higher p_T ranges with this study [44]. The dijet azimuthal decorrelation was previously measured in $p\bar{p}$ collisions at $\sqrt{s}$= 1.96 TeV by the DØ Collaboration based on an integrated luminosity of 150 pb^{-1} [45]. The CMS Collaboration has studied $\Delta\phi$ in pp collisions at $\sqrt{s}$= 7 TeV with an integrated luminosity of 2.9 pb^{-1} [46].

The measured differential cross sections in the data are corrected for experimental resolution with an unfolding method using the PYTHIA Monte Carlo LO particle-level generator. The corrected data distributions are compared to next-to-leading order (NLO) pQCD for up to three-parton production. We also compare the data to other Monte Carlo generators such as the LO generator HERWIG and to higher-order tree-level pQCD diagrams from particle-level event generator ALPGEN, which includes up to $2 \rightarrow 6$ particle production. Verification of the performance of the Monte Carlo event generators using high-statistics is of clear interest for applications that require accurate description of processes with several jets. The QCD radiation is similar to that in W and Z production with additional jets, which are background processes in top quark studies and searches for the Higgs boson.

4.2 Anti-k$_T$ Algorithm

The jets in this analysis were reconstructed using the anti-k$_T$ algorithm [47] with a cone size of 0.6. This algorithm was found to be 98% efficient over our p_T region of interest [48].

The anti-k$_T$ is the preferred jet algorithm because it is infrared and collinear (IRC) safe. The anti-k$_T$ algorithm is not adaptable to soft-radiation near the jet which would otherwise lead to an irregular cone boundary. This is different from traditional "iterative cone" algorithms.

The family of general sequential recombination algorithms, of which the anti-k$_T$ algorithm is an example, can be described by the equation

$$\begin{aligned} d_{ij} &= min\left(k_{T,i}^{2p}, k_{T,j}^{2p}\right)\frac{\Delta_{ij}^2}{R^2} \\ d_{iB} &= k_{T,i}^{2p} \end{aligned} \tag{4.1}$$

where $\Delta_{ij}^2 = (y_i - y_j)^2 + (\phi_i - \phi_j)^2$ and the $k_{T,i}, y_i, \phi_i$ are the transerve momentum, rapidity, and aziumuthal angle of a particle i, raised to the power p, and with radius parameter R, which for our case is $R = 0.6$. The algorithm is seeded by particle i and builds the jet as a function of the transverse momenta i and j with distance between the seed particle and pseudojet entities j around it. The clustering of particles proceeds from the smallest distance and recombines entities i and j within a distance d_{ij}. Beam interference is removed by defining the distance from the particle i and the beam B, called d_{iB} such if d_{iB} is smaller than all d_{ij}, the entity is not considered for recombination.

The minimization is taken as a function of k_T taken to the power $2p$. There are different algorithms for each of the special cases:

- $p > 0$, defines a class of algorithms that have behavior with respect to soft radiation similar to the k_T algorithm ($p = 1$)
- $p = 0$, defines the Cambridge/Aachen algorithm
- $p < 0$, defines a class of algorithms that have behavior with respect to soft radiation similar to the anti-k_T algorithm ($p = -1$)

A comparison of these different algorithms along with another IRC algorithm, SiSCone, is shown in Fig. 4.2 [47]. Each color represents a different jet reconstructed using each of the algorithms. The algorithms were run over the same event. The height of the "lego towers" is proportional to the energy reconstructed for each jet.

The boundary, in (ϕ, η)-space, of jets reconstructed with the anti-k_T algorithm is unaffected by soft radiation. This leads to an area independent of the distance Δ_{12} between between a hard particle p_1 and a soft particle p_2. Define the passive area (a) measures a jet's susceptibility to point-like radiation and the active area (A) which measures the susceptibility to diffuse radiation. The active area of the anti-k_T jet is defined as

$$A_{\text{anti-}k_T,R}(\Delta_{12}) = a_{\text{anti-}k_T,R}(\Delta_{12}) = \pi R^2 \tag{4.2}$$

where the passive area $a_{\text{anti-}k_T,R}(\Delta_{12})$ is defined as $a_{\text{anti-}k_T,R}(\Delta_{12}) = \pi R^2$ when $\Delta_{12} = 0$. Since the anti-k_T algorithm is unaffected by soft radiation, the passive area does not increase when $\Delta_{12} > 0$.

In order for a cell in the calorimeter to seed the jet algorithm, it must have an energy deposition where $|E_{cell}| > 4\sigma$ with respect to the noise rms σ. In order for nearby cells to be considered for inclusion in the jet, they must have an energy deposition of $|E_{cell}| > 2\sigma$ above the noise rms σ. These cells are then considered for jet-building candidates. These cells are then group together in a cluster called a "topocluster". The anti-k_T algorithm builds the topocluster from the cell entities.

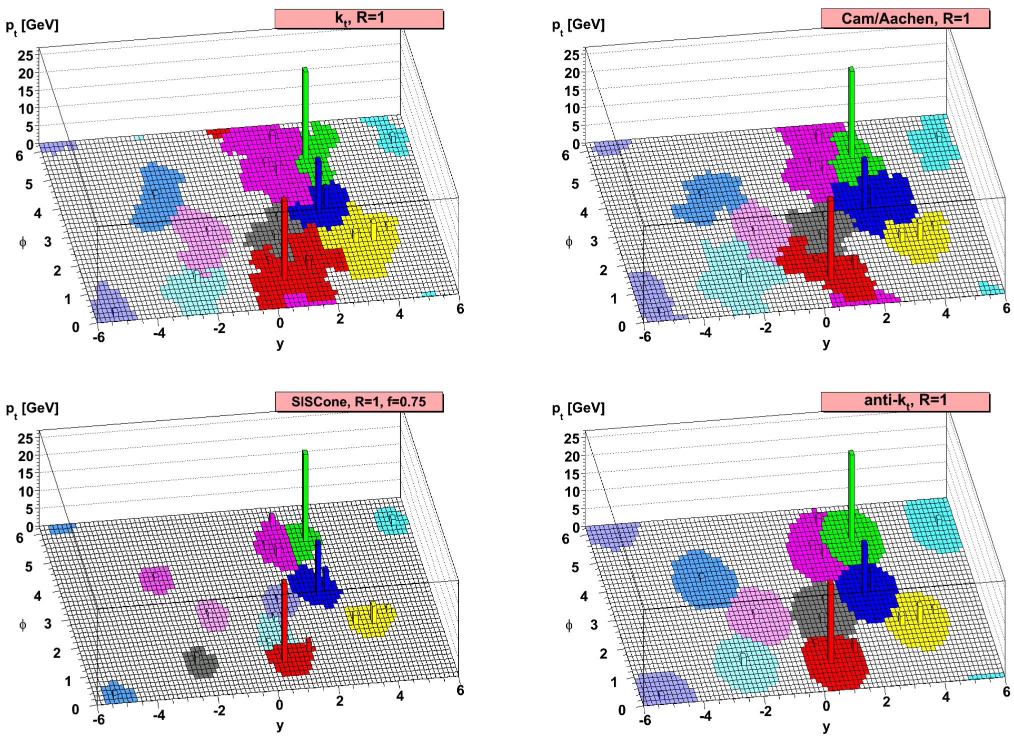

Figure 4.2: HERWIG generated parton-level event with jets reconstructed using different jet algorithms. The colored spikes represent the seed entity and the full reconstructed jets and their boundaries are shown with the colored regions. The anti-k_T algorithm can be seen in the lower right corner.

4.3 Observable Definition

The $\Delta\phi$ and Δy are formed for the two highest transverse momentum jets reconstructed in the events passing our selection criteria, defined as

$$\Delta\phi = |\phi_1 - \phi_2|, \quad \pi/2 < |\Delta\phi| < \pi \tag{4.3}$$

$$\Delta y = |y_1 - y_2| \tag{4.4}$$

The range of $\Delta\phi$ considered is $[\pi/2,\pi]$ and is expected to have contributions mostly from events with four or fewer jets, see Fig. 4.1. This range was chosen for statistical reasons because the generation of events with >4 jets with current generators does not give adequate statistics for $\Delta\phi< \pi/2$. In addition, the NLO order calculation was done for 3 jets at NLO and 4 jets at LO. Thus, the NLO calculation is not valid for $\Delta\phi< \pi/2$. We will show that events with four or fewer jets are well modeled by the Monte Carlo generators used in this study, see Sec. 6.3.

The range of Δy taken between the two highest p_T jets is chosen to select jets reconstructed in the barrel and endcap regions of the detector out to rapidities of $|y| < 2.8$. This acceptance should be sensitive to the low-x space to explore the transition from DGLAP to the BFKL-dominated jet evolution. Within this rapidity acceptance, Δy is in the range $|\Delta y| < 5.6$.

The binning chosen in $\Delta\phi$ and Δy has been crosschecked against the resolution of these observables. The bin sizes used for each observable are larger than 3σ, where σ is the resolution in the variable considered, see Chap. 7 for details.

Anti-k$_T$ algorithms also produce well-defined "cone-like" jets in QCD data and can be utilized for jet reconstruction in NLO pQCD, MC event generators, and data with detector energy depositions, see Sec. 4.2.

The $\Delta\phi$ and Δy observables are formed from jets passing the quality cuts, see Sec. 6.2, with the additional requirements that each jet $p_T \geq 80$ GeV and within $|y| < 2.8$ for those jets to be taken into consideration for the observable and for crosschecks.

The events are binned in the leading jet's transverse momentum, p_T^{max}. The data is divided in nine p_T^{max} bins: $110-160$ GeV, $160-210$ GeV, $210-260$ GeV, $260-310$ GeV, $310-400$ GeV, $400-500$ GeV, $500-600$ GeV, $600-800$ GeV, or > 800 GeV. Depending on the statistics within the selected rapidity ranges, the upper bins may be merged.

Chapter 5

Event Selection

The data used in this analysis is from the LHC 2010 proton-proton collision campaign which ran from April 2010 through the end of October 2010. The data used are from runs 152166-167844 during data taking periods A-I. The integrated luminosity during this data taking period was $\int \mathcal{L} dt = (36 \pm 4)\,\mathrm{pb}^{-1}$. The total uncertainty in the luminosity measurement for this period is 11%, dominated by the uncertainty in the LHC beam current [49]. The event selection for this analysis is based on the appropriate triggers and quality status as a “good” run. See Appendix A for the complete list of data samples used in this analysis.

5.1 Data Quality

The data quality is ensured by using only runs that were qualified as good runs and were included in the Good Runs List (GRL). The GRL is determined by several criteria, all of which must be satisfied to qualify the run as a good run. These criteria include:

- The LHC is operating with stable beams and the ”Stable Beams” flag is set
- The Tier0 projet flag is set to data10_7TeV indicating that beam setup and detector were in data taking mode
- The data quality information is reviewed by shifter for problems such as noise bursts or unexpected holes in detector coverage
- The data header and clock have no problems
- The ATLAS solenoid and toroid magnets are on and operating normally
- The inner detector (Pixel, SCT, and TRT) is operating at normal voltage and 98% or more of channels are read out without error

- The calorimeters (LAr and Tile) are operating at nominal voltage and without readout errors
- The jet trigger is valid

The data quality tags for each period and its corresponding runs are list in Tab. 5.1 [50].

The data luminosity is calculated by the Luminosity Working Group and is corrected for data quality. The absolute luminosity is measured from the machine with van der Meer scans and the relative luminosity measurement is made using specialized detectors, such as LUCID, ZDC, and diamond beam counters [49]. The luminosity information is stored in the ATLAS offline conditions database (COOL) indexed by run number and lumiblock. The luminosity is then recalculated given specific conditions for an analysis, such as the GRL, using the code iLumiCalc.exe. The data quality tags listed in Tab. 5.1 along with the luminosity tag OflLumi-7TeV-002 were used to calculate the luminosity for the conditions of this analysis.

Table 5.1: The Data Quality tags for data taking periods with corresponding runs.

Period	Runs	Data Quality Tags
A	152166-153200	LBSUMM#DetStatus-v02-repro04-01
B	153565-155160	LBSUMM#DetStatus-v02-repro04-01
C	155228-156682	LBSUMM#DetStatus-v03-pass1-analysis-2010C
D	158045-159224	LBSUMM#DetStatus-v03-pass1-analysis-2010D-RPCloose
E	160387-161948	LBSUMM#DetStatus-v03-pass1-analysis-2010E
F	162347-162882	LBSUMM#DetStatus-v03-pass1-analysis-2010F
G	165591-166383	LBSUMM#DetStatus-v03-pass1-analysis-2010G
H	166466-166964	LBSUMM#DetStatus-v03-pass1-analysis-2010H
I	167575-167844	LBSUMM#DetStatus-v03-pass1-analysis-2010I

5.2 Trigger Requirements

The required jet trigger changed for the different data periods in this analysis. In periods A-F, the trigger decision was made at Level 1 (L1). Periods G-I used the Level 2 (L2) trigger decision. The L1 trigger is a hardware-based decision using a sliding-window algorithm [51] to identify the energy deposits in the LAr and Tile calorimeters in "towers" the of size 0.8×0.8 in $\Delta\eta \times \Delta\phi$. The L2 trigger makes a decision based on a software cone clustering algorithm. For more on the triggers, see Sec. 2.5. The trigger selection requires at least one jet to have a transverse energy above the threshold. The triggers were chosen such that the p_T^{max} bin's minimum p_T is well in the trigger efficiency plateau, see Fig. 5.1 [48]. The triggers used for the leading jet p_T^{max} bins are summarized in Tab. 5.2.

Table 5.2: Trigger decisions and collected luminosity for different p_T^{max} regions.

$p_{T,1}$ (GeV)	L1 Trigger (GeV)	L2 Trigger (GeV)	Luminosity (pb^{-1})
110-160	30	45	2.3
160-210 210-260	55	70	9.6
260>	95	–	36

5.3 Pile-up

For the 2010 dataset, contributions from events with pile-up are minimal. "Out-of-time" pile-up occurs when the signals from the last bunch crossing are not completely read out and electronic hit signals returned to their pedestal values before the next bunch crossing. "In-time" pile-up occurs because tracks and energy deposits from unrelated interactions in the same bunch crossing are included in the interaction of interest.

As one sees from Tab. 5.3, events in data that have only one reconstructed vertex make up almost 44% of the total. The majority of the other contributions to our dataset comes from crossings with two reconstructed vertices. The Monte Carlo used for the unfolding, see Sec. 7.4, does not incorporate "out-of-time" pile-up in the event reconstruction, but it does include effects from "in-time" pile-up. "Out-of-time" pile-up contributions were minimal, and the effects were mitigated due to the negative energy pedestal of the LAr calorimeter. The distributions in data were shown to be stable with respect to events with one vertex and with multiple vertices, see Fig. 35 in [52]. To see how "in-time" pile-up affects the unfolding, a comparison is made between events with only one reconstructed vertex and events with more than one reconstructed vertex in PYTHIA.

There is statistics for events with more than one vertex, and enough to do a reasonable comparison. A ratio of events with more than one vertex is taken to those with only one vertex, see Figs. 5.2-5.3. Where points are missing in the plots, it is due to a lack of statistics in those regions of phase space. There is some indication that there is a slight deviation from unity for events with

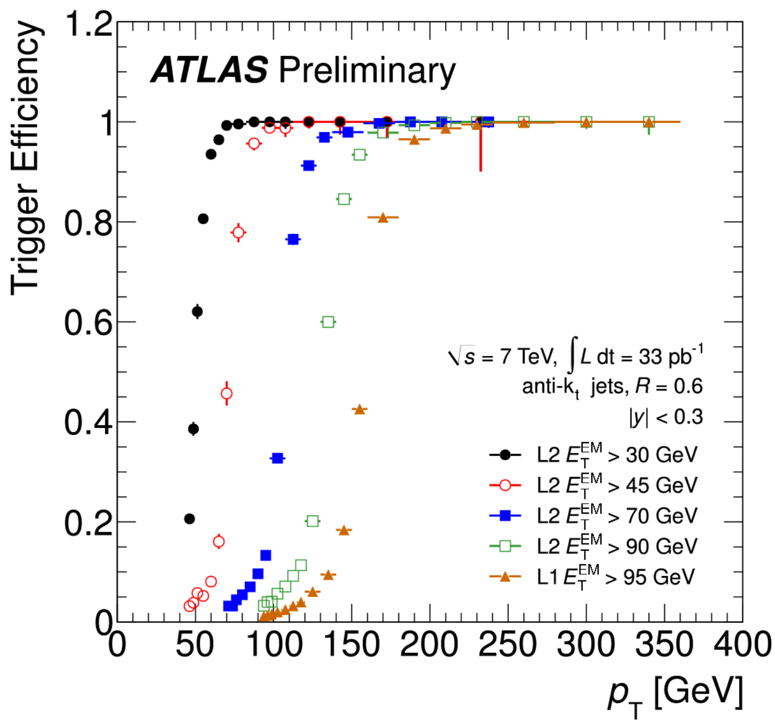

Figure 5.1: Combined L1+L2 jet trigger efficiency as a function of reconstructed jet p_T for anti-kt jets with $R = 0.6$ in the central region $\Delta y < 0.3$ shown for different L2 trigger thresholds. The trigger thresholds are at the electromagnetic scale, while the jet p_T is at the calibrated jet scale. The highest trigger chain does not apply a threshold at L2, so its L1 threshold is listed.

Table 5.3: Percentage of vertex candidates in data for inclusive $p_T^{max} > 110$ GeV and $|y| < 2.8$.

Number of Vertex Candidates	Fraction of Events in Data (%)
1	43.8
2	33.8
3	14.7
4	4.7
5	1.2
6	0.3
7	0.06
8	0.01
9	0.002
10	0.0004

more than two jets or three jets when looking at the $\Delta\phi$ and Δy distribution. Since there are orders of magnitude fewer events with multiple jets than with two jets, it is a reasonable assumption that the effect of pile-up will be small in our results.

5.4 Monte Carlo Samples

Monte Carlo uses random process to generate events from the many possible outcomes predicted by theory. These events are generated from various event generators such as PYTHIA, HERWIG, or ALPGEN. To simulate how these events would look in our detector, the events are run through a detector simulation such as GEANT [53]. One can then compare the predicted theoretical outcome to the observed outcome in data.

There were several different full simulation Monte Carlos used in this analysis:

- PYTHIAversion 6.421 [54]
- HERWIGversion 6.510 [55] + JIMMY [56] version 4.3
- ALPGEN [57] version 2.13 interfaces to HERWIG+ JIMMY

A GEANT-based simulation was used to simulated detector effects [53] [11] using the standard MC10 ATLAS tune. See Appendix B for the list of samples used in this analysis.

Some next to leading order (NLO) fast simulation was calculated at generator level to allow for direct comparison to theory. The generator level produc-

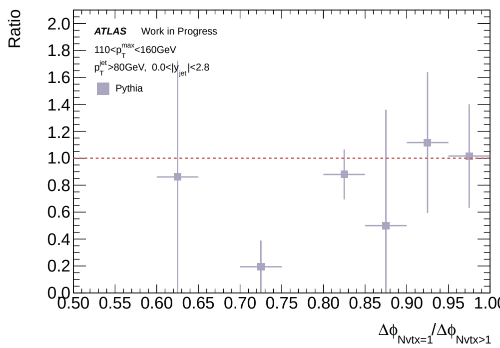

(a)

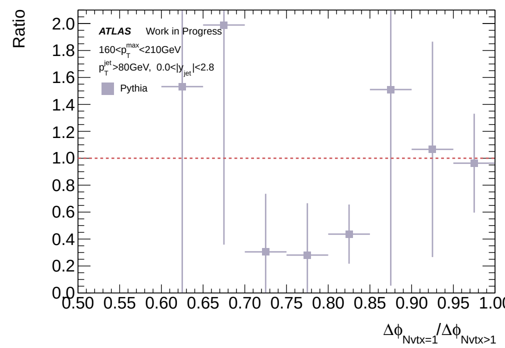

(b)

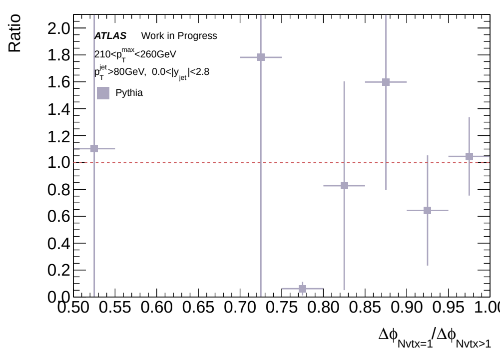

(c)

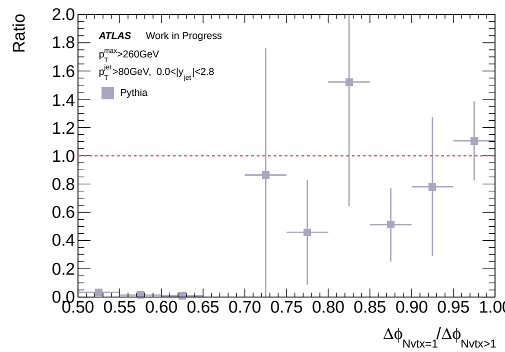

(d)

Figure 5.2: The ratio of the unfolded $\Delta\phi$ distributions for events with a single vertex and multiple vertices in PYTHIA in $p_{\mathrm{T}}^{\max}$ bins $110-160$ GeV, $160-210$ GeV, $210-260$ GeV, and >260 GeV for each trigger selection.

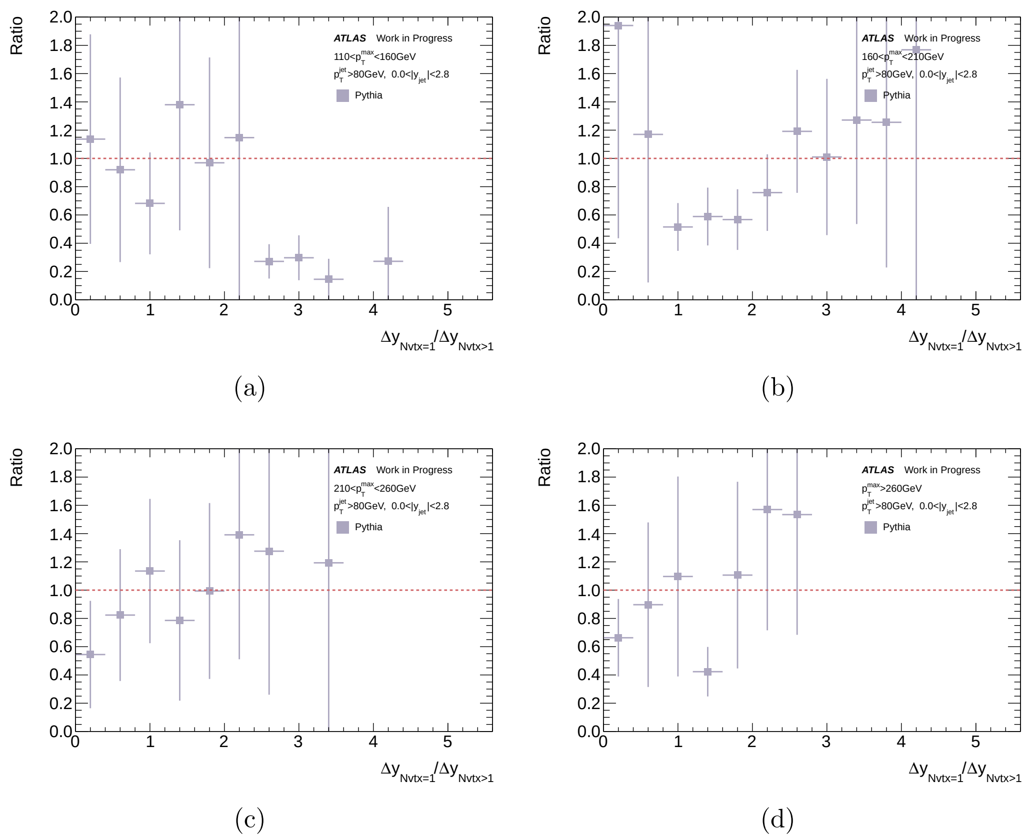

(a) (b) (c) (d)

Figure 5.3: The ratio of the unfolded Δy distributions for events with a single vertex and multiple vertices in PYTHIA in $p_{\mathrm{T}}^{\mathrm{max}}$ bins $110-160$ GeV, $160-210$ GeV, $210-260$ GeV, and > 260 GeV for each trigger selection.

tion generates all particles in the final state as 4-vectors but does not simulate their detection and registration ("hits") in the ATLAS detector. These samples were produced using APPLGrid [58] dijet production with CTEQ6.6 [59] Les Houches PDF. One hundred million events were used to generate the $\Delta\phi$ distribution and a billion events were produced to populate the Δy distribution.

Chapter 6

Jet Selection

The jets in our study are reconstructed using the anti-k$_T$ algorithm with a cone size of $R = 0.6$. The algorithm uses topological clusters formed from the calorimeter cell energies. The jet energy calibration was done using a numerical inversion technique to estimate the jet p_T at hadronic scale given an electromagnetic scale measurement based on a full ATLAS GEANT4 simulation of jets within $|y| < 2.8$ and with $p_T > 20$ GeV. See Sec. 4.2 for more information on the reconstruction with the anti-k$_T$ algorithm and Sec. 6.1 for more information on the jet energy scale conversion from the electromagnetic scale to hadronic scale. After reconstruction, the jets were subject to quality cuts.

6.1 Jet Energy Scale

Jets are reconstructed at the electromagnetic scale in the ATLAS calorimeters. The Jet Energy Scale (JES) calibration aims to correct the energy and momentum of the jets measured in the calorimeter to the hadronic jet energy scale.

The electromagnetic scale is first determined through muon measurements from test beams and cosmic rays. A correction is applied from the measured invariant mass $Z \to ee$ events from collisions. The electromagnetic scale is then corrected to the hadronic jet energy scale with a jet-by-jet correction as a function of the jet energy and pseudorapidity. A pile-up correction is applied before the hadronic energy scale correction. The average pile-up is subtracted using a correction derived from an in-situ calibration [60]. The position of the jet is then corrected such that it points back to the primary vertex of the interaction instead of the geometrical origin of the ATLAS detector. The jet energy correction constants are derived from a comparison of the kinematics of reconstructed (full ATLAS GEANT4 simulation) and truth (particle level) jets in Monte Carlo and applied to each jet. The reconstructed and truth jets are matched using isolated truth jets only and a cone of $\Delta R = 0.3$. See Fig. 6.1 for the jet energy scale (JES) correction as a function of jet p_T for three η ranges of interest.

There are several sources of uncertainty on the JES. There is an uncertainty due to the JES calibration method itself, the calorimeter response, the detector simulation, the physics model assumed by the Monte Carlo sample, and the relative calibration for jets with $\eta > 0.8$. The JES uncertainty for the η regions probed by this study are shown in Figs. 6.2. Additional information on the JES correction and uncertainty can be found in reference [60].

A correction must be applied to each jet in data and Monte Carlo to translate the JES measured at the electromagnetic scale to the hadronic scale. The JES correction is applied as a function of jet energy and rapidity. The correction is provided by the OffsetEtaJES package from the ATLAS Standard Model JetMET group.

6.2 Jet Quality

Events under consideration satisfy our data quality and jet trigger requirements, see Sec. 5.1. In addition to these criteria, events are also required to have a reconstructed primary vertex with at least 5 associated tracks.

Jets are reconstructed using the anti-k_T jet algorithm with a distance parameter of $R = 0.6$. Data quality requirements are applied to each reconstructed jet based on its properties. Based on the recommendations of the ATLAS Jet/Etmiss Working Group, "loose bad" jets are rejected, where a loose bad jet is defined according to the following criteria [61] [62]:

- $f_{\mathrm{HEC}} > 0.5$ and $|q_{\mathrm{HEC}}| > 0.5$ or $|NegativeE| > 60$ GeV, where f_{HEC} was the fraction of the jet energy in the LAr hadronic endcap (HEC), q_{HEC} was the fraction of jet energy from HEC cells with a measured pulse shape that was significantly different from the reference pulse shape, and $NegativeE$ is the energy sum of all cells with energies below the pedestal. Jets that satisfied these requirements were caused by "sporadic noise bursts".
- $|f_{\mathrm{quality}}| > 0.8$ and $f_{\mathrm{EM}} > 0.95$ and $|\eta| < 2.8$, where f_{quality} is the fraction of jet energy from calorimeter cells with a measured pulse shape that was significantly different from the reference pulse shape, f_{EM} is the fraction of jet energy in the electromagnetic (EM) calorimeter, and η is the angle

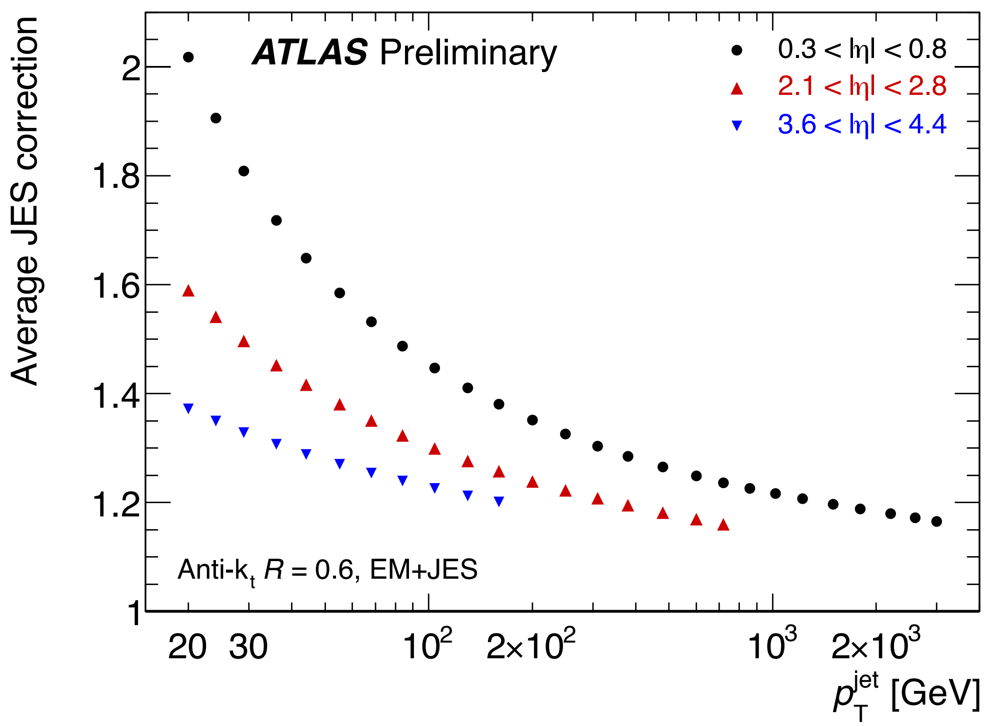

Figure 6.1: Average jet energy scale correction as a function of calibrated jet transverse momentum for three representative eta-intervals. The correction is shown over the accessible kinematic range, i.e. values for jets above the kinematic limit are not shown.

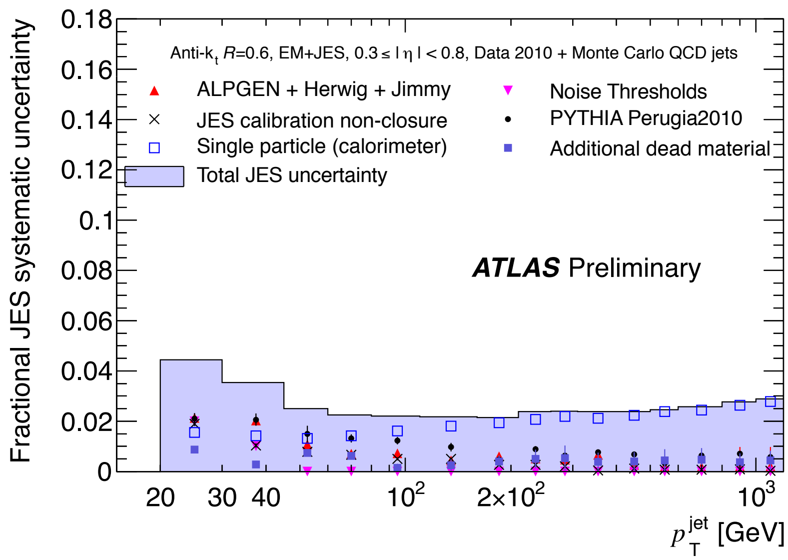

(a)

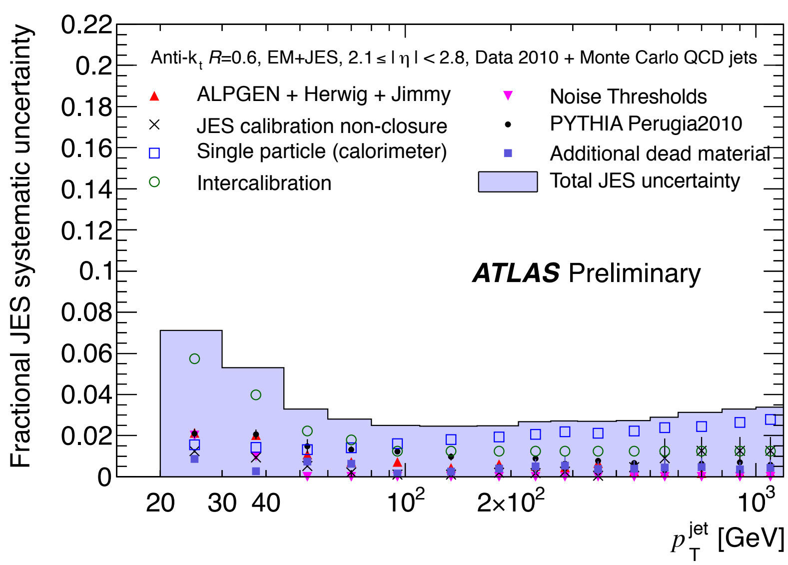

(b)

Figure 6.2: Fractional jet energy scale systematic uncertainty as a function of p_T for jets in the pseudorapidity region $0.3 < |\eta| < 0.8$ in the calorimeter barrel and the pseudorapidity region $2.1 < |\eta| < 2.8$. The total uncertainty is shown as the solid light blue area. The individual sources are also shown, with uncertainties from the fitting procedure if applicable.

with respect to the beam taken at EM scale. This criterion identifies fake jets caused by coherent noise bursts.

- $|t_{\rm jet}| > 25\,{\rm ns}$ or $f_{\rm EM} < 0.05$ and $f_{ch} < 0.05$ and $|\eta| < 2$ or $f_{max} > 0.99$ and $|\eta| < 2$, where $t_{\rm jet}$ is the timing of the jet with respect to the event time, f_{ch} is the charged jet fraction taken as the sum of $p_{\rm T}$ of tracks associated to the jet divided by calibrated jet $p_{\rm T}$, and f_{max} is the maximum energy fraction in a single calorimeter layer. This requirement eliminates jets reconstructed from out-of-time energy depositions in the calorimeter and from cosmic rays.

These criteria correspond to the jet cleaning cuts recommended for Athena v16.0.x reconstruction. The "loose bad" jet cuts are only applied to data.

6.3 Jet Kinematics in Data and Monte Carlo

The kinematic distributions for the leading and sub-leading jets in events which satisfy the event quality cuts and where the reconstructed jets satisfy the jet quality criteria can be seen in Figs. 6.4-6.9 before the observable requirements for $\Delta\phi$ and Δy are imposed. The data is reconstructed and the Monte Carlo is full-simulation PYTHIA with GEANT. The jet multiplicity for all these events is plotted in Fig. 6.3. The PYTHIA Monte Carlo distributions are normalized to the number of dijet events in data. The comparison is done for all jets within $|y| < 2.8$ and for the four different trigger regions consisting of p_T^{max} bins $110-160$ GeV, $160-210$ GeV, $210-260$ GeV, and > 260 GeV. There is reasonable agreement between data and Monte Carlo within errors and an unfolding of data with PYTHIA Monte Carlo seems reasonable. The kinematic distributions for the third-leading and fourth-leading jets can be found in Appendix C and also show good agreement between PYTHIA and data.

6.4 Monte Carlo Statistical Uncertainty

The statistical uncertainty must be taken into account when deciding the binning for our distributions. The statistical uncertainty per bin must be reasonably small for our results to be meaningful. There are kinematic regions in our distributions that naturally have low statistics such as regions of high Δy values. In order to aid in populating these regions, some rapidity-weighted PYTHIA samples were used in this analysis. The events were generated with a

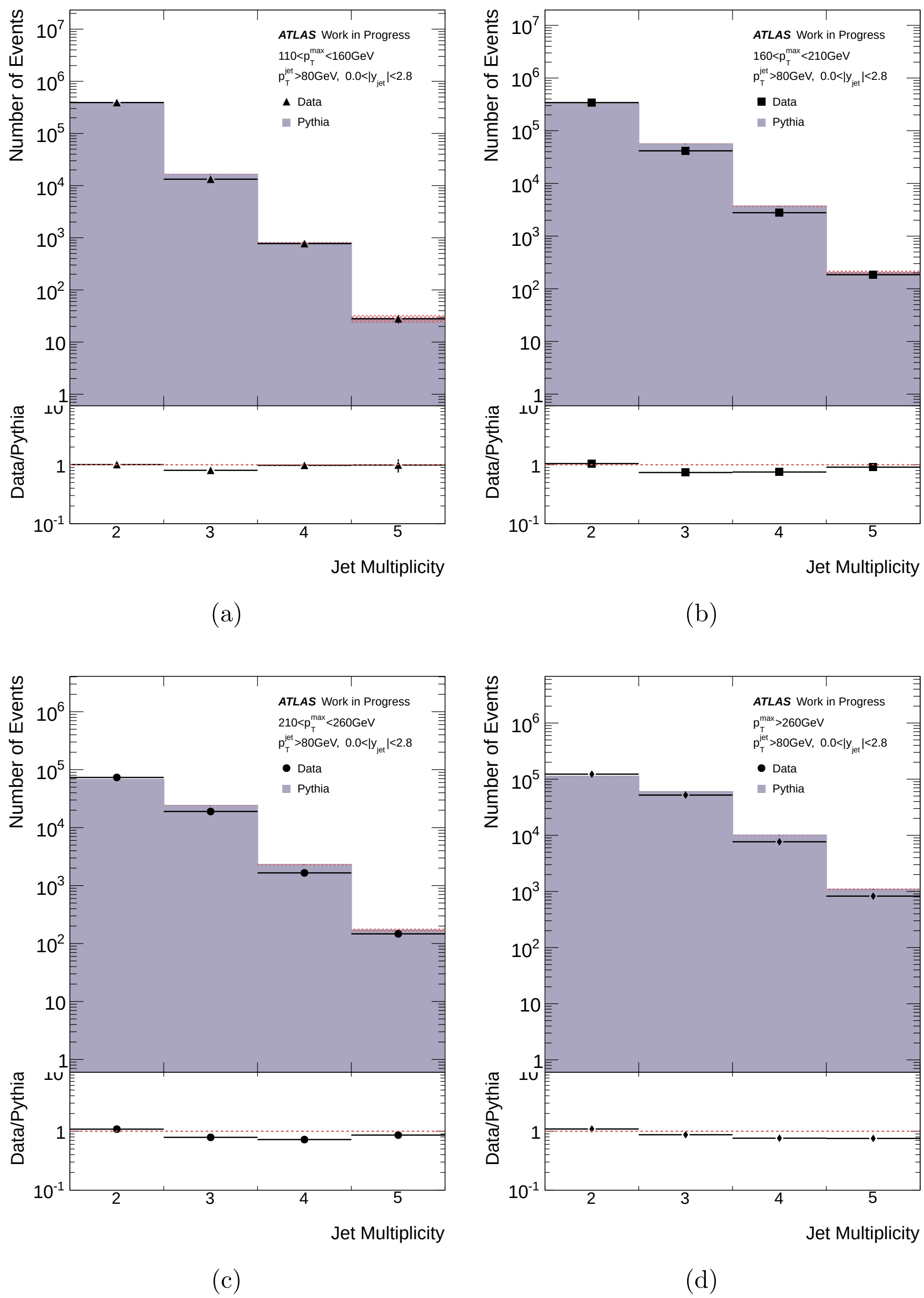

Figure 6.3: The jet multiplicity for $p_{\mathrm{T}}^{\mathrm{max}}$ bins $110-160$ GeV, $160-210$ GeV, $210-260$ GeV, and > 260 GeV with statistical errors in hashed area.

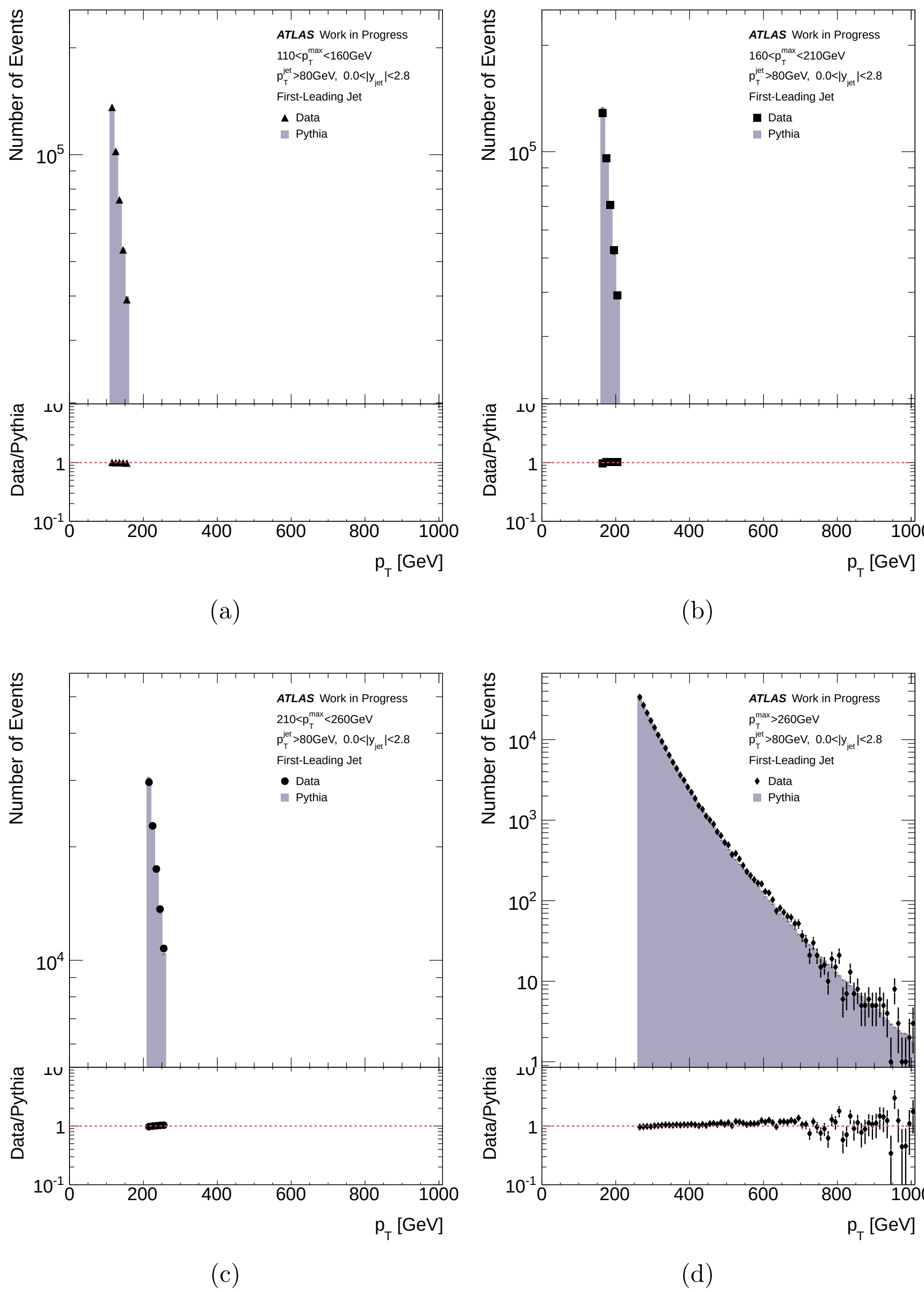

Figure 6.4: The p_{T} of the first-leading jet for $p_{\mathrm{T}}^{\max}$ bins $110-160$ GeV, $160-210$ GeV, $210-260$ GeV, and >260 GeV with statistical errors in hashed area.

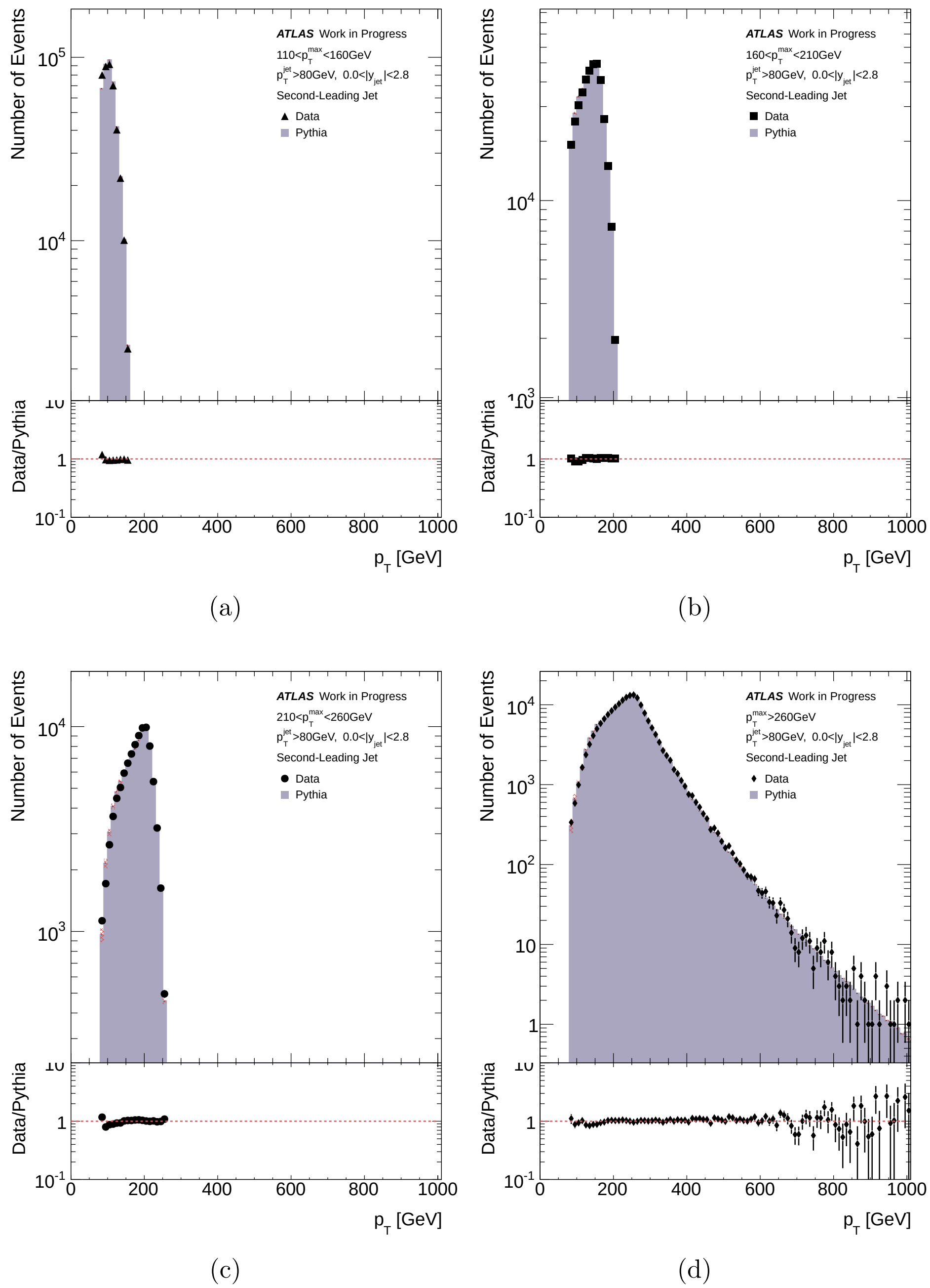

Figure 6.5: The p_{T} of the second-leading jet for $p_{\mathrm{T}}^{\max}$ bins $110 - 160$ GeV, $160 - 210$ GeV, $210 - 260$ GeV, and > 260 GeV with statistical errors in hashed area.

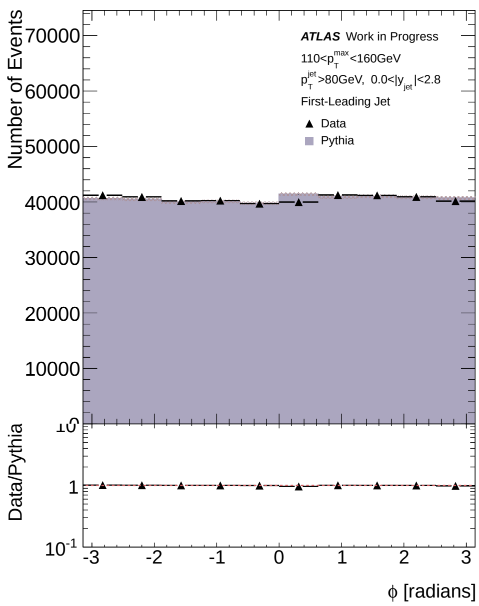

(a)

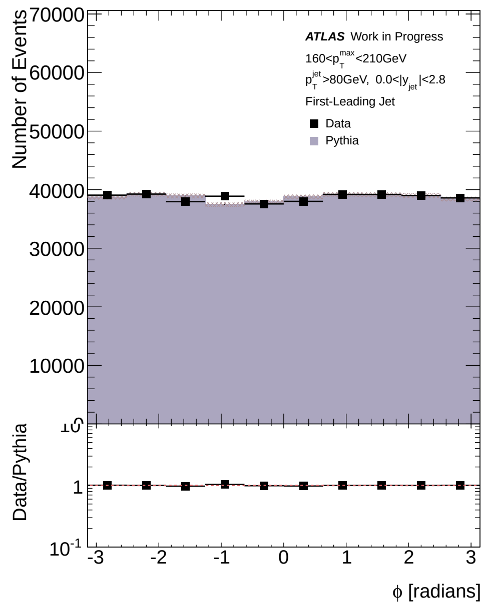

(b)

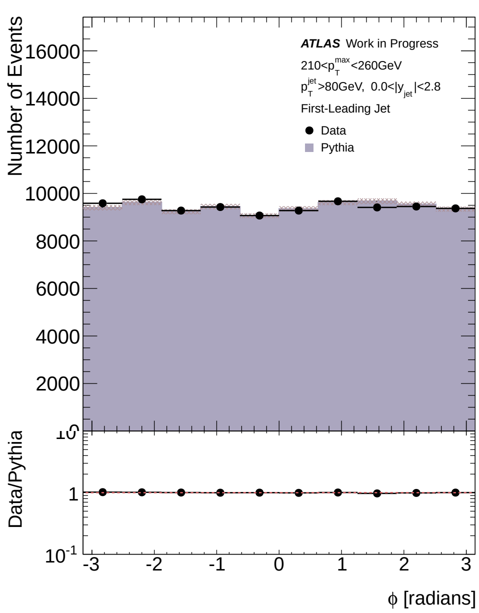

(c)

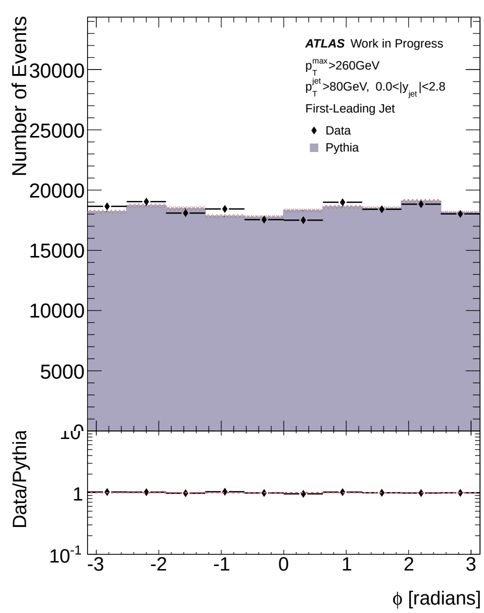

(d)

Figure 6.6: The ϕ of the first-leading jet for $p_{\mathrm{T}}^{\mathrm{max}}$ bins $110-160$ GeV, $160-210$ GeV, $210-260$ GeV, and > 260 GeV with statistical errors in hashed area.

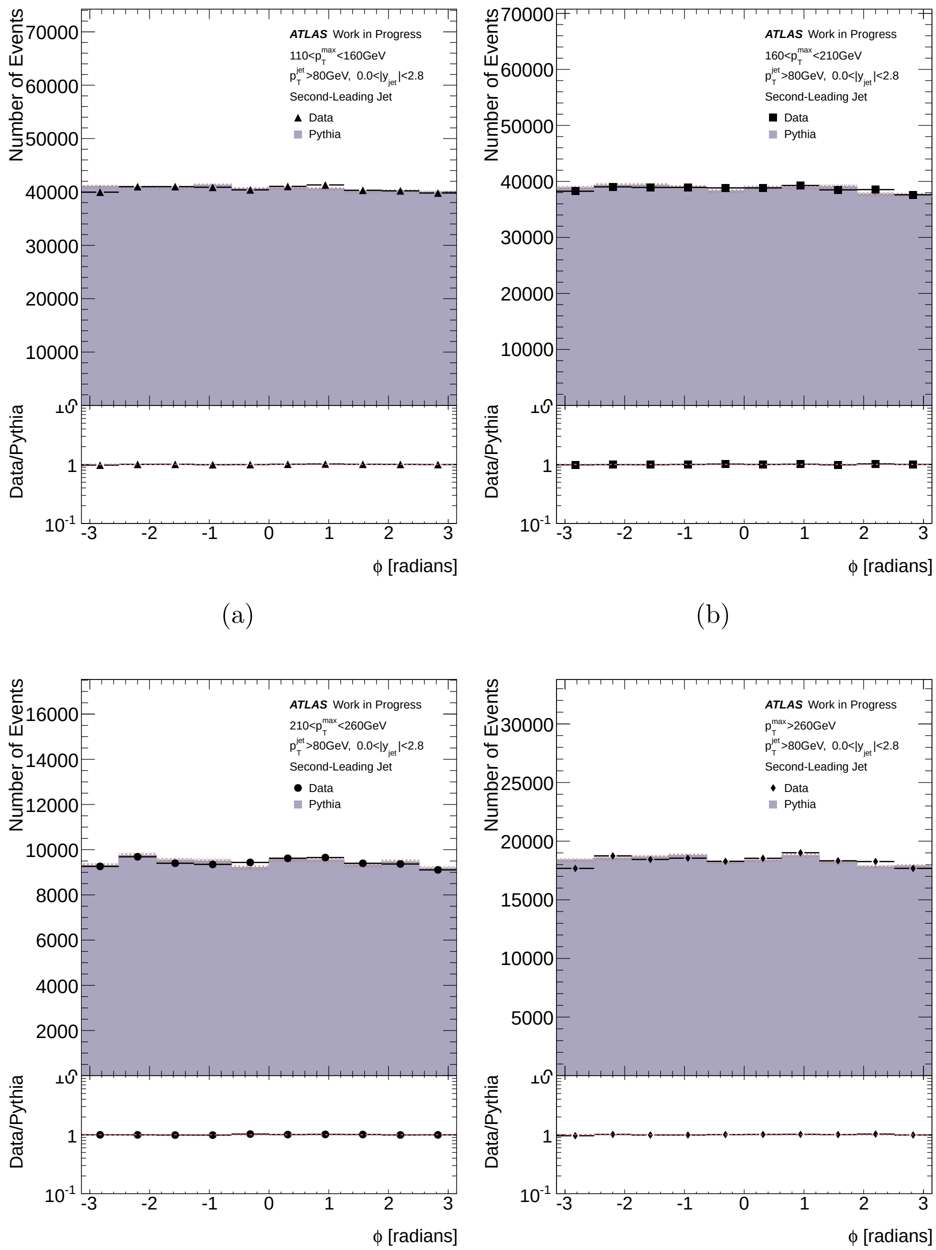

(a) (b)

(c) (d)

Figure 6.7: The ϕ of the second-leading jet for $p_{\mathrm{T}}^{\max}$ bins $110-160$ GeV, $160-210$ GeV, $210-260$ GeV, and >260 GeV with statistical errors in hashed area.

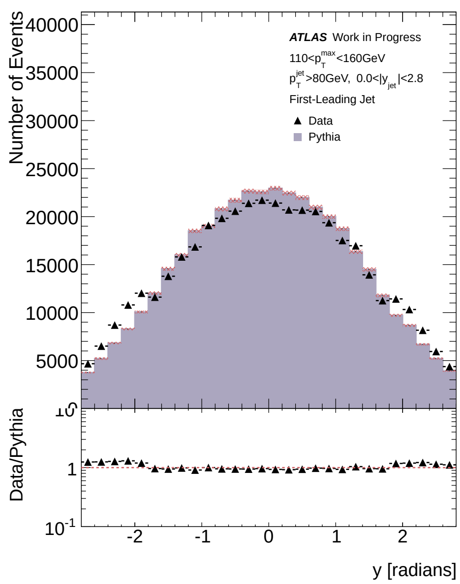

(a)

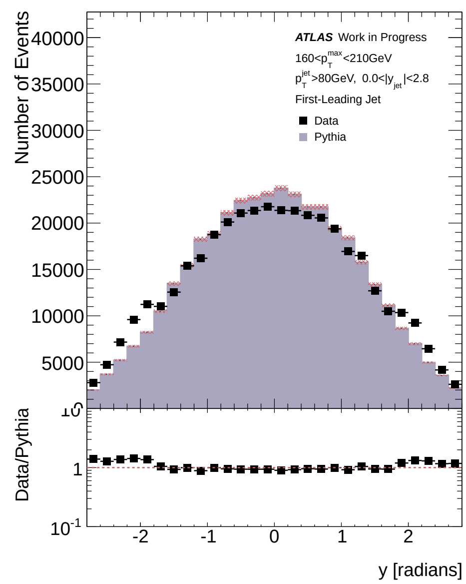

(b)

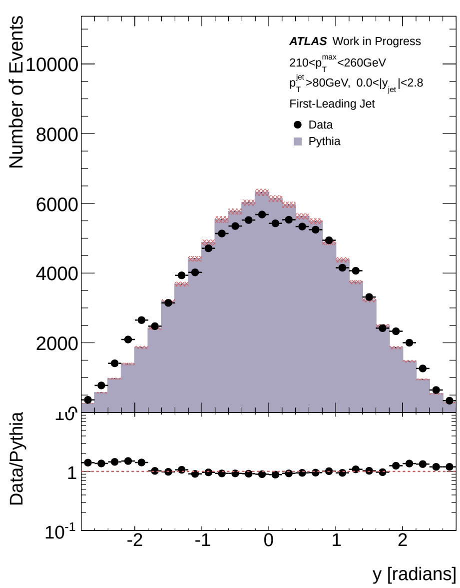

(c)

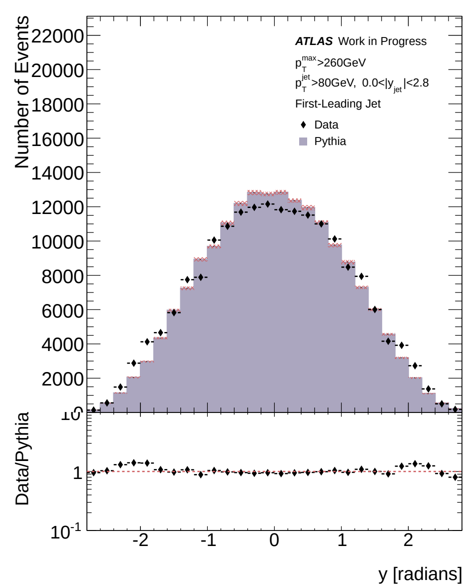

(d)

Figure 6.8: The y of the first-leading jet for $p_{\mathrm{T}}^{\mathrm{max}}$ bins $110-160$ GeV, $160-210$ GeV, $210-260$ GeV, and >260 GeV with statistical errors in hashed area.

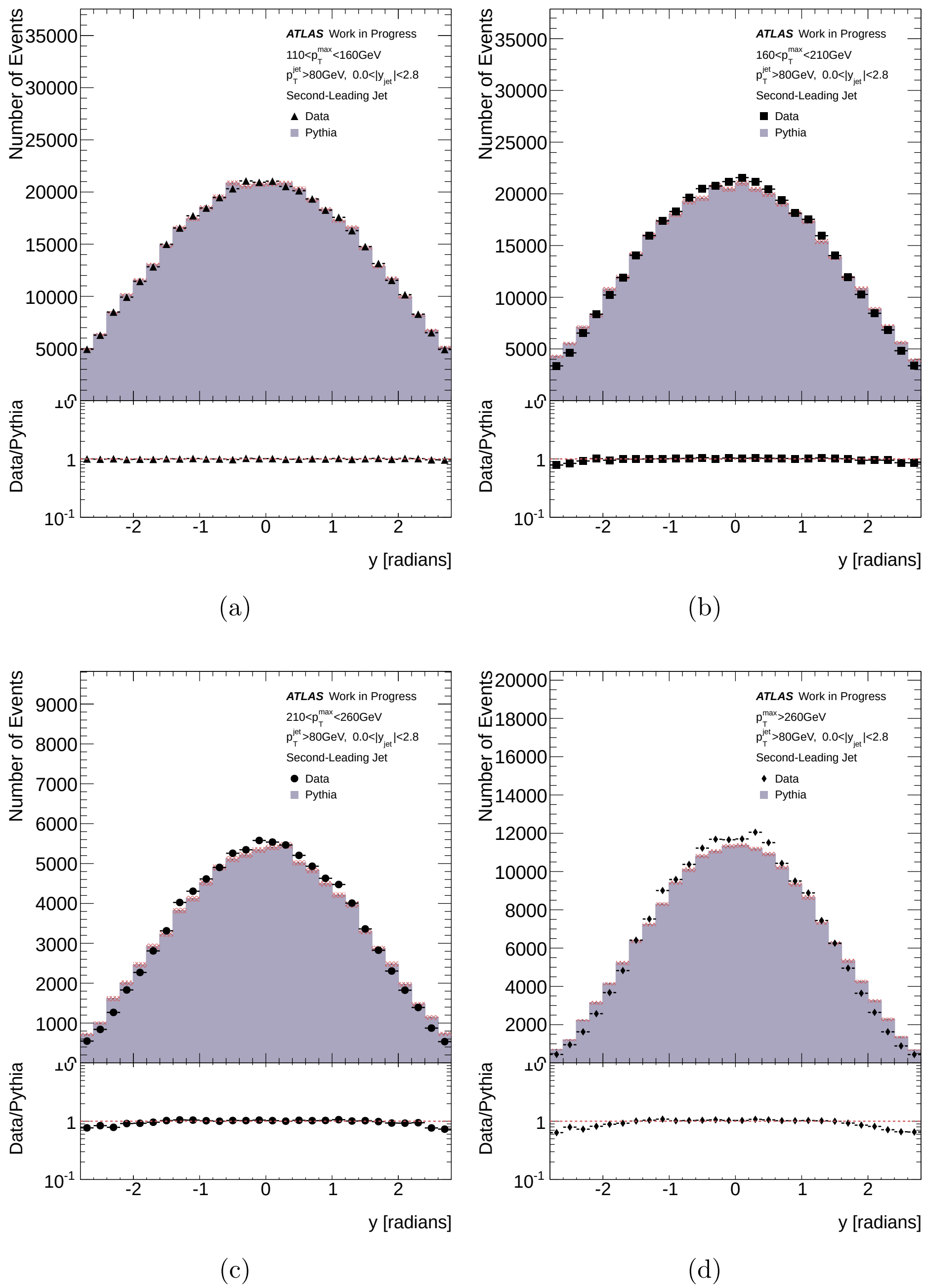

Figure 6.9: The y of the second-leading jet for $p_{\mathrm{T}}^{\max}$ bins $110 - 160$ GeV, $160-210$ GeV, $210-260$ GeV, and > 260 GeV with statistical errors in hashed area.

weighted probability to produce events at high rapidity values. The events then have individual weighting so that the events yield the correct cross sections.

The samples are then combined for each of our p_T^{max} bins. Each of the PYTHIA J samples represents a different p_T range, see Tab. 6.1. Different J samples are combined for each p_T^{max} bin as one would not expect the low p_T J samples to populate the higher p_T^{max} bins and vice versa. If an event from a low p_T J sample were to pass our selection criteria for a higher p_T^{max} bin it is most likely be due to a corrupt event and will bias our distributions.

Table 6.1: The p_T ranges for each of the Jx samples for the Monte Carlo samples.

Jx sample	p_T (GeV)
J2	35-70
J3	70-140
J4	140-280
J5	280-560
J6	560-1120
J7	1120-2240
J8	>2240

The number of events which pass all our selection criteria in each sample can be found in Tab. 6.2. For each p_T^{max} bin, samples which have a small fraction the total number of events passing will not be combined and used in the analysis. Weighted samples which have orders of magnitude more events passing than the their unweighted counterparts are also not combined and used in the analysis.

The statistical uncertainty is taken as the simple error propagation of variance for partial derivatives on the unfolding factor:

$$\begin{aligned} \sigma^2_{f(t,r)} &= \left(\frac{\partial f(t,r)}{\partial t}\sigma_t\right)^2 + \left(\frac{\partial f(t,r)}{\partial r}\sigma_r\right)^2 \\ &= \left(\frac{\partial}{\partial t}\frac{t}{r}\sigma_t\right)^2 + \left(\frac{\partial}{\partial r}\frac{t}{r}\right)^2 \\ \sigma_{f(t,r)} &= \sqrt{\left(\frac{1}{r}\sigma_t\right)^2 + \left(\frac{-t}{r^2}\sigma_r\right)^2} \end{aligned} \tag{6.1}$$

where $\sigma^2_{f(t,r)}$ is the error in the unfolding factor $f(t,r)$ which is the ratio of numbers of truth t to reconstructed r Monte Carlo events passing the selection criteria. Truth Monte Carlo is the generated event before detector simulation with GEANT. The reconstructed event has been simulated for the detector response with GEANT. The relative uncertainty is then divided by the original

Table 6.2: Number of unweighted events passing $\Delta\phi$ selection for each J sample for the leading jet p_T bins for the rapidities $|y_1| < 2.8$ and $|y_2| < 2.8$ in PYTHIA.

p_T (GeV)	110-160	160-210	210-260	260-310	310-400	400-500	500-600	600-800	> 800
J2	25	0	0	0	0	0	0	0	0
y-weighted	30213	360	13	4	6	0	1	0	0
J3	113996	6000	286	2	0	0	0	0	0
y-weighted	39546	56299	262708	18413	282	4	0	0	0
J4	375861	468313	128885	28725	4645	214	4	0	0
y-weighted	27311	32403	65953	44649	94500	233557	4474	31	0
J5	1115	7753	35623	306974	533800	137872	26685	2694	40
y-weighted	68637	115596	32009	23691	45500	74057	46677	256842	64037
J6	20	60	199	530	4255	20646	267743	687232	115149
y-weighted	14485	46726	55207	42963	71984	101800	43347	138750	320182
J7	0	1	1	5	39	127	337	3094	1386404
J8	0	0	0	1	0	1	3	17	1348209

distribution and then presented as a percentage. The statistical uncertainty per bin for the distribution for each of the p_T^{max} bins is presented in Fig. 6.10 for $\Delta\phi$ and Fig. 6.11 for Δy. The statistical uncertainty can be as high as 40% in bins with low statistics; however, it is usually on the order of 20% or less.

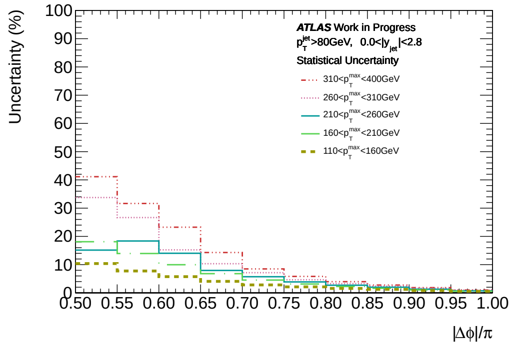

(a)

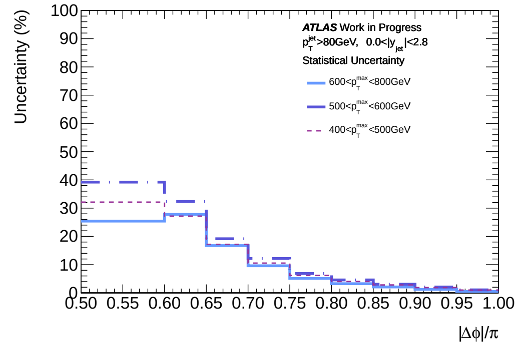

(b)

Figure 6.10: The $\Delta\phi$ statistical uncertainty in $p_{\mathrm{T}}^{\mathrm{max}}$ bins, see text.

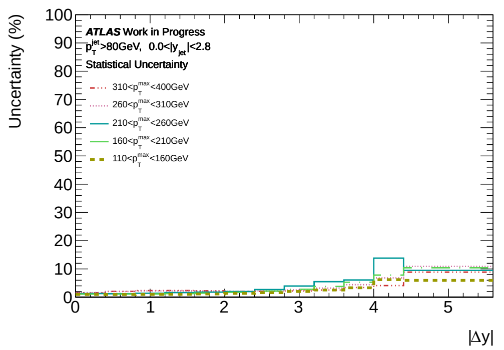

(a)

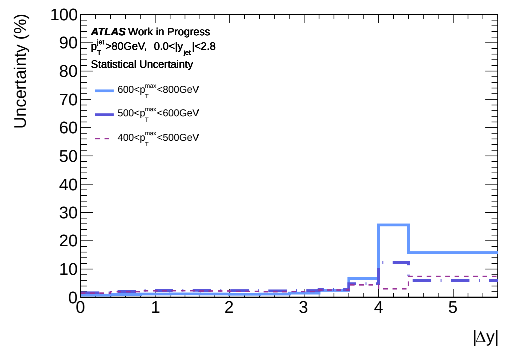

(b)

Figure 6.11: The Δy statistical uncertainty in $p_{\mathrm{T}}^{\mathrm{max}}$ bins, see text.

Chapter 7

Experimental Resolutions and Unfolding

In order to compare our unfolded data, which is corrected back to the particle level, directly to theory, we must remove the effect of resolution on our measurement caused by bin migration in the steeply falling $\Delta\phi$ and Δy distributions. Any cuts we make before forming our observables can affect our final distribution as there will always be events near the threshold. As we make a cut on the p_T, the effect on our distributions of the jet energy resolution must be known. As we make cuts on rapidity and bin our distributions as a function of rapidity and ϕ, we must also find the resolution in both of these observables. There is also an uncertainty on the jet energy scale correction, which converts the electromagnetic energy scale read out by the EM calorimeter to the hadronic scale energy of the jets. The correction and its uncertainty is applied as a function of the p_T and the rapidity of the jet.

The error on our bin-to-bin migration due to resolution effects is found using the reconstructed Monte Carlo. A smearing of the cut variables by their resolution for each jet in an event before the observables are formed is done for each resolution separately, and then the resultant distribution is compared to the original unfolded Monte Carlo distribution without any smearing. The error is taken as the percent difference between the distributions caused by bin-to-bin migration from that variable's resolution. The cumulative effect of all the experimental resolutions is found by adding the error from each resolution in quadrature.

7.1 Jet Angular Resolution

The angular resolution is defined as the largest difference between the PYTHIA truth and reconstructed jet ϕ and y for all good jets in an event as a function of the p_T^{max}. The resolution is plotted for all events per each

p_T^{max} bin, see Appendix D for the resolution distribution and the Gaussian fits for each p_T^{max} bin. The distribution is fitted by a Gaussian, and the width of the Gaussian (σ) is extracted. The mean value of the Gaussian is expected to be zero. The resolution is the width σ of the Gaussian fit. This is plotted in Fig. 7.1.

The error on σ is too small to be seen in Fig. 7.2. Refer to Tab. 7.1 for the errors on σ. The Gaussian width is plotted for each p_T^{max} bin, see Fig. 7.2.

Table 7.1: The Gaussian width and it's error for the resolution fits per p_T^{max} bins for ϕ and rapidity.

	ϕ		y	
p_TGeV	width	error	width	error
110-160	0.013	2.2×10^{-5}	0.012	2.1×10^{-5}
160-210	0.011	2.3×10^{-5}	0.0099	2.0×10^{-5}
210-260	0.0098	2.5×10^{-5}	0.0085	1.8×10^{-5}
260-310	0.0089	2.1×10^{-5}	0.0079	1.8×10^{-5}
310-400	0.0082	1.7×10^{-5}	0.0074	1.5×10^{-5}
400-500	0.0077	1.9×10^{-5}	0.0069	1.5×10^{-5}
500-600	0.0073	1.8×10^{-5}	0.0066	1.9×10^{-5}
600-800	0.0072	1.6×10^{-5}	0.0064	1.4×10^{-5}

The widths as a function of p_T^{max} are fit by a cubic polynomial. The fitted expression is used to generate the smearing in ϕ and rapidity as a function of leading jet p_T for our unfolding distribution. See Eqs. 7.1-7.2 for the fitted smearing equations for our ϕ and rapidity, respectively. Extrapolating the downturn in the fit for $p_T > 800$ GeVis non-physical. However, the effect on our overall distributions for events with $p_T^{max} \gg 800$ GeV is negligible.

$$\begin{aligned}\Delta(\phi) = 0.021 + (-7.5 \times 10^{-5} \cdot p_T^{max}) \\ +(1.4 \times 10^{-7} \cdot p_T^{2,max}) + (-8.5 \times 10^{-11} \cdot p_T^{3,max})\end{aligned} \tag{7.1}$$

$$\begin{aligned}\Delta(y) = 0.019 + (-7.2 \times 10^{-5} \cdot p_T^{max}) \\ +(1.4 \times 10^{-7} \cdot p_T^{2,max}) + (-9.0 \times 10^{-11} \cdot p_T^{3,max})\end{aligned} \tag{7.2}$$

These expressions are used to smear the rapidity and ϕ of each jet as a function of p_T^{max}. This is done before the selection cuts are made and the $\Delta\phi$ and

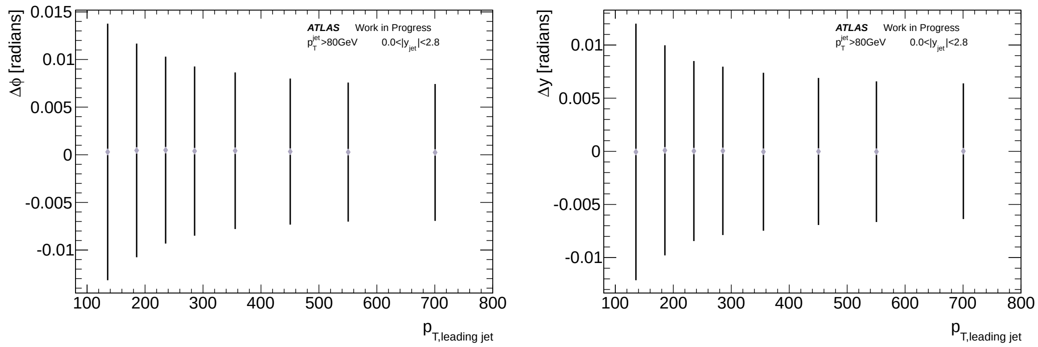

(a) (b)

Figure 7.1: The jet resolutions for ϕ and y as a function of $p_{\mathrm{T}}^{\max}$ for each of the $p_{\mathrm{T}}^{\max}$ bins $110-160$ GeV, $160-210$ GeV, $210-260$ GeV, $260-310$ GeV, $310-400$ GeV, $400-500$ GeV, $500-600$ GeV, and $600-800$ GeV.

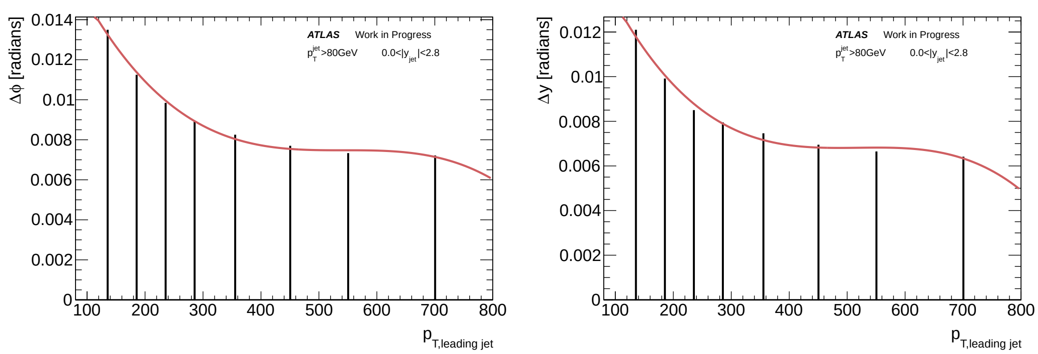

(a) (b)

Figure 7.2: The fit to the resolutions for ϕ and y as a function of $p_{\mathrm{T}}^{\max}$.

Δy distributions are plotted. Each smearing is done separately. The resultant smeared distributions differ from the original distributions, see Figs. 7.4-7.5 to see the uncertainty due to the ϕ and rapidity resolutions as well as the other experimental resolution uncertainties.

7.2 Jet Energy Resolution

A detailed study was done to find the jet energy resolution (JER) [63]. Two methods were used to determine the jet energy resolution: the di-jet balance and bi-sector techniques, see Fig. 7.3. The results of this study were used to generate an interactive user package which provides the jet energy resolution per jet in each event. The package is called the "JetEnergyResolutionProvider". It applies the resolution smearing as a function of jet p_T and η. This is done before making any selection cuts. The $\Delta\phi$ and Δy distributions are made after the selection cuts are made on the energy-smeared jets. These distributions vary from the original distributions, see Figs. 7.4-7.5 for the systematic uncertainty contribution from this effect. The JER has a very small effect on the overall uncertainty, and the uncertainty in the plots is scaled by a factor of ten for the contribution of the JER to the total uncertainty to be visible in the plots.

7.3 Jet Energy Scale Uncertainty

The jet energy scale (JES) uncertainty was found to be smaller than $\pm10\%$ for jets within $|y| < 2.8$ and with a $p_T > 20$ GeV [63]. The JES is also found to be a function of jet p_T and η. The package "JESUncertaintyProvider" yields the JES uncertainty interactively for each event. The jet energy is smeared up by a positive energy scale uncertainty and then smeared down by a negative energy scale uncertainty using the uncertainty provider.

Each smearing is done separately, and the systematic uncertainty for each bin is taken to be the larger of the two from each smearing. The final contribution to the systematic uncertainty from the JES uncertainty can be seen in Figs. 7.4-7.5. The JES uncertainty is one of the larger overall contributors to the total experimental uncertainty. The total systematic uncertainty is determined by adding all components in quadrature and never exceeds 20%.

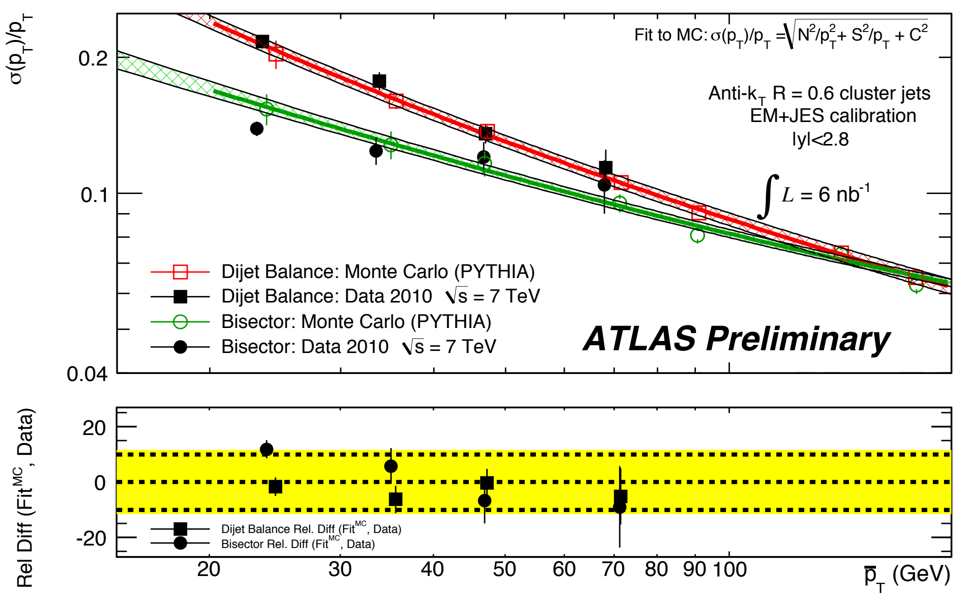

Figure 7.3: Jet energy resolution for the di-jet balance and bi-sector techniques as a function of the average jet transverse momenta. The lower plot shows the relative difference between the Monte Carlo fit and the data results. The yellow band indicates a relative uncertainty of ± 10%.

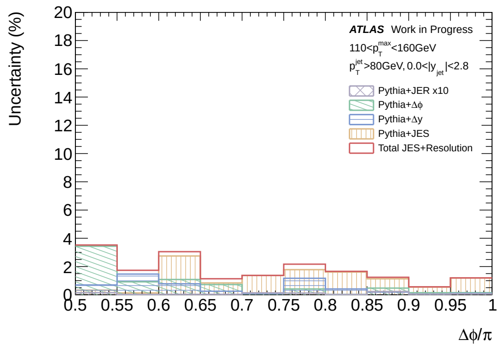

(a)

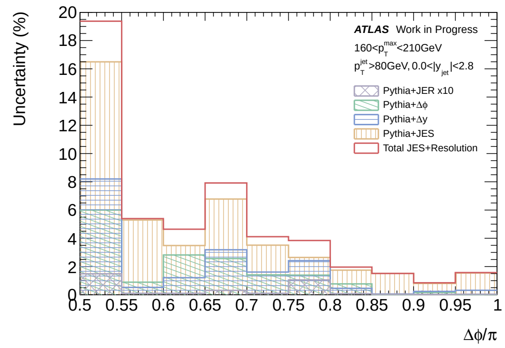

(b)

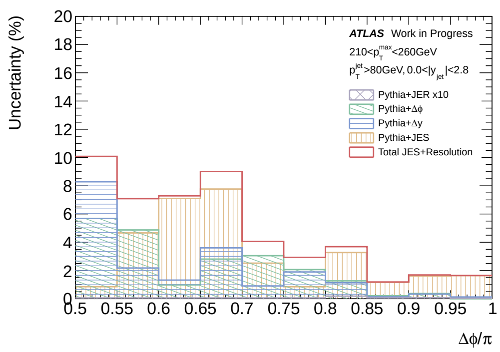

(c)

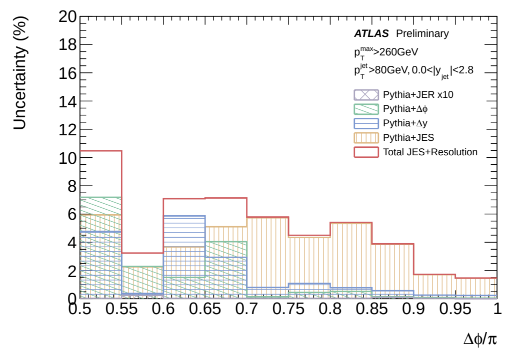

(d)

Figure 7.4: The $\Delta\phi$ systematic uncertainty for $p_{\mathrm{T}}^{\max}$ bins $110-160$ GeV, $160-210$ GeV, $210-260$ GeV, and >260 GeV.

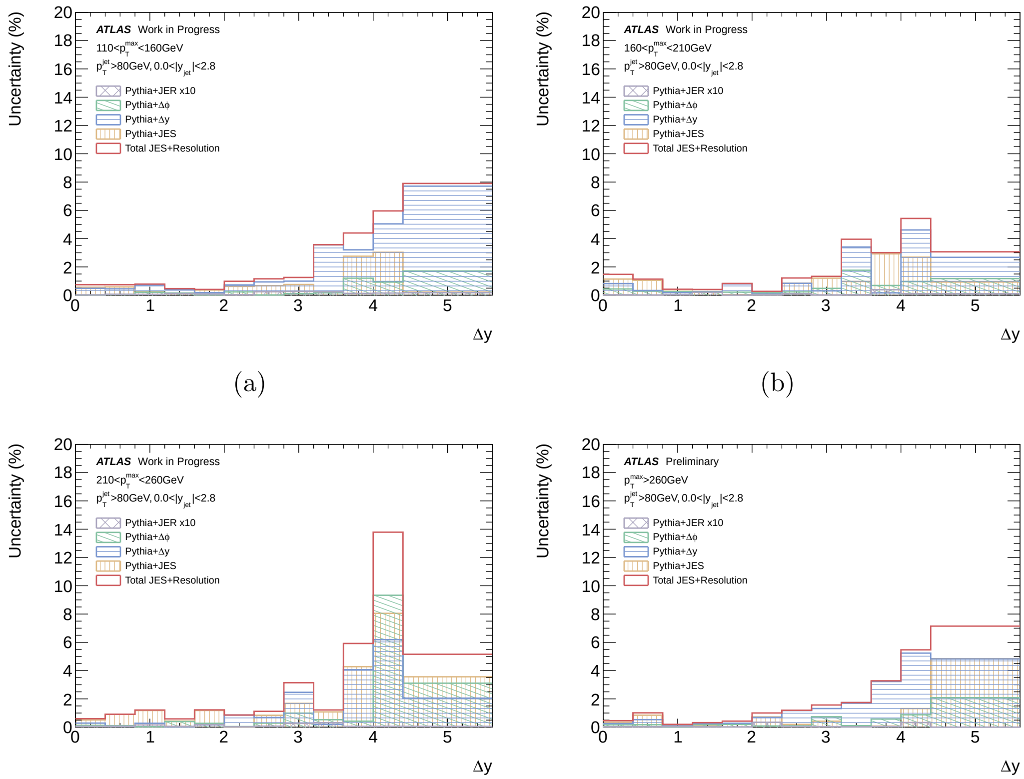

(a) (b) (c) (d)

Figure 7.5: The Δy systematic uncertainty for $p_{\mathrm{T}}^{\max}$ bins $110-160$ GeV, $160-210$ GeV, $210-260$ GeV, and >260 GeV.

7.4 Unfolding

In order to get our $\Delta\phi$ and Δy distributions from data to the theory level, we must remove the detector effects. Assuming our Monte Carlo (MC) along with GEANT and reconstruction models our data sufficiently well, we can use a comparison of reconstructed MC to truth level MC to derive correction values for our data distribution. This is called unfolding. There are several unfolding methods which may be used to derive our correction values. A bin-by-bin unfolding method is used in this study.

The PYTHIA distributions for $\Delta\phi$ and Δy are plotted and compared to data as a function of inclusive jet multiplicity for different minimum jet p_T. This is done for reconstructed-level jets in data and Monte Carlo to see if there is good agreement between data and PYTHIA. If there is good agreement, it demonstrates that unfolding the data to theory level using reconstructed PYTHIA Monte Carlo is a reasonable endeavor. This is done for events with ≥ 2, ≥ 3, ≥ 4, ≥ 5, and ≥ 6 jets with jet $p_T \geq$ 20 GeV, $\geq$ 40 GeV, $\geq$ 60 GeV, and $\geq$ 80 GeV. See Figs. 7.6-7.9 for the $\Delta\phi$ and Δy distributions and their ratio of data to PYTHIA.

While PYTHIA is a $2 \rightarrow 2$ particle-level Monte Carlo model, it does a good job of simulating data up through six inclusive jets in an event. This is due to optimal ATLAS tuning for the MC generator. Given that the number of events with 5 or more jets is already two orders of magnitude less than the number of events with 2 jets for all p_T bins, it is sufficient to show good agreement up through 6 jets to demonstrate agreement with data. See Fig. 6.3 for the jet multiplicity in PYTHIA and data.

7.4.1 1-Dimensional Unfolding Method

The observables $\Delta\phi$ and Δy are formed as outlined in Chap. 4 for the truth and reconstructed jets in PYTHIA using the event and jet selection described in Chaps. 5-6, see Figs. 7.10-7.11.

Then the truth distribution is divided by the reconstructed distribution. The result gives the unfolding factors used for correcting the reconstructed distribution back to the truth information. This is done for each of our observables, see Figs. 7.12-7.13. These same unfolding factors are applied to data to correct for experimental effects and bring the data back to the particle level.

The unfolding factors are applied by multiplying the reconstructed distribution by the unfolding correction factors. The resultant distributions, seen in Figs. 7.14-7.15, are the same as the truth distributions by design. The data is also multiplied bin-by-bin by the unfolding factors; the resultant distributions

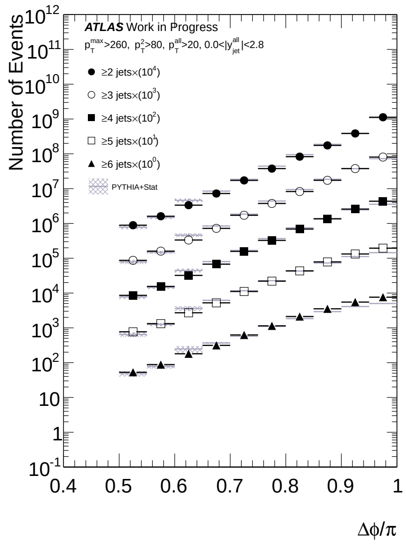

(a)

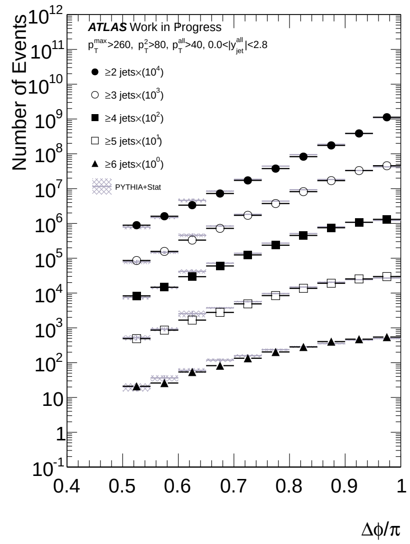

(b)

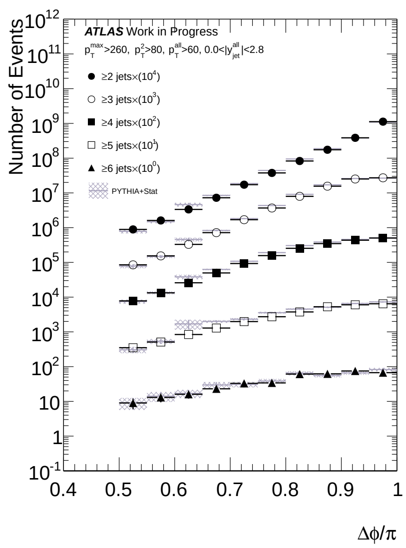

(c)

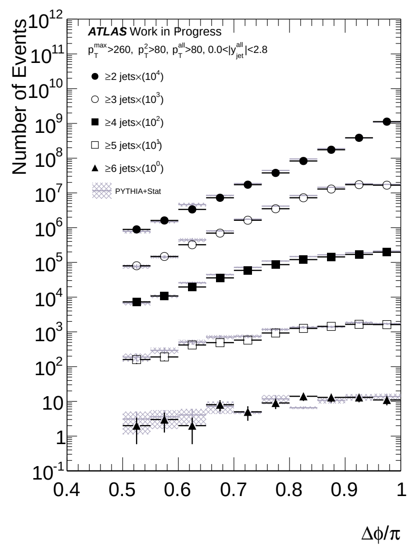

(d)

Figure 7.6: The reconstructed distributions in data and PYTHIA for $\Delta\phi$ as a function of jet multiplicity for $p_{\mathrm{T}}^{\mathrm{max}} > 260$ GeV and subleading jet $p_{\mathrm{T},2}$ for different jet p_T cutoffs for the rest of the jets in the event.

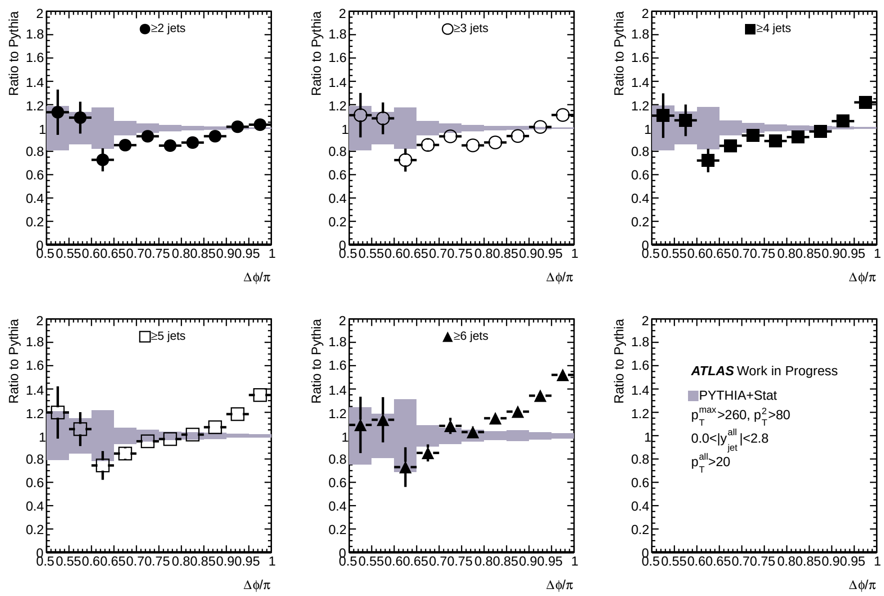
≥2 jets
≥3 jets
≥4 jets
≥5 jets
≥6 jets
Ratio to Pythia
Δφ/π
ATLAS Work in Progress
PYTHIA+Stat
p_T^{max}>260, p_T^2>80
0.0<$|y_{jet}^{all}|$<2.8
p_T^{all}>20

(a)

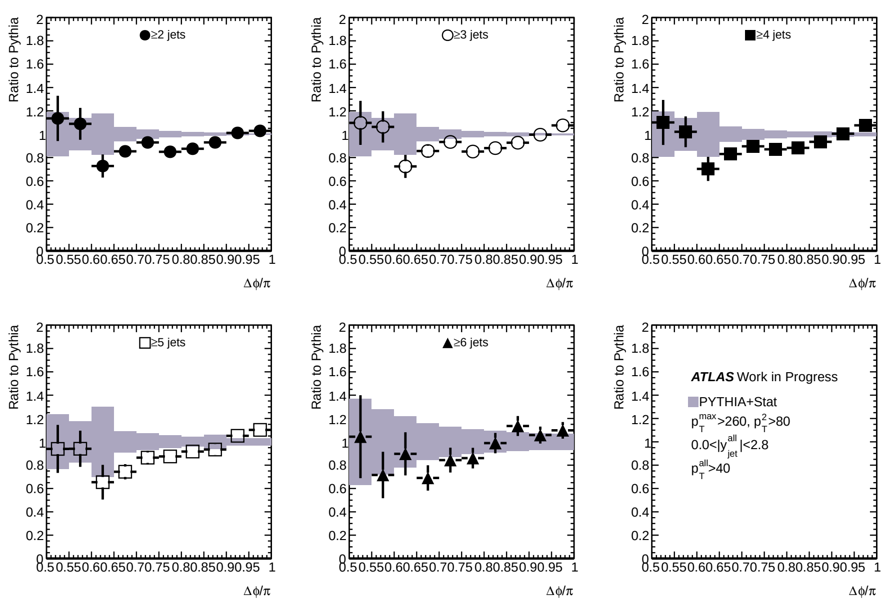
≥2 jets
≥3 jets
≥4 jets
≥5 jets
≥6 jets
Ratio to Pythia
Δφ/π
ATLAS Work in Progress
PYTHIA+Stat
p_T^{max}>260, p_T^2>80
0.0<$|y_{jet}^{all}|$<2.8
p_T^{all}>40

(b)

Figure 7.7

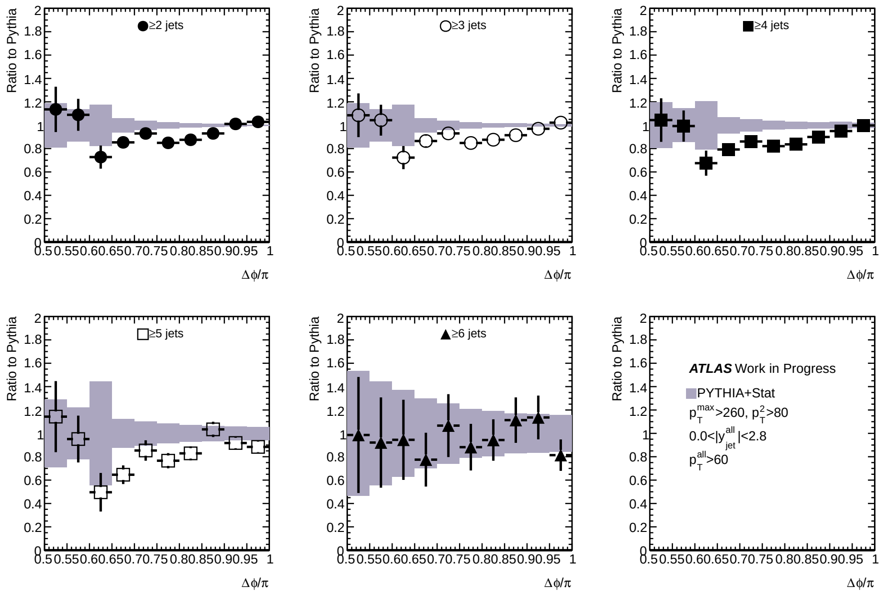

(c)

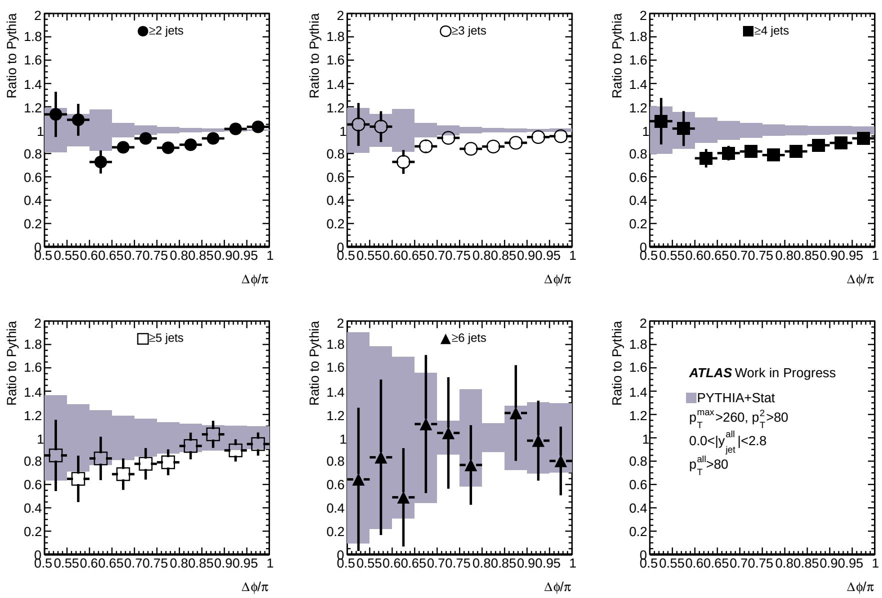

(d)

Figure 7.7: The ratio of data to PYTHIA for $\Delta\phi$ as a function of jet multiplicity for $p_{\mathrm{T}}^{\mathrm{max}} > 260$ GeV and subleading jet $p_{\mathrm{T},2}$ for different jet p_T cutoffs for the rest of the jets in the event.

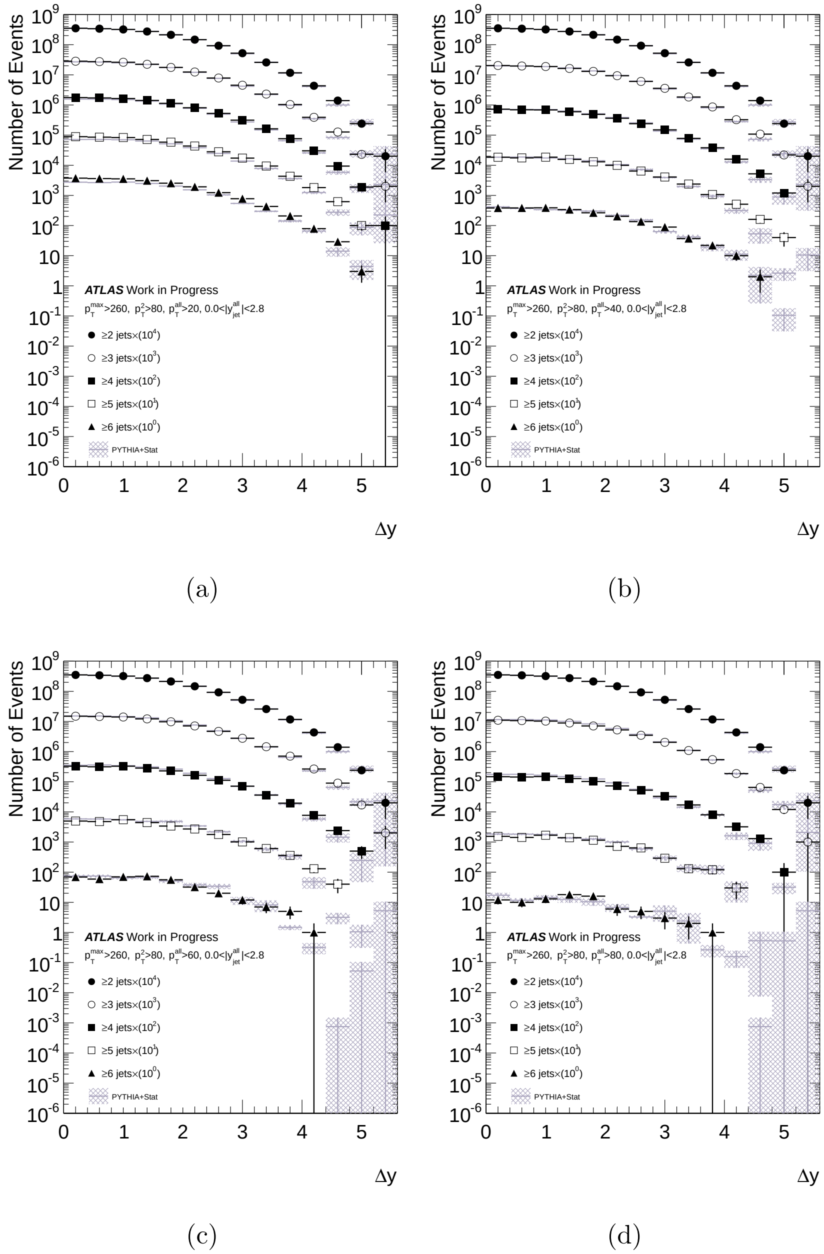

(a) (b)

(c) (d)

Figure 7.8: The reconstructed distributions in data and PYTHIA for Δy as a function of jet multiplicity for $p_{\mathrm{T}}^{\max} > 260$ GeV and subleading jet $p_{\mathrm{T},2}$ for different jet p_T cutoffs for the rest of the jets in the event.

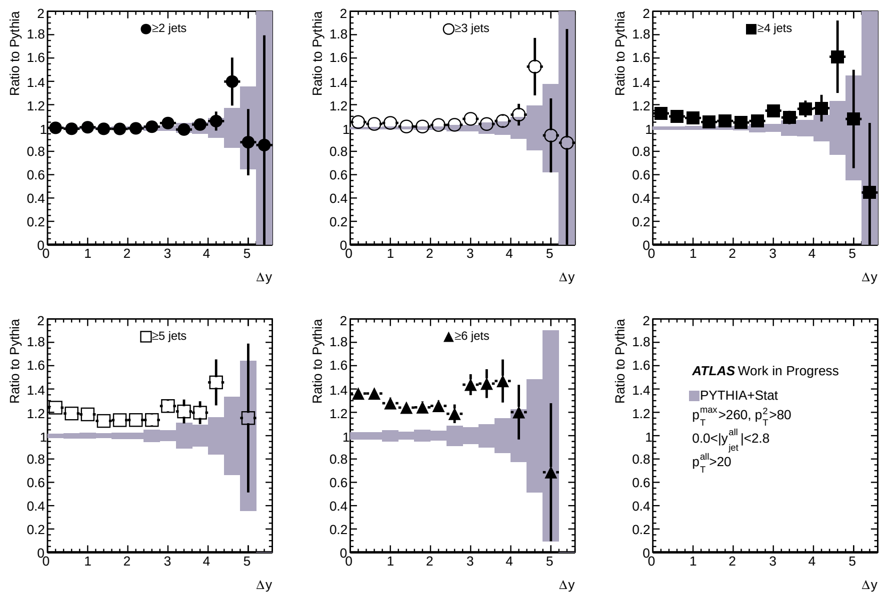
Ratio to Pythia
≥2 jets
≥3 jets
≥4 jets
≥5 jets
≥6 jets
Δy
ATLAS Work in Progress
PYTHIA+Stat
p_T^max>260, p_T^2>80
0.0<|y_jet^all|<2.8
p_T^all>20

(a)

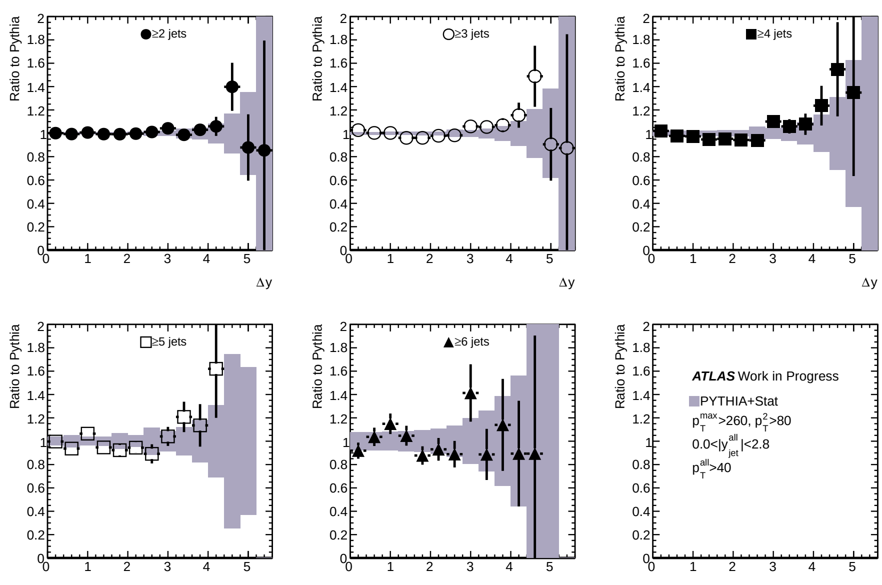
Ratio to Pythia
≥2 jets
≥3 jets
≥4 jets
≥5 jets
≥6 jets
Δy
ATLAS Work in Progress
PYTHIA+Stat
p_T^max>260, p_T^2>80
0.0<|y_jet^all|<2.8
p_T^all>40

(b)

Figure 7.9

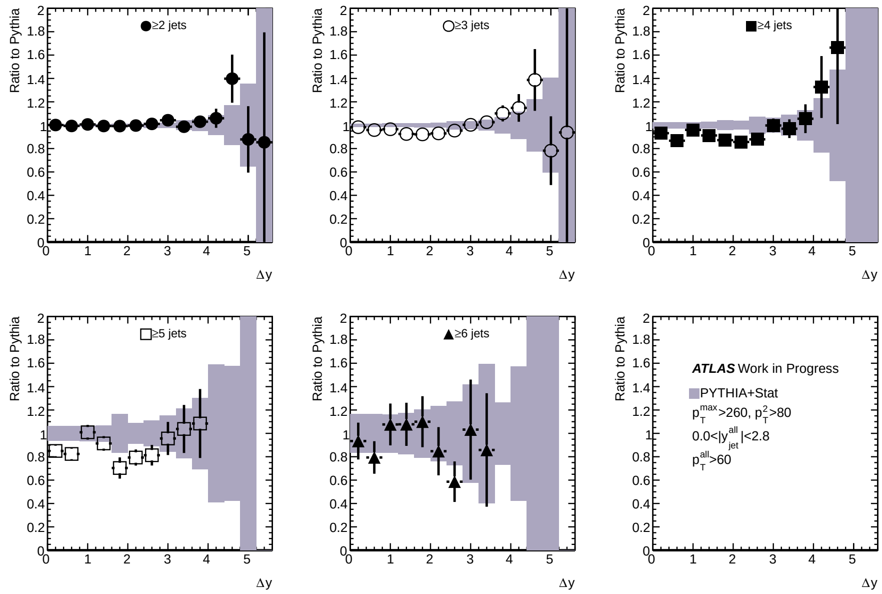

(c)

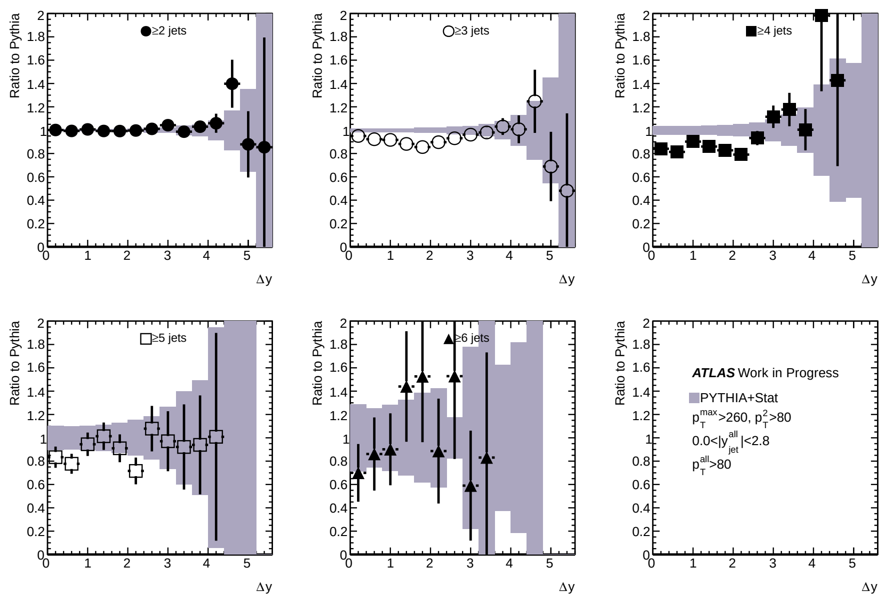

(d)

Figure 7.9: The ratio in data to PYTHIA for Δy as a function of jet multiplicity for $p_{\mathrm{T}}^{\mathrm{max}} > 260$ GeV and subleading jet $p_{\mathrm{T},2}$ for different jet p_T cutoffs for the rest of the jets in the event.

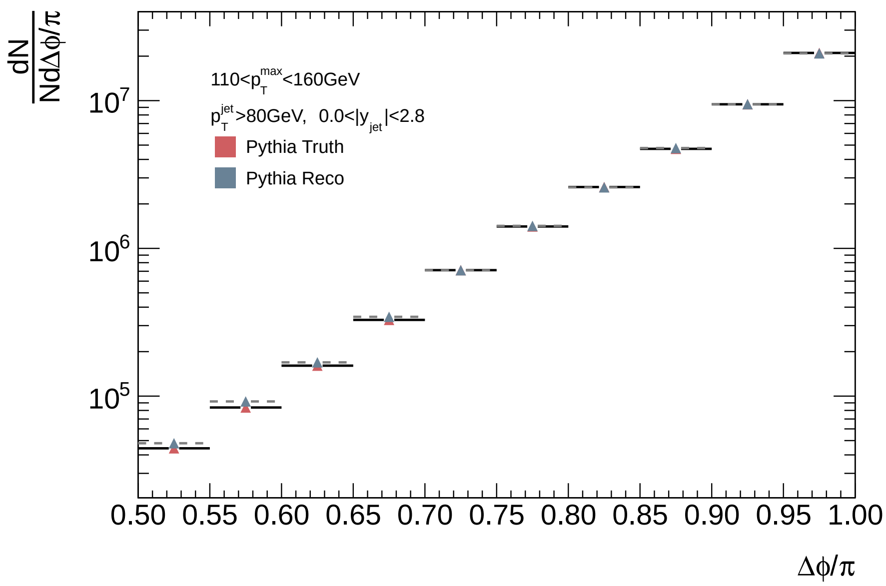

(a)

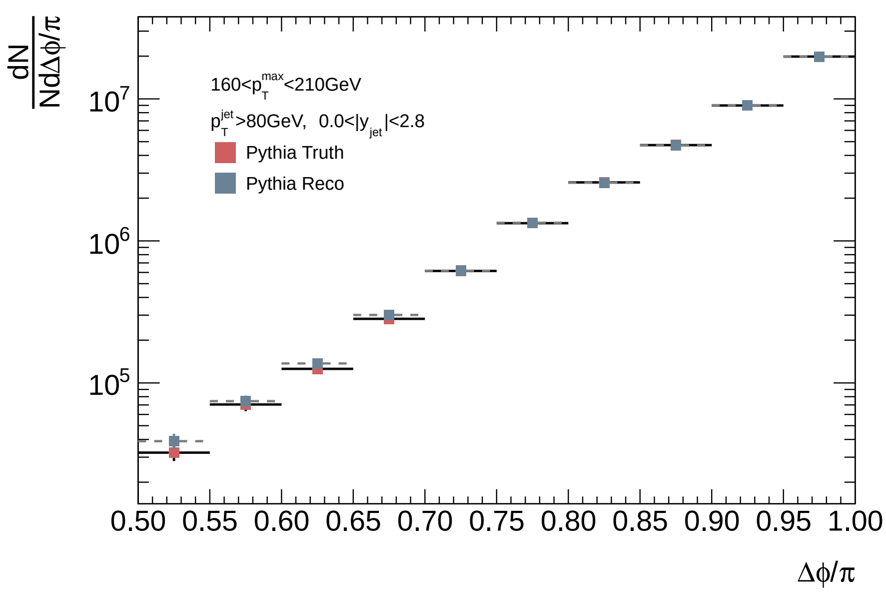

(b)

Figure 7.10

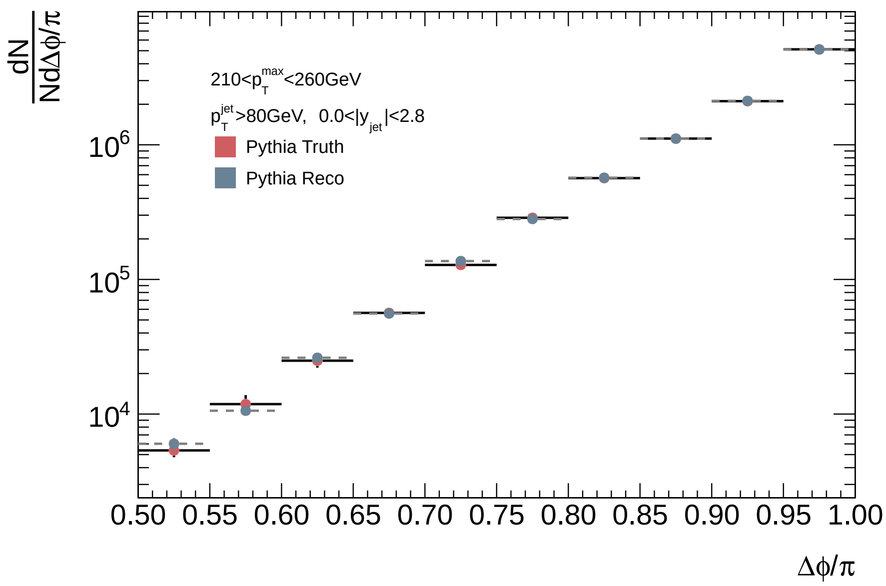

(c)

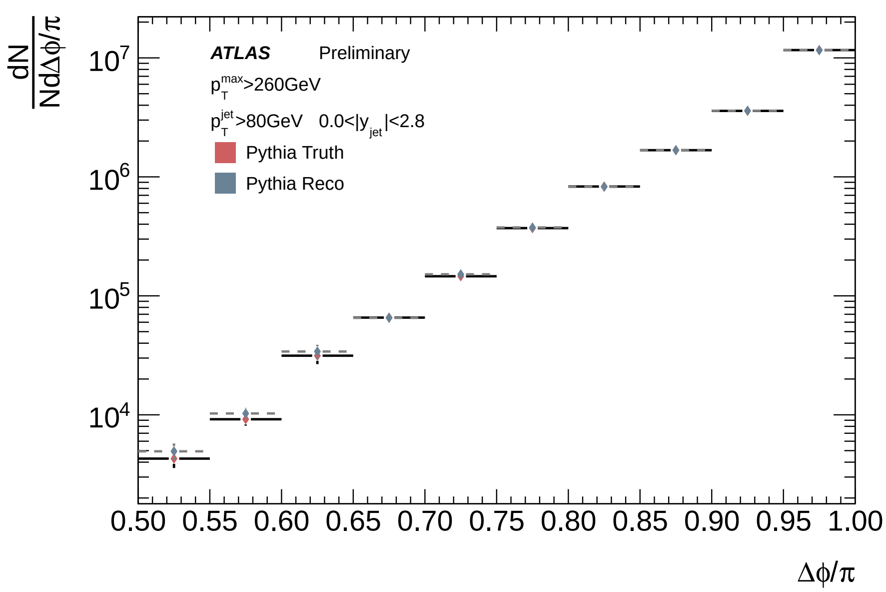

(d)

Figure 7.10: The $\Delta\phi$ distributions for truth and reconstructed PYTHIA in $p_{\mathrm{T}}^{\max}$ bins $110-160$ GeV, $160-210$ GeV, $210-260$ GeV, and >260 GeV for each trigger selection.

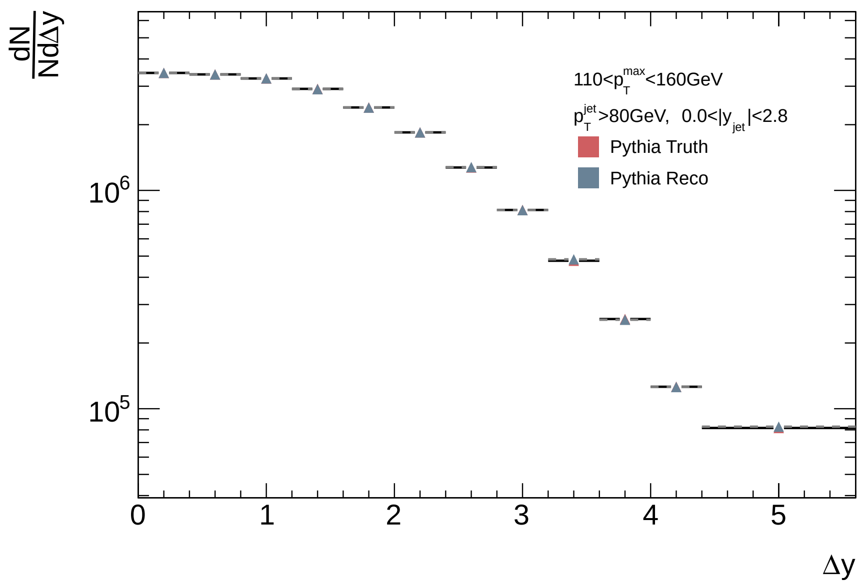

(a)

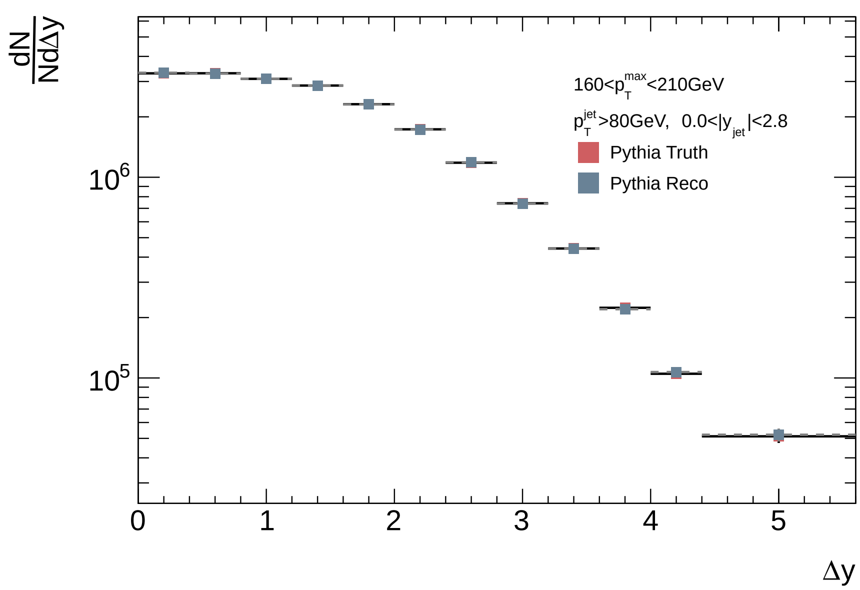

(b)

Figure 7.11

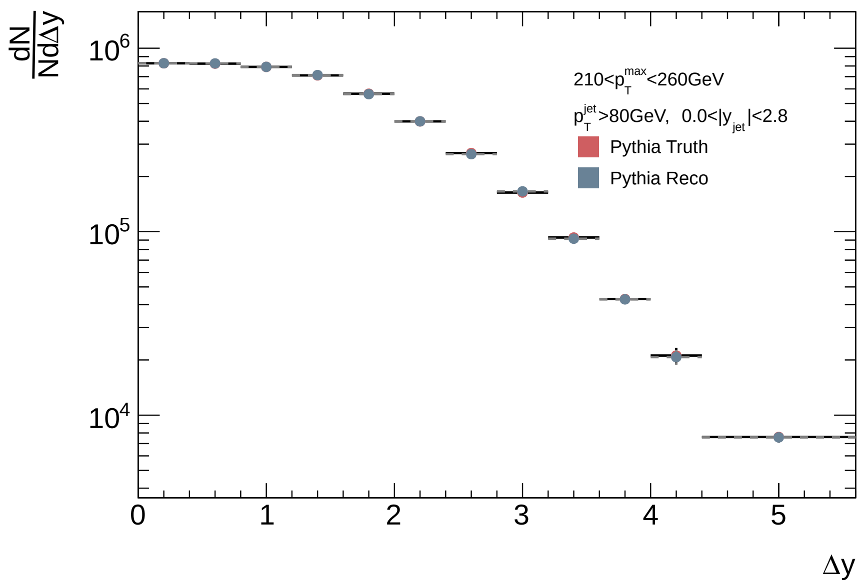

(c)

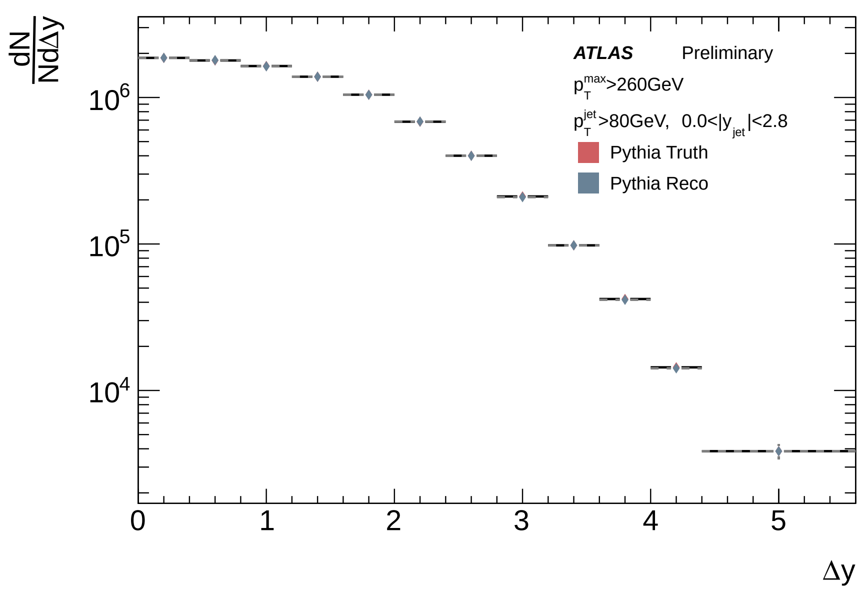

(d)

Figure 7.11: The Δy distributions for truth and reconstructed PYTHIA in $p_{\mathrm{T}}^{\max}$ bins $110-160$ GeV, $160-210$ GeV, $210-260$ GeV, and >260 GeV for each trigger selection.

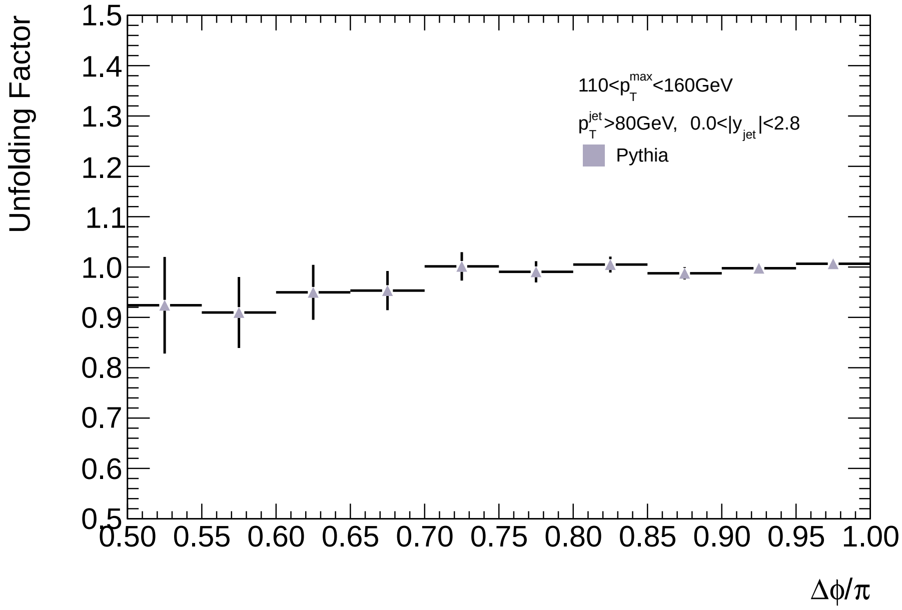

(a)

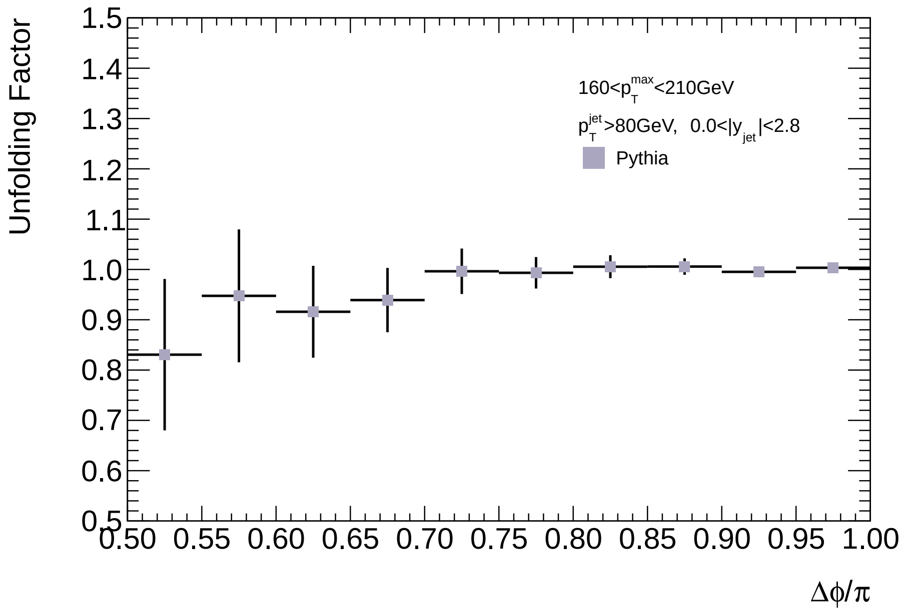

(b)

Figure 7.12

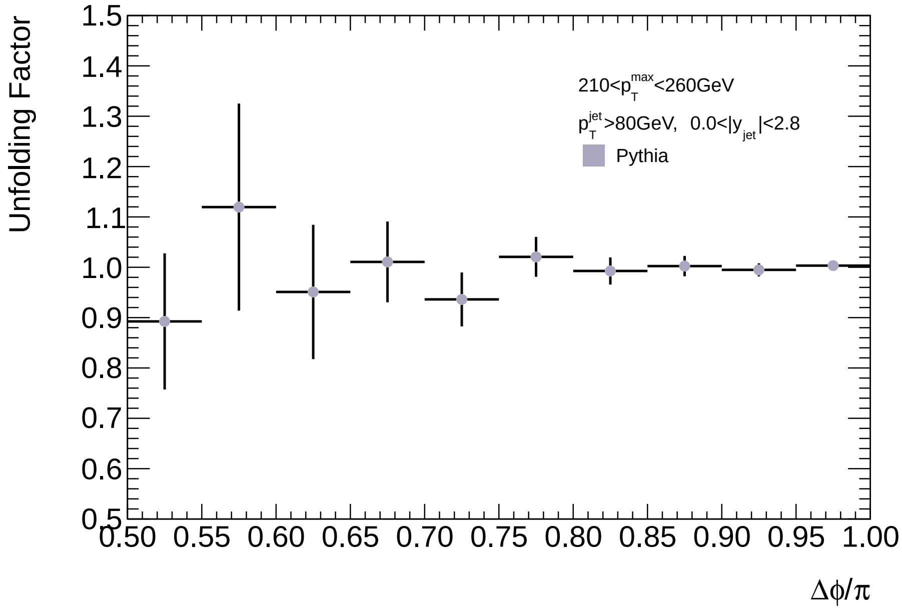

(c)

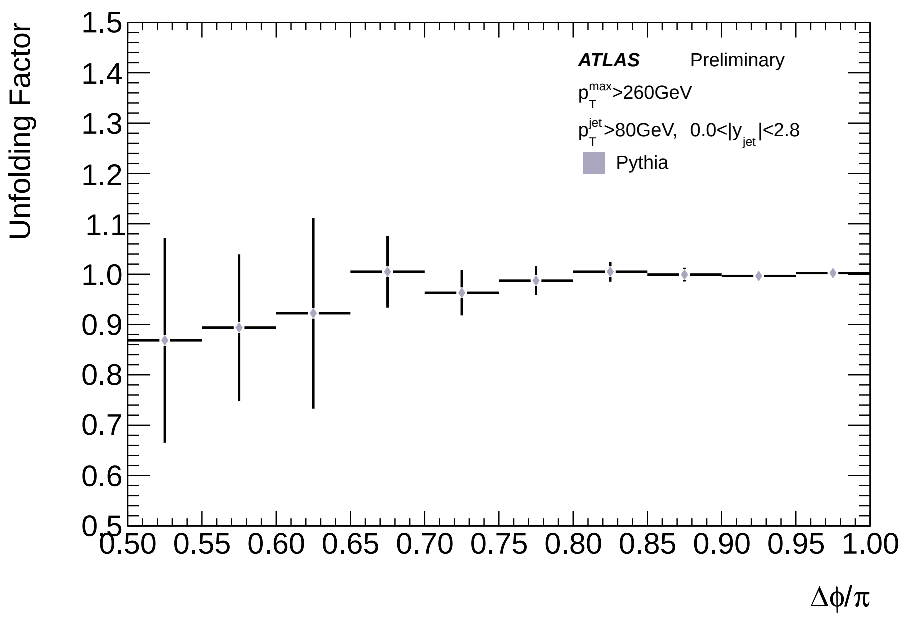

(d)

Figure 7.12: The $\Delta\phi$ unfolding factors for $p_{\mathrm{T}}^{\mathrm{max}}$ bins $110-160$ GeV, $160-210$ GeV, $210-260$ GeV, and >260 GeV for each trigger selection.

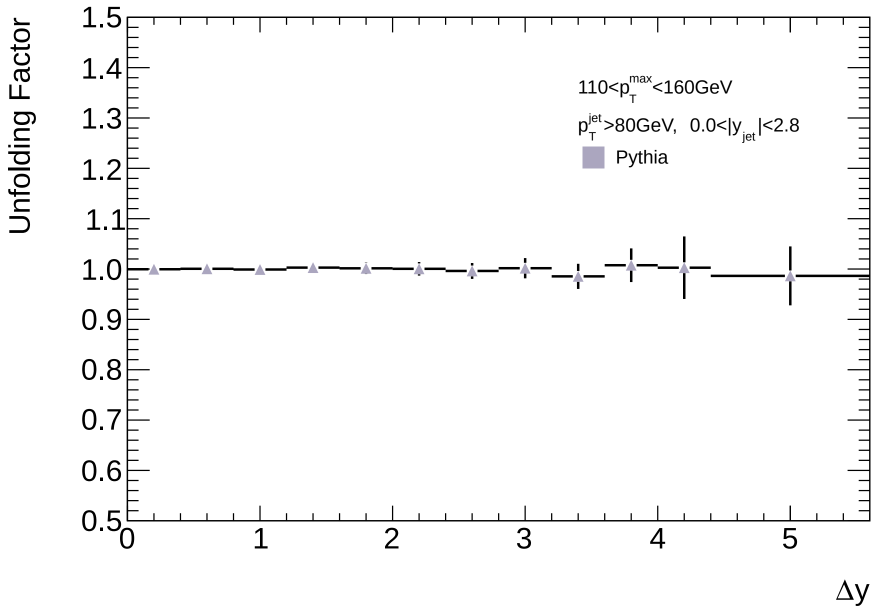

(a)

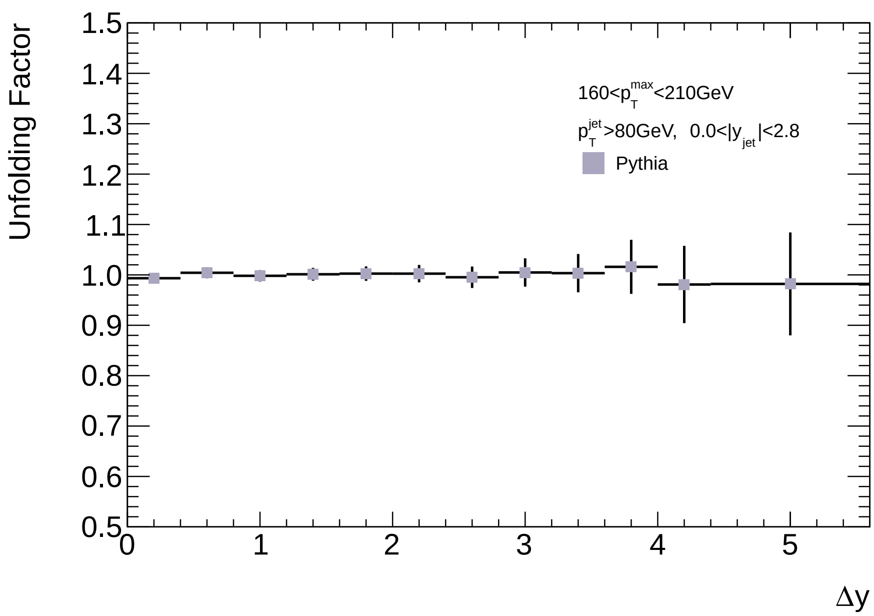

(b)

Figure 7.13

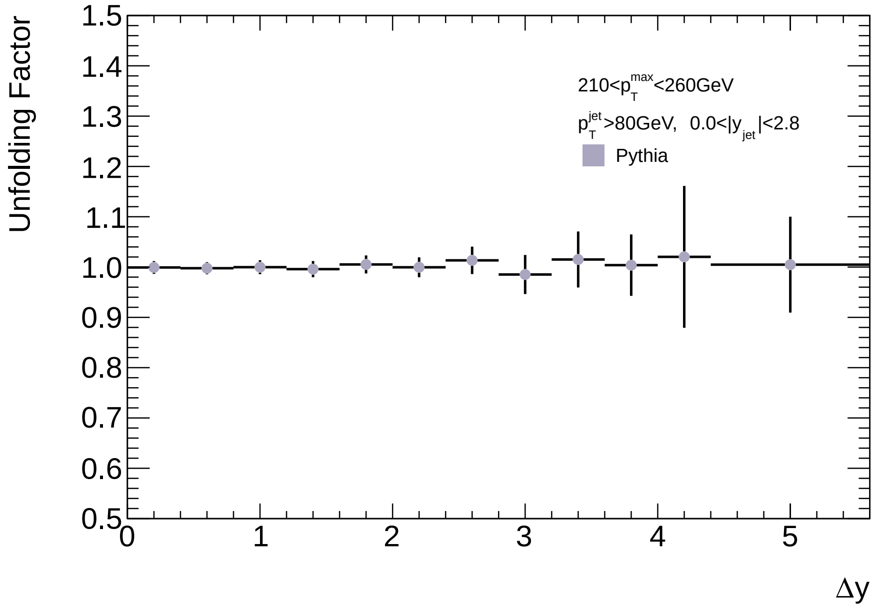

(c)

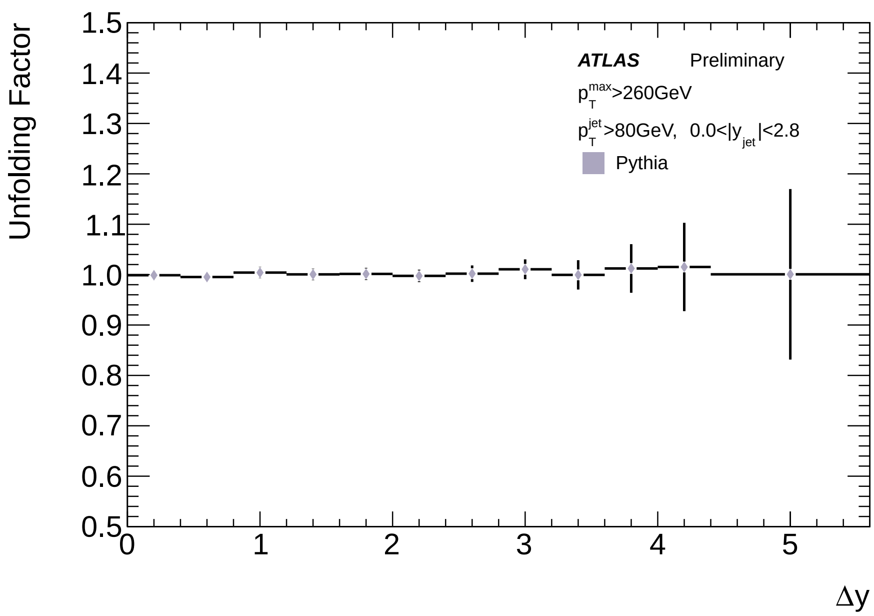

(d)

Figure 7.13: The Δy unfolding factors for $p_{\mathrm{T}}^{\max}$ bins $110 - 160$ GeV, $160 - 210$ GeV, $210 - 260$ GeV, and > 260 GeV for each trigger selection.

are the unfolded data at theory level. The statistical error is shown for both data and PYTHIA.

To test that the corrected reconstructed distribution is the same as the truth distribution, the unfolded reconstructed distribution is divided by the truth distribution. Closure is achieved. This is seen as Figs. 7.16-7.17, the closure test distribution, is one for every bin. The unfolded data is also divided by the PYTHIA truth distribution. This is done to more clearly show the agreement between unfolded data and PYTHIA. The unfolded data deviates from the unfolded MC $\Delta\phi$ distribution at around $5/6\pi$, which corresponds to predominant contributions from events with three jets. The data also begins to pull away from the unfolded MC Δy distribution for high values of Δy for increasing p_T^{max} bins. While overall we observe reasonable agreement between unfolded data and unfolded PYTHIA, there are some significant deviations in those regions.

The unfolded distributions for $\Delta\phi$ and Δy are plotted for data and reconstructed MC. There is good agreement between data and PYTHIA along all p_T^{max} bins. To make the distributions easier to discern, the different p_T^{max} bins are scaled by increasing factors of ten making a shape comparison possible, see Fig. 7.18.

A comparison is made of the highest statistic, lower p_T^{max} to the highest p_T^{max} bins with the same trigger for both the $\Delta\phi$ and Δy distributions. This is done to better illustrate the trend in $\Delta\phi$ and Δy distribution shape as it evolves with increasing p_T^{max} to supplement the shape comparison in Fig. 7.18.

The ratio of the $\Delta\phi$ distributions at different p_T^{max} has sensitivity to the running of α_s. The higher p_T^{max} $\Delta\phi$ distributions have a sharper peak than the lower p_T^{max} distribution at around π implying they have a higher contribution from events with only two jets in the event. For all other bins, the higher p_T^{max} distributions have smaller contributions than the lower p_T^{max} distribution demonstrating they have less contributions from events with more than two events in the event.

For Δy, the higher p_T^{max} distributions have an increasingly sharp peak at Δy=0 which falls off with increasing Δy. This is indicative of more contributions from two and three jets with increasing p_T^{max} as 2 and 3-jet contributions peak more at $\Delta y = 0$ than do contributions from four or more jets.

The ratio is taken for the $\Delta\phi$ distribution formed in the case for the first leading jet in the rapidity region of $0.0 \leq |y_{jet}| < 0.8$ and the second leading jet in the region of $2.0 < |y_{jet}| < 2.8$, and for the case for the first leading jet in the rapidity region of $2.0 < |y_{jet}| < 2.8$ and the second leading jet in the region of $0.0 \leq |y_{jet}| < 0.8$, see Fig. 7.21. There are small deviations where three and four jets dominate the contributions to the distributions. However,

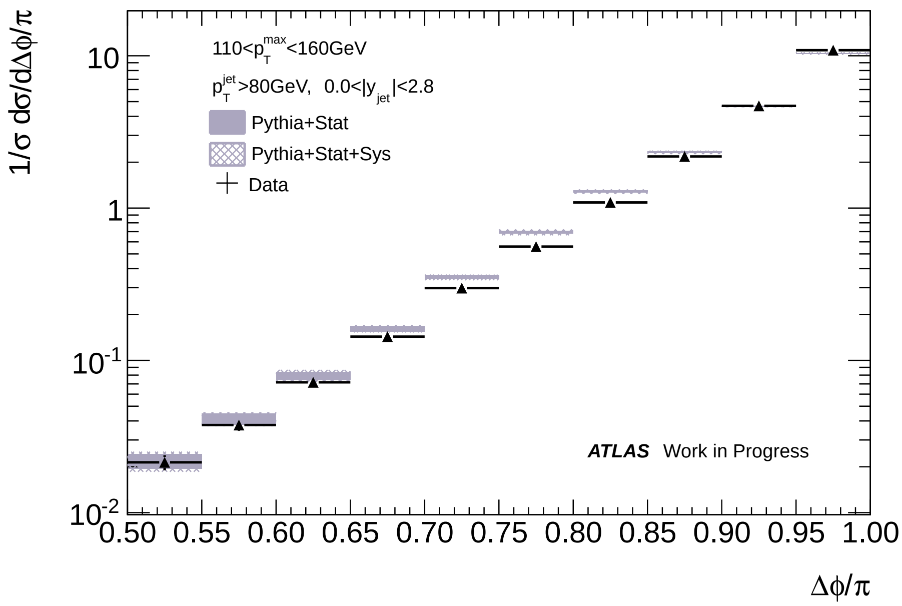

(a)

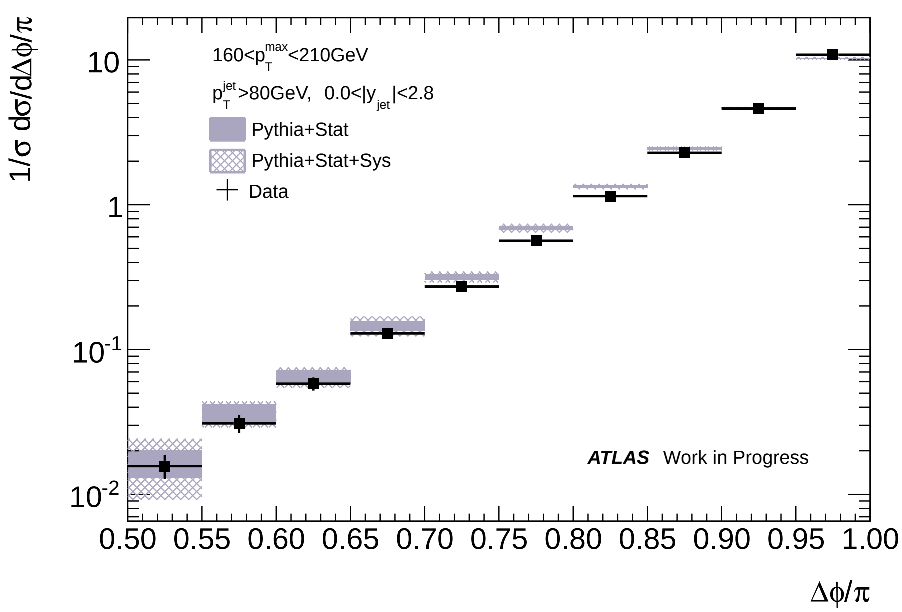

(b)

Figure 7.14

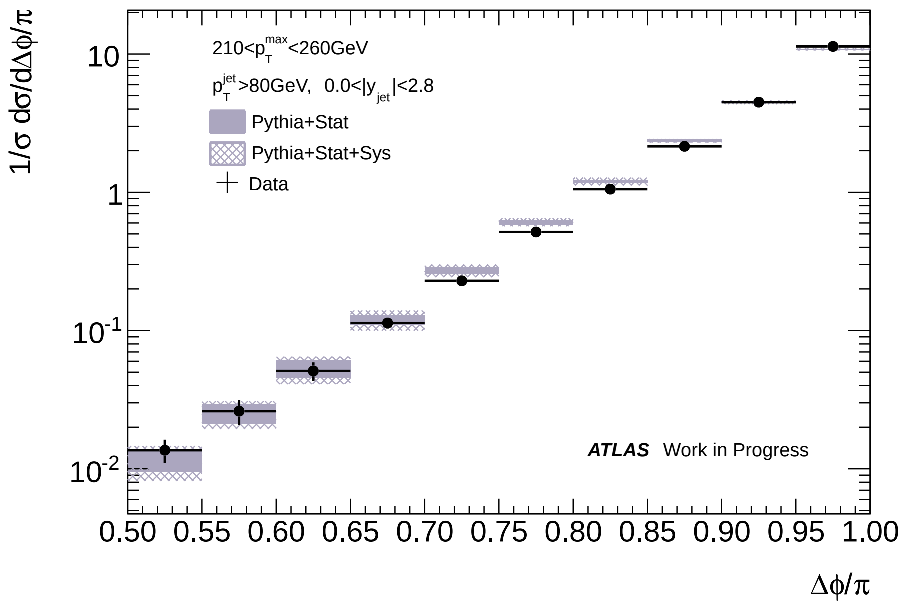

(c)

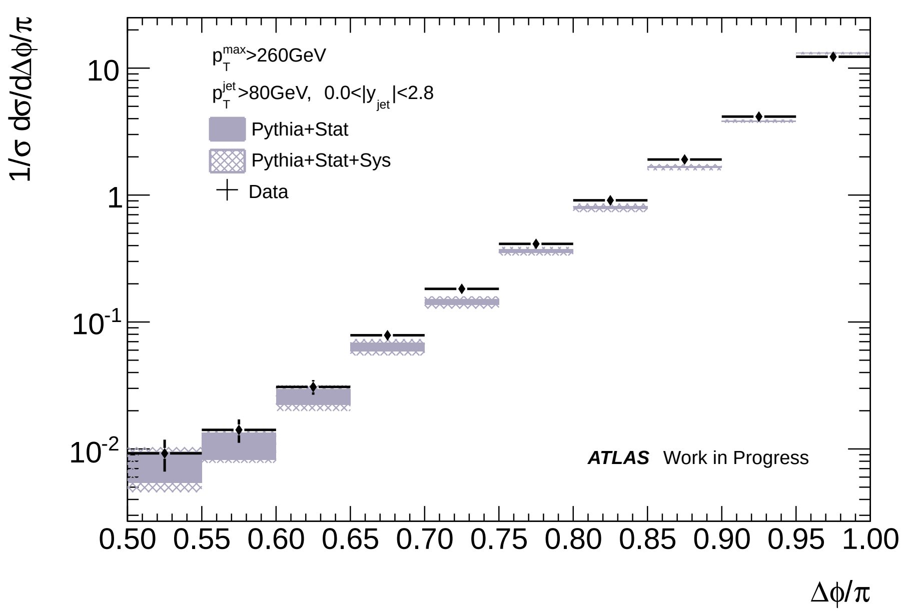

(d)

Figure 7.14: The $\Delta\phi$ unfolding for $p_{\mathrm{T}}^{\mathrm{max}}$ bins $110-160$ GeV, $160-210$ GeV, $210-260$ GeV, and >260 GeV for each trigger selection.

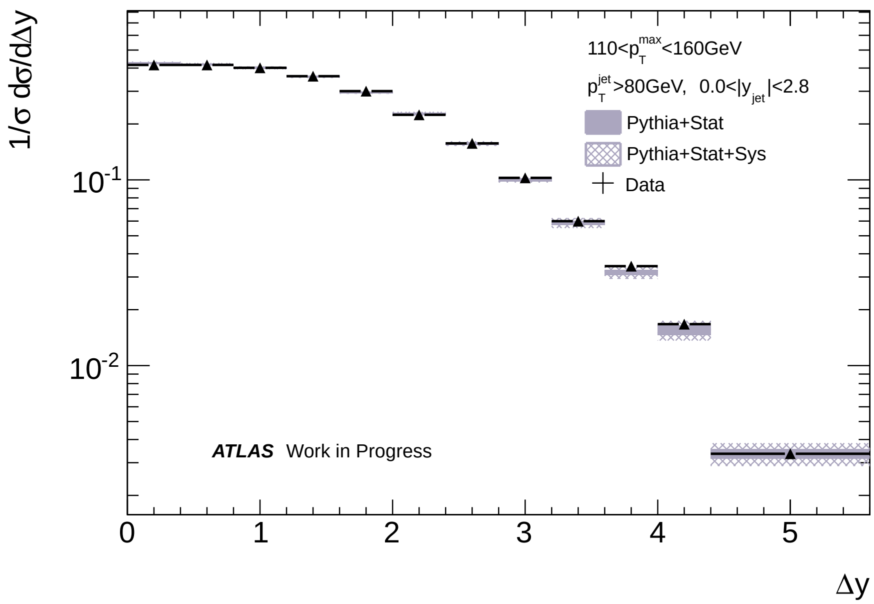

(a)

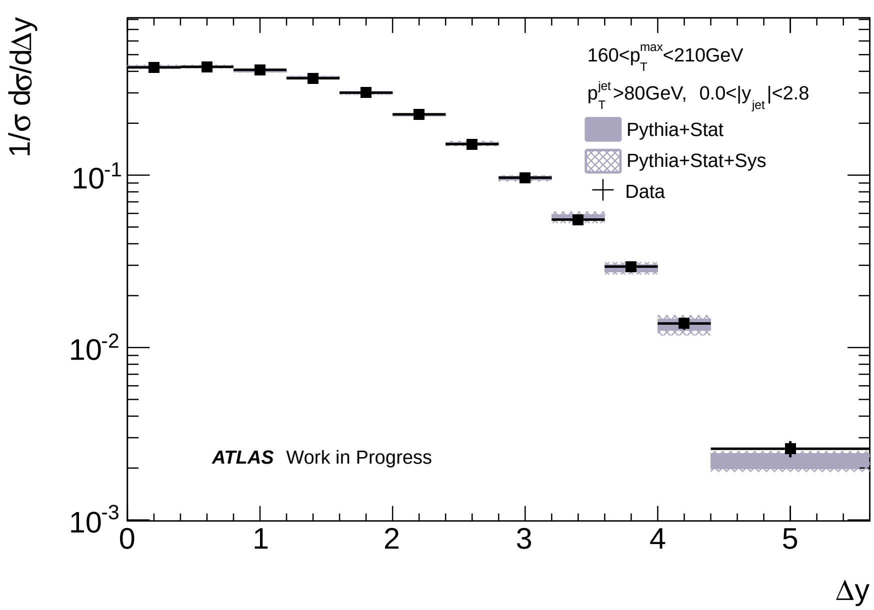

(b)

Figure 7.15

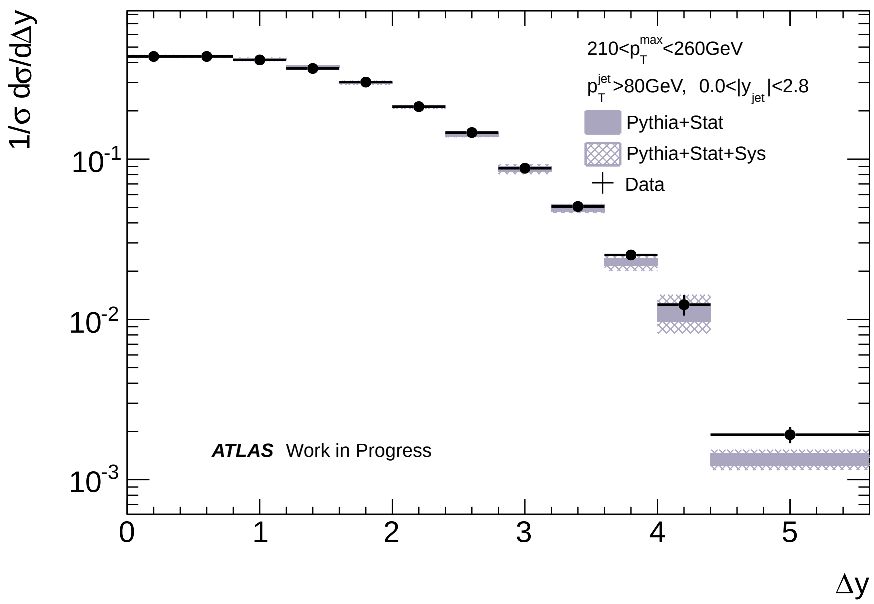

(c)

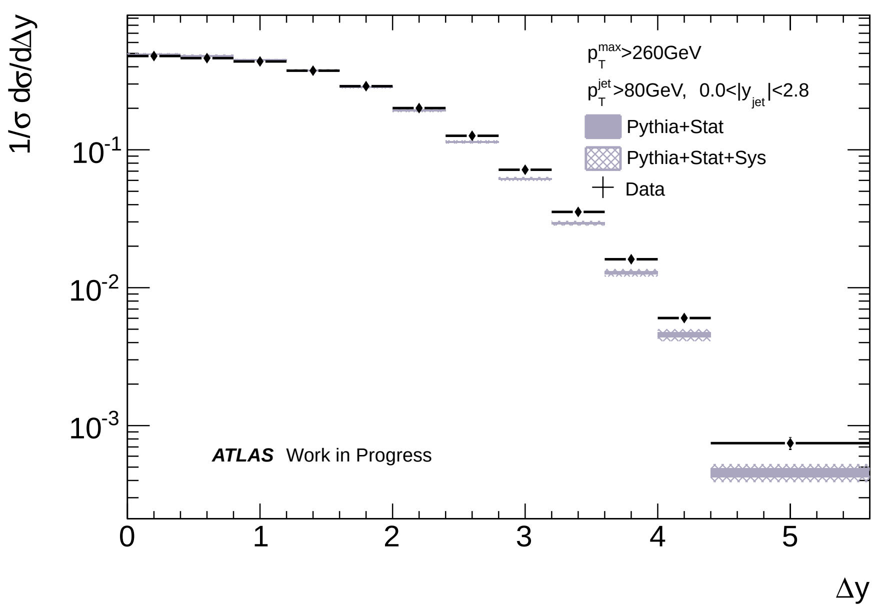

(d)

Figure 7.15: The Δy unfolding for $p_{\mathrm{T}}^{\max}$ bins $110 - 160$ GeV, $160 - 210$ GeV, $210 - 260$ GeV, and > 260 GeV for each trigger selection.

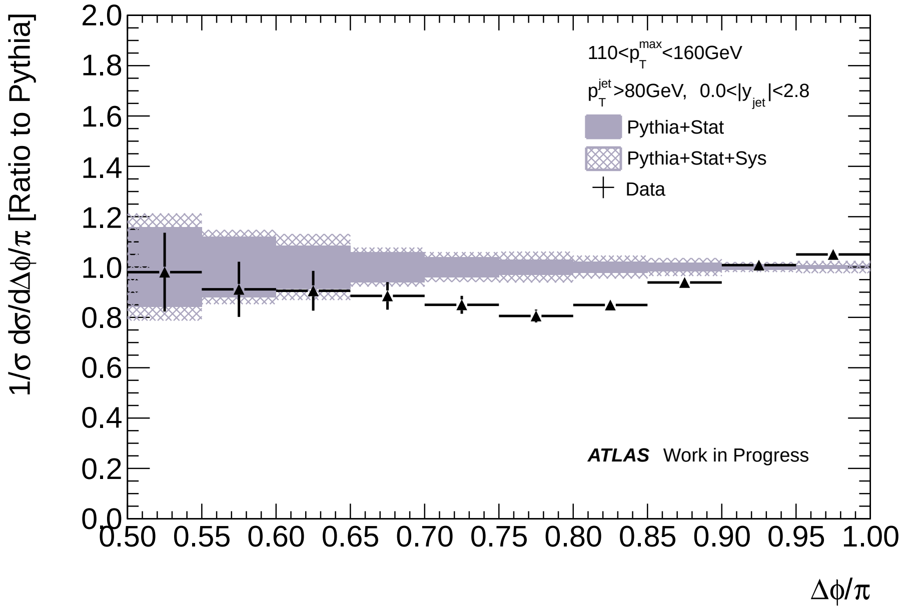

(a)

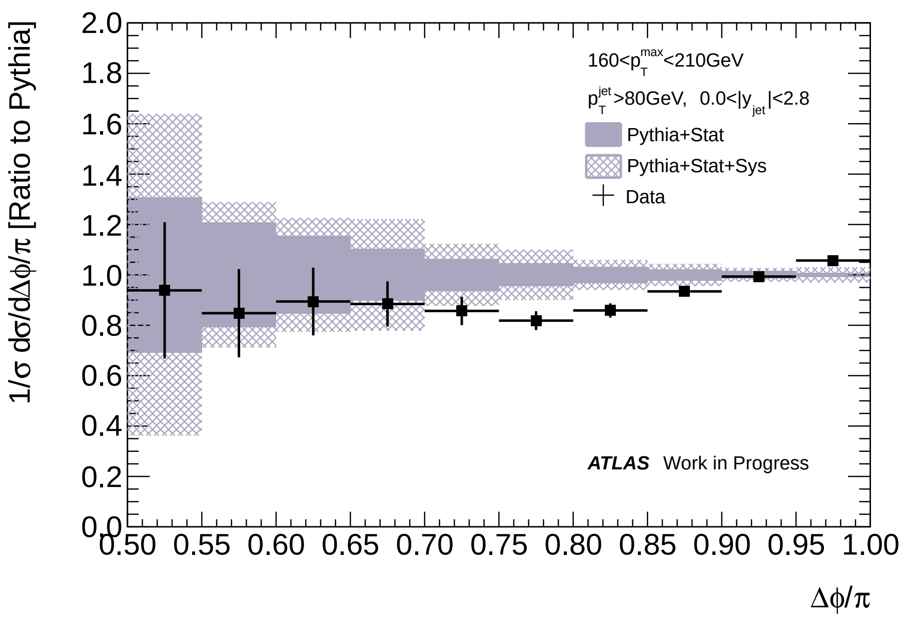

(b)

Figure 7.16

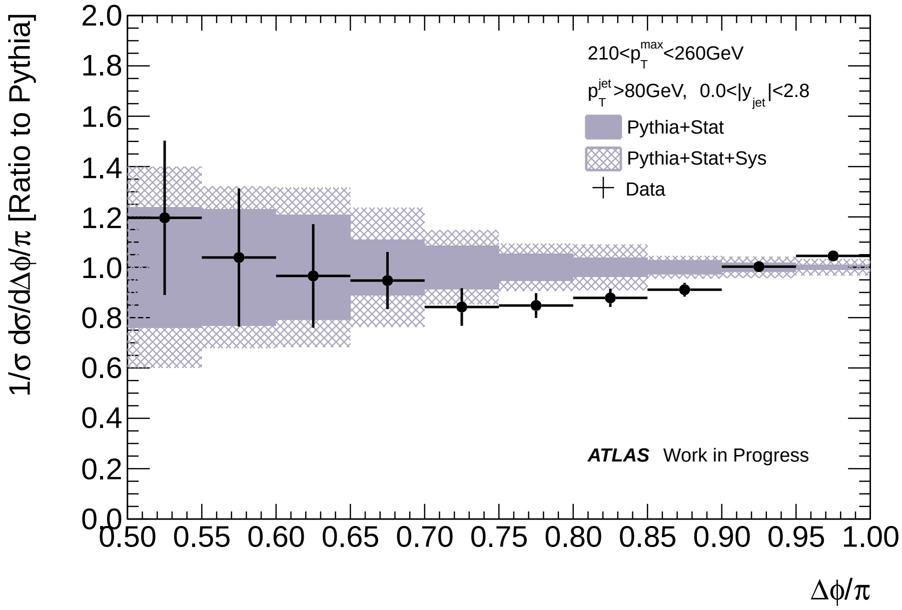

(c)

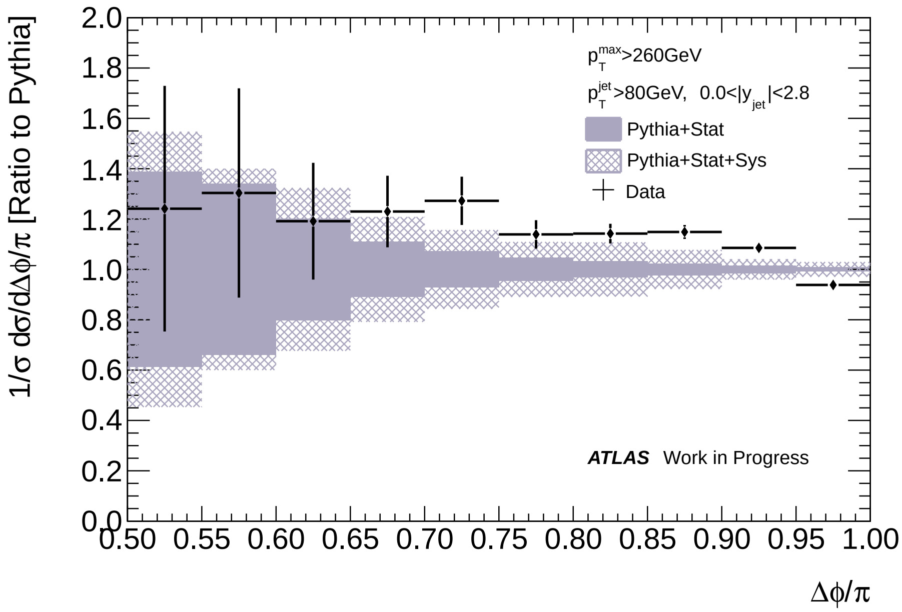

(d)

Figure 7.16: The closure test for $\Delta\phi$ unfolding for $p_{\mathrm{T}}^{\mathrm{max}}$ bins $110 - 160$ GeV, $160 - 210$ GeV, $210 - 260$ GeV, and > 260 GeV for each trigger selection.

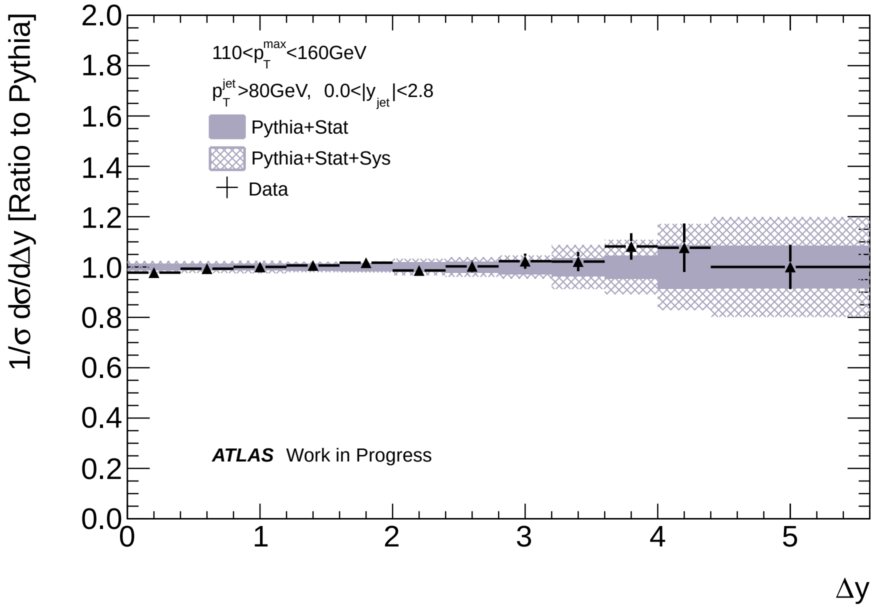

(a)

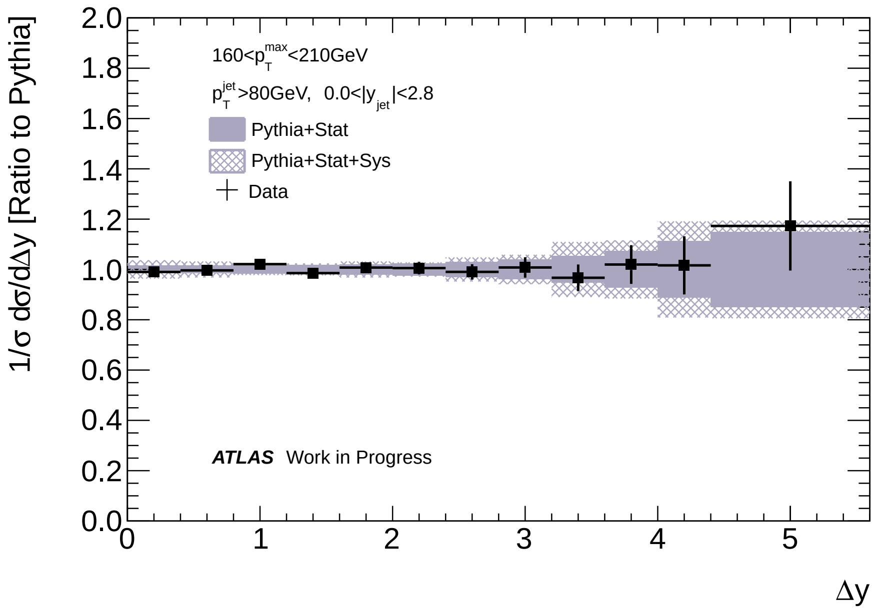

(b)

Figure 7.17

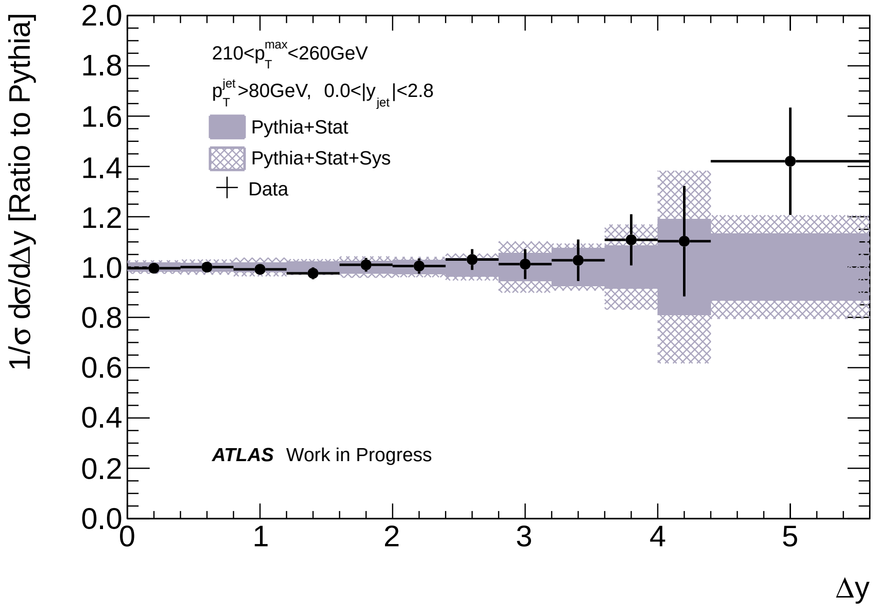

(c)

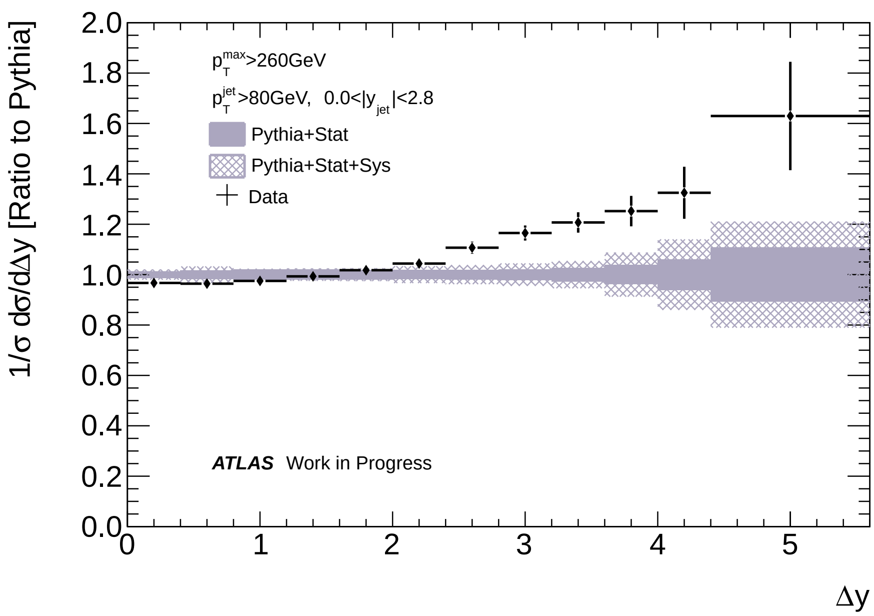

(d)

Figure 7.17: The closure test for Δy unfolding for $p_{\mathrm{T}}^{\mathrm{max}}$ bins $110 - 160$ GeV, $160 - 210$ GeV, $210 - 260$ GeV, and > 260 GeV for each trigger selection.

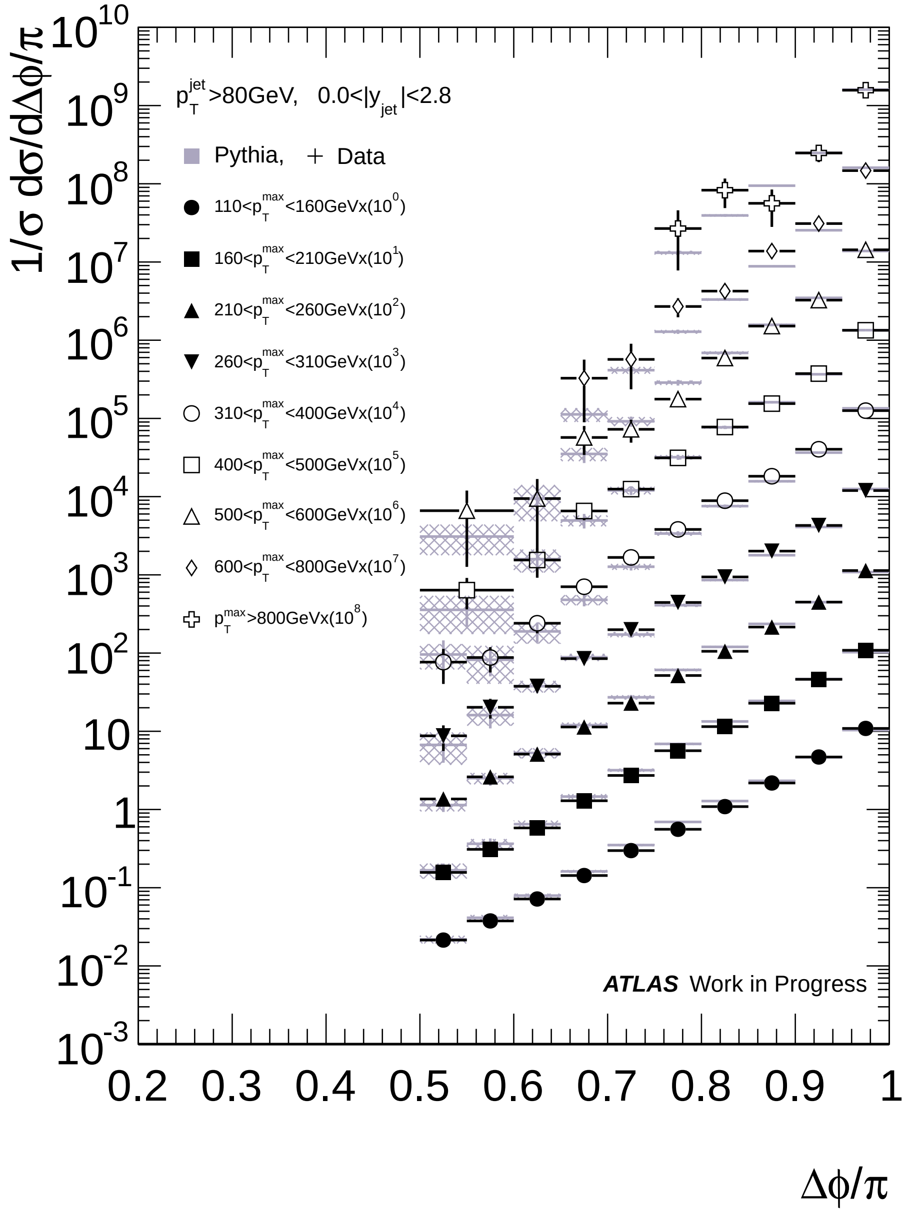

p_T^{jet}>80GeV, 0.0<$|y_{jet}|$<2.8
Pythia, + Data
110<p_T^{max}<160GeVx(10^0)
160<p_T^{max}<210GeVx(10^1)
210<p_T^{max}<260GeVx(10^2)
260<p_T^{max}<310GeVx(10^3)
310<p_T^{max}<400GeVx(10^4)
400<p_T^{max}<500GeVx(10^5)
500<p_T^{max}<600GeVx(10^6)
600<p_T^{max}<800GeVx(10^7)
p_T^{max}>800GeVx(10^8)
ATLAS Work in Progress
$1/\sigma\, d\sigma/d\Delta\phi/\pi$
$\Delta\phi/\pi$

(a)

Figure 7.18

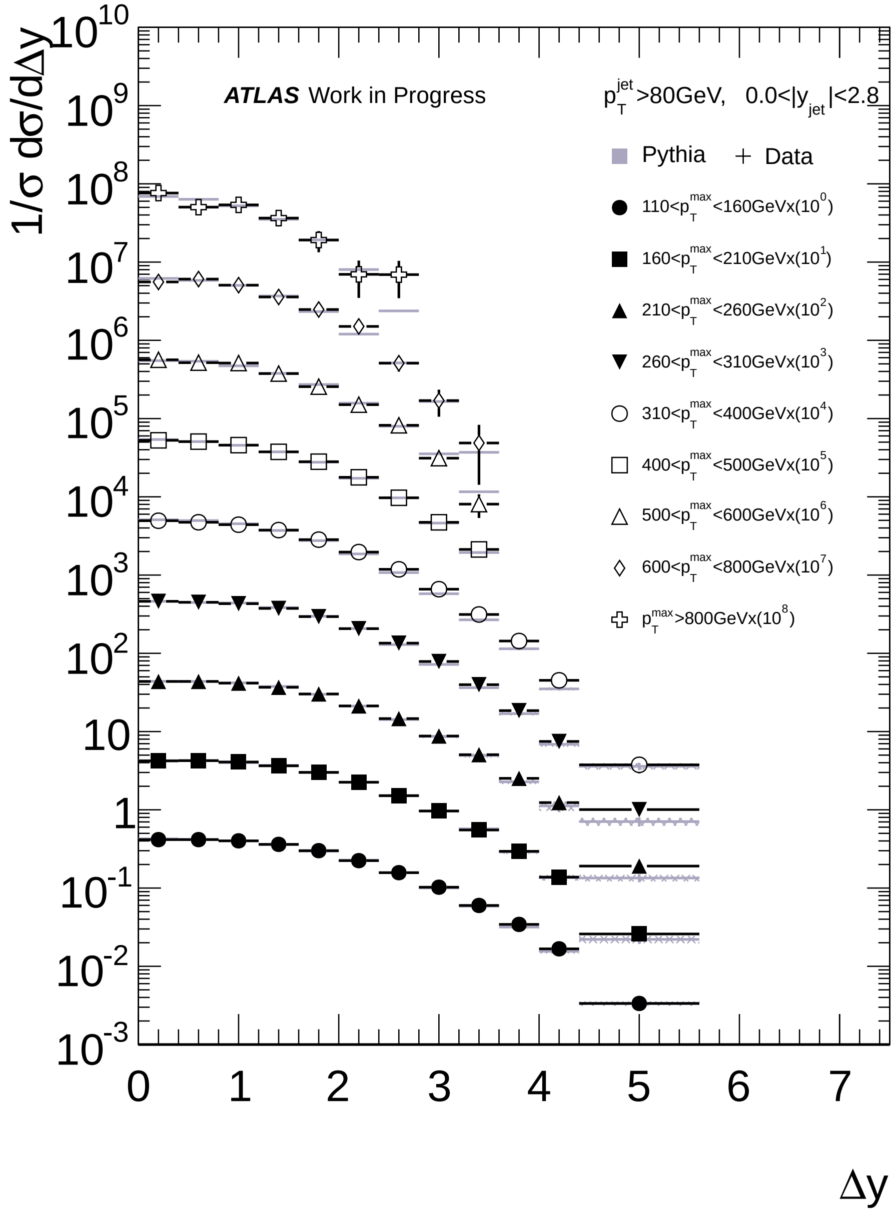

(b)

Figure 7.18: The $\Delta\phi$ and Δy unfolding distributions for $p_{\mathrm{T}}^{\max}$ bins $110 - 160$ GeV, $160 - 210$ GeV, $210 - 260$ GeV, $260 - 310$ GeV, $310 - 400$ GeV, $400 - 500$ GeV, $500 - 600$ GeV, $600 - 800$ GeVand > 800 GeV.

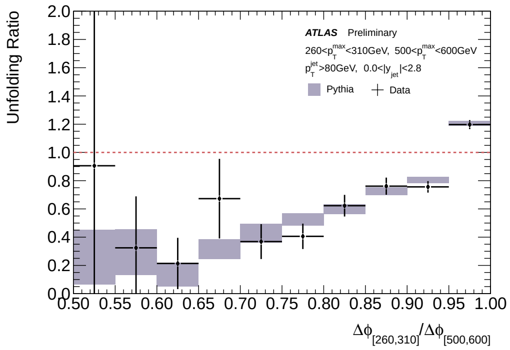

(a)

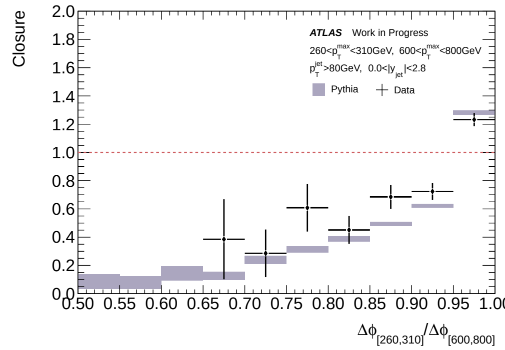

(b)

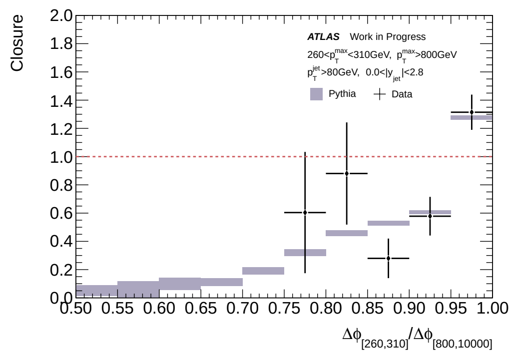

(c)

Figure 7.19: The ratio of the unfolded distributions for $\Delta\phi$ between the cases of $260 - 310$ GeVand $500 - 600$ GeV, $260 - 310$ GeVand $600 - 800$ GeV, and $260 - 310$ GeVand > 800 GeV.

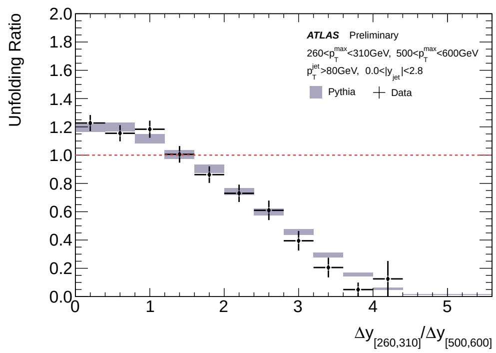

(a)

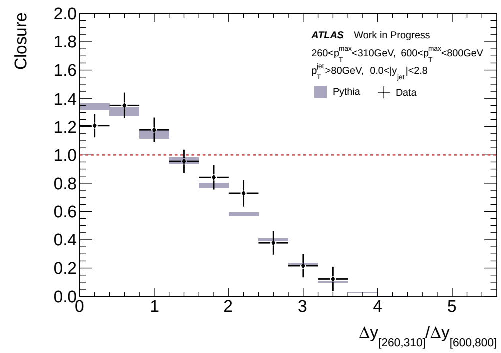

(b)

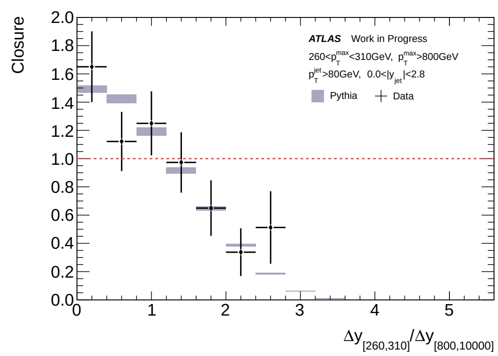

(c)

Figure 7.20: The ratio of the unfolded distributions for $\Delta\phi$ between the cases of $260 - 310$ GeVand $500 - 600$ GeV, $260 - 310$ GeVand $600 - 800$ GeV, and $260 - 310$ GeVand > 800 GeV.

the deviations are not significant beyond 1σ.

7.4.2 2-Dimensional Unfolding Method

The observables $\Delta\phi$, Δy are formed for both truth and reconstructed jets as outlined in Chap. 4. Each of the observables is plotted in a correlated two dimensional histogram such that the observables are plotted against each other. One dimensional projections of one observable in slices of the other are shown in Figs. 7.22-7.23.

The two dimensional truth distribution is divided by the reconstructed distribution. The resultant unfolding factor, as seen in Fig. 7.24, is used for correcting the reconstructed distribution back to the truth information. This is done for each permutation of our correlated observables.

The unfolding factor is applied by multiplying the reconstructed distribution by the unfolding correction factors bin-by-bin. The resultant distributions should be the same as the truth distributions. To test that the corrected reconstructed distribution is the same as the truth distribution, the unfolded reconstructed distribution is divided by the truth distribution. Closure was achieved. This is seen as Fig. 7.25, the closure test distribution is one for every bin.

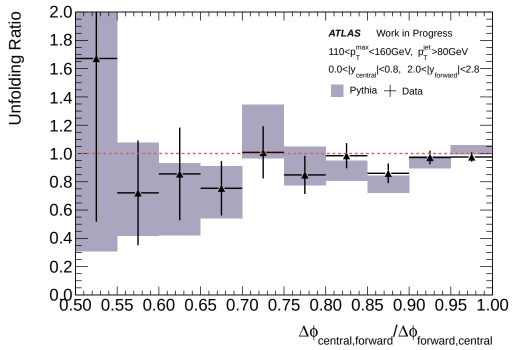

(a)

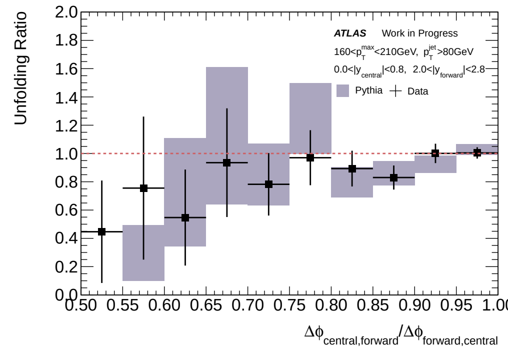

(b)

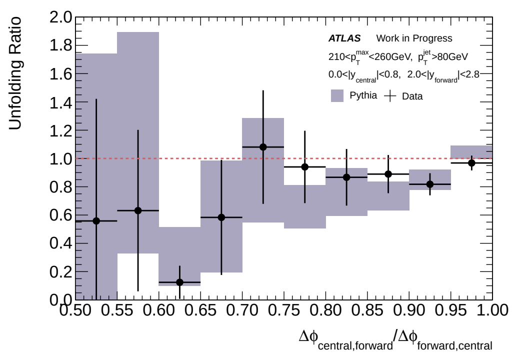

(c)

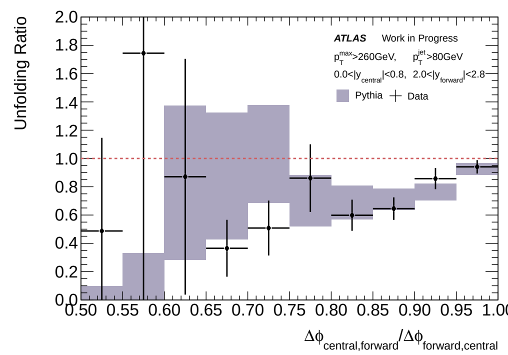

(d)

Figure 7.21: The ratio of the unfolded distributions for $\Delta\phi$ for the case where the first leading jet is central and the second leading jet is forward and the case where the first leading jet is forward and the second leading jet is central for $p_{\mathrm{T}}^{\max}$ bins $110 - 160$ GeV, $160 - 210$ GeV, $210 - 260$ GeV, and > 260 GeV for each trigger selection.

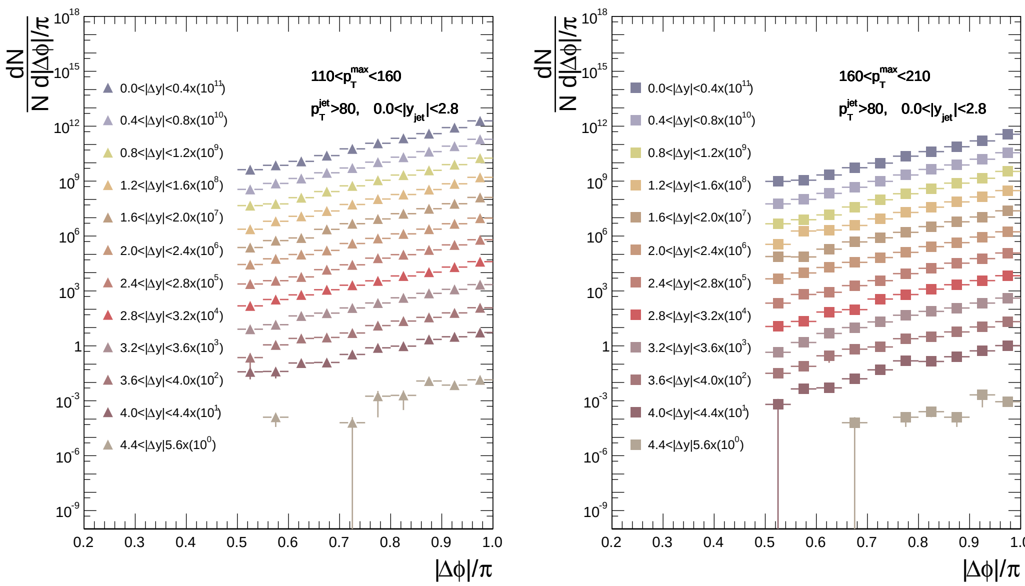

(a) (b)

Figure 7.22

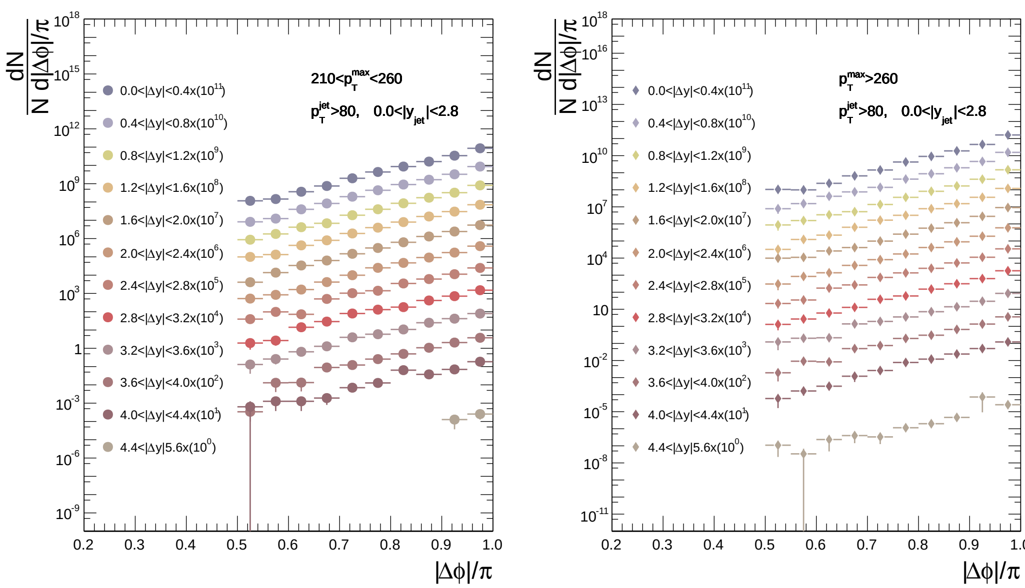

(c) (d)

Figure 7.22: The projection of $\Delta\phi$ in slices of Δy for $p_{\mathrm{T}}^{\max}$ bins $110-160$ GeV, $160-210$ GeV, $210-260$ GeV, and > 260 GeV.

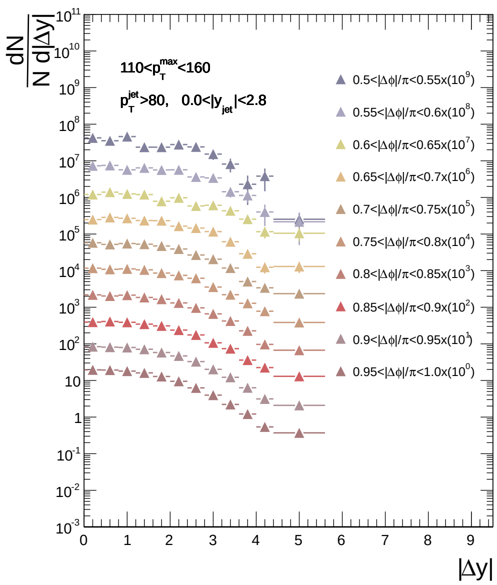

(a)

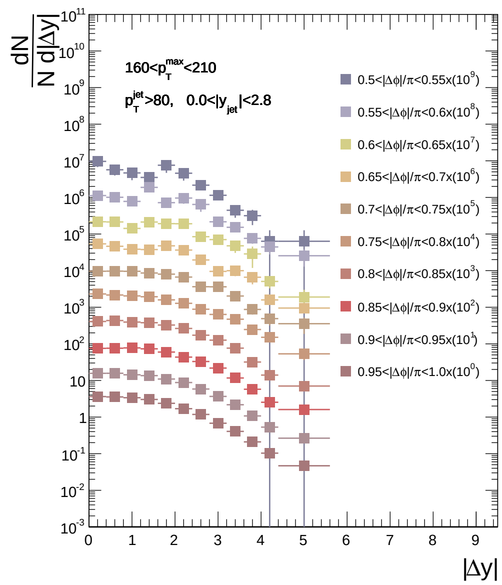

(b)

Figure 7.23

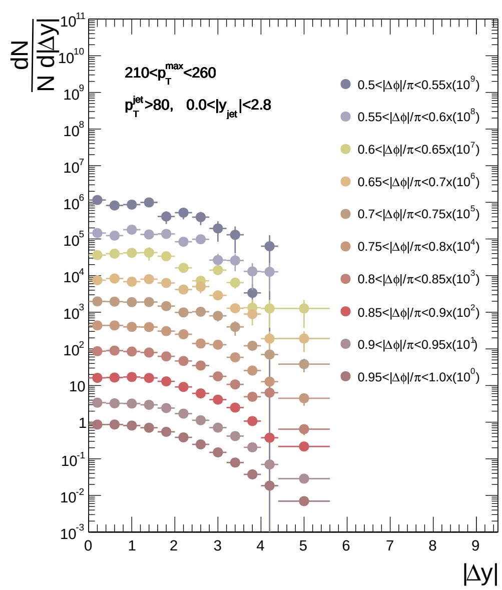

(c)

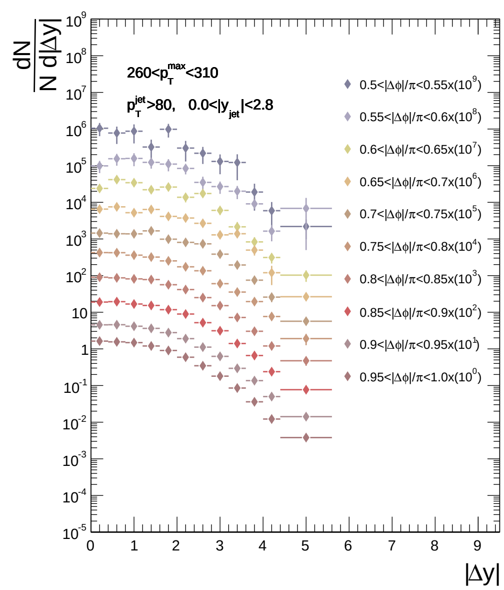

(d)

Figure 7.23: The projection of Δy in slices of $\Delta\phi$ for $p_{\mathrm{T}}^{\max}$ bins $110-160$ GeV, $160-210$ GeV, $210-260$ GeV, and > 260 GeV.

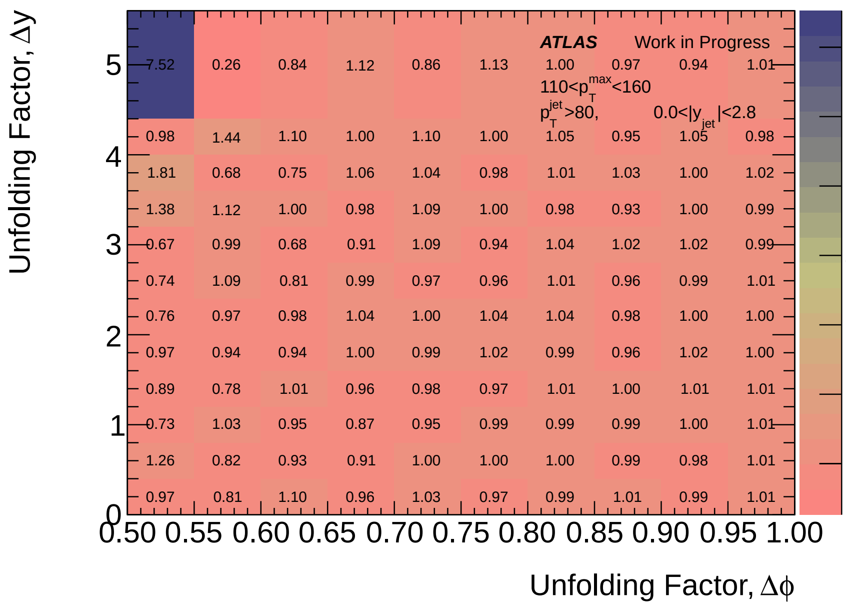

(a)

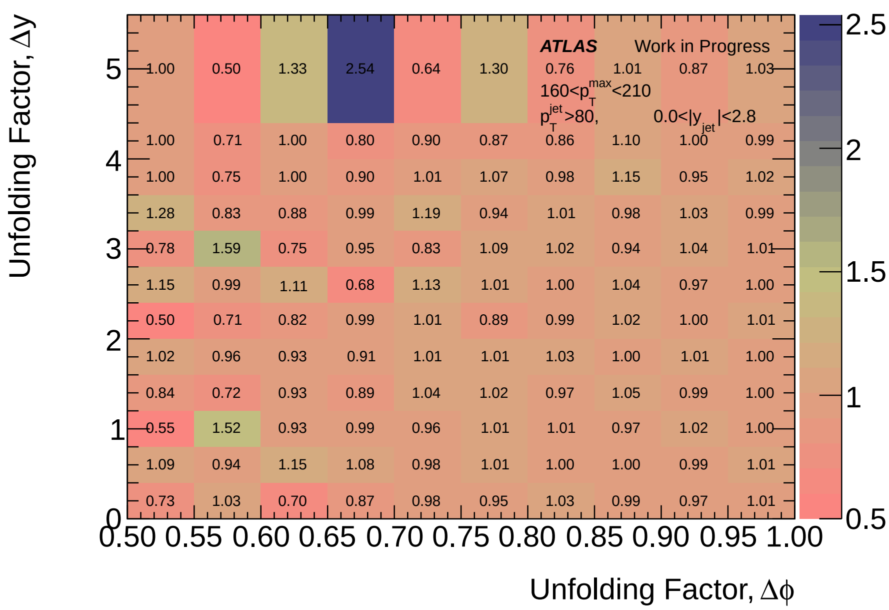

(b)

Figure 7.24

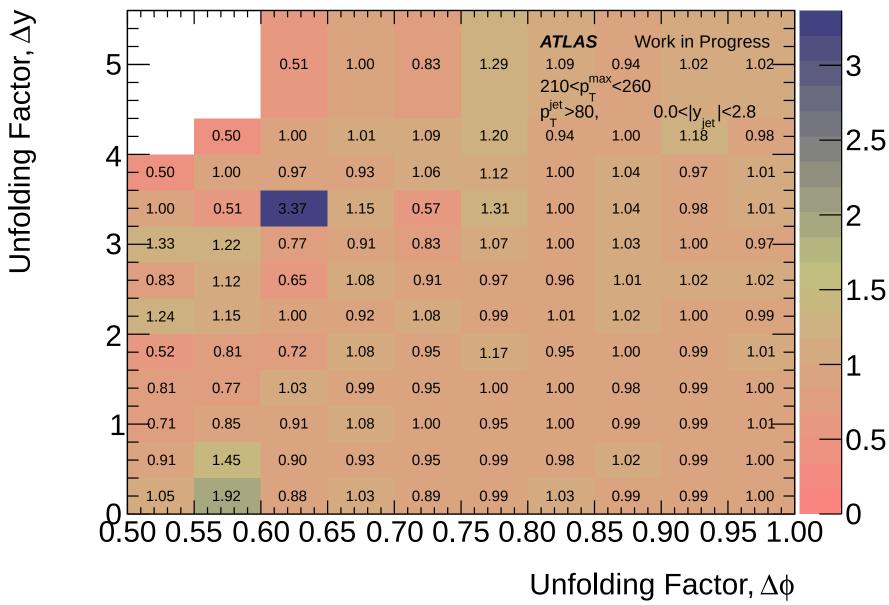

(c)

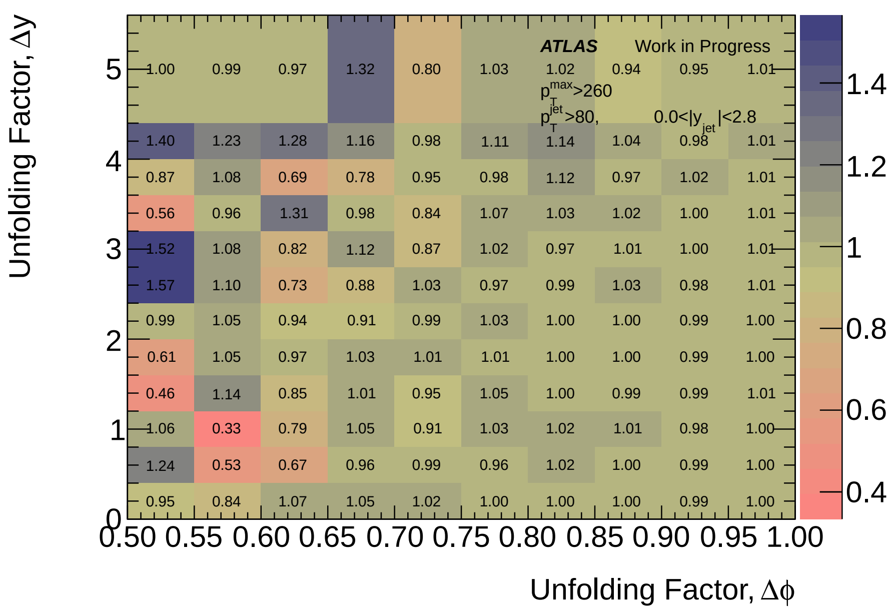

(d)

Figure 7.24: The two dimensional unfolding for $\Delta\phi$ vs. Δy for $p_{\mathrm{T}}^{\max}$ bins $110-160$ GeV, $160-210$ GeV, $210-260$ GeV, $260-310$ GeV, and > 260 GeV.

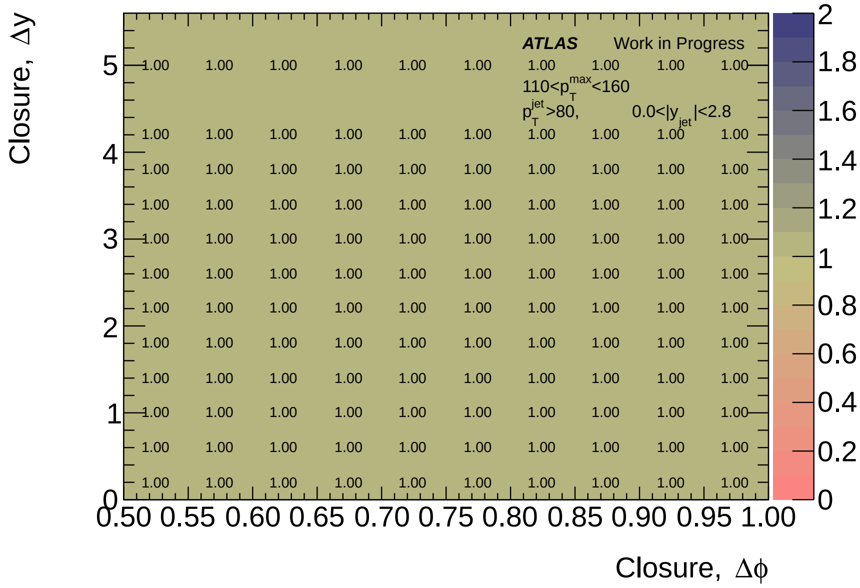

(a)

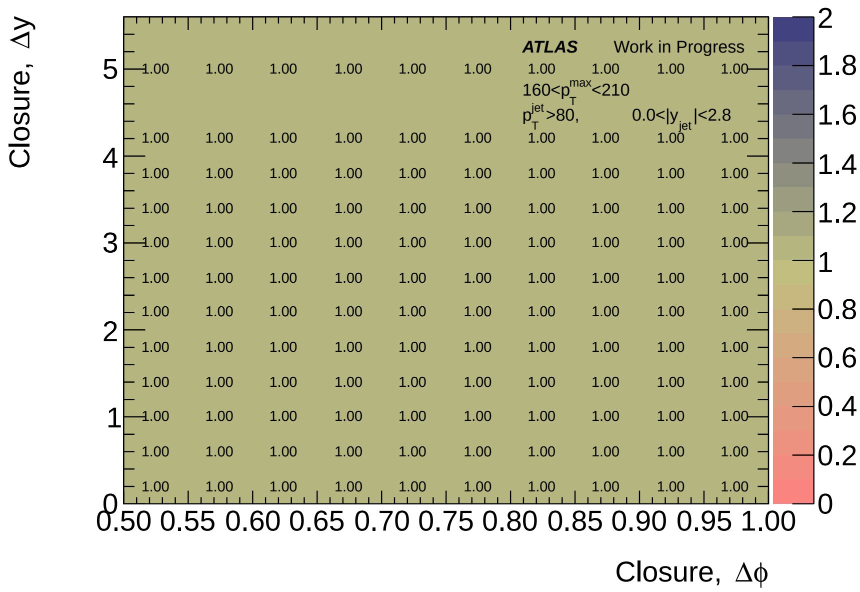

(b)

Figure 7.25

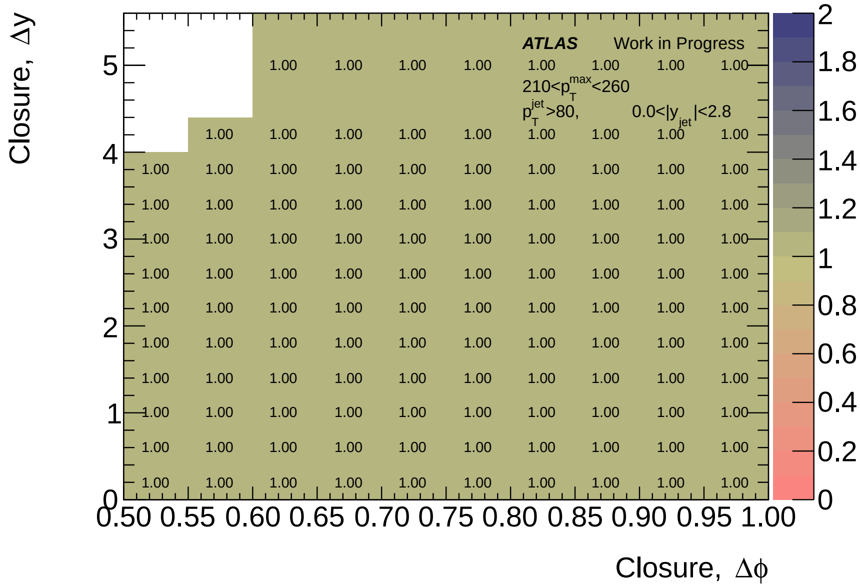

(c)

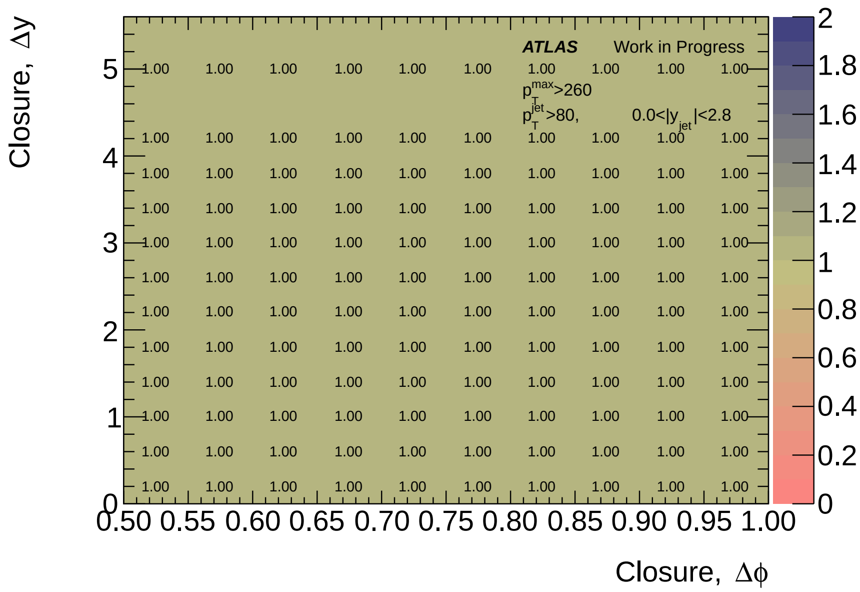

(d)

Figure 7.25: The closure test for the two dimensional unfolding for $\Delta\phi$ vs. Δy for $p_{\mathrm{T}}^{\max}$ bins $110-160$ GeV, $160-210$ GeV, $210-260$ GeV, $260-310$ GeV, and > 260 GeV.

Chapter 8

Comparison to Monte Carlos and NLO

A comparison is done between data and Monte Carlo event generators PYTHIA, HERWIG, and ALPGEN with an ATLAS GEANT detector simulation as well as a comparison with NLO calculation. The comparison to different Monte Carlo event generators is done to study how PYTHIA performs in comparison to other particle level generators such as HERWIG and ALPGEN. The final comparison to NLO calculation is done with unfolded data.

8.1 Other Monte Carlo Generators

All of the Monte Carlo generators used in this study are particle-level generators. Both PYTHIA and HERWIG are 2→2 jet generators. The ALPGEN samples used in this study are 2→2, 2→3, 2→4, 2→5, and 2→6 jets. A comparison between PYTHIA and these two generators allows for tuning of PYTHIA as the differences in fits of the generators to data can show how the variables in PYTHIA may be tuned so that PYTHIA better models data. The $\Delta\phi$ distribution is sensitive to the PYTHIA initial state radiation parameter PARP[67], and the Δy distribution is sensitive to forward energy flow parameters in PYTHIA [64].

The reconstructed HERWIG and ALPGEN distributions are unfolded with unfolding factors derived from their truth information and from PYTHIA truth information. The closure plot of HERWIG and ALPGEN to themselves and to PYTHIA can be seen in Figs. 8.1-8.4 for both $\Delta\phi$ and Δy.

The unfolded distributions for $\Delta\phi$ and Δy in data are compared to the unfolded distributions for all three generators, HERWIG, PYTHIA, and ALPGEN, see Fig. 8.5. For the $\Delta\phi$ distribution, the ALPGEN generator does the best job modeling data at the lower p_T^{max} bins while for the higher p_T^{max} bins

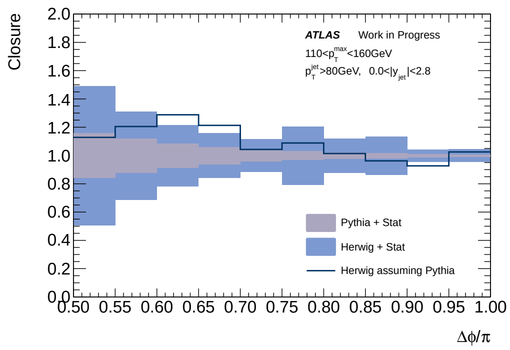

(a)

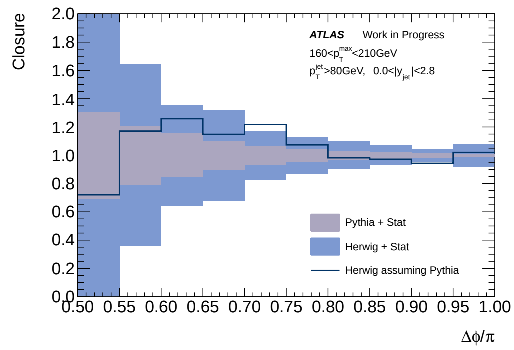

(b)

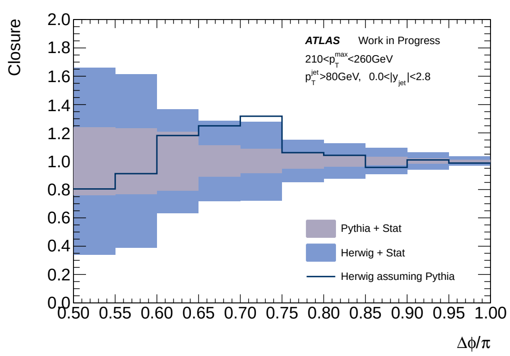

(c)

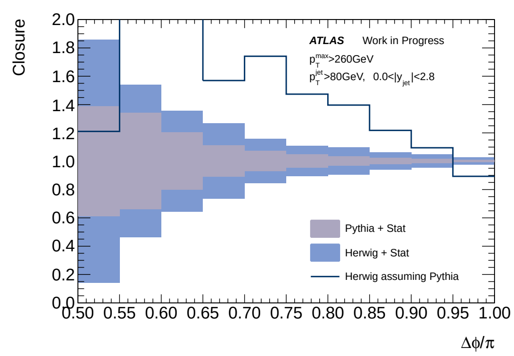

(d)

Figure 8.1: The closure test for $\Delta\phi$ unfolding for $p_{\mathrm{T}}^{\mathrm{max}}$ bins $110 - 160$ GeV, $160 - 210$ GeV, $210 - 260$ GeV, and > 260 GeV for each trigger selection for Herwig compared to Pythia.

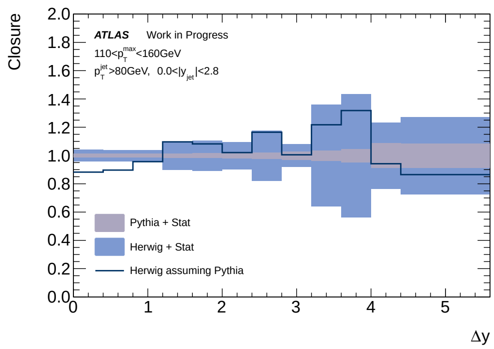

(a)

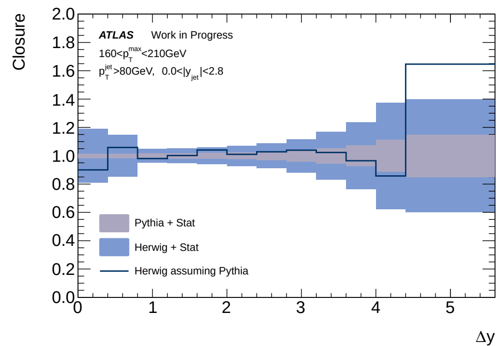

(b)

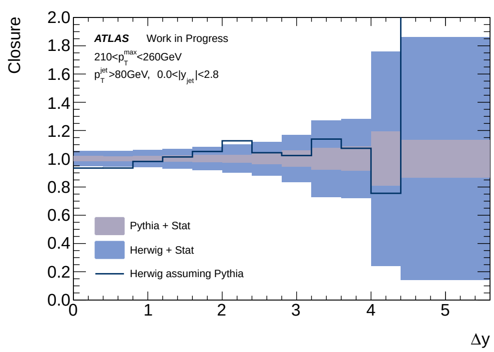

(c)

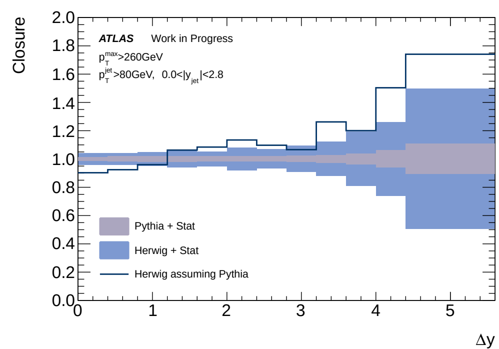

(d)

Figure 8.2: The closure test for Δy unfolding for $p_{\mathrm{T}}^{\mathrm{max}}$ bins $110 - 160$ GeV, $160 - 210$ GeV, $210 - 260$ GeV, and > 260 GeV for each trigger selection for Herwig compared to Pythia.

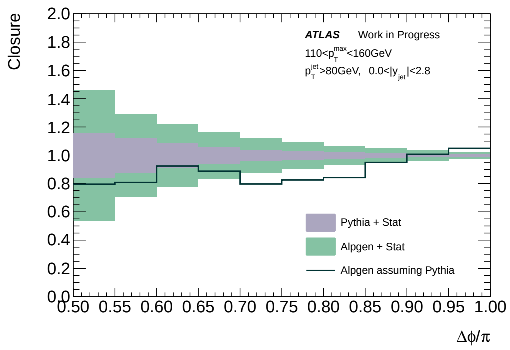

(a)

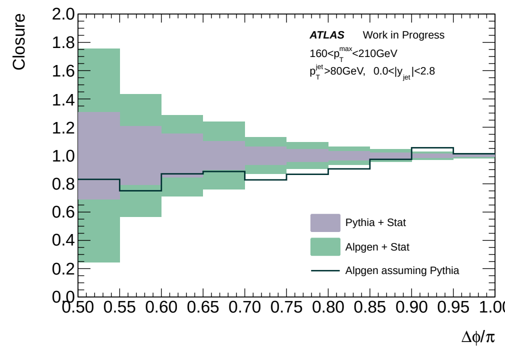

(b)

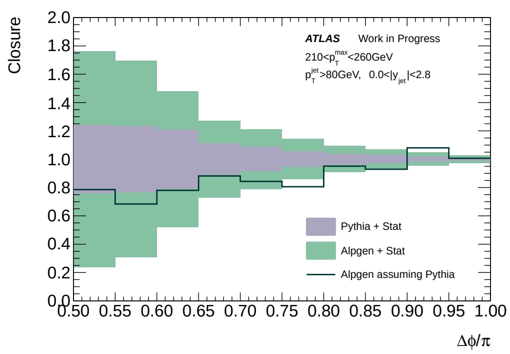

(c)

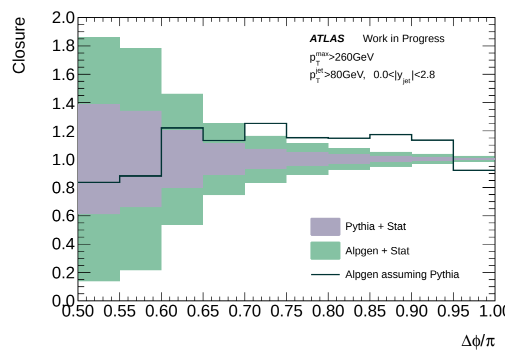

(d)

Figure 8.3: The closure test for $\Delta\phi$ unfolding for $p_{\mathrm{T}}^{\max}$ bins $110-160$ GeV, $160-210$ GeV, $210-260$ GeV, and >260 GeV for each trigger selection for Alpgen compared to Pythia.

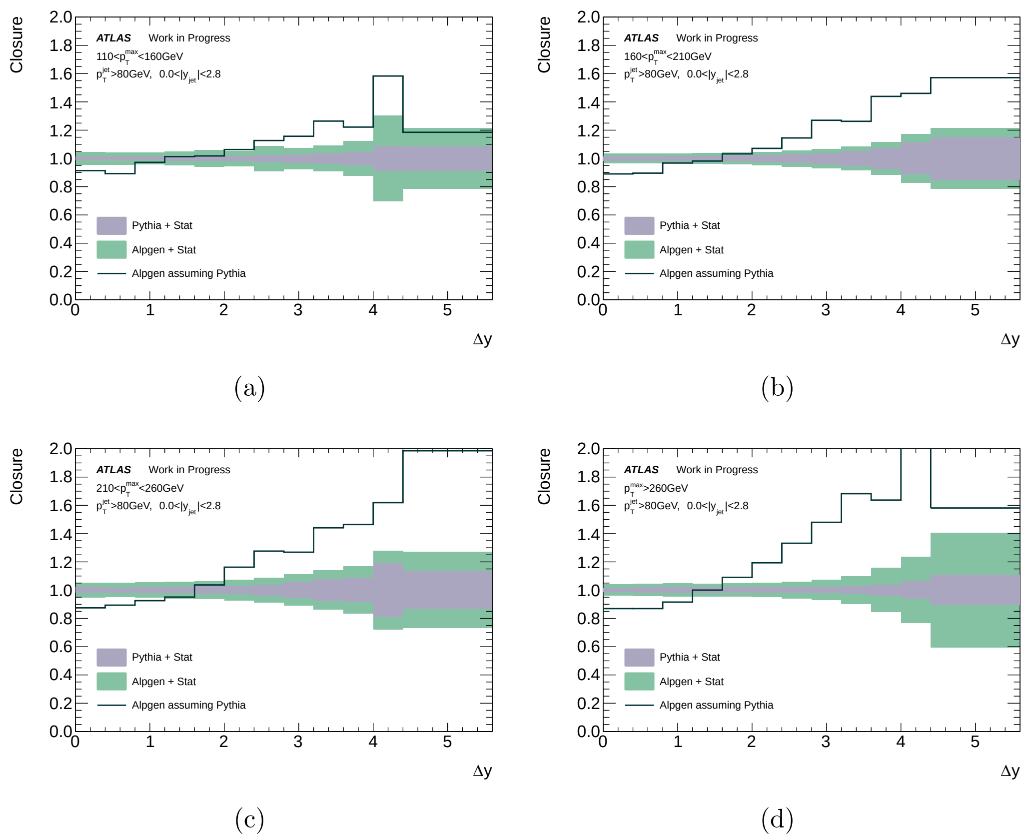

Figure 8.4: The closure test for Δy unfolding for $p_{\mathrm{T}}^{\mathrm{max}}$ bins $110-160$ GeV, $160-210$ GeV, $210-260$ GeV, and >260 GeV for each trigger selection for Alpgen compared to Pythia.

the statistics makes it more difficult to differentiate the performance of the three generators. For Δy, however, ALPGEN begins to pull higher than data with increasing p_T^{max} and deviates from higher values of Δy. Overall, HERWIG performs best in describing the $\Delta\phi$ distributions, but it underperforms PYTHIA for the description of the Δy distributions. See Tabs. 8.1-8.2 for the χ^2 fit of the Monte Carlo to the unfolded data. The total χ^2 fit divided by the number of degrees of freedom (NDF) for $\Delta\phi$ and Δy for PYTHIA is 3.95 and 2.52, for HERWIG is 3.73 and 1.96, and for ALPGEN is 1.85 and 14.17, respectively.

The ratio of HERWIG to the unfolded data for the $\Delta\phi$ and Δy distributions at different p_T^{max} bins shows good agreement in each bin of the distributions, see Figs. 8.6-8.7. The ratio of ALPGEN to the unfolded data in $\Delta\phi$ at different p_T^{max} bins shows good agreement in each bin of the distributions, but there is poor agreement in the Δy distributions, see Figs. 8.8-8.9.

Table 8.1: Comparison of the χ^2 fit to data for the different MC generators PYTHIA, HERWIG, and ALPGEN for the $\Delta\phi$ distribution. The NDF=9 for each of the p_T^{max} bins and 36 for the total χ^2 for each of the MC generators.

Monte Carlo Generator+Error	p_T^{max} bin (GeV)	χ^2	χ^2/NDF
PYTHIA+Stat+Sys	110-160	61.01	6.78
	160-210	28.48	3.16
	210-260	17.94	1.99
	>260	34.72	3.85
	Total	142.15	3.95
HERWIG+Stat	110-160	33.01	3.67
	160-210	29.27	3.25
	210-260	26.00	2.89
	>260	45.95	3.55
	Total	134.23	3.73
ALPGEN+Stat	110-160	2.94	0.33
	160-210	42.41	4.71
	210-260	15.28	1.69
	>260	6.05	0.67
	Total	66.68	1.85

Table 8.2: Comparison of the χ^2 fit to data for the different MC generators PYTHIA, HERWIG, and ALPGEN for the $\Delta\phi$ distribution. The NDF=9 for each of the p_T^{max} bins and 36 for the total χ^2 for each of the MC generators.

Monte Carlo Generator+Error	p_T^{max} bin (GeV)	χ^2	χ^2/NDF
PYTHIA+Stat+Sys	110-160	4.15	0.38
	160-210	3.02	0.27
	210-260	5.77	0.52
	>260	77.89	7.08
	Total	90.83	2.52
HERWIG+Stat	110-160	37.57	3.41
	160-210	4.69	0.43
	210-260	13.31	1.21
	>260	15.20	1.38
	Total	70.77	1.96
ALPGEN+Stat	110-160	48.72	4.43
	160-210	242.45	22.04
	210-260	95.95	8.72
	>260	123.02	11.18
	Total	510.14	14.17

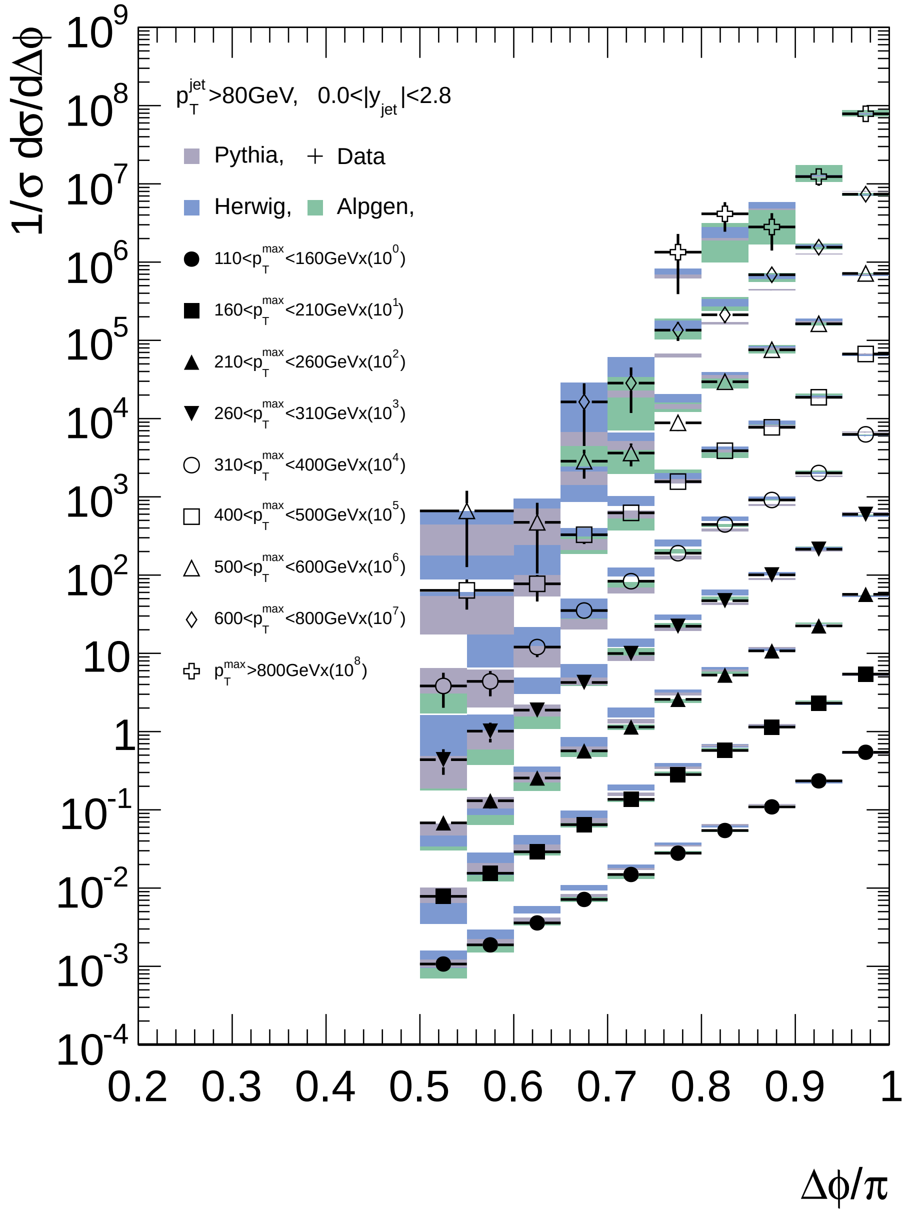

p_T^{jet}>80GeV, 0.0<|y_{jet}|<2.8
Pythia, + Data
Herwig, Alpgen,
110<p_T^{max}<160GeVx(10^0)
160<p_T^{max}<210GeVx(10^1)
210<p_T^{max}<260GeVx(10^2)
260<p_T^{max}<310GeVx(10^3)
310<p_T^{max}<400GeVx(10^4)
400<p_T^{max}<500GeVx(10^5)
500<p_T^{max}<600GeVx(10^6)
600<p_T^{max}<800GeVx(10^7)
p_T^{max}>800GeVx(10^8)
1/σ dσ/dΔφ
Δφ/π

(a)

Figure 8.5

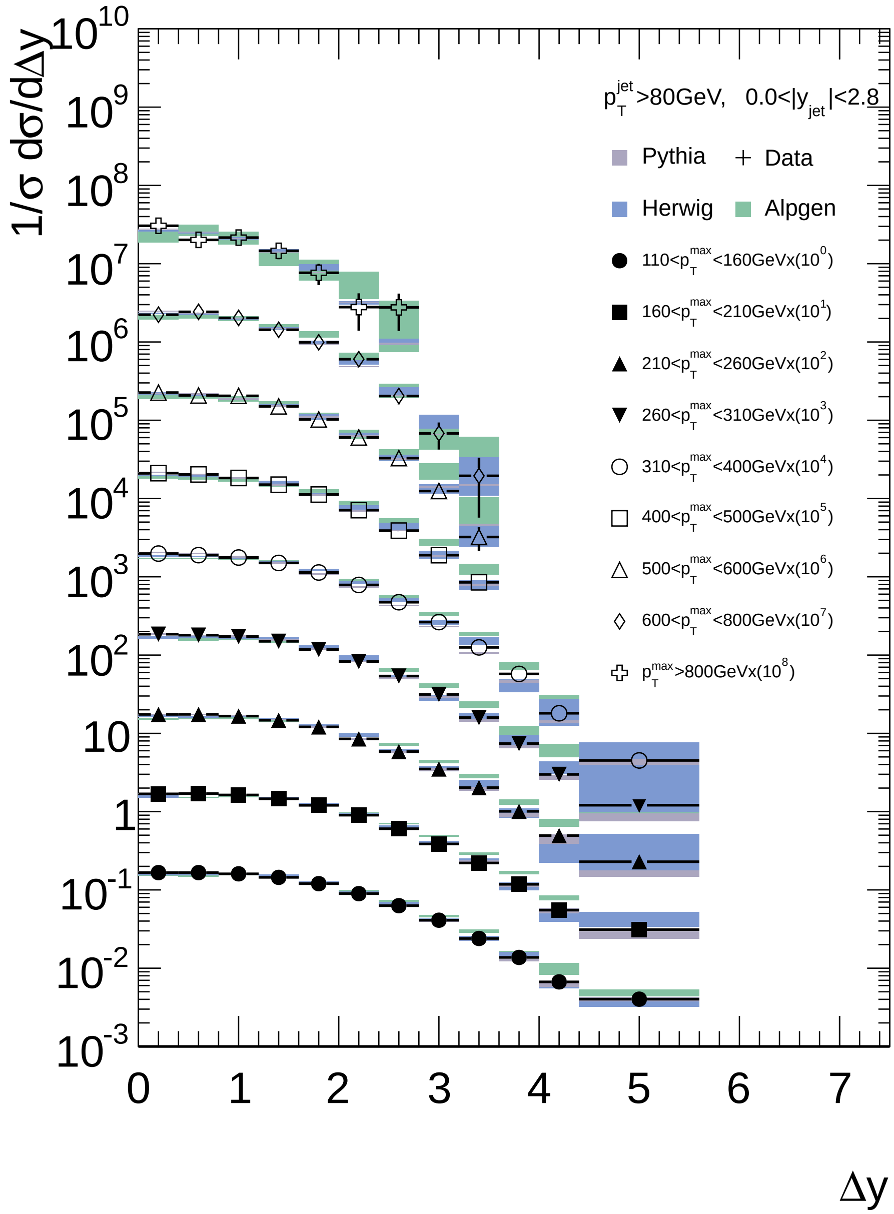

(b)

Figure 8.5: The $\Delta\phi$ and Δy unfolding distributions for p_T^{max} bins $110-160$ GeV, $160-210$ GeV, $210-260$ GeV, $260-310$ GeV, $310-400$ GeV, $400-500$ GeV, $500-600$ GeV, $600-800$ GeVand >800 GeV.

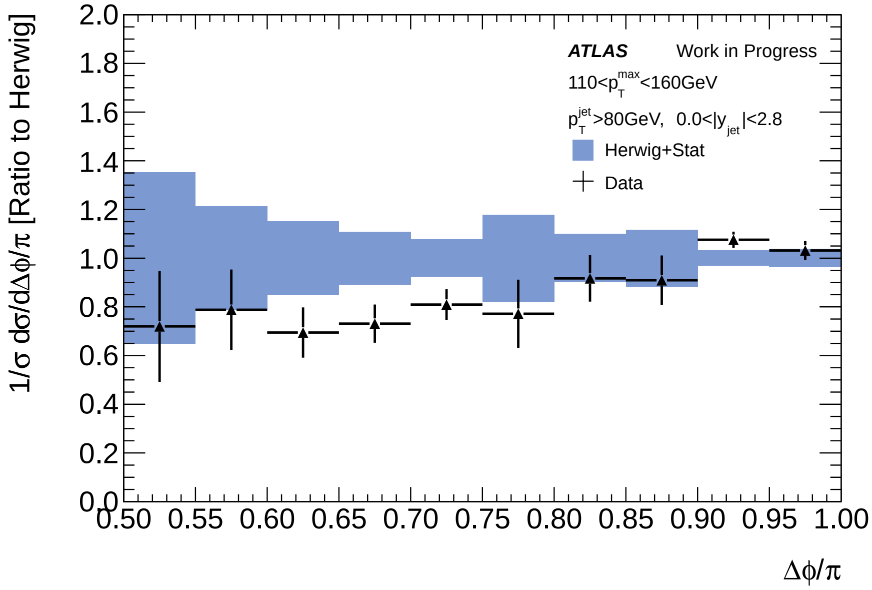
ATLAS Work in Progress
110<p_T^max<160GeV
p_T^jet>80GeV, 0.0<|y_jet|<2.8
Herwig+Stat
Data
1/σ dσ/dΔφ/π [Ratio to Herwig]
Δφ/π

(a)

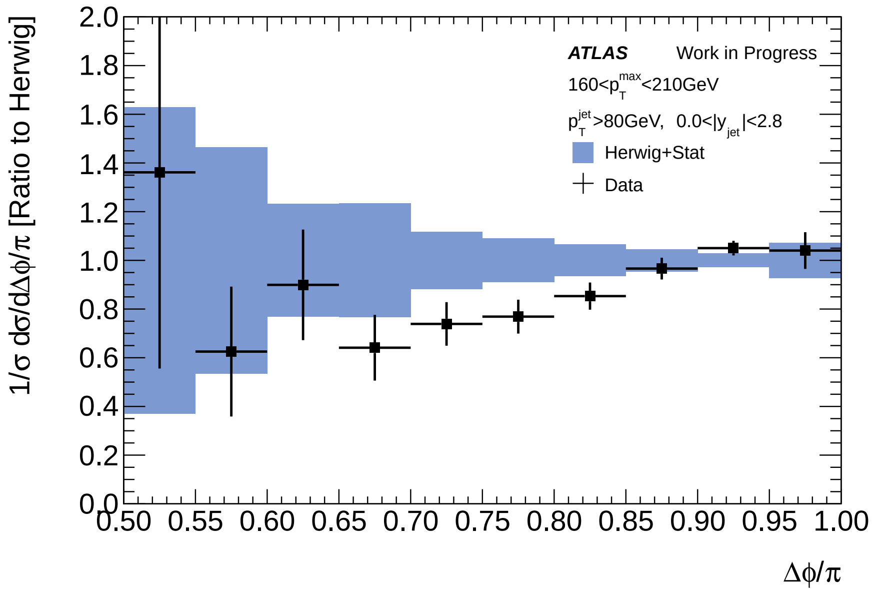
ATLAS Work in Progress
160<p_T^max<210GeV
p_T^jet>80GeV, 0.0<|y_jet|<2.8
Herwig+Stat
Data
1/σ dσ/dΔφ/π [Ratio to Herwig]
Δφ/π

(b)

Figure 8.6

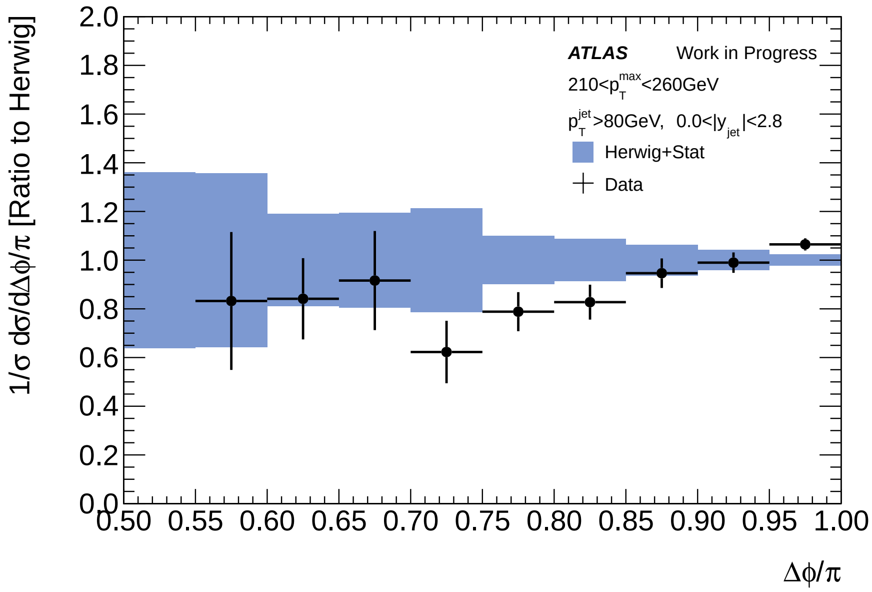

(c)

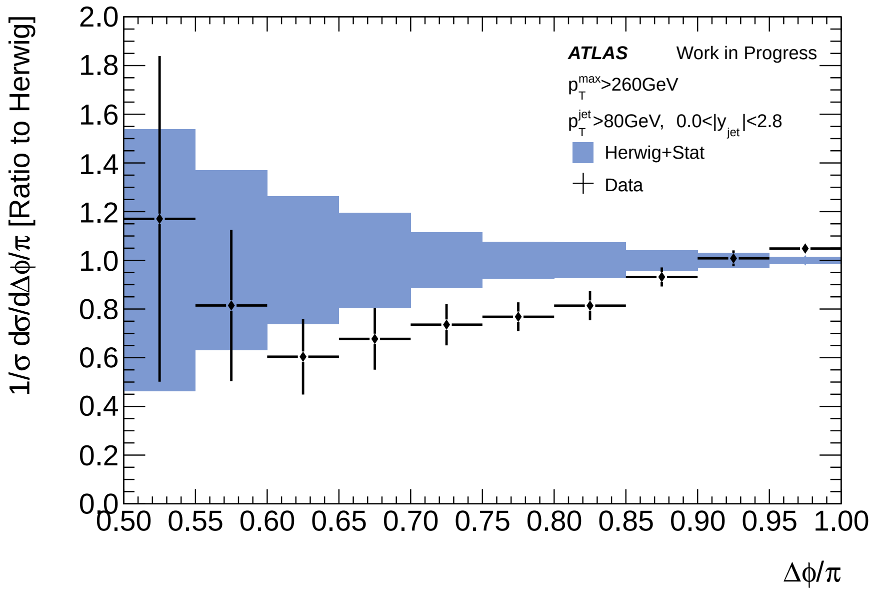

(d)

Figure 8.6: The closure test for data unfolded by Herwig for $\Delta\phi$ unfolding for $p_{\mathrm{T}}^{\mathrm{max}}$ bins 110 – 160 GeV, 160 – 210 GeV, 210 – 260 GeV, and $>$ 260 GeV for each trigger selection.

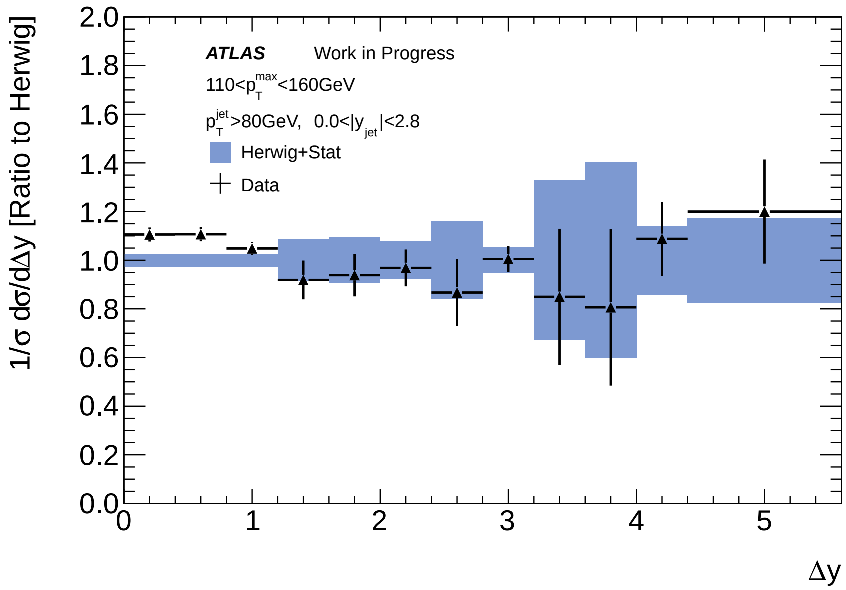
ATLAS Work in Progress
110<p_T^max<160GeV
p_T^jet>80GeV, 0.0<|y_jet|<2.8
Herwig+Stat
Data
1/σ dσ/dΔy [Ratio to Herwig]
Δy

(a)

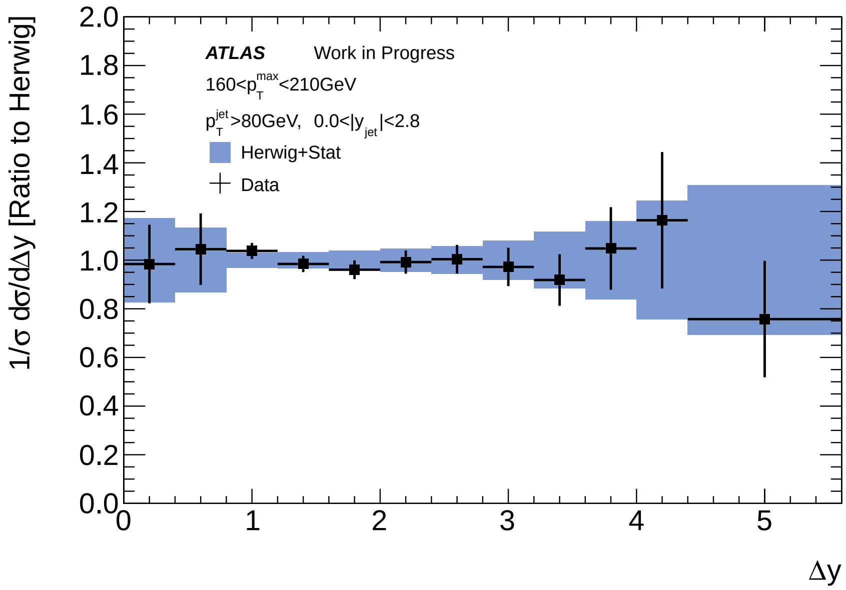
ATLAS Work in Progress
160<p_T^max<210GeV
p_T^jet>80GeV, 0.0<|y_jet|<2.8
Herwig+Stat
Data
1/σ dσ/dΔy [Ratio to Herwig]
Δy

(b)

Figure 8.7

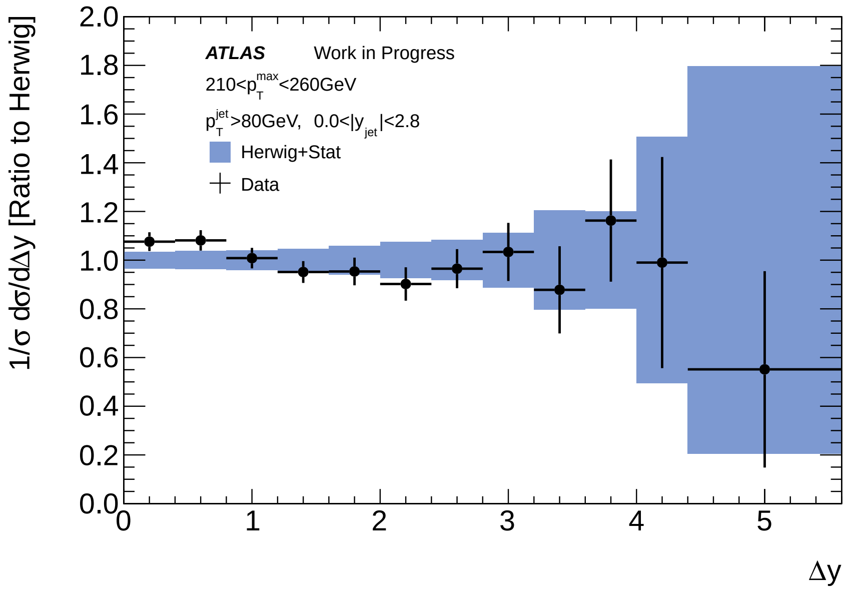

(c)

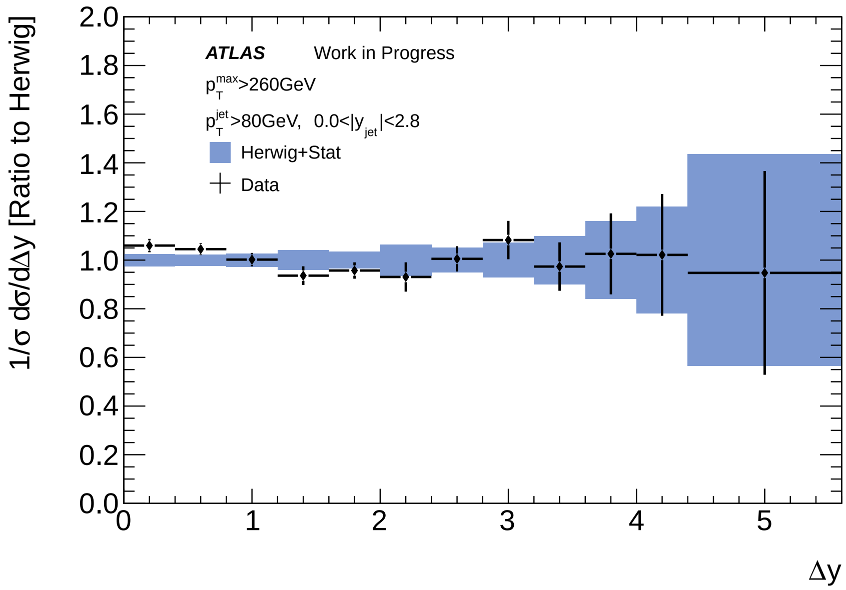

(d)

Figure 8.7: The closure test for data unfolded by Herwig for dy unfolding for $p_T^{\max}$ bins $110-160$ GeV, $160-210$ GeV, $210-260$ GeV, and > 260 GeV for each trigger selection.

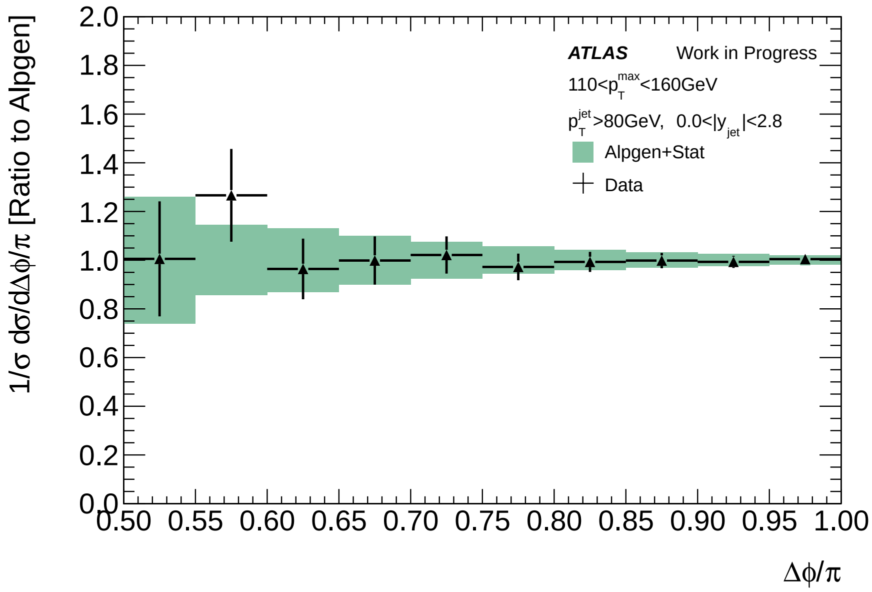
ATLAS Work in Progress
110<p_T^max<160GeV
p_T^jet>80GeV, 0.0<|y_jet|<2.8
Alpgen+Stat
Data
1/σ dσ/dΔϕ/π [Ratio to Alpgen]
Δϕ/π

(a)

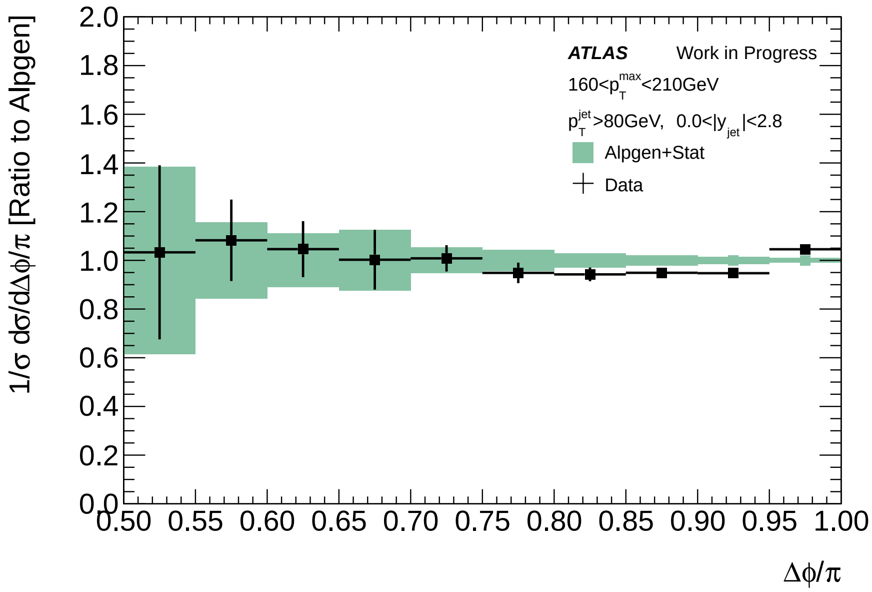
ATLAS Work in Progress
160<p_T^max<210GeV
p_T^jet>80GeV, 0.0<|y_jet|<2.8
Alpgen+Stat
Data
1/σ dσ/dΔϕ/π [Ratio to Alpgen]
Δϕ/π

(b)

Figure 8.8

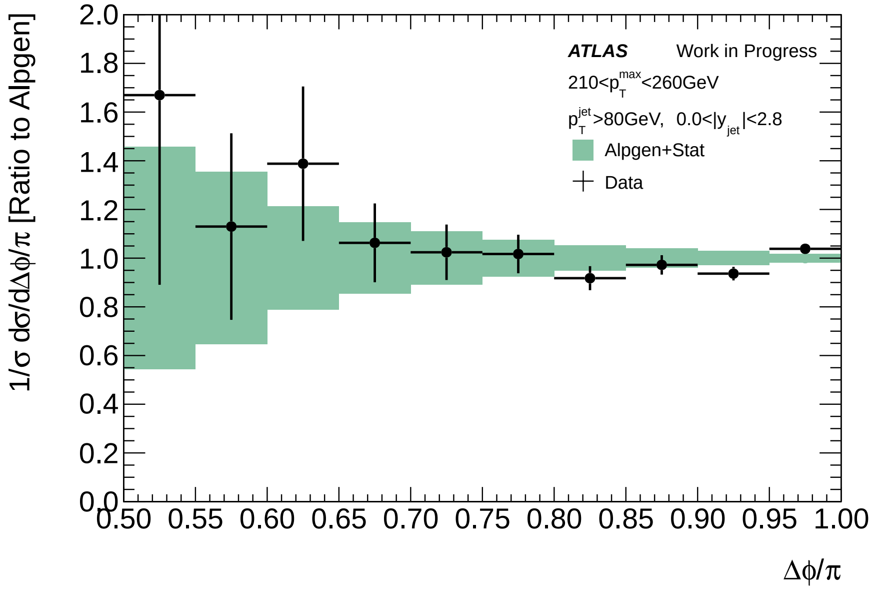

(c)

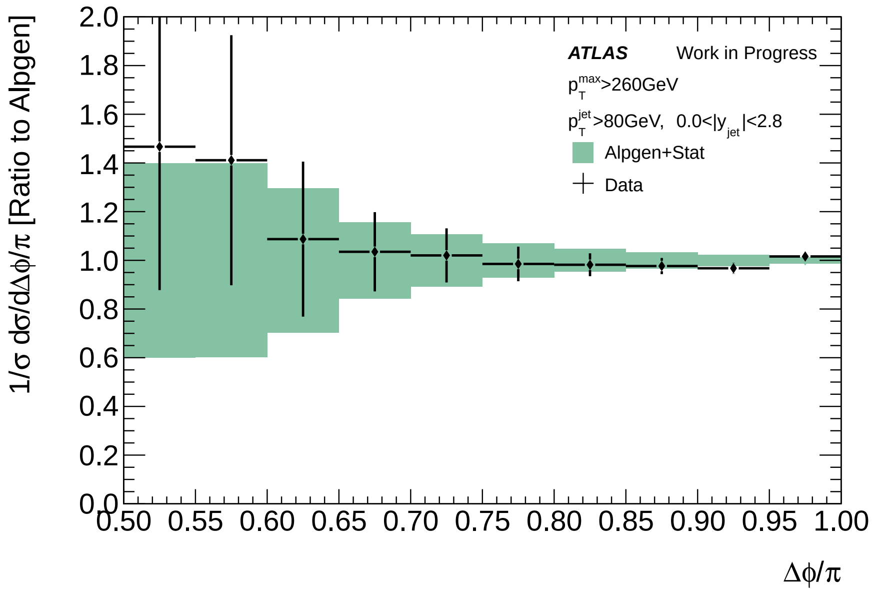

(d)

Figure 8.8: The closure test for data unfolded by Alpgen for dphi unfolding for $p_{\mathrm{T}}^{\max}$ bins $110-160$ GeV, $160-210$ GeV, $210-260$ GeV, and >260 GeV for each trigger selection.

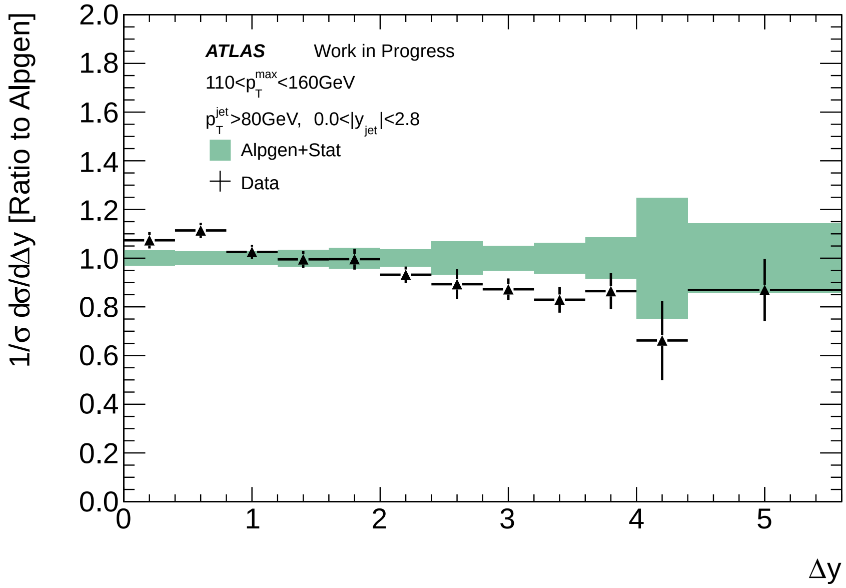
ATLAS Work in Progress
110<p_T^{max}<160GeV
p_T^{jet}>80GeV, 0.0<|y_{jet}|<2.8
Alpgen+Stat
Data
1/σ dσ/dΔy [Ratio to Alpgen]
Δy

(a)

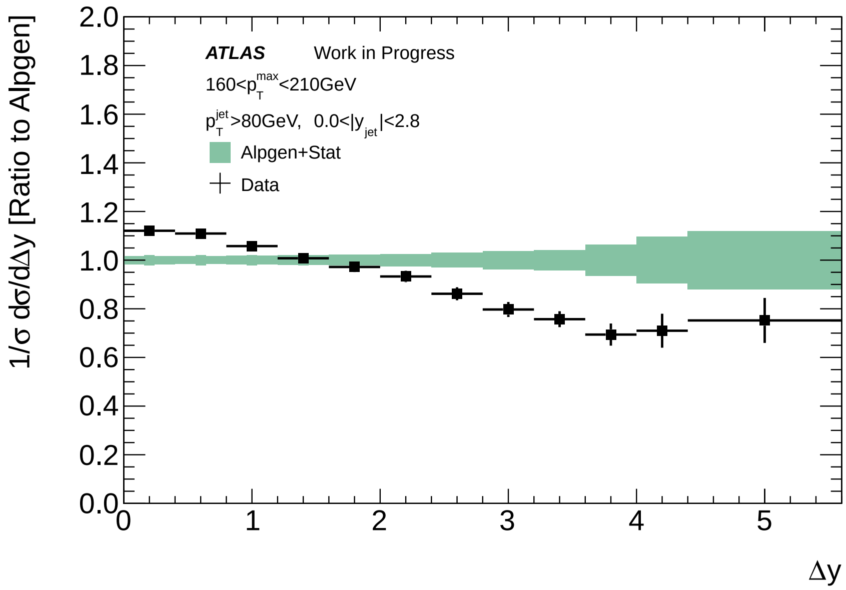
ATLAS Work in Progress
160<p_T^{max}<210GeV
p_T^{jet}>80GeV, 0.0<|y_{jet}|<2.8
Alpgen+Stat
Data
1/σ dσ/dΔy [Ratio to Alpgen]
Δy

(b)

Figure 8.9

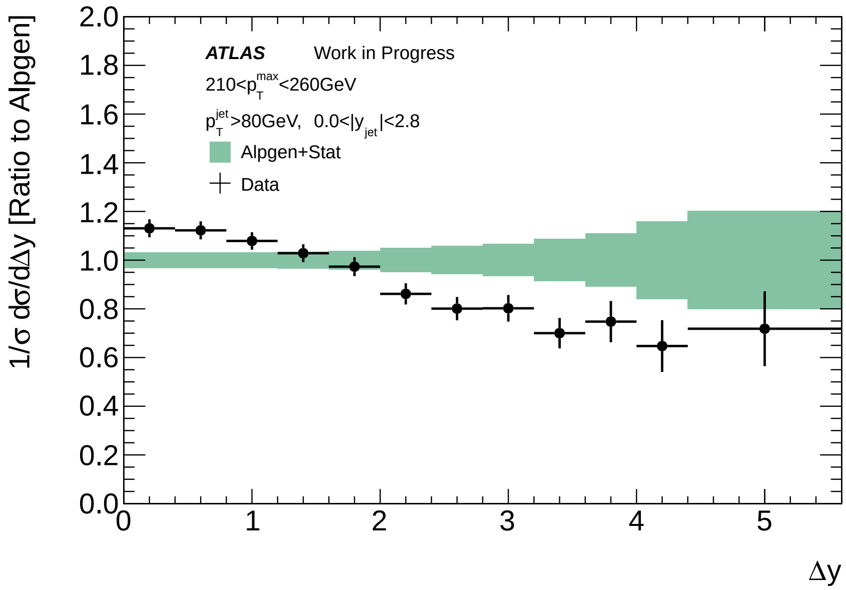

(c)

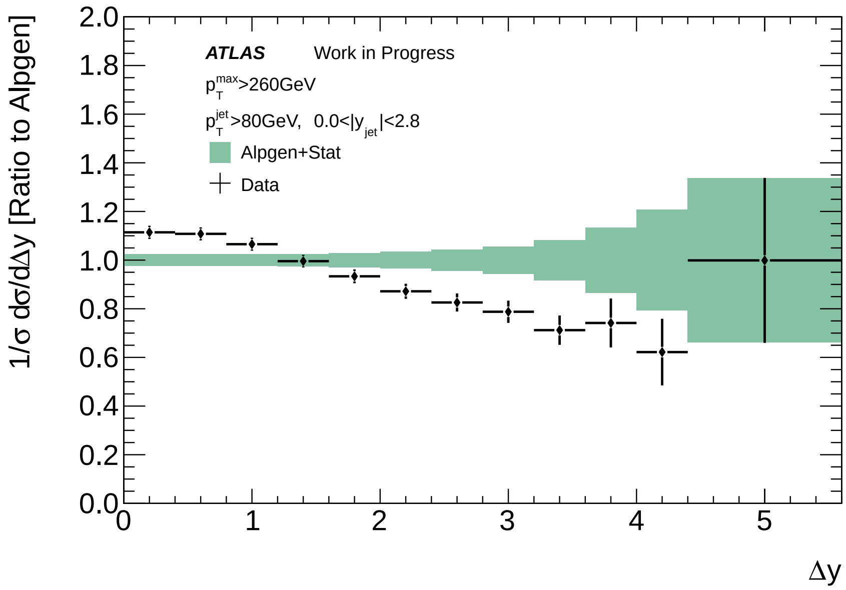

(d)

Figure 8.9: The closure test for data unfolded by Alpgen for Δy unfolding for $p_{\mathrm{T}}^{\mathrm{max}}$ bins $110-160$ GeV, $160-210$ GeV, $210-260$ GeV, and > 260 GeV for each trigger selection.

8.2 NLO Simulation

The NLO pQCD calculation is done using a fast simulation with NLO-Jet++ [65] interfaced to the PDFs [66] [67] with applgrid [58]. The CTEQ 6.6 [59] PDFs were used in this study. A sample of 100 million events were generated to produce a prediction for the $\Delta\phi$ distribution and 5 billion events for the Δy distribution. The scale uncertainty and PDF uncertainty are shown in the distributions in Figs. 8.10-8.11 .

The scale uncertainty is calculated by fluctuating the scale μ independently up and down by a factor of two. The PDF uncertainty is found by taking an envelope [68] of the distributions generated from the PDFs contained in the CTEQ6.6 package, of which there are 44. The normalization of the cross section is done separately for each p_T^{max} bins using NLOJet++ for two jets. The two-jet cross section is used for the normalization because the NLOJet++ for three jets has a divergence at π caused by the absence of resummation in the generator. There is a gap in the $\Delta\phi$ distribution at $0.60 > |\Delta\phi| > 0.65$ for $210 - 260$ GeV due to statistics so a fit is done to the distribution to interpolate the value for those bins and the scale uncertainty is interpolated as well. The unfolded data, using unfolding factors derived from PYTHIA, is in general agreement with NLOJet++ where two and three jets contribute most to the distribution and begins to rise above the NLOJet++ prediction where higher jet multiplicities contribute. This is to be expected as NLOJet++ is producing at most three partons in the final state. NLOJet++ is a DGLAP model and does not take into account BFKL in its modeling. A BKFL-based NLO calculation is being done with HEJ [69] but is not part of this report.

The Δy cross section normalization is done using the cross section for NLO-Jet++ for three jets as there is no divergence in Δy over the range of interest. Almost ten times as many events were produced in Δy in an attempt to populate the full range of the distributions. The NLOJet++ points follow the data closely; however, the scale uncertainty is too large to conclude anything. PDF uncertainties are shown only, see Figs. 8.12-8.13. In regions of low statistics, extremely large and non-physical spikes developed in the calculations which would effect the cross section normalization. When possible, the spikes were removed by setting the bin equal to the average of the values of the two bins above and below the spike. When the spike is too broad, the bins in the spike were set to zero. This is done for the tail of the $110 - 160$ GeV and $210 - 260$ GeV bins.

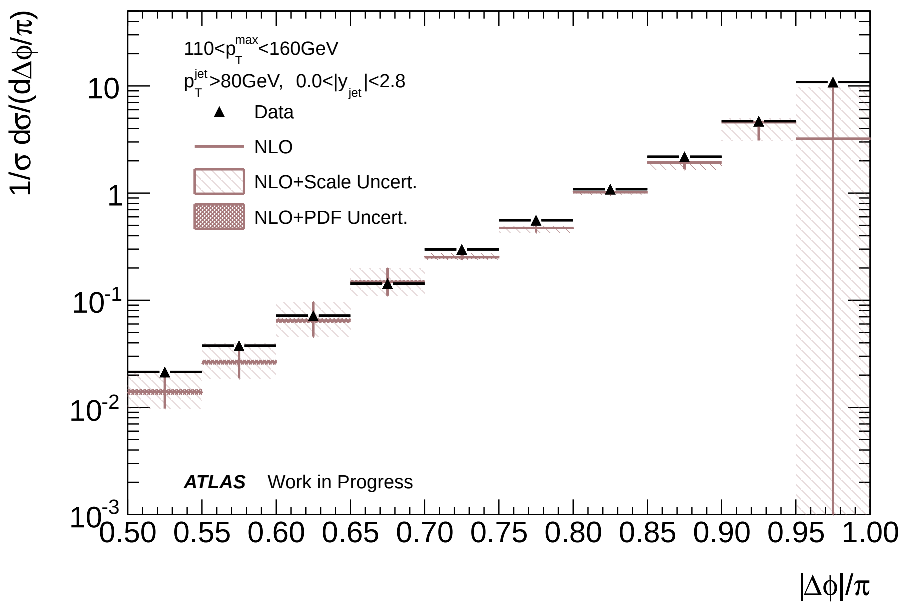

(a)

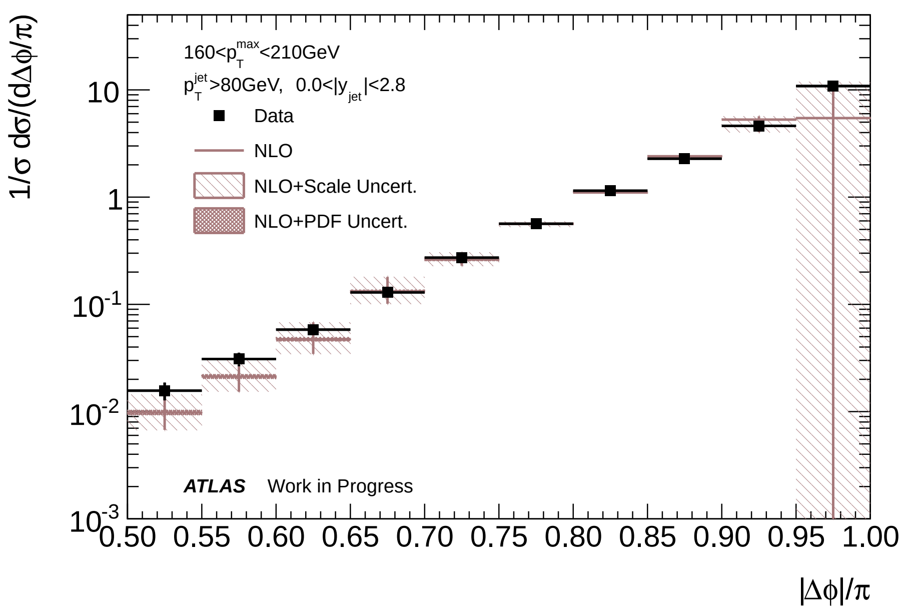

(b)

Figure 8.10

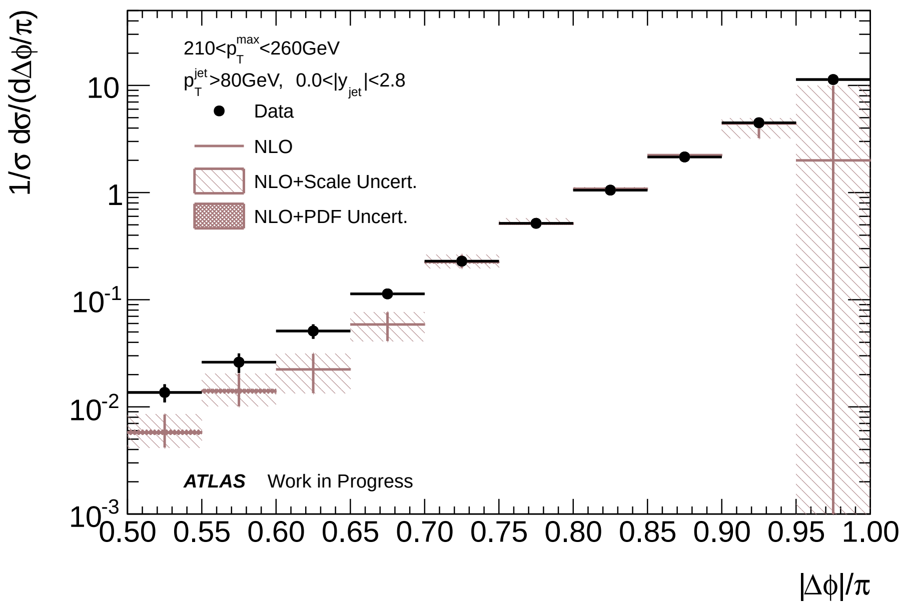

(c)

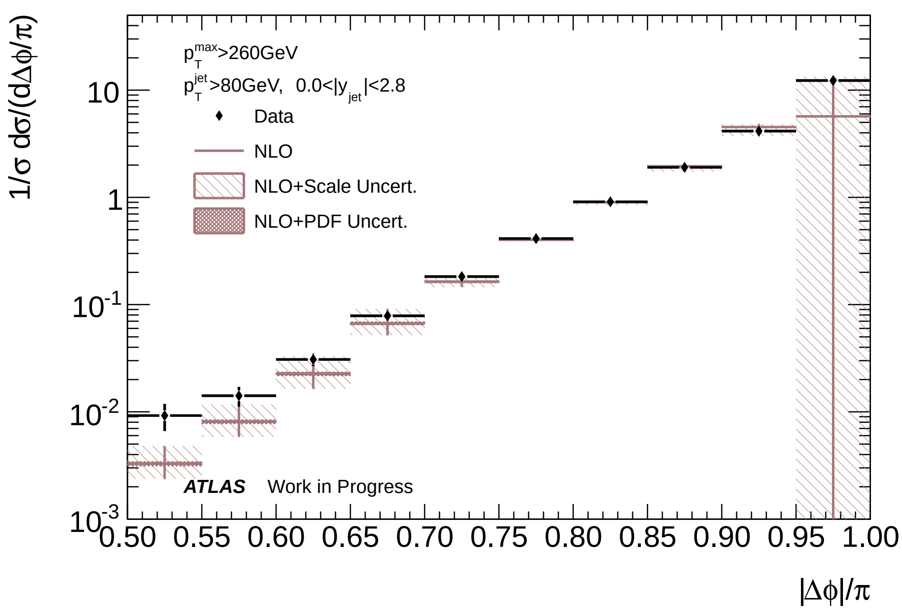

(d)

Figure 8.10: The closure test for Δy unfolding for $p_{\mathrm{T}}^{\mathrm{max}}$ bins $110 - 160$ GeV, $160 - 210$ GeV, $210 - 260$ GeV, and > 260 GeV for each trigger selection.

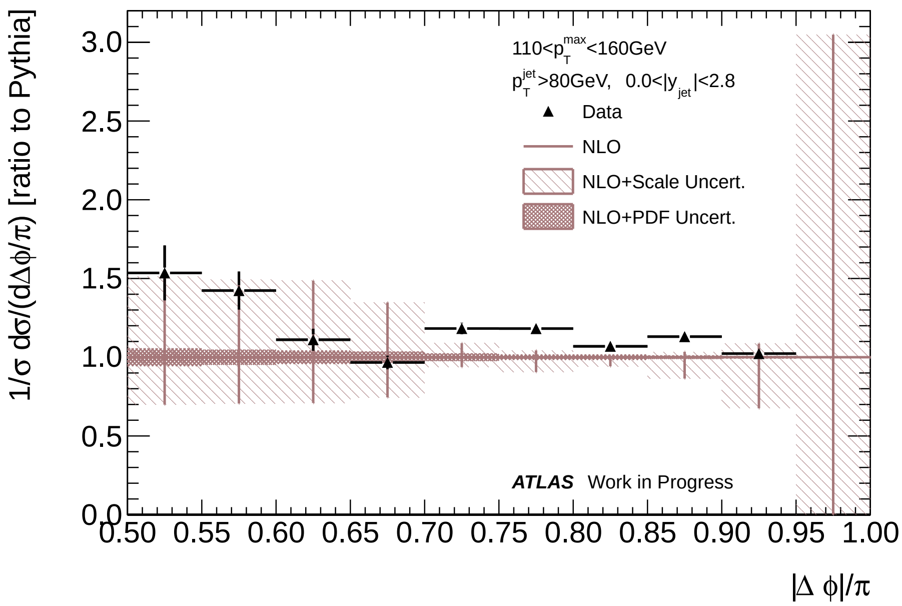

(a)

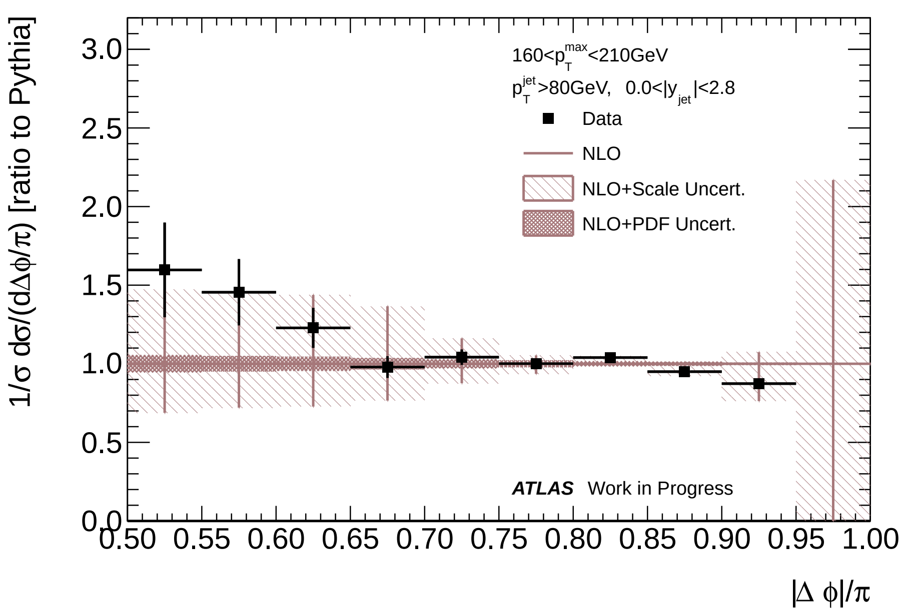

(b)

Figure 8.11

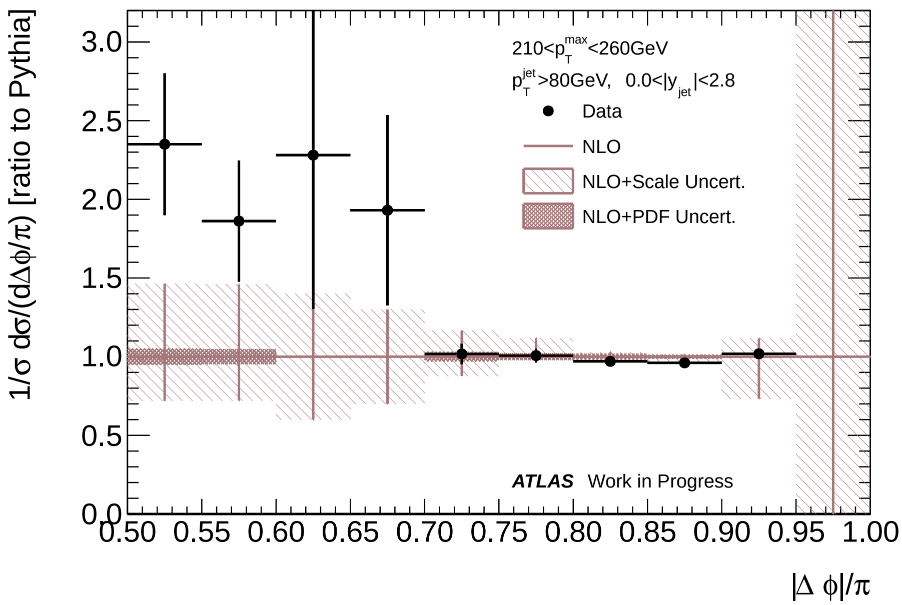

(c)

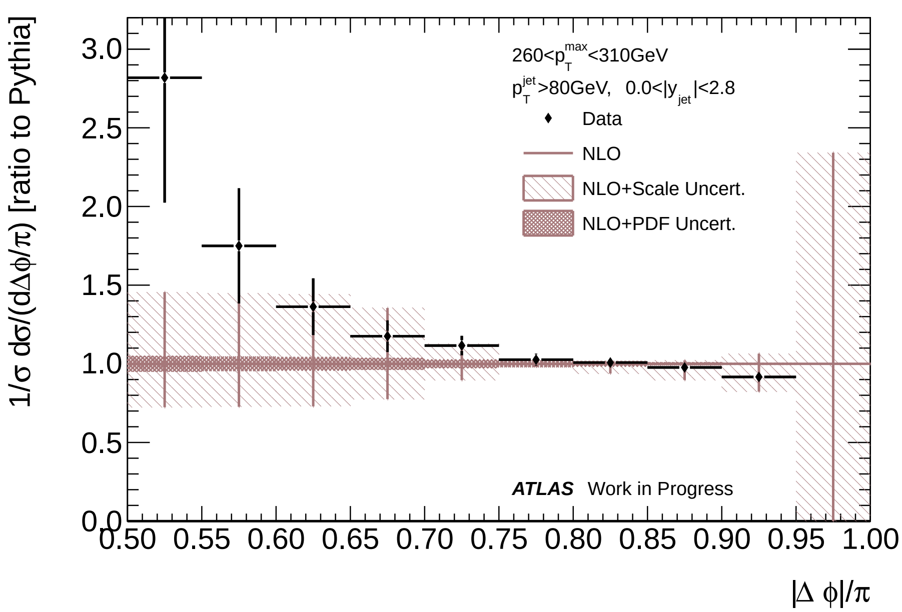

(d)

Figure 8.11: The closure test for Δy unfolding for $p_{\mathrm{T}}^{\mathrm{max}}$ bins $110 - 160$ GeV, $160 - 210$ GeV, $210 - 260$ GeV, and > 260 GeV for each trigger selection.

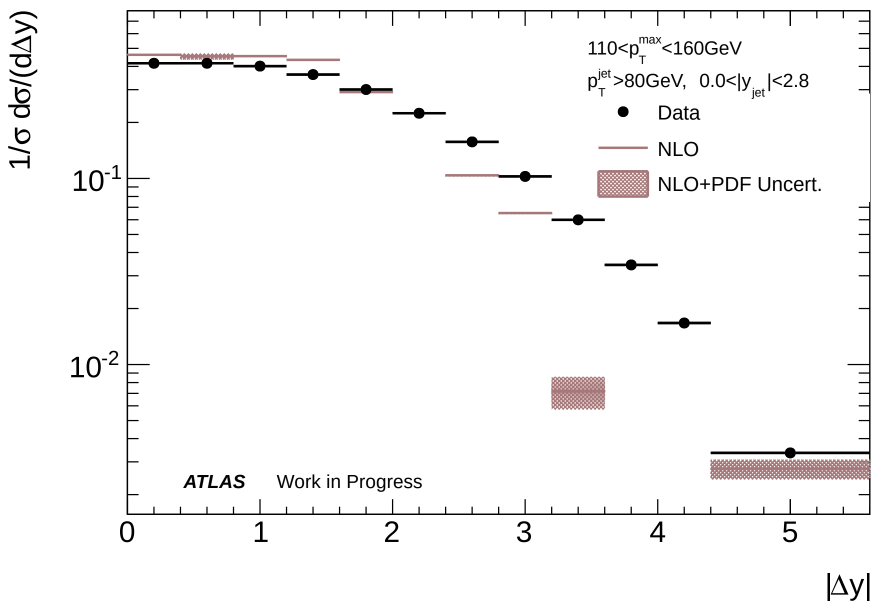

(a)

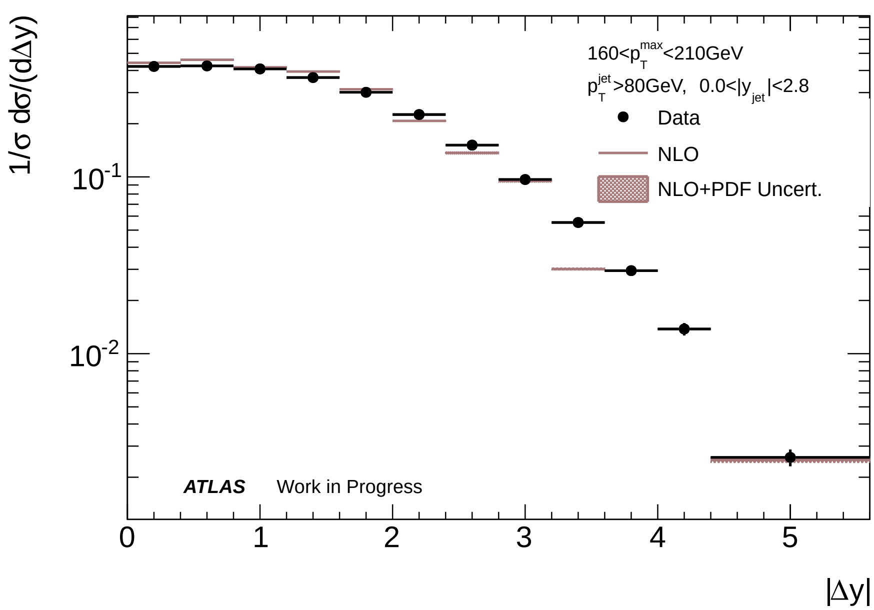

(b)

Figure 8.12

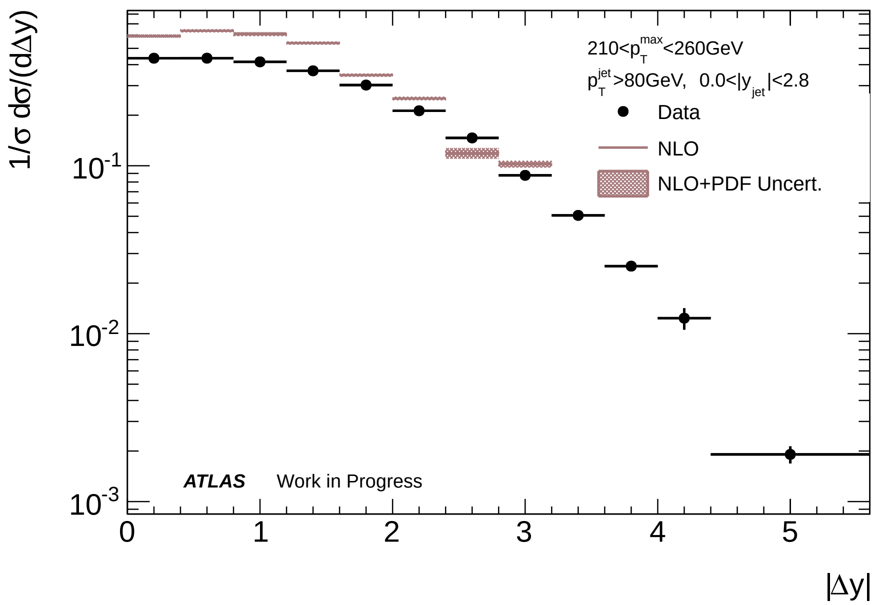

(c)

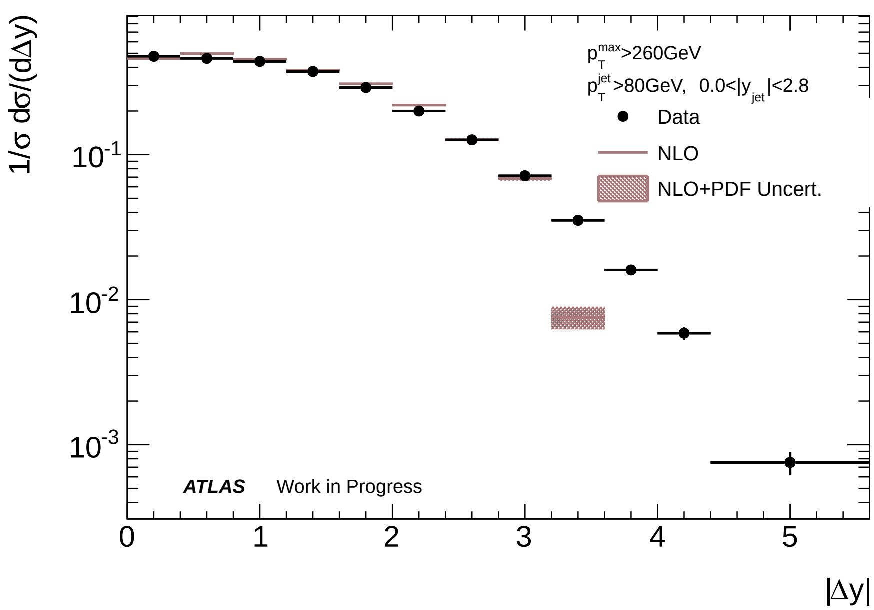

(d)

Figure 8.12: The closure test for Δy unfolding for $p_{\mathrm{T}}^{\mathrm{max}}$ bins $110-160$ GeV, $160-210$ GeV, $210-260$ GeV, and >260 GeV for each trigger selection.

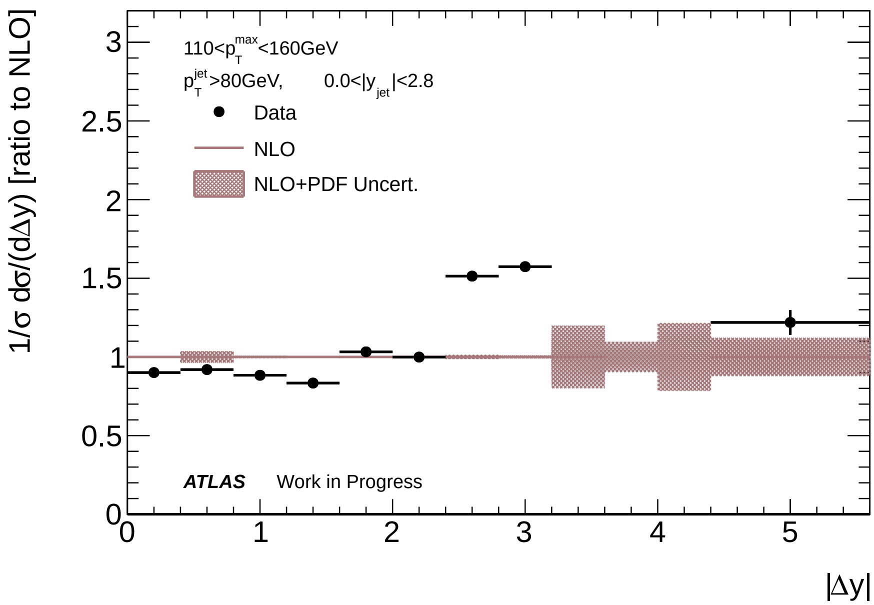

(a)

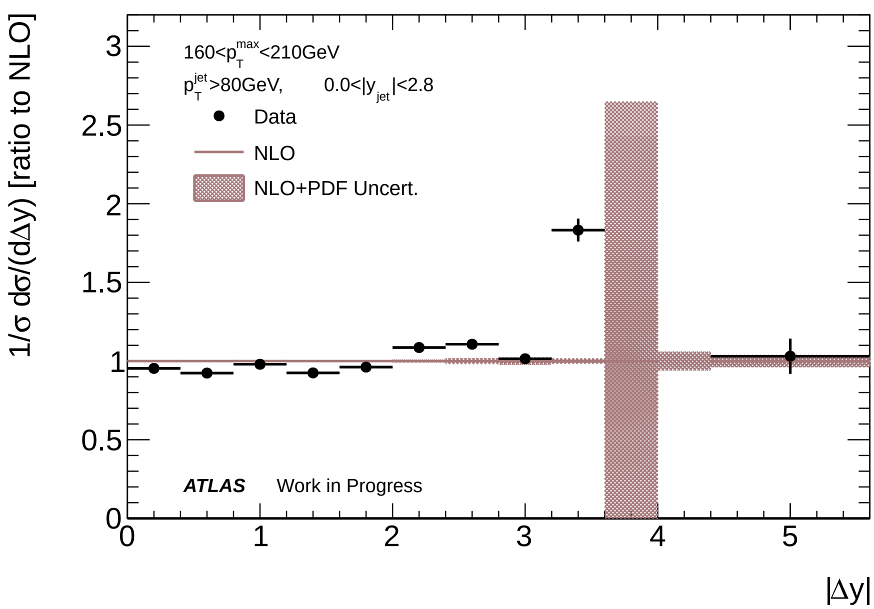

(b)

Figure 8.13

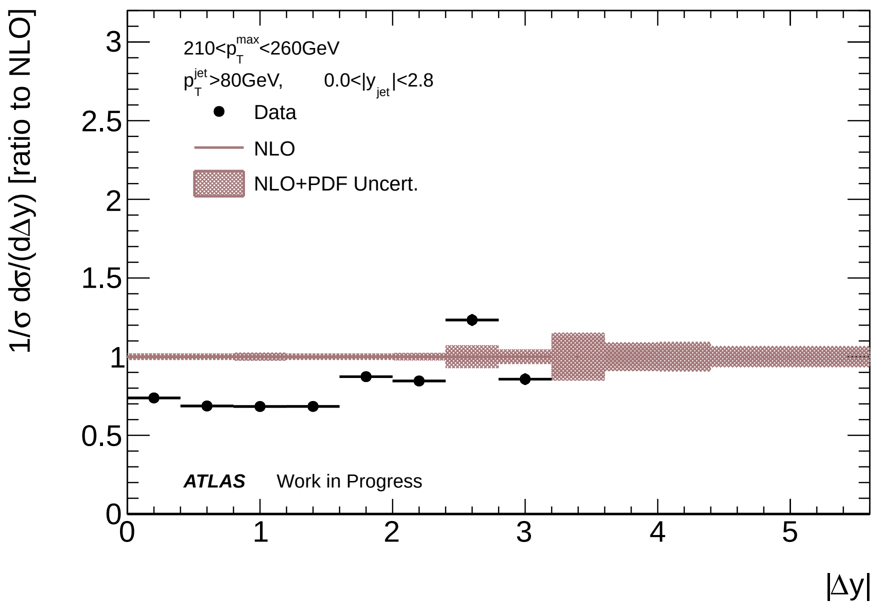

(c)

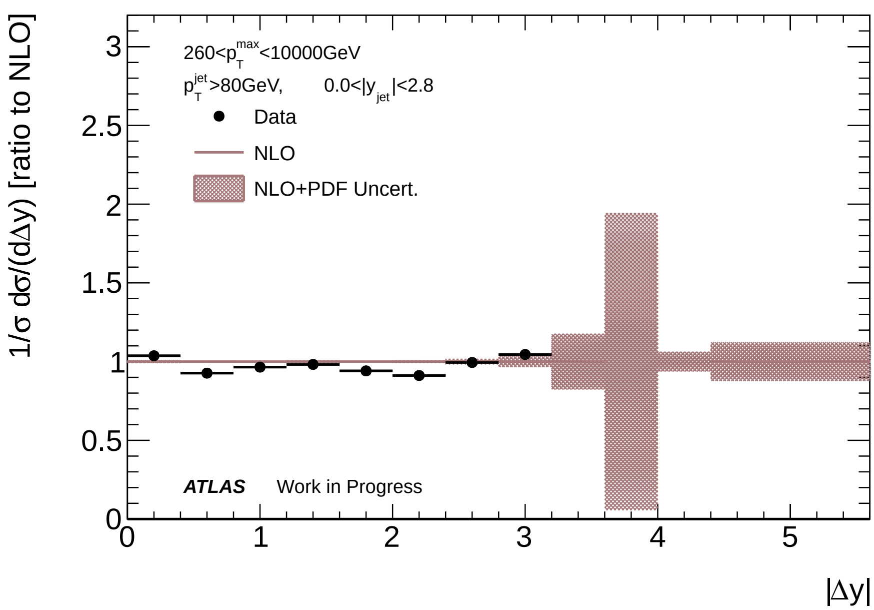

(d)

Figure 8.13: The closure test for Δy unfolding for $p_{\mathrm{T}}^{\mathrm{max}}$ bins $110 - 160$ GeV, $160 - 210$ GeV, $210 - 260$ GeV, and > 260 GeV for each trigger selection.

Chapter 9

Conclusions

The $\Delta\phi$ and Δy distributions for the two leading p_T jets are formed with the full 2010 data set with the LHC pp collision program using at $\sqrt{(s)} = 7$ TeV and $\int \mathcal{L} dt = (36 \pm 4)\,\mathrm{pb}^{-1}$. Events were selected with the two leading jets are within $|y| < 2.8$ and $p_T > 80$ GeV. The distributions are formed several event samples selected according to the p_T of the leading jet in the event.

PYTHIA is used to derive the unfolding factors to correct for effects of experimental resolutions in ϕ and y, and for the effects from jet energy scale and resolution. Unfolding using PYTHIA takes data to the particle-level. There is good agreement between PYTHIA and data. The unfolding was also done with the HERWIG and ALPGEN Monte Carlos. The data unfolded with the PYTHIA Monte Carlo is also compared to the NLO calculation produced with NLOJet++. All show good agreement with data.

Of the Monte Carlo generators used in the comparison, HERWIG showed the best agreement with data for the Δy distribution and ALPGEN showed the best agreement with data for the $\Delta\phi$ distribution. PYTHIA Monte Carlo did not provide the best agreement out of the three generators for either the $\Delta\phi$ distribution nor the Δy distribution; however, PYTHIA did provide consistently good agreement for both distributions. The comparison of performance between PYTHIA and the other two generators in this study, HERWIG and ALPGEN, can be used to tune PYTHIA to better model data for use in future studies.

The NLO calculation for $\Delta\phi$ distribution is populated well enough such that the scale uncertainty and PDF uncertainty are small enough to show definitively good agreement between data and NLOJet++. The Δy distribution has low statistics even with fifty times more events produced than for the $\Delta\phi$ distribution. There seems to be good agreement; however, the uncertainties are too large to draw any definite conclusions. NLOJet++ uses

DGLAP evolution to do the NLO calculation; it does not take into account the BFKL evolution model. The unfolded data shows very good agreement with the NLOJet++ NLO calculation, indicating good agreement with predictions from DGLAP evolution.

This study is an update of several previous studies [45] [46] [43] [44] with higher center-of-mass energies, more integrated luminosity, larger region of rapidity acceptance, and higher p_T^{max} bins. The measurement is extended to include the region $|y| < 2.8$ and studies both the Δy distribution and $\Delta\phi$ distribution.

Bibliography

[1] O. S. Brning et al. 2004. CERN-2004-003-V-1.

[2] O. S. Brning et al. 2004. CERN-2004-003-V-2.

[3] M. Benedikt et al. 2004. CERN-2004-003-V-1.

[4] ATLAS Collaboration. 1999. CERN-LHCC-99-14.

[5] ATLAS Collaboration. 1999. CERN-LHCC-99-15.

[6] CMS Collaboration, G. L. Bayatian et al. 2006. CERN-LHCC-2006-001.

[7] CMS Collaboration, G. L. Bayatian et al. J. Phys. G **34** (2006) 995.

[8] LHCb Collaboration, R. Antunes-Nobrega et al. 2003. CERN-LHCC-2003-030.

[9] ALICE Collaboration, F. Carminati et al. J. Phys. G **30** (2004) 1517.

[10] ALICE Collaboration, B. Alessandro et al. J. Phys. G **32** (2006) 1295.

[11] ATLAS Collaboration, G. Aad et al. JINST **3** (2008) S08003.

[12] ATLAS Collaboration. 1997. CERN-LHCC-97-17.

[13] ATLAS Collaboration. 1997. CERN-LHCC-97-16.

[14] ATLAS Collaboration. 1996. CERN-LHCC-96-41.

[15] A. P. Society and A. I. of Physics, *Physical Review D, Particles and Fields, Part I: Review of Particle Physics*, vol. 66. 2002.

[16] ATLAS Collaboration. 1997. CERN-LHCC-9722.

[17] ATLAS Collaboration. 1998. ATLAS-TDR12.

[18] D. Griffiths, *Introduction to Elementary Particles*. 2 ed., 2008.

[19] F. Halzen and A. Martin, *Quarks and Leptons: An Introductory Course in Modern Particle Physics*. 1984.

[20] H. Georgi and S. L. Glashow Phys. Rev. Lett. **32** (1974) 438.

[21] A. J. Buras, J. Ellis, M. K. Gaillard, and D. V. Nanopoulos Nucl. Phys. **B135** (1978) 66–92.

[22] E. Witten Nucl. Phys. **B258** (1985) 75.

[23] M. Dine et al. Nucl. Phys. **B549** (1985) 549.

[24] V. N. Gribov and L. Lipatov Phys. Lett. B **37** (1971) 78.

[25] C. Quigg, *Gauge theories of the strong, weak, and electromagnetic interactions*. 1997.

[26] M. Srednicki, *Quantum Field Theory*, .

[27] W. A. Bardeen, H. Fritzch, and M. Gell-Mann, *Light-Cone Algebra,* π^0 *Decay and* e^+ e^- *Annihilation*, CERN preprint (1972) .

[28] R. K. Ellis, S. W. J., and B. R. Webber, *QCD and Collider Physics*. 8 ed., 1996.

[29] R. K. Ellis, *Proceedings of the 1987 Theoretical Advanced Study Institute in Elementary Particle Physics*, . The Santa Fe TASI, Jul 5 - 1 Aug 1987, Santa Fe, N. Mex.

[30] A. Martin, R. G. Roberts, W. Stirling, and R. Thorne Eur. Phys. J. **C4** (1998) 463.

[31] L. N. Lipatov Sov. J. Nucl. Phys. **20** (1975) 94.

[32] Y. Dokshitzer Sov. Phys. JETP **46** (1977) 641.

[33] G. Altarelli and G. Parisi Nucl. Phys. **B126** (1977) 298.

[34] F. A. Berends Phys. Lett. B **103** (1981) 124.

[35] E. A. Kuraev, L. N. Lipatov, and V. S. Fadin Sov. Phys. JETP **45** (1977) 199.

[36] I. I. Balitsky and L. N. Lipatov Sov. J. Nucl. Phys. **28** (1978) 822.

[37] DØ Collaboration, B. Abnott et al. Phys. Rev. Lett. **84** (2000) 5722.

[38] L. H. Orr and W. Stirling Phys. Lett. B **436** (1998) 372.

[39] L. H. Orr and W. Stirling Phys. Rev. D **56** (1997) 5875.

[40] V. S. Fadin and L. N. Lipatov Phys. Lett. **B429** (1998) 127.

[41] M. Ciafaloni and G. Camici Phys. Lett. **B430** (1998) 349.

[42] E. J. Weniger Numerical Algorithms **33** (2003) 499.

[43] ATLAS Collaboration, G. Aad et al. Phys. Rev. Lett. **106** (2011) 172002.

[44] ATLAS Collaboration, G. Aad et al. JHEP **09** (2011) 001.

[45] DØ Collaboration, V. M. Abazov et al. Phys. Rev. Lett. **94** (2005) 221801.

[46] CMS Collaboration, V. Khachatryan et al. Phys. Rev. Lett. **106** (2011) 122003.

[47] M. Cacciari, G. P. Salam, and G. Soyez JHEP **04** (2008) 063.

[48] ATLAS Collaboration ATLAS-CONF-2011-047, March 2011.

[49] ATLAS Collaboration ATL-CONF-2010-060, July 2010.

[50] M. Baak et al. ATL-COM-GEN-2009-015, Mar 2009.

[51] ATLAS Collaboration, G. Aad et al. ATLAS-CONF-2010-094, September 2010.

[52] ATLAS Collaboration ATLAS-PHYS-INT-2011-017, March 2011.

[53] S. Agostinelli et al. Nucl. Instr. and Meth. **A506** (2003) 250.

[54] T. Sjostrand, S. Mrenna, and P. Skands JHEP **05** (2006) 026.

[55] G. Corcella et al. `arXiv:hep-ph/0210213`.

[56] J. M. Butterworth et al. Z. Phys. **C72** (1996) 637.

[57] M. L. Mangano et al. JHEP **07** (2003) 001.

[58] T. Carli et al. Eur. Phys. J. **C66** (2010) 503.

[59] P. M. Nadolsky et al. Phys. Rev. **D78** (2008) 013004.

[60] ATLAS Collaboration ATLAS-CONF-2011-032, March 2011.

[61] M. Baak, M. Petteni, and N. Makovec ATLAS-COM-CONF-2010-038, May 2010.

[62] T. Carli et al., *Jet cleaning and efficiencies Rel. 16*, Jet/ETMiss Meeting P and P Week, February 2011.

[63] ATLAS Collaboration ATLAS-COM-CONF-2010-056, July 2010.

[64] R. Field, *Multiple Parton Interactions and the Underlying Event*, MPI and UE - DESY, May 2007.

[65] Z. Nagy Phys. Rev. Lett. **88** (2002) 122003.

[66] A. Martin, W. Stirling, R. Thorne, and G. Watt Eur. Phys. J. **C63** (2009) 189.

[67] R. D. Ball et al. Nucl. Phys. **B838** (2010) 136.

[68] S. Alekhin et al. `arXiv:hep-ph/1101.0536v1`.

[69] J. Andersen and J. Smillie JHEP **06** (2011) 001.

Appendices

Appendix A

Data Samples

The data used in this analysis is from the LHC 2010 proton-proton collision campaign which ran from April 2010 through the end of October 2010. The data used are from runs 152166-167844 during data taking periods A-I, see Tab. A.1 for inclusive list of samples for each run by period. The integrated luminosity during this data taking period was $\int \mathcal{L} dt = (36 \pm 4)\,\mathrm{pb}^{-1}$.

Table A.1: Samples used for data collected during the 2010 run at 7TeV.

Period	Sample
A	data10_7TeV.00152166.physics_L1Calo.merge.NTUP_JETMET.r1647_p306_p417
	data10_7TeV.00152214.physics_L1Calo.merge.NTUP_JETMET.r1647_p306_p417
	data10_7TeV.00152220.physics_L1Calo.merge.NTUP_JETMET.r1647_p306_p417
	data10_7TeV.00152221.physics_L1Calo.merge.NTUP_JETMET.r1647_p306_p417
	data10_7TeV.00152345.physics_L1Calo.merge.NTUP_JETMET.r1647_p306_p417
	data10_7TeV.00152409.physics_L1Calo.merge.NTUP_JETMET.r1647_p306_p417
	data10_7TeV.00152441.physics_L1Calo.merge.NTUP_JETMET.r1647_p306_p417
	data10_7TeV.00152508.physics_L1Calo.merge.NTUP_JETMET.r1647_p306_p417
	data10_7TeV.00152777.physics_L1Calo.merge.NTUP_JETMET.r1647_p306_p417
	data10_7TeV.00152844.physics_L1Calo.merge.NTUP_JETMET.r1647_p306_p417
	data10_7TeV.00152845.physics_L1Calo.merge.NTUP_JETMET.r1647_p306_p417
	data10_7TeV.00152878.physics_L1Calo.merge.NTUP_JETMET.r1647_p306_p417
	data10_7TeV.00152933.physics_L1Calo.merge.NTUP_JETMET.r1647_p306_p417
	data10_7TeV.00152994.physics_L1Calo.merge.NTUP_JETMET.r1647_p306_p417
	data10_7TeV.00153030.physics_L1Calo.merge.NTUP_JETMET.r1647_p306_p417
	data10_7TeV.00153134.physics_L1Calo.merge.NTUP_JETMET.r1647_p306_p417
	data10_7TeV.00153136.physics_L1Calo.merge.NTUP_JETMET.r1647_p306_p417
	data10_7TeV.00153159.physics_L1Calo.merge.NTUP_JETMET.r1647_p306_p417
	data10_7TeV.00153200.physics_L1Calo.merge.NTUP_JETMET.r1647_p306_p417
B	data10_7TeV.00153565.physics_L1Calo.merge.NTUP_JETMET.r1647_p306_p417
	data10_7TeV.00153599.physics_L1Calo.merge.NTUP_JETMET.r1647_p306_p417
	data10_7TeV.00154810.physics_L1Calo.merge.NTUP_JETMET.r1647_p306_p417
	data10_7TeV.00154813.physics_L1Calo.merge.NTUP_JETMET.r1647_p306_p417
	data10_7TeV.00154815.physics_L1Calo.merge.NTUP_JETMET.r1647_p306_p417
	data10_7TeV.00154817.physics_L1Calo.merge.NTUP_JETMET.r1647_p306_p417
	data10_7TeV.00154822.physics_L1Calo.merge.NTUP_JETMET.r1647_p306_p417
	data10_7TeV.00155073.physics_L1Calo.merge.NTUP_JETMET.r1647_p306_p417
	data10_7TeV.00155112.physics_L1Calo.merge.NTUP_JETMET.r1647_p306_p417
	data10_7TeV.00155116.physics_L1Calo.merge.NTUP_JETMET.r1647_p306_p417
	data10_7TeV.00155118.physics_L1Calo.merge.NTUP_JETMET.r1647_p306_p417

continued on next page.

Period	Sample
	data10_7TeV.00155160.physics_L1Calo.merge.NTUP_JETMET.r1647_p306_p417
C	data10_7TeV.00155228.physics_L1Calo.merge.NTUP_JETMET.r1647_p306_p417
	data10_7TeV.00155280.physics_L1Calo.merge.NTUP_JETMET.r1647_p306_p417
	data10_7TeV.00155569.physics_L1Calo.merge.NTUP_JETMET.r1647_p306_p417
	data10_7TeV.00155634.physics_L1Calo.merge.NTUP_JETMET.r1647_p306_p417
	data10_7TeV.00155669.physics_L1Calo.merge.NTUP_JETMET.r1647_p306_p417
	data10_7TeV.00155678.physics_L1Calo.merge.NTUP_JETMET.r1647_p306_p417
	data10_7TeV.00155697.physics_L1Calo.merge.NTUP_JETMET.r1647_p306_p417
	data10_7TeV.00156682.physics_L1Calo.merge.NTUP_JETMET.r1647_p306_p417
D	data10_7TeV.00158045.physics_L1Calo.merge.NTUP_JETMET.r1647_p306_p417
	data10_7TeV.00158116.physics_L1Calo.merge.NTUP_JETMET.r1647_p306_p417
	data10_7TeV.00158269.physics_L1Calo.merge.NTUP_JETMET.r1647_p306_p417
	data10_7TeV.00158299.physics_L1Calo.merge.NTUP_JETMET.r1647_p306_p417
	data10_7TeV.00158392.physics_L1Calo.merge.NTUP_JETMET.r1647_p306_p417
	data10_7TeV.00158443.physics_L1Calo.merge.NTUP_JETMET.r1647_p306_p417
	data10_7TeV.00158466.physics_L1Calo.merge.NTUP_JETMET.r1647_p306_p417
	data10_7TeV.00158545.physics_L1Calo.merge.NTUP_JETMET.r1647_p306_p417
	data10_7TeV.00158548.physics_L1Calo.merge.NTUP_JETMET.r1647_p306_p417
	data10_7TeV.00158549.physics_L1Calo.merge.NTUP_JETMET.r1647_p306_p417
	data10_7TeV.00158582.physics_L1Calo.merge.NTUP_JETMET.r1647_p306_p417
	data10_7TeV.00158632.physics_L1Calo.merge.NTUP_JETMET.r1647_p306_p417
	data10_7TeV.00158801.physics_L1Calo.merge.NTUP_JETMET.r1647_p306_p417
	data10_7TeV.00158975.physics_L1Calo.merge.NTUP_JETMET.r1647_p306_p417
	data10_7TeV.00159041.physics_L1Calo.merge.NTUP_JETMET.r1647_p306_p417
	data10_7TeV.00159086.physics_L1Calo.merge.NTUP_JETMET.r1647_p306_p417
	data10_7TeV.00159113.physics_L1Calo.merge.NTUP_JETMET.r1647_p306_p417
	data10_7TeV.00159179.physics_L1Calo.merge.NTUP_JETMET.r1647_p306_p417
	data10_7TeV.00159179.physics_L1Calo.merge.NTUP_JETMET.r1647_p306_p417
	data10_7TeV.00159202.physics_L1Calo.merge.NTUP_JETMET.r1647_p306_p417
	data10_7TeV.00159203.physics_L1Calo.merge.NTUP_JETMET.r1647_p306_p417
	data10_7TeV.00159224.physics_L1Calo.merge.NTUP_JETMET.r1647_p306_p417
E	data10_7TeV.00160387.physics_JetTauEtmiss.merge.NTUP_JETMET.r1647_p306_p417
	data10_7TeV.00160472.physics_JetTauEtmiss.merge.NTUP_JETMET.r1647_p306_p417
	data10_7TeV.00160479.physics_JetTauEtmiss.merge.NTUP_JETMET.r1647_p306_p417
	data10_7TeV.00160530.physics_JetTauEtmiss.merge.NTUP_JETMET.r1647_p306_p417
	data10_7TeV.00160613.physics_JetTauEtmiss.merge.NTUP_JETMET.r1647_p306_p417
	data10_7TeV.00160736.physics_JetTauEtmiss.merge.NTUP_JETMET.r1647_p306_p417
	data10_7TeV.00160800.physics_JetTauEtmiss.merge.NTUP_JETMET.r1647_p306_p417
	data10_7TeV.00160801.physics_JetTauEtmiss.merge.NTUP_JETMET.r1647_p306_p417
	data10_7TeV.00160879.physics_JetTauEtmiss.merge.NTUP_JETMET.r1647_p306_p417
	data10_7TeV.00160899.physics_JetTauEtmiss.merge.NTUP_JETMET.r1647_p306_p417
	data10_7TeV.00160953.physics_JetTauEtmiss.merge.NTUP_JETMET.r1647_p306_p417
	data10_7TeV.00160954.physics_JetTauEtmiss.merge.NTUP_JETMET.r1647_p306_p417
	data10_7TeV.00160958.physics_JetTauEtmiss.merge.NTUP_JETMET.r1647_p306_p417
	data10_7TeV.00160963.physics_JetTauEtmiss.merge.NTUP_JETMET.r1647_p306_p417
	data10_7TeV.00160975.physics_JetTauEtmiss.merge.NTUP_JETMET.r1647_p306_p417
	data10_7TeV.00160980.physics_JetTauEtmiss.merge.NTUP_JETMET.r1647_p306_p417
	data10_7TeV.00161118.physics_JetTauEtmiss.merge.NTUP_JETMET.r1647_p306_p417
	data10_7TeV.00161379.physics_JetTauEtmiss.merge.NTUP_JETMET.r1647_p306_p417
	data10_7TeV.00161407.physics_JetTauEtmiss.merge.NTUP_JETMET.r1647_p306_p417
	data10_7TeV.00161520.physics_JetTauEtmiss.merge.NTUP_JETMET.r1647_p306_p417
	data10_7TeV.00161562.physics_JetTauEtmiss.merge.NTUP_JETMET.r1647_p306_p417
	data10_7TeV.00161948.physics_JetTauEtmiss.merge.NTUP_JETMET.r1647_p306_p417
F	data10_7TeV.00162347.physics_JetTauEtmiss.merge.NTUP_JETMET.r1647_p306_p417
	data10_7TeV.00162526.physics_JetTauEtmiss.merge.NTUP_JETMET.r1647_p306_p417
	data10_7TeV.00162576.physics_JetTauEtmiss.merge.NTUP_JETMET.r1647_p306_p417
	data10_7TeV.00162577.physics_JetTauEtmiss.merge.NTUP_JETMET.r1647_p306_p417
	data10_7TeV.00162620.physics_JetTauEtmiss.merge.NTUP_JETMET.r1647_p306_p417

continued on next page.

Period	Sample
	data10_7TeV.00162623.physics_JetTauEtmiss.merge.NTUP_JETMET.r1647_p306_p417
	data10_7TeV.00162690.physics_JetTauEtmiss.merge.NTUP_JETMET.r1647_p306_p417
	data10_7TeV.00162764.physics_JetTauEtmiss.merge.NTUP_JETMET.r1647_p306_p417
	data10_7TeV.00162843.physics_JetTauEtmiss.merge.NTUP_JETMET.r1647_p306_p417
	data10_7TeV.00162882.physics_JetTauEtmiss.merge.NTUP_JETMET.r1647_p306_p417
G	data10_7TeV.00165591.physics_JetTauEtmiss.merge.NTUP_JETMET.r1647_p306_p417
	data10_7TeV.00165632.physics_JetTauEtmiss.merge.NTUP_JETMET.r1647_p306_p417
	data10_7TeV.00165703.physics_JetTauEtmiss.merge.NTUP_JETMET.r1647_p306_p417
	data10_7TeV.00165732.physics_JetTauEtmiss.merge.NTUP_JETMET.r1647_p306_p417
	data10_7TeV.00165767.physics_JetTauEtmiss.merge.NTUP_JETMET.r1647_p306_p417
	data10_7TeV.00165815.physics_JetTauEtmiss.merge.NTUP_JETMET.r1647_p306_p417
	data10_7TeV.00165817.physics_JetTauEtmiss.merge.NTUP_JETMET.r1647_p306_p417
	data10_7TeV.00165818.physics_JetTauEtmiss.merge.NTUP_JETMET.r1647_p306_p417
	data10_7TeV.00165821.physics_JetTauEtmiss.merge.NTUP_JETMET.r1647_p306_p417
	data10_7TeV.00165954.physics_JetTauEtmiss.merge.NTUP_JETMET.r1647_p306_p417
	data10_7TeV.00165956.physics_JetTauEtmiss.merge.NTUP_JETMET.r1647_p306_p417
	data10_7TeV.00166094.physics_JetTauEtmiss.merge.NTUP_JETMET.r1774_p327_p417
	data10_7TeV.00166097.physics_JetTauEtmiss.merge.NTUP_JETMET.r1774_p327_p417
	data10_7TeV.00166142.physics_JetTauEtmiss.merge.NTUP_JETMET.r1774_p327_p417
	data10_7TeV.00166143.physics_JetTauEtmiss.merge.NTUP_JETMET.r1774_p327_p417
	data10_7TeV.00166198.physics_JetTauEtmiss.merge.NTUP_JETMET.r1774_p327_p417
	data10_7TeV.00166305.physics_JetTauEtmiss.merge.NTUP_JETMET.r1774_p327_p417
	data10_7TeV.00166383.physics_JetTauEtmiss.merge.NTUP_JETMET.r1774_p327_p417
H	data10_7TeV.00166466.physics_JetTauEtmiss.merge.NTUP_JETMET.r1774_p327_p417
	data10_7TeV.00166658.physics_JetTauEtmiss.merge.NTUP_JETMET.r1774_p327_p417
	data10_7TeV.00166786.physics_JetTauEtmiss.merge.NTUP_JETMET.r1774_p327_p417
	data10_7TeV.00166850.physics_JetTauEtmiss.merge.NTUP_JETMET.r1774_p327_p417
	data10_7TeV.00166850.physics_JetTauEtmiss.merge.NTUP_JETMET.r1774_p327_p417
	data10_7TeV.00166856.physics_JetTauEtmiss.merge.NTUP_JETMET.r1774_p327_p417
	data10_7TeV.00166924.physics_JetTauEtmiss.merge.NTUP_JETMET.r1774_p327_p417
	data10_7TeV.00166925.physics_JetTauEtmiss.merge.NTUP_JETMET.r1774_p327_p417
	data10_7TeV.00166927.physics_JetTauEtmiss.merge.NTUP_JETMET.r1774_p327_p417
	data10_7TeV.00166964.physics_JetTauEtmiss.merge.NTUP_JETMET.r1774_p327_p417
I	data10_7TeV.00167575.physics_JetTauEtmiss.merge.NTUP_JETMET.r1774_p327_p417
	data10_7TeV.00167576.physics_JetTauEtmiss.merge.NTUP_JETMET.r1774_p327_p417
	data10_7TeV.00167607.physics_JetTauEtmiss.merge.NTUP_JETMET.r1774_p327_p417
	data10_7TeV.00167661.physics_JetTauEtmiss.merge.NTUP_JETMET.r1774_p327_p417
	data10_7TeV.00167680.physics_JetTauEtmiss.merge.NTUP_JETMET.r1774_p327_p417
	data10_7TeV.00167776.physics_JetTauEtmiss.merge.NTUP_JETMET.r1774_p327_p417
	data10_7TeV.00167844.physics_JetTauEtmiss.merge.NTUP_JETMET.r1774_p327_p417

Appendix B

Monte Carlo Samples

There were several different full simulation Monte Carlo used in this analysis: PYTHIA, HERWIG, or ALPGEN. To simulate how these events would look in our detector, the events are run through an ATLAS detector simulation using GEANT. See Tab. B.1.

Table B.1: Datasets for the Monte Carlo samples used in this analysis. There are several datasets for the generators; each represents a specific p_T range. The samples are combined together, with appropriate weights, to produce a smooth spectrum.

PYTHIA	mc10_7TeV.105011.J2_pythia_jetjet.merge.NTUP_JETMET.e574_s934_s946_r1653_p417
	mc10_7TeV.105012.J3_pythia_jetjet.merge.NTUP_JETMET.e574_s934_s946_r1653_p417
	mc10_7TeV.105013.J4_pythia_jetjet.merge.NTUP_JETMET.e574_s934_s946_r1653_p417
	mc10_7TeV.105014.J5_pythia_jetjet.merge.NTUP_JETMET.e574_s934_s946_r1653_p417
	mc10_7TeV.105015.J6_pythia_jetjet.merge.NTUP_JETMET.e574_s934_s946_r1653_p417
	mc10_7TeV.105016.J7_pythia_jetjet.merge.NTUP_JETMET.e574_s934_s946_r1653_p417
	mc10_7TeV.105017.J8_pythia_jetjet.merge.NTUP_JETMET.e574_s934_s946_r1653_p417
	group10.perf-jets.J4_ptAndDeltaYWeighted.EW.v2_EXT0
	group10.perf-jets.J5_ptAndDeltaYWeighted.EW.v2_EXT0
	group10.perf-jets.mc10_7TeV.J6_ptAndDeltaYWeighted.v3_EXT0
HERWIG	mc10_7TeV.126137.Jimmy_jetsJ2_AUET2.merge.NTUP_JETMET.e798_s933_s946_r1831_r2040_p418
	mc10_7TeV.126138.Jimmy_jetsJ3_AUET2.merge.NTUP_JETMET.e798_s933_s946_r1831_r2040_p418
	mc10_7TeV.126139.Jimmy_jetsJ4_AUET2.merge.NTUP_JETMET.e798_s933_s946_r1831_r2040_p418
	mc10_7TeV.126140.Jimmy_jetsJ5_AUET2.merge.NTUP_JETMET.e798_s933_s946_r1831_r2040_p418
	mc10_7TeV.126141.Jimmy_jetsJ6_AUET2.merge.NTUP_JETMET.e798_s933_s946_r1831_r2040_p418
ALPGEN	mc10_7TeV.113130.AlpgenJimmyNjetsNp2_J2.merge.NTUP_JETMET.e600_s933_s946_r1652_p417
	mc10_7TeV.113131.AlpgenJimmyNjetsNp2_J3.merge.NTUP_JETMET.e600_s933_s946_r1652_p417
	mc10_7TeV.113132.AlpgenJimmyNjetsNp2_J4.merge.NTUP_JETMET.e600_s933_s946_r1652_p417
	mc10_7TeV.113133.AlpgenJimmyNjetsNp2_J5.merge.NTUP_JETMET.e600_s933_s946_r1652_p417
	mc10_7TeV.113134.AlpgenJimmyNjetsNp2_J6p.merge.NTUP_JETMET.e600_s933_s946_r1652_p417
	mc10_7TeV.113136.AlpgenJimmyNjetsNp3_J2.merge.NTUP_JETMET.e600_s933_s946_r1652_p417
	mc10_7TeV.113137.AlpgenJimmyNjetsNp3_J3.merge.NTUP_JETMET.e600_s933_s946_r1652_p417
	mc10_7TeV.113138.AlpgenJimmyNjetsNp3_J4.merge.NTUP_JETMET.e600_s933_s946_r1652_p417
	mc10_7TeV.113139.AlpgenJimmyNjetsNp3_J5.merge.NTUP_JETMET.e600_s933_s946_r1652_p417
	mc10_7TeV.113140.AlpgenJimmyNjetsNp3_J6p.merge.NTUP_JETMET.e600_s933_s946_r1652_p417
	mc10_7TeV.113142.AlpgenJimmyNjetsNp4_J2.merge.NTUP_JETMET.e600_s933_s946_r1652_p417
	mc10_7TeV.113143.AlpgenJimmyNjetsNp4_J3.merge.NTUP_JETMET.e600_s933_s946_r1652_p417
	mc10_7TeV.113144.AlpgenJimmyNjetsNp4_J4.merge.NTUP_JETMET.e600_s933_s946_r1652_p417
	mc10_7TeV.113145.AlpgenJimmyNjetsNp4_J5.merge.NTUP_JETMET.e600_s933_s946_r1652_p417
	mc10_7TeV.113146.AlpgenJimmyNjetsNp4_J6p.merge.NTUP_JETMET.e600_s933_s946_r1652_p417
	mc10_7TeV.113148.AlpgenJimmyNjetsNp5_J2.merge.NTUP_JETMET.e600_s933_s946_r1652_p417
	mc10_7TeV.113149.AlpgenJimmyNjetsNp5_J3.merge.NTUP_JETMET.e600_s933_s946_r1652_p417
	mc10_7TeV.113150.AlpgenJimmyNjetsNp5_J4.merge.NTUP_JETMET.e600_s933_s946_r1652_p417
	mc10_7TeV.113151.AlpgenJimmyNjetsNp5_J5.merge.NTUP_JETMET.e600_s933_s946_r1652_p417
	mc10_7TeV.113152.AlpgenJimmyNjetsNp5_J6p.merge.NTUP_JETMET.e600_s933_s946_r1652_p417
	mc10_7TeV.113154.AlpgenJimmyNjetsNp6_J2.merge.NTUP_JETMET.e600_s933_s946_r1652_p417
	mc10_7TeV.113155.AlpgenJimmyNjetsNp6_J3.merge.NTUP_JETMET.e600_s933_s946_r1652_p417
	mc10_7TeV.113156.AlpgenJimmyNjetsNp6_J4.merge.NTUP_JETMET.e600_s933_s946_r1652_p417
	mc10_7TeV.113157.AlpgenJimmyNjetsNp6_J5.merge.NTUP_JETMET.e600_s933_s946_r1652_p417
	mc10_7TeV.113158.AlpgenJimmyNjetsNp6_J6p.merge.NTUP_JETMET.e600_s933_s946_r1652_p417

Appendix C

Jet Kinematic Studies

The kinematic distributions for the third-leading and fourth-leading jets in events which satisfy the event quality cuts and reconstructed jets satisfy the jet quality and observable requirements for $\Delta\phi$ and Δy can be seen in Figs. C.1-C.6. The PYTHIA Monte Carlo distributions are scaled to the number of dijet events in data. The comparison is done for all jet within $|y| < 2.8$ and the four different trigger regions consisting of p_T bins $110 - 160$ GeV, $160 - 210$ GeV, $210 - 260$ GeV, and > 260 GeV. There is reasonable agreement between data and Monte Carlo within errors.

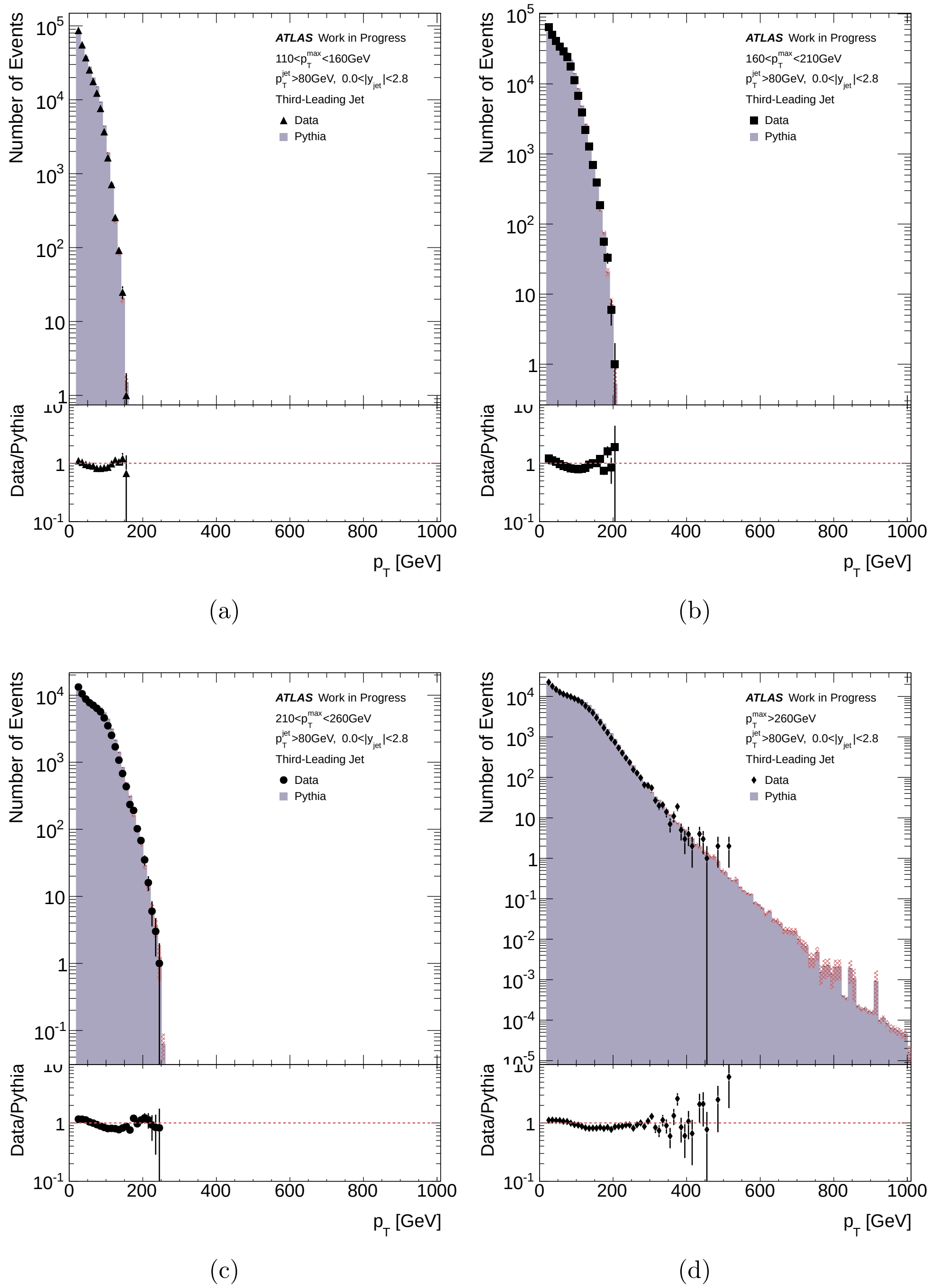

Figure C.1: The p_{T} of the third-leading jet for $p_{\mathrm{T}}^{\mathrm{max}}$ bins $110 - 160$ GeV, $160 - 210$ GeV, $210 - 260$ GeV, and > 260 GeV.

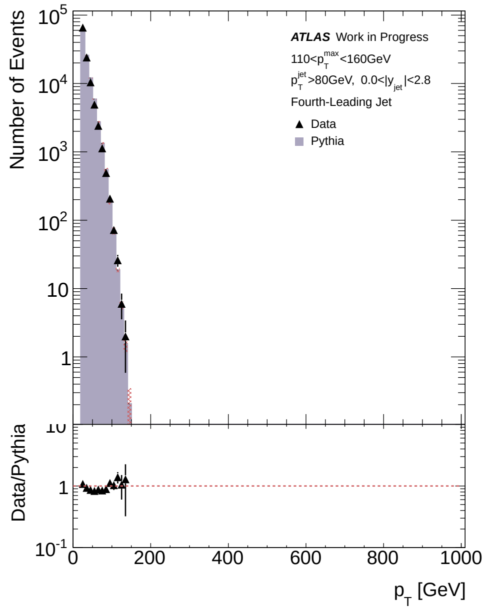

(a)

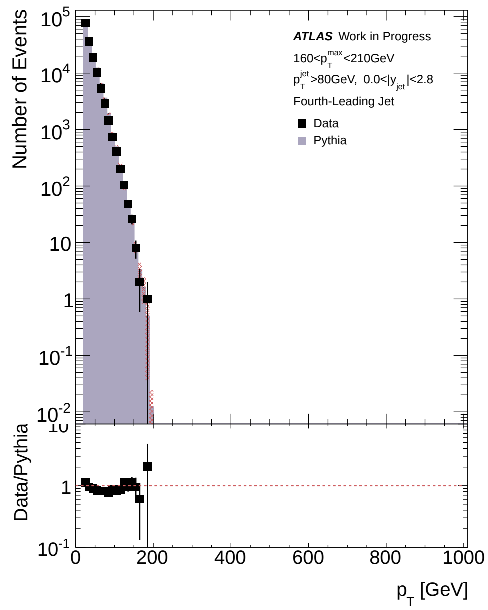

(b)

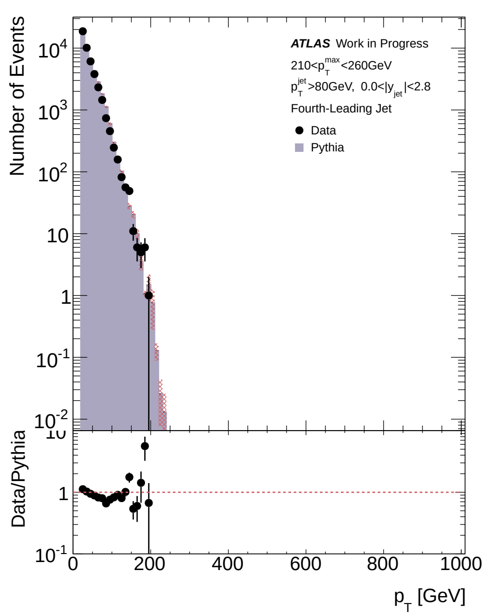

(c)

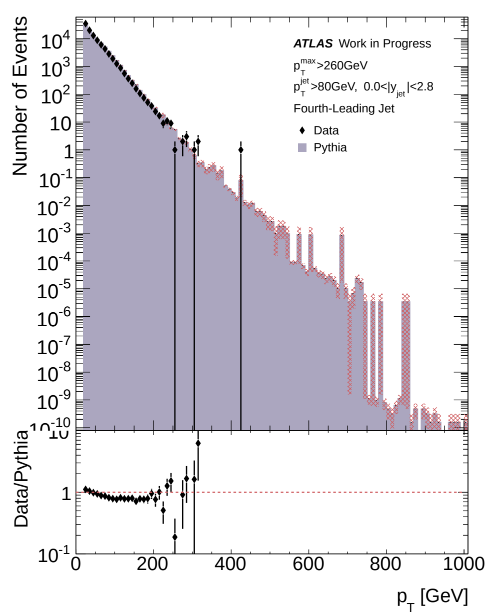

(d)

Figure C.2: The p_{T} of the fourth-leading jet for $p_{\mathrm{T}}^{\mathrm{max}}$ bins $110-160$ GeV, $160-210$ GeV, $210-260$ GeV, and > 260 GeV.

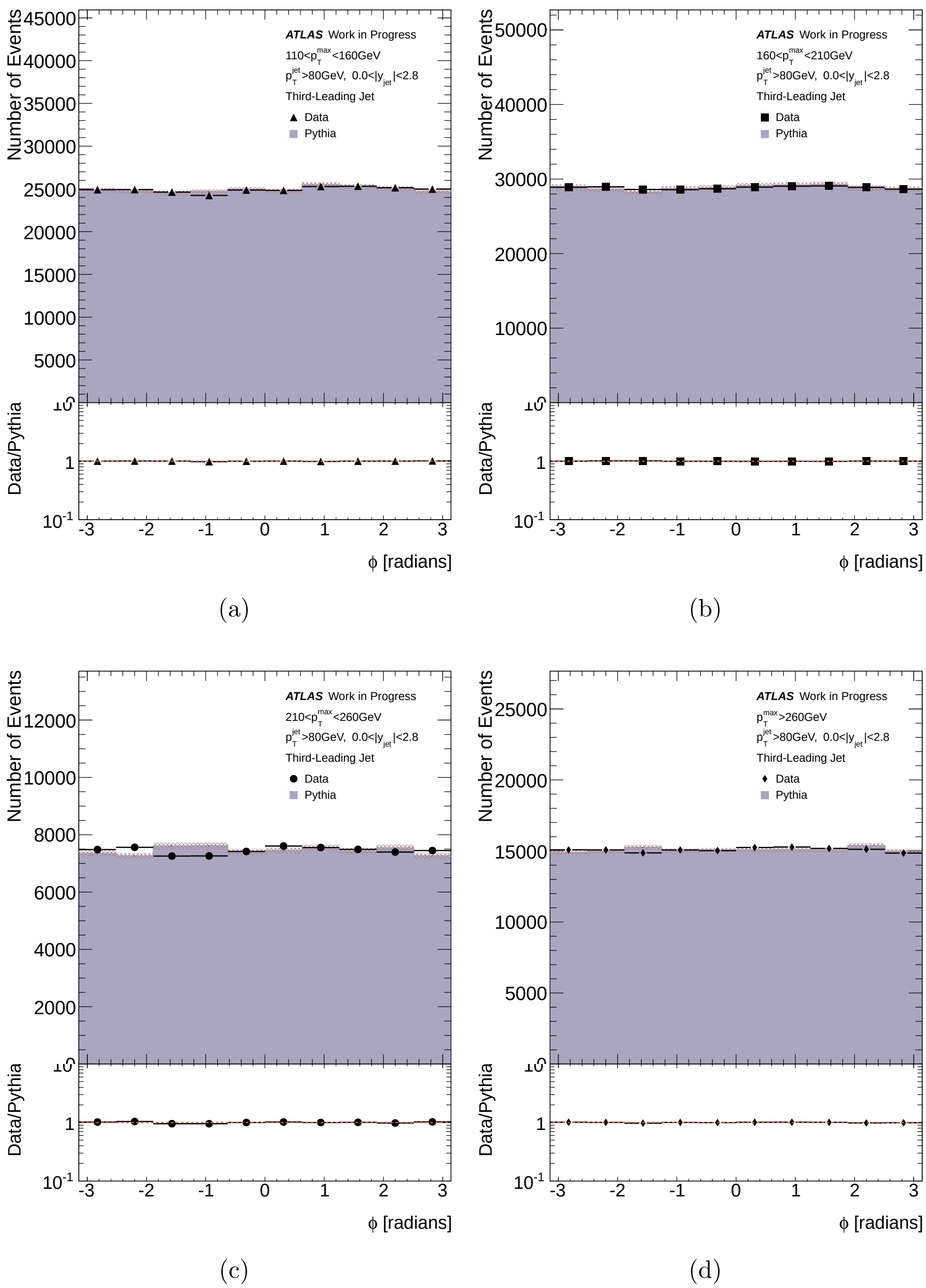

Figure C.3: The ϕ of the third-leading jet for $p_{\mathrm{T}}^{\mathrm{max}}$ bins $110-160$ GeV, $160-210$ GeV, $210-260$ GeV, and >260 GeV.

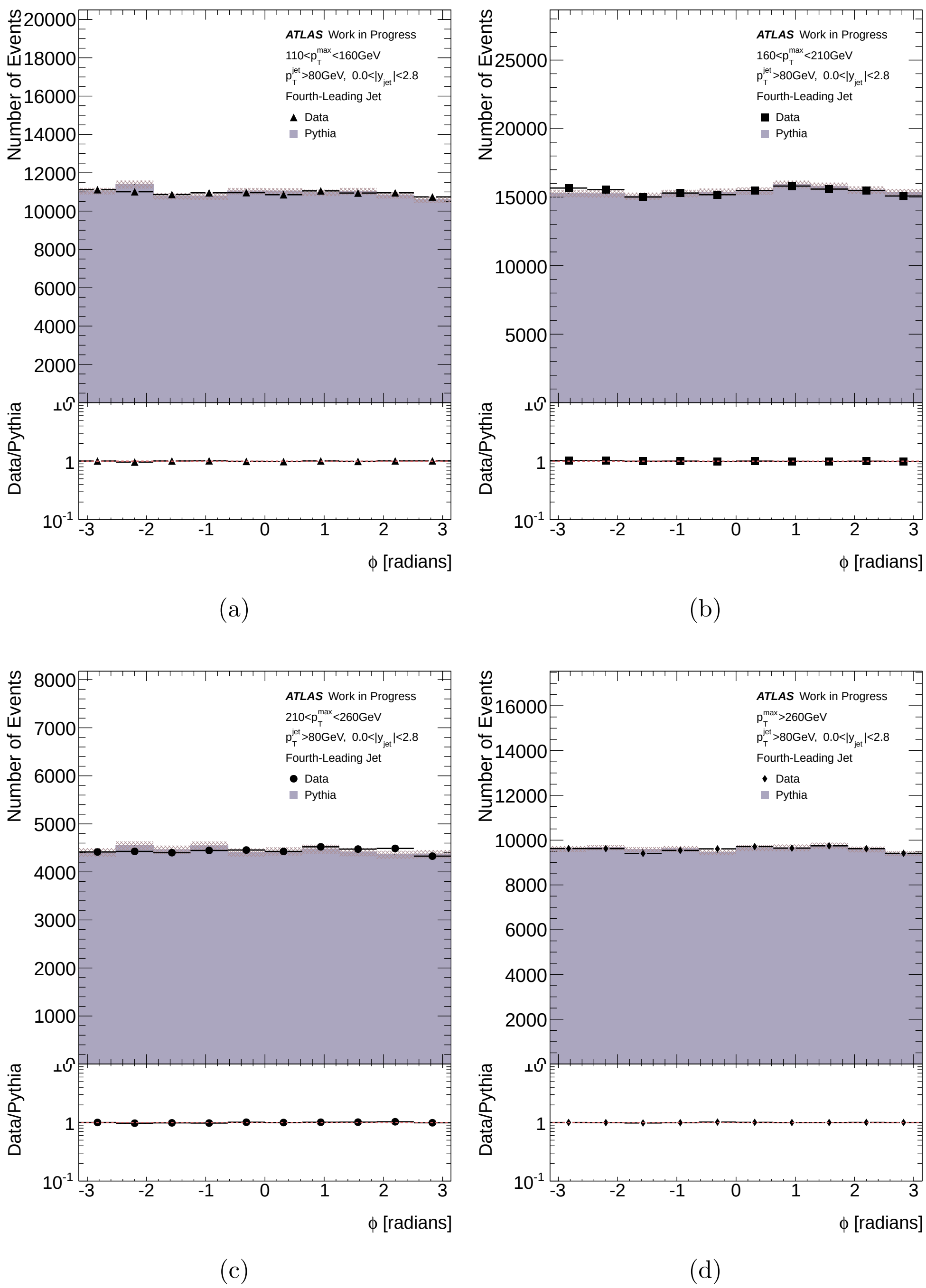

Figure C.4: The ϕ of the fourth-leading jet for $p_{\mathrm{T}}^{\mathrm{max}}$ bins $110-160$ GeV, $160-210$ GeV, $210-260$ GeV, and >260 GeV.

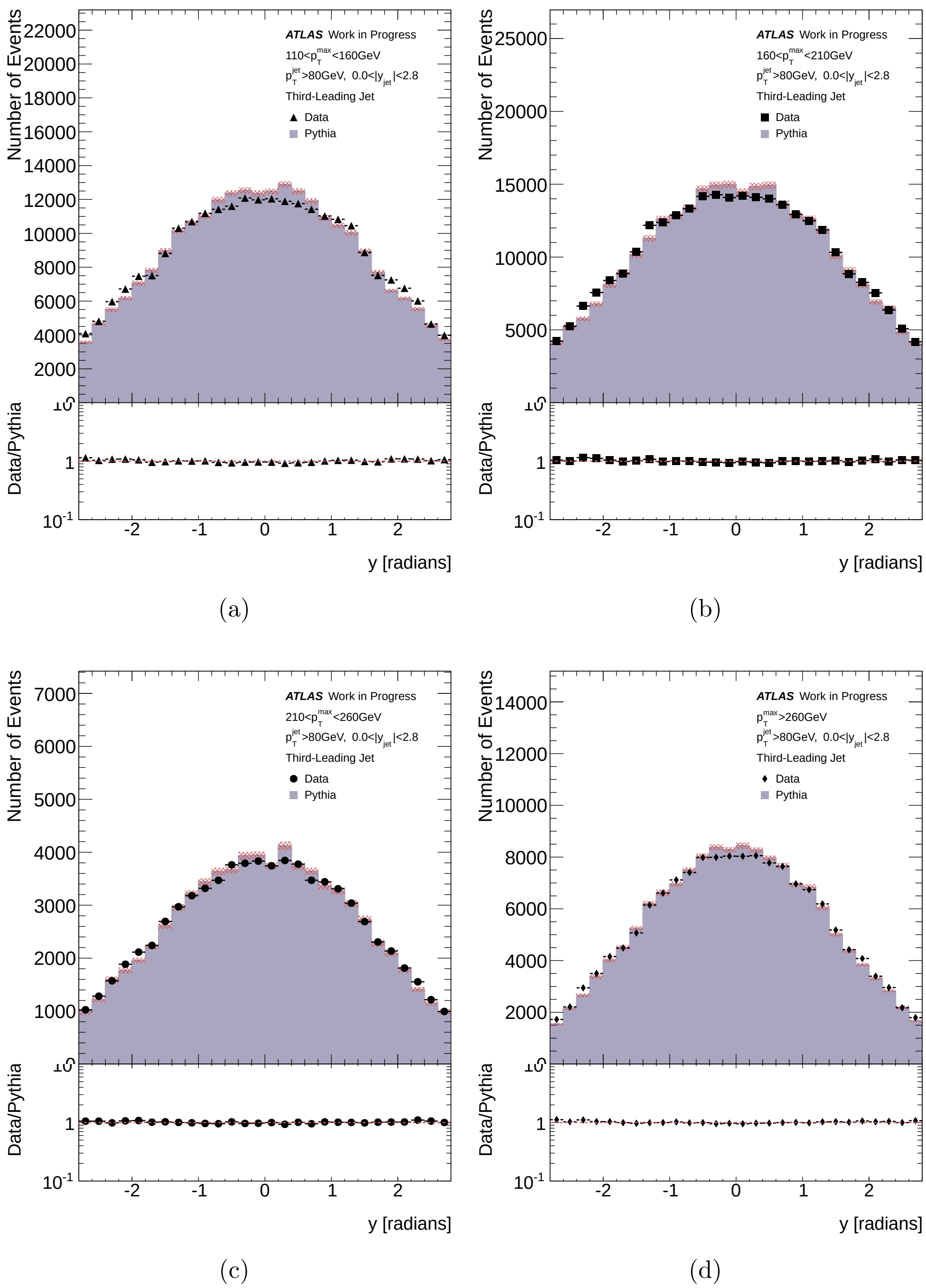

Figure C.5: The y of the third-leading jet for $p_{\mathrm{T}}^{\max}$ bins $110 - 160$ GeV, $160 - 210$ GeV, $210 - 260$ GeV, and > 260 GeV.

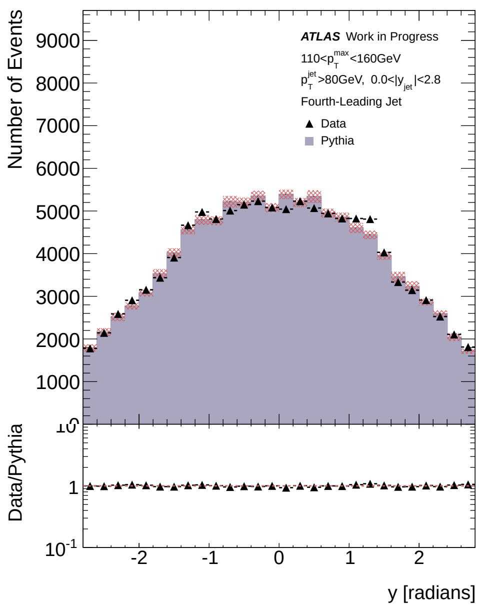

(a)

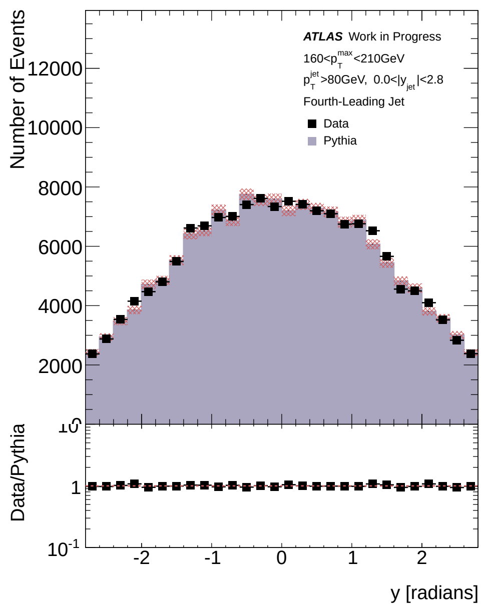

(b)

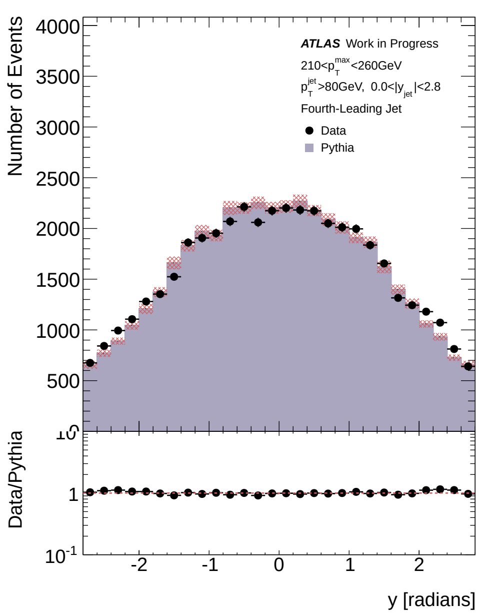

(c)

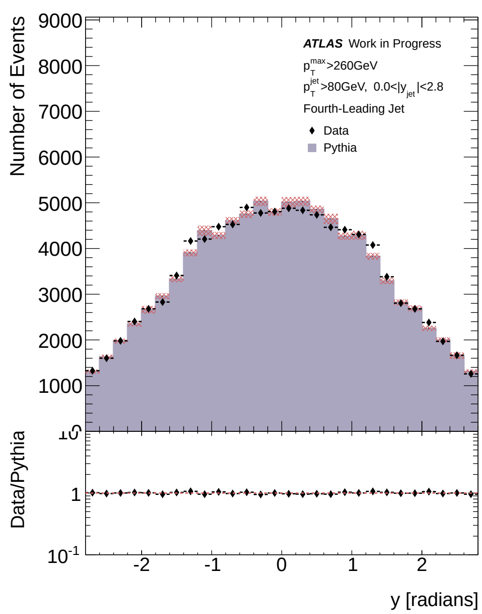

(d)

Figure C.6: The y of the fourth-leading jet for $p_{\mathrm{T}}^{\max}$ bins $110 - 160$ GeV, $160 - 210$ GeV, $210 - 260$ GeV, and > 260 GeV.

Appendix D

Resolution Studies

The angular resolution is found as the largest difference between truth and reconstruction jet ϕ and rapidity for all good jets in an event. The resolution is plotted for all events per each p_T^{max} bin. The Figs. D.1-D.2 show the resolution distribution and the Gaussian fits for each p_T^{max} bin. The distribution is fitted by a Gaussian, and the width of the Gaussian (σ) is extracted. The mean value of the Gaussian is expected to be zero. The mean is taken as the value and σ is taken as the error.

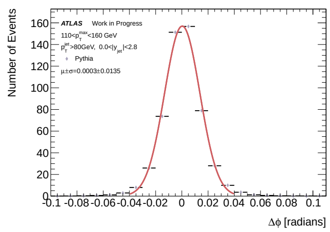

(a)

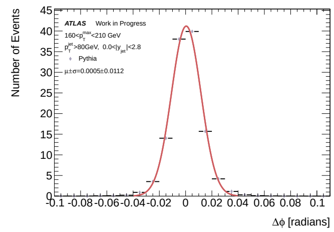

(b)

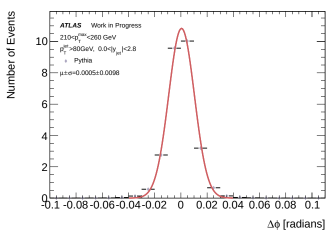

(c)

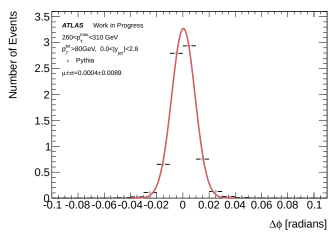

(d)

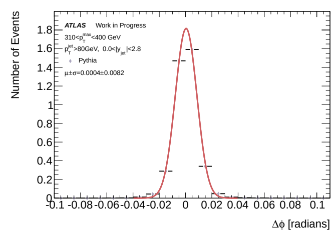

(e)

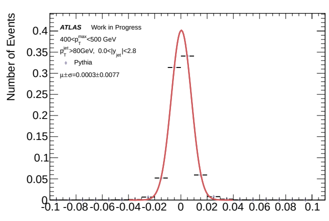

(f)

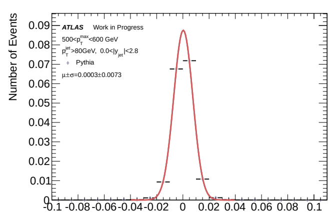

(g)

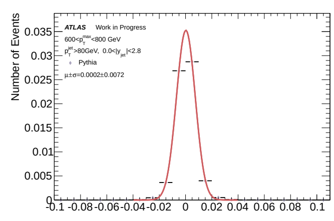

(h)

Figure D.1: The ϕ resolution and the Gaussian fit to the resultant distribution for $p_{\mathrm{T}}^{\max}$ bin $110-160$ GeV, $160-210$ GeV, $210-260$ GeV, $260-310$ GeV, $310-400$ GeV, $400-500$ GeV, $500-600$ GeV, and $600-800$ GeV.

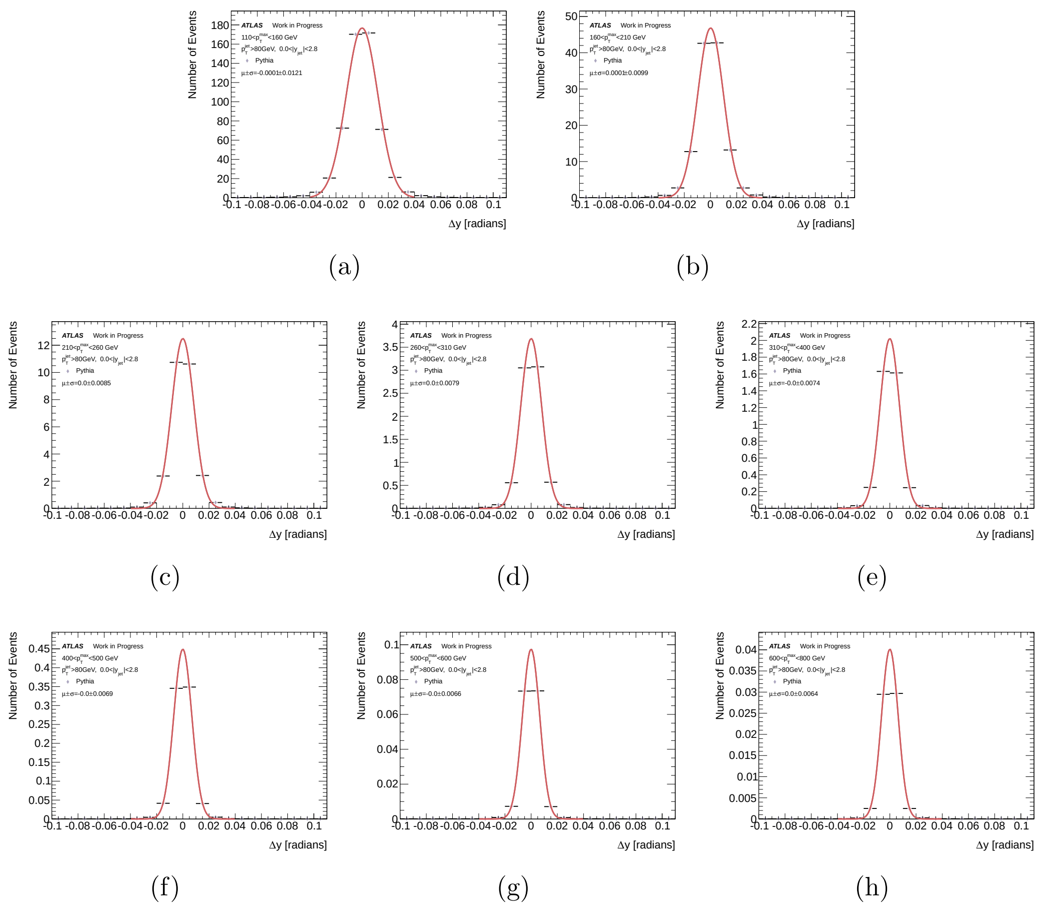

Figure D.2: The rapidity resolution and the Gaussian fit to the resultant distribution for $p_{\mathrm{T}}^{\mathrm{max}}$ bin $110-160$ GeV, $160-210$ GeV, $210-260$ GeV, $260-310$ GeV, $310-400$ GeV, $400-500$ GeV, $500-600$ GeV, and $600-800$ GeV.

Appendix E

Unfolding Studies

The observables are formed as outlined in Chap. 4 for the truth and reconstructed jets in PYTHIA using the event and jet selection described in Chaps. 6-5. This is done for both $\Delta\phi$ and Δy,

Then the truth distribution is divided by the reconstructed distribution. The result gives the unfolding factors used for correcting the reconstructed distribution back to the truth information. This is done for each of our observables. These same unfolding factors will be applied to data to correct for experimental effects and bring the data back to the particle level.

The unfolding factor is applied by multiplying the reconstructed distribution by the unfolding correction factors. The resultant distributions, seen Figs. E.1-E.2 for each p_T^{max} bin, should be the same as the truth distributions. The data is also multiplied bin-by-bin by the unfolding factors. The statistical error is shown for both data and PYTHIA.

To test that the corrected reconstructed distribution is the same as the truth distribution, the unfolded reconstructed distribution is divided by the truth distribution. Closure is achieved. This is seen as Figs. E.3-E.4, the closure test distribution is one for every bin. The data is also divided by the truth PYTHIA distribution. This is done to more clearly show the agreement between data and PYTHIA where statistics allow.

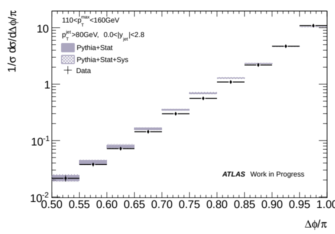

(a)

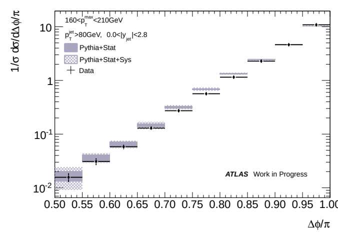

(b)

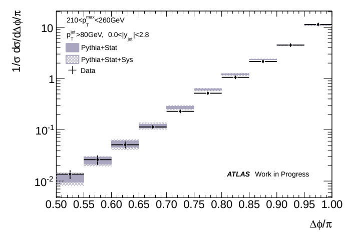

(c)

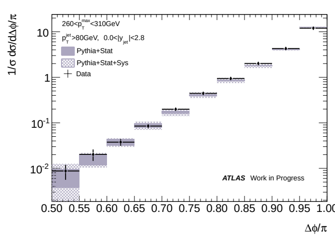

(d)

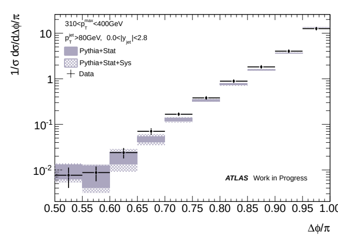

(e)

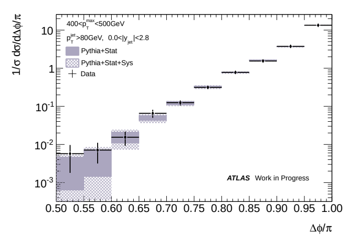

(f)

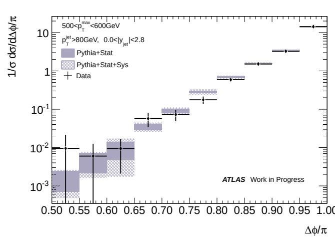

(g)

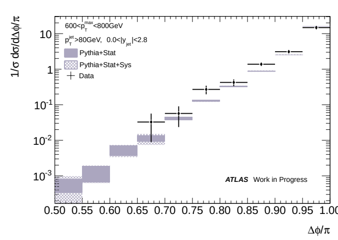

(h)

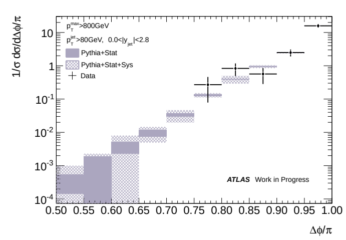

(i)

Figure E.1: The $\Delta\phi$ unfolded distributions for $p_{\mathrm{T}}^{\max}$ bin $110-160$ GeV, $160-210$ GeV, $210-260$ GeV, $260-310$ GeV, $310-400$ GeV, $400-500$ GeV, $500-600$ GeV, and $600-800$ GeV.

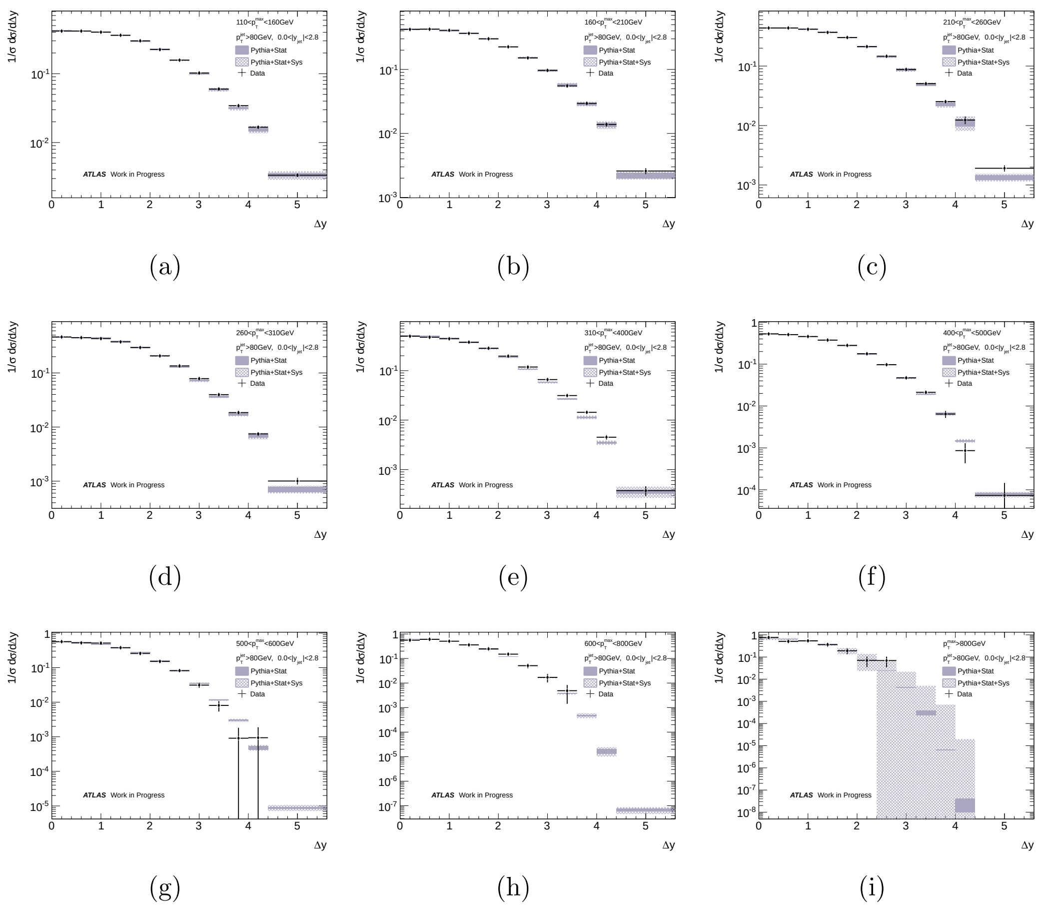

Figure E.2: The Δy unfolded distributions for $p_{\mathrm{T}}^{\mathrm{max}}$ bin $110-160$ GeV, $160-210$ GeV, $210-260$ GeV, $260-310$ GeV, $310-400$ GeV, $400-500$ GeV, $500-600$ GeV, and $600-800$ GeV.

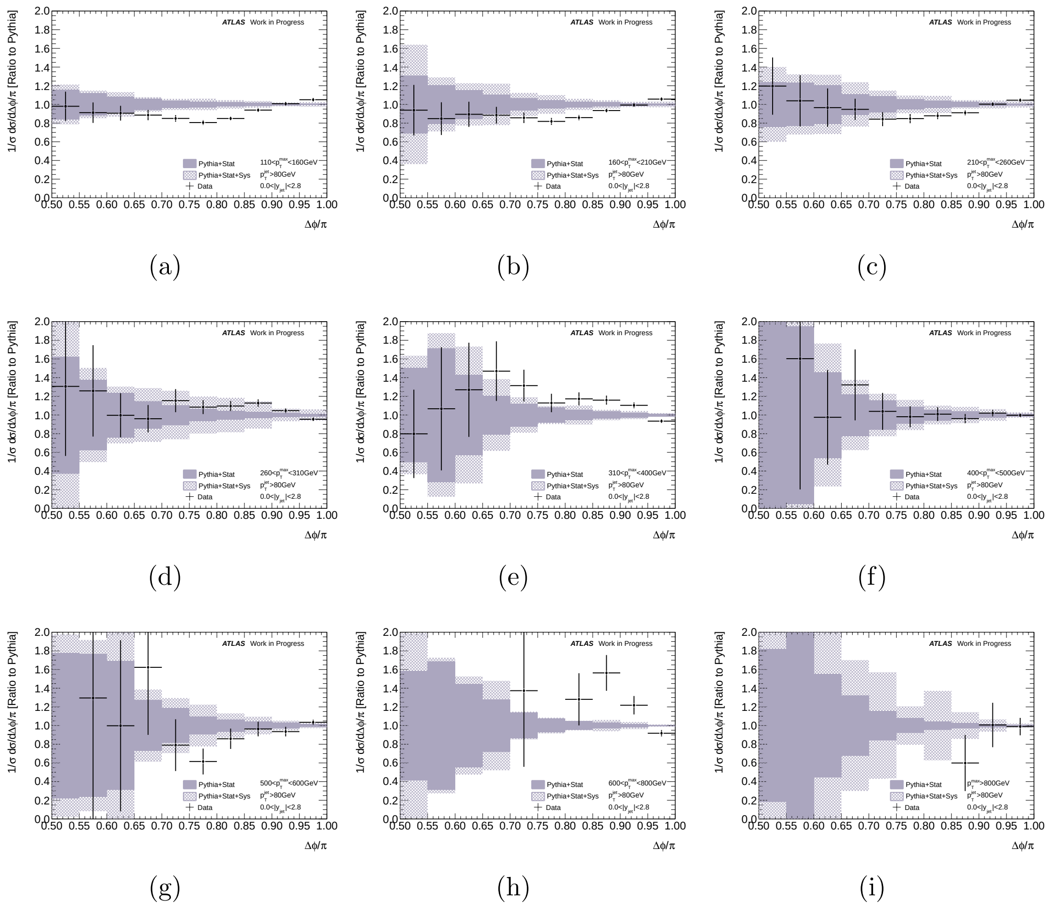

Figure E.3: The closure test for $\Delta\phi$ unfolding for $p_{\mathrm{T}}^{\max}$ bin $110-160$ GeV, $160-210$ GeV, $210-260$ GeV, $260-310$ GeV, $310-400$ GeV, $400-500$ GeV, $500-600$ GeV, and $600-800$ GeV.

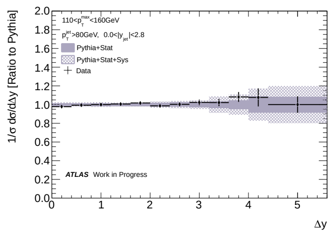

(a)

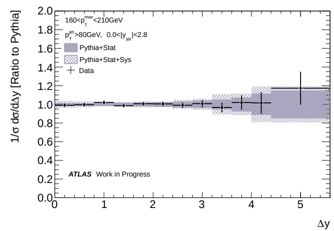

(b)

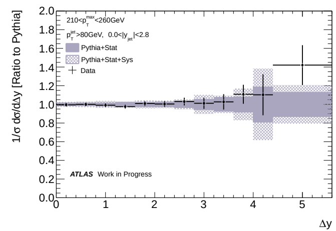

(c)

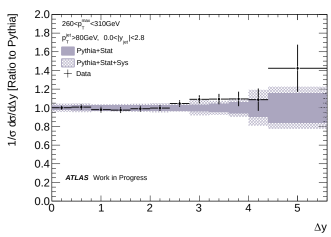

(d)

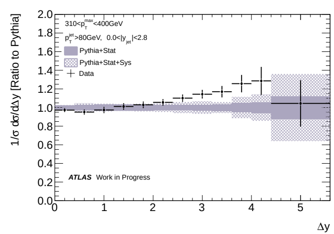

(e)

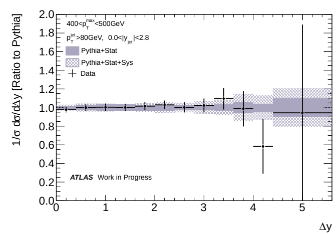

(f)

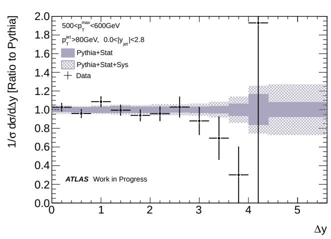

(g)

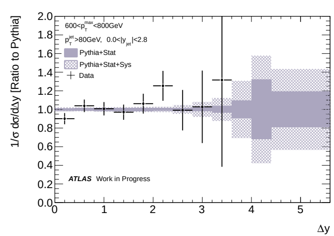

(h)

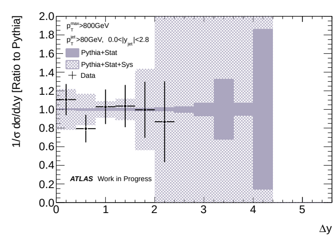

(i)

Figure E.4: The closure test for Δy unfolding for $p_{\mathrm{T}}^{\max}$ bin $110-160$ GeV, $160-210$ GeV, $210-260$ GeV, $260-310$ GeV, $310-400$ GeV, $400-500$ GeV, $500-600$ GeV, and $600-800$ GeV.